

Bangor University

DOCTOR OF PHILOSOPHY

All-dielectric superlens and applications

Yan, Bing

Award date:
2018

Awarding institution:
Bangor University

[Link to publication](#)

General rights

Copyright and moral rights for the publications made accessible in the public portal are retained by the authors and/or other copyright owners and it is a condition of accessing publications that users recognise and abide by the legal requirements associated with these rights.

- Users may download and print one copy of any publication from the public portal for the purpose of private study or research.
- You may not further distribute the material or use it for any profit-making activity or commercial gain
- You may freely distribute the URL identifying the publication in the public portal ?

Take down policy

If you believe that this document breaches copyright please contact us providing details, and we will remove access to the work immediately and investigate your claim.

Download date: 13. Mar. 2024

ALL-DIELECTRIC SUPERLENS AND APPLICATIONS



PRIFYSGOL
BANGOR
UNIVERSITY

Bing Yan

School of Electronic Engineering
Bangor University

A thesis submitted in partial fulfilment for the degree of

Doctor of Philosophy

May 2018

Acknowledgements

First and foremost, I would like to express my sincere gratitude to my supervisor Dr Zengbo Wang for giving me this opportunity to work on such an exciting topic, and for his constant support during my entire PhD study and research. His guidance helped me in all time of research and writing of this thesis. I could not have imagined having a better advisor and mentor for my PhD study.

During my PhD study, I have visited Swansea University and worked with many fascinating people for six months. Therefore, my sincere thank goes to Prof. Owen Guy, for his support and the use of equipment in their clean room. I would also like to thank Prof. Perumal Nithiarasu for his valuable guidance on the simulation works. So many interesting results were produced during that period. I have to say that I had an unforgettable half-year studying experience in Swansea University.

I would like to thank the Sêr Cymru National Research Network for the financial support during this research.

In addition, I want to thank my colleagues in Bangor: Dr Liyang Yue, Dr Rakesh Dhama Mr James Norman Monks, Dr Yanhua Hong and Dr Paul Sayers for their continuous support in research and friendly helps in my daily life. Also, I thank my friends Chen Liu, Songkun Ji, Mingliang Deng, Yixian Dong who are PhD students from different research groups in School of Electronic Engineering at Bangor University. They let me, an overseas student, have the feeling of hometown during my three-year intensive PhD life.

Without my parents I would have never accomplished so much. I would like to thank them, for giving birth to me and encouraging and supporting me financially and spiritually throughout my life.

Thank you, my wife Aijun, who is always there for me, no matter the best and the worst, the difficult and the easy. No words can express my gratitude to you. Thank you, my son Ethan, your smile is my biggest driving force.

Abstract

One of the great challenges in optics is to break the diffraction limit to achieve optical super-resolution for applications in imaging, sensing, manufacturing and characterization. In recent years we witnessed a number of exciting developments in this field, including for example super-resolution fluorescent microscopy, negative-index metamaterial superlens and super-oscillation lens. However, none of them can perform white-light super-resolution imaging until the development of microsphere nanoscopy technique, which was pioneered by the current PhD's research group.

The microscope nanoscopy technique was developed based on all-dielectric microsphere superlens which is fundamentally different from metal-based superlenses. In this research, we aim to significantly advance the technology by: (1) increasing superlens resolution to sub-50 nm scale and (2) improving superlens usability and demonstrate application in wider context including lab-on-chip devices. Our longer-term vision is to bring the all-dielectric superlens technology to market so that each microscope user can have superlens in hand for their daily examination of nanoscale objects including viruses.

To improve the superlens resolution, a systematic theoretical study was first carried out on the optical properties of dielectric microsphere superlens. New approaches were proposed to obtain precise control of the focusing properties of the microsphere lens. Using pupil mask engineering and two-material composite superlens design, one can precisely control the focusing properties of the lens and effectively surpass the diffraction limit $\lambda/2n$.

To further improve the resolution, we incorporated the metamaterial concept in our superlens design. A new all-dielectric nanoparticle metamaterial superlens design was proposed. This is realized by 3D stacking of high-index nanoparticles to form a micro-sized particle lens. This man-made superlens has unusual optical properties not found in nature: highly effective conversion of evanescent wave to propagating wave for unprecedented optical super-resolution. By using 15 nm TiO_2 nanoparticles as building blocks, the fabricated 3D all-dielectric metamaterial-based solid immersion lens (mSIL) can produce a sharp image with a super-resolution of at least 45 nm under a white-light optical microscope, significantly exceeding the classical diffraction limit and previous near-field imaging techniques. In addition to mSIL where only one kind of nanoparticle was used, we also studied two-

nanomaterial hybrid system. High-quality microspheres consisting of ZrO_2 /polystyrene elements were synthesised and studied. We show precise tuning of the refractive index of microspheres can effectively enhance the imaging resolution and quality.

To increase superlens usability and application scope, we proposed and demonstrated a new microscope objective lens that features a two times resolution improvement over conventional objective. This is accomplished by integrating a conventional microscope objective lens with a superlensing microsphere lens with a customised lens adaptor. The new objective lens was successfully demonstrated for label-free super-resolution static and scanning imaging of 100 nm features in engineering and biological samples.

In an effort to reduce superlens technology entrance barrier, we studied several spider silks as naturally occurring optical superlens. These spider silks are transparent in nature and have micron-scale cylinder structure. They can distinctly resolve $\lambda/6$ features with a large field-of-view under a conventional white-light microscope. This discovery opens a new door to develop biology-based optical systems and has enriched the superlens category.

Because microsphere superlenses are small in size, their application can be extended to lab-on-chip device. In this thesis, microsphere superlens was introduced to a microfluidic channel to build an on-chip microfluidic superlensing device for real-time high-resolution imaging of biological objects. Several biological samples with different features in size, transparency, low contrast and strong mobility have been visualised. This integrated device provides a new way to allow researchers to directly visualise details of biological specimens in real-time under a conventional white light microscope.

The work carried out in this research has significantly improved the microsphere superlens technology which opens the door for commercial exploitation.

Table of Contents

Declaration and Consent	I
Acknowledgements	V
Abstract	VI
Table of Contents	i
List of Tables	v
List of Figures	vi
List of Publications	xix
Chapter 1. Introduction.....	1
1.1 Optical super-resolution	1
1.2 Aim and objectives	2
1.3 Thesis outline.....	4
Chapter 2. Literature Review.....	7
2.1 Optical diffraction limit	7
2.2 Super-resolution with near-field optics.....	8
2.3 Super-resolution techniques.....	9
2.3.1 Near-field Scanning Optical Microscope (NSOM or SNOM).....	9
2.3.2 Metal-based Metamaterial Superlens and Hyperlens (M-MSH).....	11
2.3.3 Super-Oscillation Lenses	14
2.3.4 Structured Illumination Microscopy (SIM)	16
2.3.5 Super-resolution Fluorescent Microscopy.....	17
2.3.6 Other techniques	19
2.4 Microsphere super-resolution imaging technique	21
2.4.1 Photonic nanojet.....	21
2.4.2 Wide-field microsphere superlens.....	23

2.4.3	Confocal microsphere superlens	25
2.4.4	Scanning microsphere superlens	26
2.4.5	Other developments	28
2.5	Theoretical methods for super-resolution simulation	31
2.5.1	Mie theory.....	32
2.5.2	Numerical methods.....	35
Chapter 3.	Research Methodology	38
3.1	Introduction	38
3.2	Theoretical works	38
3.2.1	Calculation of near-field focusing of dielectric microsphere.....	38
3.2.2	Engineered microsphere: design and optimisation	41
3.3	Experimental works	45
3.3.1	limitations of ordinary microsphere superlens	45
3.3.2	Procedures for fabricating coverslip microsphere superlens (CMS)	46
3.3.3	Manufacturing of superlensing microsphere objective lens	53
3.3.4	Methods for preparing ordered array of microsphere superlens	55
3.3.5	Method for fabricating hemi-sphere metamaterial solid immersion lens (mSIL).	60
3.3.6	Fabrication of hybrid microsphere superlens.....	65
3.3.7	Spider Silk Superlens Preparation.....	67
3.3.8	On-chip Microfluidic Superlens Fabrication	68
3.3.9	Characterisation equipment	72
Chapter 4.	Near-field Super-Resolution Focusing of Microsphere Lens	74
4.1	Introduction	74
4.2	Near-fields of a dielectric sphere: focal length and super-resolution	75
4.3	Full-wave white-light spectral analysis of microsphere focusing characteristics	84

4.4	Conclusions	88
Chapter 5. Design and Optimisation of Engineered Micro-Lens for Enhanced Optical Super-resolution..... 89		
5.1	Introduction	89
5.2	Pupil mask assisted microsphere lens	90
5.3	Composite material microsphere lens	97
5.4	Combination design of pupil mask and composite materials onto microsphere lens.....	103
5.5	Dielectric nanoparticle-based metamaterial superlens	106
5.6	Conclusion.....	110
Chapter 6. Superlensing Metamaterial Solid Immersion Lens (mSIL) and Nanohybrid Lens 112		
6.1	Introduction	112
6.2	Dielectric nanoparticles derived metamaterial solid immersion lens (mSIL).....	114
6.2.1	Investigation of field-of-view and magnification factor of TiO ₂ mSIL.....	115
6.2.2	Super-resolution imaging performance of TiO ₂ mSIL.....	119
6.3	ZrO ₂ /PS nanohybrid microsphere superlens.....	123
6.3.1	Morphology and structure of the MPS/OA/ZrO ₂ nanocrystals and ZrO ₂ /Poly(St-co-DVB) composite microspheres	124
6.3.2	Super-resolution imaging: wide-field mode and white light illumination.....	130
6.3.3	Super-resolution imaging: confocal mode and laser illumination	132
6.4	Conclusion.....	133
Chapter 7. Superlensing Microscope Objective Lens 136		
7.1	Introduction	136
7.2	Superlensing microscope objective	137
7.3	Superlensing objective lens in static and scanning imaging performance	138
7.3.1	Static Imaging.....	138

7.3.2	Scanning Imaging and Image Stitch	141
7.4	Mechanism and discussion	142
7.5	Superlensing objective lens in nano-scale laser patterning performance	144
7.5.1	Patterning resolution analysis	146
7.5.2	Scanning patterning	149
7.6	Conclusion.....	152
Chapter 8.	Bio-superlens and On-chip Microfluidic Nanoscope	153
8.1	Introduction	153
8.2	Bio-superlens: spider silk.....	154
8.2.1	Optical imaging	154
8.2.2	Theoretical calculation.....	158
8.3	Bio-sample imaging through an integration device of microsphere superlens and microfluidic channel.....	160
8.3.1	Optical imaging	161
8.4	Conclusion.....	164
Chapter 9.	Conclusions and Future Work.....	166
9.1	Conclusions	166
9.2	Future work.....	169
References	171

List of Tables

Table 3.1 Detailed data of BTG microspheres.

Table 3.2 PDMS Properties.

Table 3.3 MMA properties.

Table 3.4 BPO properties.

Table 3.5 Materials for fabricating hybrid microsphere.

Table 4.1 'Extreme' super-resolution foci for $n=1.6$ microsphere.

Table 4.2 Summarised result from Figure 3.11 and Figure 3.12.

Table 5.1 Summarised results from Figure 5.3 and Figure 5.4.

Table 5.2 Optimized FWHM with crucial cutting height for $1.76 \leq n_{p2} \leq 2.66$.

Table 5.3 Comparisons of centre and side enhancement with various sizes of mask.

Table 6.1 SEM linescan results of Zr, O, and C content in M1~M5

Table 6.2 Theoretical refractive index of M0~M5.

Table 7.1 Average patterning future size by three different size microspheres and at different focal plane.

List of Figures

FIGURE 1.1 SUMMARY OF PHD WORKS WHICH ARE GROUPED ALONG TWO PATHS, RESOLUTION ENHANCEMENT AND EASE OF USABILITY.	2
FIGURE 2.1 MODES OF NSOM. (A-D) APERTURE MODE, AND (E) APERTURELESS MODE. (A) APERTURED TIP GENERATES ILLUMINATION AND TRANSMITTED SIGNAL IS COLLECTED BY EXTERNAL DETECTOR, (B) SCATTERED SIGNAL COLLECTION BY THE TIP, (C) REFLECTED SIGNAL COLLECTION BY THE TIP, AND (D) EXTERNAL ILLUMINATION AND COLLECTION BY THE TIP. (E) ILLUMINATION FROM EXTERNAL SOURCE AND COLLECTION BY AN APERTURELESS NSOM TIP[18].	10
FIGURE 2.2 COMPARISON OF VARIOUS TYPES OF OPTICAL LENSES. BLUE AND RED CURVES ARE THE PROPAGATING AND THE EVANESCENT WAVES, RESPECTIVELY. (A) CONVENTIONAL LENS. (B) NEAR-FIELD SUPERLENS. (C) FAR-FIELD SUPERLENS. (D) HYPERLENS. THE WAVY CURVES AND SMOOTH CURVES REPRESENT PROPAGATING WAVES AND EVANESCENT WAVES, RESPECTIVELY[23].	12
FIGURE 2.3 (A) SCHEMATIC CONFIGURATION FOR THE SILVER SUPERLENS EXPERIMENT. PR, PHOTORESIST LAYER; PMMA, POLYMETHYLMETHACRYLATE. THE SUPERLENS IMAGE WAS REVEALED BY MEANS OF PHOTOLITHOGRAPHY AT WAVELENGTH $\lambda = 365$ NM. (B) FOCUSED ION BEAM (FIB) IMAGE OF THE OBJECT. THE LINEWIDTH OF THE “NANO” OBJECT WAS 40 NM. (C) AFM OF THE DEVELOPED IMAGE ON PHOTORESIST WITH A SILVER SUPERLENS. SCALE BAR IS 2 MM IN (B) AND (C) [26].	13
FIGURE 2.4 SCHEMATIC DESIGN OF FAR-FIELD SUPERLENS (FSL). A FSL IS CONSTRUCTED BY ADDING A SUBWAVELENGTH GRATING ONTO A THIN SILVER SLAB. A FSL IS INSERTED BETWEEN THE SPECIMEN AND OBJECTIVE OF OPTICAL MICROSCOPE TO REALISE FAR-FIELD SUPER-RESOLUTION IMAGING. [28].	13
FIGURE 2.5 (A) SCHEMATIC OF EXPERIMENTAL SET-UP FOR OPTICAL HYPERLENS AND NUMERICAL SIMULATION OF SUB-DIFFRACTION-LIMIT IMAGING. (B) SEM IMAGE OF CROSS-SECTION OF A CYLINDRICAL HYPERLENS. (C) SEM IMAGE OF OBJECT WITH 50 NM LINEWIDTH AND 80 NM GAP[31].	14
FIGURE 2.6 SUBWAVELENGTH IMAGING WITH A SUPER-OSCILLATORY LENS. (A) SEM IMAGE OF THE SUPER-OSCILLATION LENS. (B) CALCULATED ENERGY DISTRIBUTION OF THE SUPER-OSCILLATORY LENS AT $10.3 \mu\text{m}$ FROM THE LENS. (C) THE ACTUAL FOCAL POINT, $\lambda=640\text{nm}$. (D) SEM IMAGE OF A 112 NM SLIT AND (E) ITS SUPER-OSCILLATORY LENS IMAGE; (F) A DOUBLE SLIT AND (G) ITS SUPER-OSCILLATORY LENS IMAGE. (H) THE IMAGE OF THE SAME DOUBLE SLIT IS NOT RESOLVED USING A CONVENTIONAL LENS OF $\text{NA}=1.4$ [6].	15
FIGURE 2.7 (A-C) SCHEMATIC OF STRUCTURED ILLUMINATION MICROSCOPY. COMPARISON OF (D) CONVENTIONAL MICROSCOPY IMAGE AND (E) STRUCTURED ILLUMINATION MICROSCOPY IMAGE OF MITOCHONDRIAL AND ACTIN CYTOSKELETON[44].	16
FIGURE 2.8 (A) MECHANISM OF STED MICROSCOPY. COMBINED BEAM FROM EXCITATION AND DEPLETION IN STED MICROSCOPY. (B) CONVENTIONAL CONFOCAL MICROSCOPE IMAGE OF LAMIN AND TUBULIN SAMPLE AND (C) STED MICROSCOPE IMAGE OF SAME SAMPLE[45].	17

FIGURE 2.9 SUPER-RESOLUTION IMAGING BY SINGLE-MOLECULE LOCALISATION METHOD. (A) AT ANY TIME, ONLY A SPARSE SET OF FLUOROPHORES DECORATING THE SAMPLE ARE SWITCHED ON (GREEN CIRCLES), AND THEIR POSITIONS ARE DETERMINED (CROSSES). OVER TIME, MANY MOLECULES HAVE BEEN LOCALIZED, AND THEIR POSITIONS ARE PLOTTED TO CREATE THE STORM IMAGE. (B) COMPARISON OF CONVENTIONAL (LEFT) AND STORM (RIGHT) IMAGES OF A CIRCULAR RECA FILAMENT. (C) COMPARISON OF CONVENTIONAL (LEFT) AND TWO-COLOR STORM (RIGHT) IMAGES OF MICROTUBULES (GREEN) AND CLATHRIN (RED) IN A CELL. (D) (LEFT) XY-CROSS-SECTION OF A 3D STORM IMAGE OF CLATHRIN-COATED PITS IN A CELL. (RIGHT) MAGNIFIED IMAGE OF A SINGLE COATED PIT. UPPER PANEL: AN XY CROSS-SECTION OF THE PIT. LOWER PANEL: AN XZ CROSS-SECTION OF THE PIT[47]. 19

FIGURE 2.10 SCHEMATIC OF SCATTERING SUPERLENS PRINCIPLE. (A) LIGHT FOCUSING COMPARISON OF CONVENTIONAL LENS, RANDOM NANOPARTICLE MEDIA LAYER AND INCIDENT WAVEFRONT CONTROL. CONVENTIONAL LENS CANNOT FOCUS BEYOND DIFFRACTION LIMIT DUE TO THE LACK OF HIGH TRANSVERSE WAVE VECTOR (LEFT). IN RANDOM NANOPARTICLE MEDIA, INCIDENT WAVES ARE SCATTERED INSIDE MEDIA AND COUPLED TO PROPAGATING WAVES VIA SPECKLE WAVES (MIDDLE), AND DUE TO THE WAVEFRONT CONTROL (RIGHT), PHASE-MATCHED LIGHT IS FOCUSED IN SUB-WAVELENGTH SCALE. (B–D) IMAGE RECONSTRUCTION THROUGH RANDOM MEDIA. (B) THE MOVEMENT OF THE TIP APERTURES, (C) CONVOLUTION OF THE TIP MOVEMENT, AND (D) FINAL RECONSTRUCTED IMAGES BY NEAR-FIELD TRANSFER MATRIX OF RANDOM PARTICLE, INDICATING SUB-WAVELENGTH IMAGING[49], [50]. 20

FIGURE 2.11 SCHEMATIC OF 4PI MICROSCOPY (A) A LASER LIGHT IS SPLIT INTO TWO BEAMS THAT FOCUS ONTO A SAMPLE THROUGH TWO OPPOSING LENSES CONVERTING THE PARTIAL WAVEFRONT INTO SPHERICAL WAVEFRONT. (B) IMAGING PERFORMANCE COMPARISON OF A CONVENTIONAL CONFOCAL MICROSCOPE AND 4PI MICROSCOPE[53]. 21

FIGURE 2.12 AN EXAMPLE OF PNJ GENERATED BY 1MM PS ($n=1.6$) MICROSPHERE. ILLUMINATED BY A LASER AT $\lambda=248\text{NM}$. (A) ELECTRIC FIELD INTENSITY DISTRIBUTION, $|E|^2$, AT XZ-PLANE (PARALLEL TO POLARISATION) AND (B) YZ-PLANE (PERPENDICULAR TO POLARISATION). (C) SHOWS THE INTENSITY ALONG Z-AXIS (PROPAGATION DIRECTION). (C) LATERAL FIELD DISTRIBUTION (XY-PLANE) OF FOCAL SPOT UNDER THE MICROSPHERE ($z=a$). THE MAXIMUM INTENSITY ENHANCEMENT IS ABOUT 60 TIMES AND MINIMUM LATERAL FOCUS SIZE IS 0.39λ 22

FIGURE 2.13 SCHEMATIC DIAGRAM AND IMAGING PERFORMANCE OF SiO_2 MICROSPHERE SUPERLENS. (A) EXPERIMENTAL CONFIGURATION OF MICROSPHERE SUPERLENS INTEGRATED WITH A CLASSICAL OPTICAL MICROSCOPE. (B–G) EXPERIMENTAL RESULTS FOR MICROSPHERE SUPERLENS IMAGING. (B) SEM IMAGE OF A BLU-RAY DVD DISC (200 NM LINES AND 100 NM GROOVES). (C) OPTICAL IMAGING BY MICROSPHERE IN REFLECTION MODE. (D) SHOWS SEM IMAGE OF A DIFFRACTION GRATING WITH 300 NM WIDE LINES SPACED 130 NM APART. (E) SHOWS THE LINES ARE CLEAR RESOLVED BY MICROSPHERE WITH A 4.17X

MAGNIFICATION IN TRANSMISSION MODE. (F) SHOWS THE SEM IMAGE OF A GOLD-COATED FISHNET MEMBRANE SAMPLE WITH 50 NM PORES SPACED 50 NM APART. (G) SHOWS THE OPTICAL IMAGE BY MICROSPHERE SUPERLENS WITH 8X MAGNIFICATION IN TRANSMISSION MODE[14].	23
FIGURE 2.14 (A) SCHEMATIC OF SCANNING LASER CONFOCAL MICROSCOPE. (B) SEM IMAGE OF NANO-FEATURE SAMPLE WITH 40-NM-WIDE LINES AND 140 NM SPACING. (C) CORRESPONDING MICROSPHERE LASER CONFOCAL MICROSCOPE IMAGE, TAKEN BY LEXT4100 LASER CONFOCAL MICROSCOPE WITH 405 NM LASER ILLUMINATION, 50X NA0.95 OBJECTIVE LENS. (D) ARTEFACTS DUE TO NEIGHBOURING MICROSPHERE INTERFERENCE VERSUS TRUE PATTERN UNDER SINGLE MICROSPHERE[71].	25
FIGURE 2.15 (A) EXPERIMENT LAYOUT OF MICROPIPETTE ATTACHED MICROSPHERE SUPERLENS SCANNING IMAGING. (B) 170 NM STRIPES WITH 550 NM GAPS ARE IMAGED BY MICROSPHERE LENS. (C) SQUARES OF 500x500 NM ² SEPARATED BY A 73 NM GAP ARE IMAGED BY MICROSPHERE LENS[73].	26
FIGURE 2.16 SWIMMING LENS DESIGN. (A) SCHEMATIC ILLUSTRATION. (B) SCHEMATIC ILLUSTRATION OF THE CHEMICALLY POWERED PROPULSION AND LIGHT ILLUMINATION THROUGH THE MICROSPHERE. (C) SEM OF 10 MM PS MICROSPHERE ON A 320 NM GRATING STRUCTURE. (D) MICROSPHERE IMAGING AND ARROW SHOWS THE SCANNING MOTION. (E) RECONSTRUCTED IMAGE BY STITCHING FROM INDIVIDUAL VIDEO FRAME[74].	27
FIGURE 2.17 MICROSPHERE-BASED SCANNING SUPERLENS MICROSCOPY (SSUM). (A) SCHEMATIC OF THE CONSTRUCTION OF A MICROSPHERE-BASED SSUM THAT INTEGRATES A MICROSPHERE SUPERLENS INTO AN AFM SCANNING SYSTEM BY ATTACHING THE MICROSPHERE TO AN AFM CANTILEVER. THE OBJECTIVE PICKS UP THE VIRTUAL IMAGES CONTAINING SUB-DIFFRACTION-LIMITED OBJECT INFORMATION AND SIMULTANEOUSLY FOCUSES AND COLLECTS THE LASER BEAM USED IN THE CANTILEVER DEFLECTION DETECTION SYSTEM. (B) AN ORIGINAL VIRTUAL IMAGE OBSERVED USING THE MICROSPHERE SUPERLENS. THE INSET SHOWS AN SEM IMAGE. (C, D) BACKSIDE AND FRONTSIDE IMAGES, RESPECTIVELY, OF THE AFM CANTILEVER WITH AN ATTACHED MICROSPHERE SUPERLENS. SCALE BARS, 2 MM (B); 50 MM (C, D)[75].	28
FIGURE 2.18 (A) EXPERIMENTAL SCHEMATIC ILLUSTRATION OF MANIPULATION AND DETECTION OF A SINGLE NANOPARTICLE BY NANOJET GENERATED FROM MICROLENS BINDING ON THE FIBRE PROBE. (B) THE REAL-TIME TRACE OF THE REFLECTED 808-NM SIGNAL IN THE TRAPPING PROCESS OF AN 85-NM FLUORESCENT PS NANOPARTICLE. THE INSETS SHOW THE FLUORESCENT IMAGES B1 BEFORE TRAPPING, B2 DURING TRAPPING AND B3 IN THE RELEASE[77].	29
FIGURE 2.19 MICROSPHERE DECORATED WITH CONCENTRIC RINGS. (A) SCHEMATIC OF OBSERVING PNJ BY AN OPTICAL MICROSCOPE. THE LENS LOCATED BETWEEN THE OBJECTIVE LENS AND CCD REPRESENTS FOR THE FOCUSING LENSES IN THE OPTICAL MICROSCOPE. (B) TOP AND (C) SIDE VIEWS[82].	30
FIGURE 2.20 DESIGN OF THE CENTER-COVERED ENGINEERED MICROSPHERE FOR SUPER-FOCUSING OF RADIAL POLARIZED BEAM[81].	31
FIGURE 3.1 USER INTERFACE OF DSI MIE SOFTWARE.	39

FIGURE 3.2 EXAMPLE OF SIMULATION CONDITION. SCALE IS NORMALISED WITH RESPECT TO THE PARTICLE RADIUS, A.	40
FIGURE 3.3 SCHEMATIC DIAGRAM OF ENGINEERED MICROSPHERES. (A) REFERENCING DESIGN OF SINGLE HOMOGENEOUS MICROSPHERE. (B) PUPIL MASK ASSISTED MICROSPHERE. (C) COMPOSITED MATERIAL IN MICROSPHERE WITH HIGHER REFRACTIVE INDEX LOCATED AT BOTTOM PORTION. (D) COMBINATION OF PUPIL MASK AND COMPOSITE DESIGN.	42
FIGURE 3.4 SIMULATION SCHEMATIC OF NANOPARTICLE-BASED DIELECTRIC METAMATERIAL. (A) 15-NM ANATASE TiO_2 NANOPARTICLES ($n=2.55$) ARRANGED IN HEXAGONALLY CLOSE-PACKED FORM UNDER A 550 NM WAVELENGTH PLANE WAVE ILLUMINATION. TWO INCOHERENT POINT SOURCES (45 NM SEPARATION) ILLUMINATING FROM BOUNDARY OF (B) HOMOGENEOUS ($n=2.55$) AND (C) NANOPARTICLE COMPOSITE MATERIAL.	44
FIGURE 3.5 FABRICATION PROCEDURE OF COVERSIP MICROSPHERE SUPERLENS (CMS).	47
FIGURE 3.6 SPIN COATER (MODEL WS-650MZ-8NPP/A1/AR1).	48
FIGURE 3.7 POLYDIMETHYLSILOXANE SYLGARD 184 (A) SILICONE ELASTOMER AND (B) CURING AGENT.	49
FIGURE 3.8 VACUUM DESICCATOR.	50
FIGURE 3.9 CHEMICALS FOR PREPARING PMMA, (A) MMA AND (B) BPO.	51
FIGURE 3.10 THE CMS PEEL-OFF AND TRANSFER ONTO SAMPLES. (A) THE SIDE VIEW SHOWING THE THICKNESS. (B) TOP VIEW. THE PARTICLES IN YELLOW CIRCLE IS LARGE (60~100NM) MICROSPHERES, WHILE PARTICLES IN BLUE CIRCLE IS SMALL (3~25NM) MICROSPHERES. (C) AND (D) SHOW THAT CMS EXHIBITS FLEXIBLE BODY AND CAN STRONGLY ADHERE ON CURVED SURFACE.	52
FIGURE 3.11 SUPERLENSING OBJECTIVE LENS. (A) THE BaTiO_3 SUPERLENS WAS FABRICATED BY ENCAPSULATING A MONOLAYER OF BaTiO_3 MICROSPHERE INSIDE A PDMS MATERIAL. (B) THE SUPER OBJECTIVE WAS MADE BY INTEGRATING A CONVENTIONAL MICROSCOPE OBJECTIVE LENS (E.G. 50X, NA: 0.70, OR 100X, NA:0.95) WITH A BaTiO_3 MICROSPHERE SUPERLENS USING A 3D PRINTED ADAPTOR (C) EXPERIMENTAL CONFIGURATION FOR SUPER-RESOLUTION IMAGING USING DEVELOPED OBJECTIVE WHICH WAS FITTED ONTO A STANDARD WHITE LIGHT OPTICAL MICROSCOPE.	53
FIGURE 3.12 3D DESIGN OF ADAPTOR BY SOLIDWORKS. THE ADAPTOR HAS A TUBE SIZE FITTING TO THE OBJECTIVE LENS TUBE. (B) SHOWS CROSS-SECTION OF LENS ADAPTOR. IT CAN BE ADJUSTED VERTICALLY TO REACH BEST FOCUS POSITION.	54
FIGURE 3.13 TEMPLATE PREPARED BY PHOTOLITHOGRAPHY AND PDMS MOULDING TRANSFER MICRO-STRUCTURE FROM TEMPLATE. (A) NEGATIVE PHOTORESIST IS DEPOSITED ON GLASS SUBSTRATE AND EXPOSED BY UV LIGHT. (B) UNEXPOSED AREA IS DEVELOPED BY AZ 726 MF DEVELOPER. (C) PDMS SOLUTION IS DEPOSITED ONTO MICRO-STRUCTURED SURFACE AND (D) DUPLICATING OPPOSITE MICRO-STRUCTURE. (E) BTG MICROSPHERES DISPERSION DROPLET IS SPREAD ACROSS SURFACE AND MICRO-WELL STRUCTURE HELPS TO TRAP THEM. (F) STACKING PARTICLES ARE WASHED AWAY AND REMAINING PARTICLES IN MICRO-WELLS.	56

FIGURE 3.14 PHOTOLITHOGRAPHY CHEMICALS AND EQUIPMENT. (A) A CROSS-LINKING NEGATIVE PHOTORESIST AZ [®] 125 NXT (MICROCHEMICALS), (B) AZ 726 MIF DEVELOPER, (C) MODEL WS-650MZ-8NPP SPIN COATER (LAURELL TECHNOLOGIES), (D) SUSS MICROTEC MA8 CONTACT MASK ALIGNER.	57
FIGURE 3.15 PHOTORESIST TEMPLATE OF MICRO-PILLAR ARRAY WITH (A-C) APPROXIMATE 27 MM DIAMETER AND 100 MM SPACING AND (D-F) APPROXIMATE 16 MM DIAMETER AND 100 MM SPACING.	58
FIGURE 3.16 REPLICATION OF MICRO-STRUCTURE ONTO PDMS TO FORM MICRO-WELL ARRAYS WITH (A-C) APPROXIMATE 31 MM DIAMETER AND 98 MM SPACING AND (D-F) APPROXIMATE 18 MM DIAMETER AND 98 MM SPACING.	59
FIGURE 3.17 PARTICLES TRAPPING BY MICRO-WELLS (A, B) 31 MM WELLS (A, B) 18 MM WELLS.	60
FIGURE 3.18 FABRICATION PROCEDURE OF TiO ₂ NANOPARTICLES-BASED HEMISPHERICAL OR SUPER-HEMISPHERICAL MSILS.	61
FIGURE 3.19 FORMING OF TiO ₂ HEMISPHERES WITHOUT THE AID OF HEXANE. (A) THE OPTICAL MICROGRAPH SHOWS THAT THE TiO ₂ NANOPARTICLES DROPLETS SUSPENDED ONLY IN TETRACHLOROETHYLENE WOULD FORM PALE HEMISPHERES ON A WAFER PATTERN WITH 50 NM FEATURES. (B) CORRESPONDING SEM IMAGE OF THE BOTTOM SURFACE OF A HEMISPHERE PREVIOUSLY LOCATED ON THE WATER PATTERN. THE RESULTS INDICATE THAT THE RELATIVELY HIGH SURFACE TENSION OF TETRACHLOROETHYLENE (31.7 mN/m AT 20 °C) MAY NOT FULLY WET THE SAMPLE SURFACE AND IS NOT EFFECTIVE IN IMPROVING THE PENETRATION OF TiO ₂ NANOPARTICLES INTO THE NANOSCALE SURFACE TEXTURE ON THE OBSERVED SAMPLE, AND THE RESULTING AIR GAPS BETWEEN HEMISPHERE AND SAMPLE WOULD PREVENT THE COLLECTION AND PROPAGATION OF LIGHT. SCALE BARS, 5 MM IN (A) AND 500 NM IN (B).	64
FIGURE 3.20 HEMISPHERES (A-C) WERE PREPARED WITHOUT THIN LAYER OF ORGANIC SOLVENT AND SUPER-HEMISPHERES (D-F) WERE PREPARED WITH PRE-COATED THIN LAYER OF ORGANIC SOLVENT. THE HEIGHT-TO-WIDTH RATIO ARE (A) 0.4428, (B) 0.5830, (C) 0.6681, (D) 0.7580, (E) 0.8180, (F) 0.8256.	64
FIGURE 3.21 (A) NEPHILA EDULIS SPIDER, (B) SCHEMATIC DRAWING OF REFLECTION MODE SILK BIO-SUPERLENS IMAGING. THE SPIDER SILK WAS PLACED DIRECTLY ON TOP OF THE SAMPLE SURFACE BY USING A TRANSPARENT CELLULOSE-BASED TAPE. THE GAPS BETWEEN SILK AND SAMPLE WAS FILLED WITH IPA WHICH IMPROVES IMAGING CONTRAST. THE SILK LENS COLLECTS THE UNDERLYING NEAR-FIELD OBJECT INFORMATION AND PROJECTS A MAGNIFIED VIRTUAL IMAGE INTO A CONVENTIONAL OBJECTIVE LENS (100x, NA:0.9).	68
FIGURE 3.22 FABRICATION PROCEDURE OF INTEGRATION OF MICROFLUIDICS CHANNEL AND MICROSPHERE LENS.	69
FIGURE 3.23 MICROFLUIDIC CHIP DESIGN.	70
FIGURE 3.24 (A) PLASMA ETCHER (OXFORD PLASMALAB 80PLUS RIE) FOR OXIDISING PDMS SURFACES. (B) CORRESPONDING STETTING PARAMETERS.	71
FIGURE 3.25 (A) COMPLETED MICROFLUIDIC CHIP WITH INTEGRATION OF CMS AND MICRO-CHANNEL. (B) MICROFLUIDIC CHIP INTERFACE AND CONNECTOR (C) SYRINGE INFUSION PUMP.	71

FIGURE 4.1 (A) NORMALIZED FOCUS POSITION OF $ E ^2$ FIELD AS A FUNCTION OF SIZE PARAMETER q_0 . THE INSET SHOWS THE OVERALL VIEW INCLUDING THE NEGATIVE FOCAL LENGTH. (B) CORRESPONDING FIELD ENHANCEMENT FACTOR. NOTE Y SCALES ARE DIFFERENT IN BOTH PLOTS AND INSETS.	75
FIGURE 4.2 FOUR REPRESENTATIVE $ E ^2$ FIELD INTENSITY DISTRIBUTIONS ACROSS INVESTIGATION RANGE $\pi \leq q_0 \leq 20\pi$. (A) $q_0 = 20$ AND (B) $q_0 = 31.66$ (C) $q_0 = 46.2$ (D) $q_0 = 54.2$	76
FIGURE 4.3 LATERAL FWHM OF $ E ^2$ FOCUS AS A FUNCTION OF SIZE PARAMETER Q_0 , THE SIZE OF FWHM WAS NORMALISED TO PARTICLE RADIUS. COMPARISONS OF FWHM SIZES IN X AND Y DIRECTION WITH RESPECT TO (A) FOCUS INSIDE PARTICLE AND (B) FOCUS OUTSIDE PARTICLE.	77
FIGURE 4.4 DIFFERENCE OF FOCUS SIZE ALONG X-DIRECTION AND Y-DIRECTION (DEVIATION FACTOR VALUE), WHICH PRODUCES AN ELLIPTICAL FOCUS.	78
FIGURE 4.5 AXIAL FWHM OF $ E ^2$ FOCUS AS A FUNCTION OF SIZE PARAMETER Q_0 , THE SIZE OF FWHM WAS NORMALISED TO PARTICLE RADIUS.....	79
FIGURE 4.6 FWHM(X) MINUS RAYLEIGH (DOT) AND FWHM(Y) MINUS RAYLEIGH (SQUARE) AS A FUNCTION OF SIZE PARAMETER Q_0 . BOTH INSIDE AND OUTSIDE CASES ARE PRESENT. NEGATIVE VALUES REPRESENT SUPER-RESOLUTION.	80
FIGURE 4.7 SUPER-RESOLUTION ELECTRIC FIELD INTENSITY ($ E ^2$) SPOTS WITHIN SIZE PARAMETER RANGE $\pi \leq q_0 \leq 20\pi$ WITH REFRACTIVE INDEX $n_p=1.6$ AND $n_m=1.0$. BLUE SQUARES INDICATE EXTERNAL FOCUS AND RED CIRCLES INDICATE INTERNAL FOCUS.	81
FIGURE 4.8 THE $ E ^2$ INTENSITY DISTRIBUTION OF BEST SUPER-RESOLUTION OF EXTERNAL, $q_0=22.26$, AND INTERNAL, $q_0=56.94$, RESPECTIVELY. (A) AND (B) ARE FIELD DISTRIBUTION OF $q_0=22.26$ IN XZ AND YZ-PLANE. (C) INDICATES THAT THE FOCUS IS LOCATED ON THE BOUNDARY OF PARTICLE ($z=1$). (D) AND (E) ARE FIELD DISTRIBUTION OF $q_0=56.94$ IN XZ AND YZ-PLANE. (F) INDICATES THAT THE HIGHEST PEAK IS GENERATED INSIDE PARTICLE (AT $z=0.786$).	83
FIGURE 4.9 AN EXAMPLE OF EXTERNAL RESOLUTION OBTAINED BY A 5 μ m DIAMETER $n_p=1.6$ MICROSPHERE. THE BEST EXTERNAL SUPER-RESOLUTION WAS ACHIEVED BY A 705.7 NM INCIDENT WAVELENGTH, WHICH $Q_0=22.26$	84
FIGURE 4.10 SPECTRUM OF TUNGSTEN-HALOGEN LAMP (THORLABS, QTH10).	85
FIGURE 4.11 NORMALISED FIELD INTENSITY OF 5 MM MICROSPHERE UNDER THREE INCIDENT SOURCES ALONG PROPAGATIONAL DIRECTION Z-AXIS. THE INSERT IS ZOOM-IN OF PEAK AREA.	86
FIGURE 4.12 ELECTRIC FIELD $ E ^2$ DISTRIBUTIONS OF 5 MM MICROSPHERE ($n_p=1.6$, $n_m=1$) IN (A, C AND E) XZ-PLANE AND (B, D AND F) YZ-PLANE BY (A, B) MONOCHROMATIC 600 NM INCIDENT, (C, D) UNIFORM INTENSITY INCIDENT (390-700 NM) AND (E, F) TUNGSTEN-HALOGEN LAMP (390-700 NM).	87
FIGURE 5.1 SCHEMATIC DIAGRAMS AND $ E ^2$ INTENSITY FIELD DISTRIBUTIONS FOR TWO MICROSPHERE SYSTEMS. (A, B) SINGLE MICROSPHERE, (C, D) PROPOSED MICROSPHERE WITH PUPIL MASK SYSTEM. PARAMETERS:	

WAVELENGTH 600NM, MICROSPHERE DIAMETER 3 MM, AND (C) WITH MASK DIAMETER 2 MM, REFRACTIVE INDEX (RI) OF MICROSPHERE IS 1.46 AND MASK MATERIAL PEC).	91
FIGURE 5.2 (A) $ E ^2$ INTENSITY FIELD DISTRIBUTION ALONG PROPAGATION AXIS Z ACROSS 3MM-DIAMETER MICROSPHERE CENTRE, WITH VARYING PUPIL MASK DIAMETER FROM 0 TO 3 MM (B) CORRESPONDING EXTERIOR FOCUS FIELD PROFILE ALONG Y-AXIS WHICH MEASURES FOCUSING RESOLUTION.	92
FIGURE 5.3 CORRESPONDING (A) FOCAL LENGTH AND (B) FOCUS RESOLUTION (FWHM OF FOCUS SPOT) AT EXTERNAL PEAK LOCATION AS A FUNCTION OF MASK AREA SIZE, DERIVED FROM FIGURE 5.3 FOR 3 MM-DIAMETER MICROSPHERE LENS COUPLED WITH VARYING SIZE PUPIL MASKS.	94
FIGURE 5.4 FOCUSING RESOLUTION AS A FUNCTION OF MASK AREA PERCENTAGE (MAP) FOR SMALLER DIAMETER MICROSPHERE LENSES: (A) 1.0 MM, (B) 1.5 MM, (C) 2.0 MM AND (D) 2.5 MM.	95
FIGURE 5.5 CONCEPT OF REALISING THE PUPIL MASK BY PROJECTING A MILLIMETRE SCALE MASK THROUGH DEMAGNIFICATION EFFECT.	97
FIGURE 5.6 SCHEMATIC DIAGRAMS AND $ E ^2$ INTENSITY FIELD DISTRIBUTIONS FOR TWO MICROSPHERE SYSTEMS. (A, B) SINGLE MICROSPHERE, (C, D) PROPOSED COMPOSITE MATERIAL MICROSPHERE. PARAMETERS: WAVELENGTH 600NM, MICROSPHERE DIAMETER 3 MM, AND (C) LOWER PART CUTTING HEIGHT 75 NM, REFRACTIVE INDEX (RI) OF MICROSPHERE IS 1.46 AND BOTTOM MATERIAL IS 2.16.	98
FIGURE 5.7 FOCUS RESOLUTION FWHM ALONG Y-DIRECTION AT EXTERNAL PEAK LOCATION AS A FUNCTION OF CUTTING HEIGHT FOR REFRACTIVE INDEX $1.76 \leq n_{p2} \leq 2.66$	99
FIGURE 5.8 CUTTING HEIGHT VS. RI (n_{p2}) TO ACHIEVE BEST SUPER-RESOLUTION.	100
FIGURE 5.9 FOCUS RESOLUTION FWHM ALONG Y-DIRECTION AT EXTERNAL PEAK LOCATION AS A FUNCTION OF CUTTING HEIGHT FOR REFRACTIVE INDEX $n_{p2} = 2$. THE MINIMUM VALUE IS 103 NM AT CUTTING HEIGHT OF 90 NM.	101
FIGURE 5.10 $ E ^2$ FIELD DISTRIBUTION ALONG Y-DIRECTION AT FOCUS POSITION ($z=1500$ NM) OF OPTIMIZED SUPER-RESOLUTION FOCUS (SOLID CURVES) AND ORDINARY SiO_2 (RED DOT LINE).	102
FIGURE 5.11 SCHEMATIC DIAGRAMS OF COMBINING PUPIL MASK AND COMPOSITED MICROSPHERE.	103
FIGURE 5.12 COMPARISON OF $ E ^2$ INTENSITY FROM VARIOUS MASK SIZE ON COMPOSITED MICROSPHERE WITH $n_{p2}=2.56$	104
FIGURE 5.13 COMPARISON OF FWHM WITH VARYING MASK SIZE AND n_{p2}	105
FIGURE 5.14 PROPAGATING WAVE SCATTERING BY DENSE ALL-DIELECTRIC NANOPARTICLES MEDIUM. (A) PLANE WAVE ($\lambda = 550$ NM) PASSING THROUGH THE STACKED TiO_2 NANOPARTICLES. ELECTRIC FIELD HOTSPOTS ARE GENERATED IN THE GAPS BETWEEN CONTACTING PARTICLES, WHICH GUIDES LIGHT TO THE UNDERLYING SAMPLE. (B) LARGE-AREA NANOSCALE EVANESCENT WAVE ILLUMINATION CAN BE FOCUSED ONTO THE SAMPLE SURFACE BECAUSE OF THE EXCITATION OF NANOGAP MODE. (C) THE SIZE OF THE ILLUMINATION SPOTS IS EQUAL TO THE PARTICLE SIZE, HAVING AN FWHM RESOLUTION OF ~ 8 NM.	107

FIGURE 5.15 COMPARISONS BETWEEN HOMOGENEOUS AND NANOPARTICLE COMPOSITED MEDIA. (A) MEAN ELECTRIC FIELD AMPLITUDE AS A FUNCTION OF DISTANCE FROM POINT SOURCES (Y-POLARISED, INCOHERENT). THE AMPLITUDE DECAYS EXPONENTIALLY. MOST EVANESCENT WAVE ENERGY WAS LOST WITHIN 50 NM DISTANCE. (B) IN NANOPARTICLE COMPOSITED MATERIAL, EVANESCENT WAVES INTERACT WITH TiO_2 NANOPARTICLES AND TURN INTO PROPAGATION WAVES WHICH TRAVEL OUTWARD TO FAR-FIELD. A PERIODICITY OF 160 NM WAS OBSERVED. (C-F) TWO-POINT SOURCES (45 NM SEPARATION) IMAGED WITH (C) HOMOGENEOUS AND (F) COMPOSITED MATERIAL, AT POSITIONS $Z=2$ NM (NEAR SOURCE), $Z=23$ NM (NEAR-FIELD, INSIDE SLAB) AND $Z=650$ NM (FAR-FIELD, OUTSIDE SLAB). IN FAR-FIELD, (E) THE HOMOGENEOUS MEDIA FAILS TO RESOLVE THE TWO POINTS WHILE (F) THE COMPOSITED MEDIA CAN SUCCESSFULLY RESOLVE THEM.	108
FIGURE 6.1 WAFER PATTERN USED FOR EVALUATING THE MAGNIFICATION FACTOR AND FIELD OF VIEW OF TiO_2 MSILs. (A) SEM IMAGE OF THE WAFER PATTERN, WHICH SHOWS 400-NM-WIDE SQUARES WITH AN INTERVAL OF 200 NM. (B) OPTICAL MICROGRAPH OF THE WAFER PATTERN AT A MAGNIFICATION OF $\times 2100$, INDICATING THAT THE CONVENTIONAL OPTICAL MICROSCOPE WOULD FAIL TO REVEAL THE SHAPE OF THE SQUARES DUE TO THE ABBE DIFFRACTION LIMIT. SCALE BARS, 1 MM IN (A) AND (B).	115
FIGURE 6.2 MAGNIFICATION FACTORS AND FIELD OF VIEW OF TiO_2 NANOPARTICLES-BASED HEMISPHERES OR SUPER-HEMISPHERES AS MSILs. OPTICAL MICROSCOPE IMAGES OF A WAFER PATTERN WITH A LATTICE SPACING OF 200 NM OBSERVED THROUGH TiO_2 MSILs WITH WIDTHS OF ABOUT (A-F) 10 MM, (G-L) 15MM AND (M-R) 20 MM, CORRESPONDING TO AN INCREASING MAGNIFICATION FACTORS OF (A, G, M) 1.8, (B, H, N) 2.5, (C, J, O) 3.0, (D, J, P) 3.6, (E, K, Q) 4.7, AND (F, L, R) 5.3, RESPECTIVELY. INSET: SIDE-VIEW SEM IMAGES OF THE CORRESPONDING MSILs LOCATED ON THE PATTERN.	116
FIGURE 6.3 MAGNIFICATION EFFECT OF TiO_2 MSILs WITH HIGHER HEIGHT-TO-WIDTH RATIOS. OPTICAL MICROGRAPHS OF THE WAFER PATTERN OBSERVED THROUGH TiO_2 MSILs WITH A HEIGHT-TO-WIDTH RATIO OF (A) 0.84 OR (B) 0.94, AND (C, D) THEIR CORRESPONDING SEM IMAGES, RESPECTIVELY. THE VIRTUAL IMAGE (A) HAS A MAGNIFICATION FACTOR OF 6.7 BUT SUFFERS FROM LOW CONTRAST. (B) FAILED TO RESOLVE PATTERN IN AIR CONDITION. THE MSILs HAVE WIDTHS AROUND 15 MM. SCALE BARS, 5 MM IN (A)-(D).	117
FIGURE 6.4 ESTIMATION OF THE EFFECTIVE REFRACTIVE INDEX OF TiO_2 MSILs. THE EXPERIMENTALLY OBSERVED CORRELATION (BLACK) BETWEEN THE MAGNIFICATION FACTOR AND THE HEIGHT-TO-WIDTH RATIO FOR 10 MM MSILs (RED), 15 MM MSILs (GREEN) AND 20 MM MSILs (BLUE) IN FIG. 3. THEORETICAL CURVE WAS OBTAINED USING GEOMETRY OPTICS ANALYSIS WITH AN EFFECTIVE INDEX OF 1.95.	118
FIGURE 6.5 FIELD OF VIEW OF TiO_2 MSILs. IN FIGURE 6.2, THE FIELD OF VIEW (UNDISTORTED REGION) OF MSILs INCREASES ALMOST LINEARLY WITH AN INCREASE IN THE WIDTH OF MSILs FROM 10 MM TO 20 MM, AND LESS RELATED TO THE MAGNIFICATION FACTOR (HEIGHT-TO-WIDTH RATIO) OF MSILs.	119
FIGURE 6.6 SUPER-RESOLUTION IMAGING THROUGH TiO_2 MSILs. SEM IMAGES OF (A) A BLU-RAY DISC CONTAINING 100-NM-WIDE GROOVES, AND THE WAFER PATTERNS WITH (E) 60 NM PITCHES, (I) 50 NM PITCHES OR (M)	

45 NM PITCHES AFTER GOLD COATING OF SAMPLE (I), AND (B)-(C), (G) AND (K) THE BOTTOM SURFACES OF MSILS DETACHED FROM THE SURFACE OF SAMPLES (A), (E) AND (I), RESPECTIVELY. AFM IMAGES OF THE WAFER PATTERNS WITH (F) 60 NM PITCHES OR (J) 50 NM PITCHES, RESPECTIVELY. OPTICAL MICROSCOPE IMAGES OF TiO ₂ MSILS FOCUSED ON THE SURFACE OF (D) BLU-RAY DISC, WAFER PATTERNS WITH (H) 60 NM PITCHES, (L) 50 NM PITCHES OR (N)-(P) 45 NM PITCHES, WITH A MAGNIFICATION FACTOR OF 1.8, 3.1, 3.0 AND 3.1, RESPECTIVELY. THE LAST MSIL WAS ILLUMINATED UNDER (N) WHITE LIGHT, (O) GREEN LIGHT ($\lambda \sim 540$ NM) OR (P) BLUE LIGHT ($\lambda \sim 470$ NM), RESPECTIVELY. THE MSILS HAD WIDTHS OF ABOUT 20 MM. SCALE BARS, 2 MM FOR SEM IMAGES AND 10 MM FOR OPTICAL IMAGES.	120
FIGURE 6.7 THE LIMITING RESOLUTION OBTAINED WITH A TiO ₂ HEMISPHERICAL MSIL. OPTICAL MICROGRAPHS FOCUSED ON (A) THE WAFER PATTERN, AND (B) THE 1.8 TIMES MAGNIFIED VIRTUAL IMAGE CREATED BY A TiO ₂ HEMISPHERICAL MSIL. THE CORRESPONDING SEM IMAGES OF (C) THE HEMISPHERICAL MSIL AND (D) THE WAFER PATTERN WITH 75 NM FEATURES, THE DASHED CIRCLE IN (D) REPRESENTS THE FIELD OF VIEW SEEN IN (B). THE HEMISPHERICAL MSIL HAS A WIDTH OF 15 MM. THE RESULTS INDICATE THAT THE HEMISPHERICAL MSIL WITH A MAGNIFICATION FACTOR OF 1.8 IS INSUFFICIENT TO RESOLVE THE FEATURES BELOW 75 NM. SCALE BARS, 5 MM IN (A)-(C) AND 2 MM IN (D).	121
FIGURE 6.8 THE SUPER-RESOLUTION IMAGES OBTAINED WITH A TiO ₂ SUPER-HEMISPHERICAL MSIL. OPTICAL MICROGRAPHS OF A TiO ₂ SUPER-HEMISPHERICAL MSIL FOCUSED ON THE SURFACE OF A WAFER PATTERN WITH 50 NM FEATURES (WITHOUT GOLD COATING) UNDER AN ILLUMINATION OF (A) WHITE LIGHT, (B) GREEN LIGHT ($\lambda \sim 540$ NM) OR (C) BLUE LIGHT ($\lambda \sim 470$ NM), RESPECTIVELY. THE SUPER-HEMISPHERICAL MSIL HAS A MAGNIFICATION FACTOR OF 3.0 AND A WIDTH OF 15 MM. THE OPTICAL MICROGRAPHS WERE TAKEN USING AN OLYMPUS BX63 LIGHT MICROSCOPE. SCALE BARS, 5 MM IN (A)-(C).	122
FIGURE 6.9 COMPARISONS OF TiO ₂ HEMISPHERICAL MSILS ASSEMBLED FROM 15 NM OR 45 NM ANATASE TiO ₂ NANOPARTICLES. OPTICAL MICROGRAPHS OF A BLU-RAY DISC OBSERVED THROUGH HEMISPHERICAL MSILS COMPOSED OF (A) 15 NM OR (B) 45 NM ANATASE TiO ₂ NANOPARTICLES, RESPECTIVELY. HIGH MAGNIFICATION SEM IMAGES OF (C), (D) THE TOP SURFACES, AND (E), (F) THE BOTTOM SURFACES OF THE HEMISPHERICAL MSILS COMPOSED OF 15 NM OR 45 NM TiO ₂ NANOPARTICLES, RESPECTIVELY. SCALE BARS, 2 MM IN (A), (B) AND 500 NM IN (C)-(F).	123
FIGURE 6.10 (A, B) TEM IMAGES OF MPS/OA/ ZrO ₂ NANOPARTICLE UNDER LOW AND HIGH MAGNIFICATIONS. ...	125
FIGURE 6.11 FTIR SPECTRUM OF (A) MPS/OA/ZrO ₂ NANOPARTICLES, (B) ZrO ₂ /PS NANOHYBRID COLLOIDAL MICROSPHERES AND (C) PURE PS MICROSPHERES.	126
FIGURE 6.12 SEM IMAGES OF ZrO ₂ /PS NANOHYBRID COLLOIDAL MICROSPHERES; (A)M1, (B)M3, (C)M5; TEM IMAGES OF ULTRATHIN SECTIONS OF M1(D, E, F) AND M5(G, H, I)	127
FIGURE 6.13 SEM IMAGE (A) AND SEM MAPPING PHOTOGRAPHS OF Zr (B), C (C) AND O (D) IN THE NANOHYBRID MICROSPHERES M5; A YELLOW LINE IS STRETCHED ACROSS A SELECTED MICROSPHERE IN THE TOP LEFT SEM	

IMAGE FOR SEM LINESCAN ELEMENT ANALYSIS. (E) SEM LINESCAN ELEMENT DISTRIBUTION OF Zr IN THE SELECTED MICROSPHERE OF M5. (F) THE CORRESPONDING LINESCAN EDX SPECTRUM OF THE MICROSPHERE.

..... 128

FIGURE 6.14 TGA CURVES OF MPS/OA/ZrO₂ NANOPARTICLES AND ZrO₂/PS NANOHYBRID COLLOIDAL MICROSPHERES M1-M5. 129

FIGURE 6.15 (A) SCHEMATIC OF THE DIMETHYL-SILICONE SEMI-IMMERSED MICROSPHERE FOR SUPER-RESOLUTION IMAGING UNDER WHITE-LIGHT ILLUMINATION; (B) THREE DIMENSIONAL IMAGE SHOWING THE DISTRIBUTION OF DIMETHYL-SILICONE AROUND THE SPHERE; (C) SEM IMAGE OF THE NANO-PATTERNED CHIPS WITH 75 NM AND 60 NM GAPS BETWEEN 145 NM AND 115 NM WIDE STRIPES; (D-G) OPTICAL SUPER-RESOLUTION IMAGING OF NANO-PATTERNED CHIPS BY M0 (1.590), M1 (1.600), M3 (1.634), AND M5 (1.685) IN THE SAME DIAMETERS OF 10 MM; (H-K) OPTICAL SUPER-RESOLUTION IMAGING OF THE CHIPS BY M5 WITH DIFFERENT DIAMETERS OF 2.6 MM, 8.5 MM, 13.6 MM, AND 18.5 MM, THE CORRESPONDING IMAGING MAGNIFICATIONS OF THESE PICTURES ARE X2.41, X2.31, X2.10, AND X2.08, RESPECTIVELY. THE WHITE ARROWS IN (D-K) INDICATE THE LOCATION OF THE STRUCTURE CONTAINING 75 NM GAPS IN THE IMAGE. 131

FIGURE 6.16 (A) SEM IMAGE OF THE NANO-PATTERNED CHIPS WITH 60 NM GAPS BETWEEN FOUR 115 NM WIDE STRIPES; (B) THREE DIMENSIONAL IMAGE SHOWING THE DISTRIBUTION OF CEDARWOOD-OIL AROUND THE SPHERE; (C-F) OPTICAL SUPER-RESOLUTION IMAGING OF THE CHIPS BY M0, M1, M3, AND M5, RESPECTIVELY, THE DOTTED BORDERED RECTANGLES IN THESE PICTURES INDICATE LOCATIONS OF THE STRUCTURE CONTAINING 75 NM AND 60 NM GAPS BETWEEN 145 NM WIDE STRIPES (UPPER THREE STRIPES) AND 115 NM STRIPES (LOWER FOUR STRIPES). 132

FIGURE 6.17 (A) SEM IMAGE OF THE CHIP WITH PERIODIC STRUCTURES CONTAINING 50 NM GAPS; (B) CONFOCAL IMAGE AT $\lambda = 405$ NM OF THE SAME CHIP IN (A); (C-E) IMAGING OF THE CHIPS AT $\lambda = 405$ NM THROUGH 13.3 MM SPHERES OF M1, M3, AND M5, RESPECTIVELY; THE DOTTED BORDERED RECTANGLES IN THESE IMAGES INDICATE LOCATIONS OF THE STRUCTURE CONTAINING 50 NM GAPS THAT ARE RESOLVED BY THESE SPHERES, THE CORRESPONDING MAGNIFIED IMAGES ARE SHOWN IN THE BOTTOM RIGHT CORNERS. THE PARAMETERS OF THE OBJECTIVE LENS ARE 100X, NA = 0.95, AND THE BARS ARE 2 MM IN (B-E). 133

FIGURE 7.1 SUPERLENSING OBJECTIVE LENS. (A) THE BaTiO₃ SUPERLENS WAS FABRICATED BY ENCAPSULATING A MONOLAYER OF BaTiO₃ MICROSPHERE (3-80 μ M DIAMETER) INSIDE A PDMS MATERIAL. (B) THE SUPER OBJECTIVE WAS MADE BY INTEGRATING A CONVENTIONAL MICROSCOPE OBJECTIVE LENS (E.G. 50X, NA: 0.70, OR 100X, NA:0.95) WITH A BaTiO₃ MICROSPHERE SUPERLENS USING A 3D PRINTED ADAPTOR (C) EXPERIMENTAL CONFIGURATION FOR SUPER-RESOLUTION IMAGING USING DEVELOPED OBJECTIVE WHICH WAS FITTED ONTO A STANDARD WHITE LIGHT OPTICAL MICROSCOPE. 137

FIGURE 7.2 STATIC SUPER-RESOLUTION IMAGING OF BLU-RAY AND VIRUS BY SUPERLENSING OBJECTIVE LENS. (A) SEM IMAGE OF BLU-RAY DISC. (B) 67 μ m BaTiO₃ SUPERLENS IMAGING. (C) 18 μ m BaTiO₃ SUPERLENS IMAGING.

(D) SEM OF ADENOVIRUS. (E) 70 UM BaTiO_3 SUPERLENS IMAGING OF VIRUS CLUSTER. (F) ENLARGED VIEW OF SECTION OF (E).	140
FIGURE 7.3 SCANNING SUPER-RESOLUTION IMAGING AND IMAGE STITCH. (A) SCANNING SCHEMATICS. (B) SCANNING DIRECTION OF IC CHIP SAMPLE (C) SEM OF IC CHIP. (D) IC SCANNING IMAGE POSITION 1. (E) IC SCANNING POSITION 2. INSETS SHOW STITCHED IMAGE FOLLOWING SCANNING PATHS. (F) BLU-RAY SAMPLE IMAGED BY MICROSPHERE. (G) STITCHED IMAGE OF BLU-RAY SCANNING.	142
FIGURE 7.4 ELECTRIC FIELD INTENSITY $ E ^2$ DISTRIBUTION IN CROSS SECTIONAL PLANE OF 18 MM AND 67 MM DIAMETER BaTiO_3 MICROSPHERE EMBEDDED IN PDMS MATERIAL ILLUMINATED BY DIFFERENT VISIBLE WAVELENGTHS. THE LIGHT IS INCIDENT FROM TOP TO BOTTOM, WITH ELECTRIC FIELD POLARISED FROM LEFT TO RIGHT. Q IS THE SIZE PARAMETER DEFINED AS $Q = \pi D / \lambda$, WHERE D IS THE PARTICLE DIAMETER AND λ THE WAVELENGTH; SEE VISUALIZATION 2 FOR THE ANIMATION OF FIELD EVOLUTION AS A FUNCTION OF SIZE PARAMETER Q.	144
FIGURE 7.5 EXPERIMENT SETUP OF LASER-ASSISTED SCANNING MODE NANO-PATTERNING. INSERT IS THE XYZ SERVO NANO-STAGE WITH CMS LENS FIXING ON IT.....	145
FIGURE 7.6 MICROSPHERE SUPERLENS PATTERNING. SEM IMAGES OF LASER MACHINED HOLE PATTERNS BY (B-C) 24.7 MM MICROSPHERE, (E-F) 16.6 MM AND (H-I) 7.5 MM. NOTE SCALE BAR IN (I) IS 1 MM DIFFERENT FROM OTHERS IN THE COLUMN.....	147
FIGURE 7.7 SEM IMAGES FOR (A, C, E) 24.7 MM AND (B, D, F) 16.6 MM MICROSPHERE WITH DIFFERENT Z FOCUS POSITION. (A,B) 25MM (C,D) 27MM AND (E,F) 29MM AWAY FROM LASER FOCUS POSITION. SCALE BAR IS 1 MM.	148
FIGURE 7.8 'P' LETTER PATTERN BY MICROSPHERE SUPERLENS SCANNING PATTERNING. (A) DESIGNED PATTERN (B) 'P' LETTER WITH MEASUREMENT BY 17.66 MM MICROSPHERE. (B) A GROUP OF 'P' LETTER PATTERNS (C) GENERATED BY CORRESPONDING MICROSPHERE.	150
FIGURE 7.9 SCANNING PATTERNING FOR (A) A STRING OF NUMBER '0123' AND (B) FULL WORD 'BANGOR' PATTERNING. SCALE BAR IN BOTH FIGURE IS 50 MM.	151
FIGURE 7.10 SCANNING PATTERNING BY MICROSPHERE ARRAY.	151
FIGURE 8.1 A TYPICAL IMAGING EXAMPLE OF SILK SUPERLENS NANOSCOPE IN REFLECTION MODE IMAGING A SURFACE OF AN INTEGRATED CIRCUIT AND COMMERCIAL BLU-RAY DISC. THE 100- μm THICK TRANSPARENT PROTECTION LAYER OF THE BLU-RAY DISC HAS BEEN REMOVED PRIOR TO USING THE MINOR AMPULLATE SPIDER SILK (DIAMETER OF 6.8 μm). MICRO DIMENSIONAL INTEGRATED SURFACE PATTERN (A; OPTICAL IMAGING) IS MAGNIFIED BY THE SPIDER SILK (B; OPTICAL NANOSCOPE IMAGE). THE SUB-DIFFRACTION 100 NM CHANNELS (C; SEM IMAGE) ARE RESOLVED BY THE SPIDER SILK SUPERLENS (D; OPTICAL NANOSCOPE IMAGE) AND CORRESPOND TO A MAGNIFICATION FACT OF 2.1X.	155

FIGURE 8.2 MICROSPHERE POSITIONED BESIDE THE MINOR AMPULLATE SPIDER SILK IN REFLECTION MODE, IMAGES A COMMERCIAL BLU-RAY DISC. THE IMAGE RESOLVED WITHIN THE SPIDER SILK IS ROTATED BY APPROXIMATELY FOUR DEGREES COMPARED TO THE REAL DIRECT OF THE SUB-DIFFRACTION 100 NM CHANNELS SHOWN BY THE MICROSPHERE.....	157
FIGURE 8.3 (A) LIGHT FOCUSING BY THE 6.8 μ M-DIAMETER MINOR AMPULLATE SPIDER SILK IMMERSSED IN IPA SOLUTION UNDER 600 NM WAVELENGTH ILLUMINATION INCIDENT AT 30 DEGREE ANGLE. (B) SCHEMATICS FOR MAGNIFICATION FACTOR M CALCULATION, THE M GENERALLY INCREASES WITH INCIDENT ANGLE.	159
FIGURE 8.4 SCHEMATIC SETUP OF ON-CHIP MICROFLUIDIC SUPERLENS. THE MICROFLUIDIC SUPERLENS IS PLACED ONTO AN INVERTED WHITE LIGHT MICROSCOPE.	161
FIGURE 8.5 HUMAN RED BLOOD CELLS (RBC) IMAGING. (A) SEM IMAGE. (B) RBCs FLOW IN MICROFLUIDIC CHANNEL. (C-E) SINGLE RBC IMAGING AT DIFFERENT FOCUSES. (F-H) AGGREGATION OF RBCs IN CHAIN FORM IS CAPTURED BY MICROSPHERE LENS AT DIFFERENT FOCUSES.	162
FIGURE 8.6 TRYPANOSOME SAMPLE IMAGING. (A) DIAGRAM OF TRYPANOSOME. (B) LIVE TRYPANOSOME FLOWS IN MICROFLUIDIC CHANNEL. (C-F) FROM LEFT TO RIGHT. MAGNIFIED IMAGES ARE CAPTURED BY MICROSPHERE SUPERLENS.	163
FIGURE 8.7 IMAGING OF ADENOVIRUSES WITH SIZE ABOUT 90-100 NM. (A) SEM IMAGE. (B) 70 μ M MICROSPHERE-LENS LOCATED ON TOP OF 10 μ M WIDTH FLUIDIC CHANNEL. (C-F) ADENOVIRUSES FLOW INSIDE CHANNEL FROM TOP TO BOTTOM. ADENOVIRUSES LABELLED BY ARROWS ARE MAGNIFIED IMAGES CAPTURED BY MICROSPHERE-LENS.	164
FIGURE 8.8 MICROSPHERE SUPERLENS COOPERATING WITH MULTIFUNCTIONAL MICROFLUIDIC CHIP.	165

List of Publications

Journal papers:

- [1]. **B. Yan**, L. Yue, Z. B. Wang, "Engineering near-field focusing of a microsphere lens with pupil masks", *Opt. Commun.*, 370, 140-144 (2016).
- [2]. **B. Yan**, Z. B. Wang, A.L. Parker, Y. Lai, P.J. Thomas, L. Yue, J. N. Monks, "Superlensing microscope objective lens", *Appl. Opt.*, 56, 3142-3147 (2017).
- [3]. **B. Yan**, L. Yue, J. N. Monks, R. Dhama, O. Guy, P. Nithiarasu, Z. B. Wang, "On-chip superlensing microfluidic device" (being prepared for submission).
- [4]. **B. Yan**, L. Yue, J. N. Monks, R. Dhama, Z. B. Wang, "Full-wave near-field focusing of dielectric microspheres under white-light spectrum" (being prepared for submission).
- [5]. H. Zhu, **B. Yan**, S. Zhou, Z. B. Wang, L. Wu, "Synthesis and super-resolution imaging performance of refractive-index-controllable microsphere superlens", *J. Mater. Chem. C*, 3, 10907-10915.
- [6]. W. Fan, **B. Yan**, Z. B. Wang, L. Wu, Three-dimensional all-dielectric metamaterial solid immersion lens for subwavelength imaging at visible frequencies, *Sci. Adv.* 2, e1600901 (2016).
- [7]. J. N. Monks, **B. Yan**, N. Hawkins, F. Vollrath, Z. B. Wang, Spider silk: Mother Nature's Bio-superlens, *Nano Lett.*, 16(9), 5842–5845.
- [8]. L. Yue, **B. Yan**, Z. B. Wang, "Photonic nanojet of cylindrical metalens assembled by hexagonally arranged nanofibers for breaking the diffraction limit", *Opt. Lett.*, 41, 1336-1339 (2016).
- [9]. L. Yue, **B. Yan**, M. Attridge, Z. B. Wang, "Light absorption in perovskite solar cell: Fundamentals and plasmonic enhancement of infrared band absorption", *Sol. Energy*, 124 143–152 (2016).
- [10]. L. Yue, J.N. Monks, **B. Yan**, Z. B. Wang, "Large-area formation of microsphere arrays using laser surface texturing technology", *Appl. Phys. A*, 123: 318 (2017).
- [11]. L. Yue, **B. Yan**, J. N. Monks, Z.B. Wang, N.T. Tung, V.D. Lam, O. Minin, I. Minin, "Production of photonic nanojets by using pupil-masked 3D dielectric cuboid", *J. Phys. D: Appl. Phys.* 50, 175102(6pp), (2017).

Conference:

- [1]. **B. Yan**, L. Yue, J. N. Monks, Z. Wang, “Advanced optical superlens for nano imaging and patterning” Sêr Cymru Postgraduate Conference 2017, Cardiff (**Oral Presentation Award**).
- [2]. L. Yue, **B. Yan**, Z. Wang, “Light absorption in perovskite solar cell: Fundamentals and plasmonic enhancement of infrared band absorption” Solar Energy Society’s PVSAT 13 (Photovoltaic Science, Application and Technology) 2017, Bangor.
- [3]. **B. Yan**, L. Yue, Z. Wang, “Near-field Focusing of Dielectric Microspheres: Super-resolution and Field-invariant Parameter Scaling”. PIERS 2017 in St Petersburg, Russia (Oral presentation)
- [4]. **B. Yan**, L. Yue, Z. Wang, “A New Microsphere Superlens”. Inaugural Sêr Cymru Postgraduate Conference 2016, Swansea (Poster)
- [5]. Z. Wang, B. Yan “Subwavelength Imaging with Metamaterial Solid Immersion Lens” Work presented in NRN Distinguished Lecture.

Chapter 1. Introduction

1.1 Optical super-resolution

The optical microscope is one of the most important inventions in mankind history. The advent of the microscope has revolutionized all aspects of science fields, opening a door for scientists to explore the microcosm. With the advancement of nanotechnology and the continuous expansion of human horizon, research has evolved rapidly and extended to smaller size, for instance, molecular level. The urgent demands urge development of high resolution imaging technique. Although optical microscope is the elegant choice, due to the diffraction limit, it gradually lost competitiveness in nano-scale imaging. The mechanism for the resolution limit is related to optical diffraction and loss of evanescent waves in far-field. According to which, the resolution of a conventional microscope is around $\lambda/2$ in air. Efforts have been made to beat the diffraction limit over last decades. Owing to the development of nanophotonics, plasmonics and metamaterials, numbers of new super-resolution microscopy/nanoscopy techniques have appeared including near-field scanning optical microscopy (NSOM)[1], metamaterial superlens[2], spatially patterned excitation techniques (STED, RESOLFTs, SSIM)[3], single-molecule localisation techniques (STROM, PALM, FPALM)[3], structured illumination microscopy (SIM)[4], super-oscillation microscopy[5], [6] etc. However, none of those techniques can provide super-resolution under conventional broadband illumination, such as a halogen lamp. Meanwhile, most of the products are either expensive in price or require sophisticated processes. A simple and easy accessible way to achieve white-light super-resolution imaging is highly desired in many researches and applications.

Recently, it was discovered that all-dielectric microspheres can generate tiny focusing beyond diffraction limit, a phenomenon known as ‘photonic nanojet’ [7], [8]. This has been proven to be a simple and superior way to achieve sub-diffraction resolution[9]–[14]. Microsphere nanoscopy is able to efficiently capture the underlying near-field high frequency spatial harmonics of evanescent waves into propagational wave to form a magnified virtual image, which can be pick up by conventional objective lens[14]. Unlike other super-resolution

techniques, this new approach provides a real-time visualisation under white-light illumination, meanwhile, it is label-free and low intrinsic loss at higher optical frequency. However, due to narrow imaging window, poor manoeuvrability and varying imaging performance of microsphere lens, this advanced technique has largely remained at laboratory level and there is a great need to advance this technology to a level with greatly improved imaging performance and usability.

1.2 Aim and objectives

From the inspiration of the work by Wang et al. in 2011 [14], numerous studies with respect to microsphere-based super-resolution imaging have emerged. The motivation of this PhD was also derived from this. The main goal is to dramatically improve the technology in terms of its imaging performance (resolution and clarity), ease of use and reliability in practical applications. The vision is that our research developments will be commercialised in future, so that every microscope user will have the ‘Bangor Superlens’ products in their hand for daily use of microscopes, enabling super-resolution imaging technology fully accessible. Figure 1.1 illustrates the research that has been carried out in this thesis and links between them. They were grouped along two paths, resolution enhancement and ease of usability.

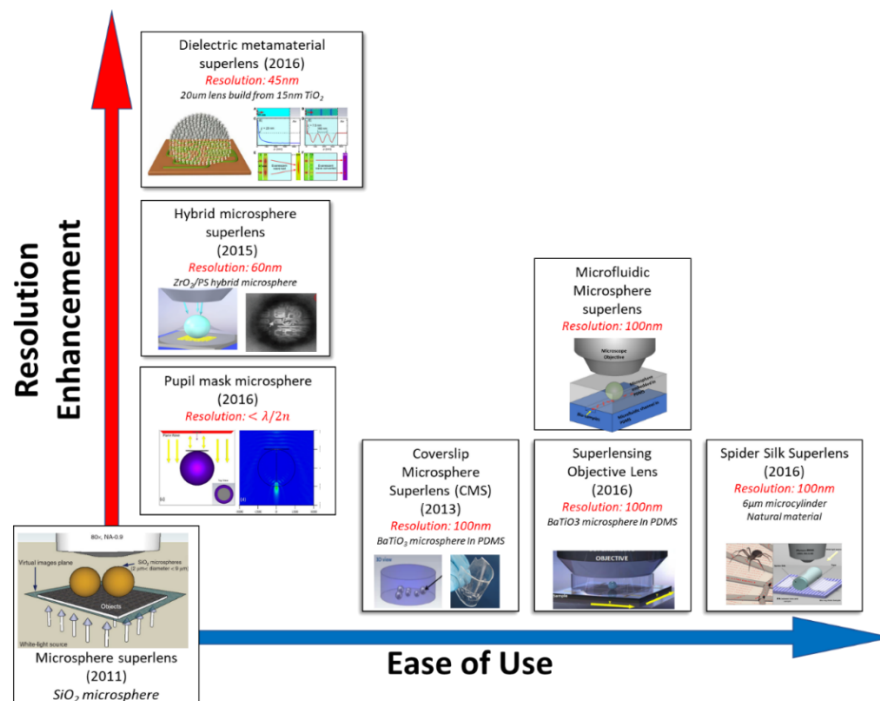


Figure 1.1 Summary of PhD works which are grouped along two paths, resolution enhancement and ease of usability.

Aim 1: Imaging performance (resolution & clarity) enhancement

In order to significantly enhance superlens optical super-resolution, the following objectives were set and have been achieved in this project:

- To systematically investigate the optical properties of microsphere superlens and understand how the super-resolution conditions can be affected by refractive-index particles, background medium, particle size and incident waves. Through these we established a systematic view of microspheres super-resolution performance. (chapter 4)
- New concepts of superlens designs, including pupil mask microsphere, high-index doping composite microsphere and nanoparticle-derived all-dielectric metamaterial superlens were proposed. These designs were theoretically analysed, and simulation results proved that they contribute significantly to control optical properties, for instance focal length, field enhancement and resolution. (chapter 5)
- High-resolution micro-lens such as high refractive index ZrO_2/PS nanohybrid colloidal microspheres and TiO_2 nanoparticle nanoparticles based superlens are fabricated by employing chemical synthesis methods. The as-synthesised ZrO_2/PS hybrid microspheres provide optical properties that are highly controllable in shape, size and refractive index, which are important for resolution enhancement. Nanoparticle derived dielectric metamaterial superlens has extraordinary optical abilities of effectively collecting and converting surface evanescent wave to propagational wave into far-field, which leads to achieve unprecedented imaging performance far beyond diffraction limit. Our proof-of-principle experiments confirmed that remarkable resolutions of 60 nm and 45 nm can be achieved under white-lights by these two superlenses, respectively. (chapter 6)

Aim 2: Ease of Use and reliability improvement

In order to achieve easy-to-use and reliable optical super-resolution imaging over a large area, the following objectives were set and met in this project:

- By encapsulating high refractive index microsphere in a polymer host medium to offer a coverslip-like superlens, it is possible to overcome the difficulty of microsphere

operation and deliver an accessible and durable method for researchers to easily access super-resolution imaging. (chapter 3)

- Some other works derived from above concept were also provided, including superlensing objective for large area scanning imaging and on-chip microfluidic nanoscope for bio-sample imaging. These superlens designs show great improvement of usability and have potential to be commercialised. (chapter 7 and 8)
- Biomining led us to look for a naturally occurring superlens in spider silks, which are transparent in nature and have micron-scale cylinder structure. It allows us to observe sub-diffraction features with a large field-of-view. This discovery opens a new door to develop biology-based optical systems and has enriched the superlens category. (chapter 8)

As a result of this research, the microsphere-based superlens technique has been effectively improved. The developed prototypes of superlens are able to overcome the difficulties and surpass the abilities of currently existing microsphere lens. Advantages of high-resolution and ease of usability offer the potentials in various practical applications, and meantime are important for commercialisation.

1.3 Thesis outline

Chapter 2 reviews some existing super-resolution imaging techniques and microsphere superlens techniques. The principle of super-resolution is provided and theoretical methods for optical simulation are discussed.

Chapter 3 details the theoretical simulation methods for analysing optical performance of microsphere and experimental methods for manufacturing superlenses. Simulation software and experimental setups are discussed in the chapter.

Chapter 4 presents a systematic investigation on small dielectric particles focusing characteristics (focal length, field enhancement, spot size) for a given refractive-index microsphere ($n=1.6$) with a varying size parameter across a wide range. Conditions for super-resolution foci were analysed in detail. It also describes the principles of field-invariant scaling of Mie parameters which is important for experimental scaling of the super-resolution designs.

Chapter 5 presents a study on engineered microsphere superlens that are designed to modulate focus properties in near-field zones. Designs are illustrated and theoretical analysis are provided. The first design is a circular pupil mask assisted microsphere lens. It provides the possibility to precisely control of near-field focusing properties by varying the mask area. The second is two-material composite microsphere with the lower part replaced by higher refractive index material, which allows new lens accessing contribution from solid immersion mechanism. The optimised focusing can be achieved by tuning refractive index and volume of lower material. The third design is the combination of pupil mask and composite designs. It has advantages of achieving resolution beyond diffraction limit and suppressing sidelobes which is unfavourable for imaging and other applications. In addition, we incorporated metamaterial concept in our superlens design. A new all-dielectric nanoparticle metamaterial superlens design was proposed. The optical properties of nanoparticles-stack metamaterial are illustrated. Detailed simulation results of designs are presents in this chapter.

Chapter 6 presents two superlens designs to enhance optical resolution. The first design is all-dielectric metamaterial-based solid immersion lens (mSIL). High refractive index nanoparticles are densely packed to form a 3D hemispherical structure on sample surface, resulting resolution of 45nm under white light condition. On the other hand, a high refractive index ZrO_2/PS nanohybrid colloidal microsphere is demonstrated in order to achieve optical properties that are highly controllable in shape, size and refractive index. The synthesis methods are introduced, and imaging performance is evaluated in this chapter.

Chapter 7 demonstrates an invention of super-resolution imaging and patterning system. A coverslip microsphere superlens (CMS) by encapsulating high-index microsphere inside a transparent host material (PDMS and PMMA) was integrated into conventional microscope objective. This design solves the synchronization problem between the coverslip superlens and the objective lens and hence provides an efficient way to manipulate particle lens for scanning operation in real-time nano imaging and nano patterning.

Chapter 8 discovers a biological superlens provided by nature: the minor ampullate spider silk spun from the *Nephila* spider. This natural bio-superlens can distinctly resolve 100 nm features under a conventional white-light microscope with peak wavelength at 600 nm, attaining a resolution of $\lambda/6$ that is well beyond the classical limit. In addition, a microfluidic

on-chip superlens device is proposed to manage live biological samples imaging. Imaging performance are evaluated by different biological samples with different features.

Chapter 9 summaries the results presented in this thesis and provide an outlook for future research possibilities.

Chapter 2. Literature Review

This chapter reviews the literature relating to the project, including fundamentals on different limit, the field of optical super-resolution, fundamentals, developments and state-of-the art of microsphere nanoscopy technique and theoretical methods for optical super-resolution simulation.

2.1 Optical diffraction limit

Diffraction occurs in all kind of waves including sound, water and electromagnetic waves. It is a phenomenon in which waves change the direction of propagation due to passing through obstacles or a medium with a non-uniform refractive index. Diffraction is an intrinsic property of light and limits smallest spot size. In 1873, Ernst Abbe firstly proposed the resolution limit of the microscope[15]. He defined that the light cannot be confined to a minimum resolvable distance, d , to be imaged smaller than one half of its wavelength. The formula of optical diffraction limit is

$$d = \frac{\lambda}{2 N.A.} \quad 2.1$$

where $N.A.$ is numerical aperture and λ is wavelength of light. This fundamental limit the resolution of images from optical systems including microscopes, cameras, and telescopes. It may be regarded as a specialisation of Heisenberg's uncertainty principle with respect to position (Δx) and momentum (Δp_x) of a photon[16].

$$\Delta p_x \Delta x \geq h \quad 2.2$$

The Δx and \vec{p}_x refer to any of the three components of the position and the momentum vector, Δp_x and Δx refer to their uncertainty, respectively. In medium i , the three components of the wavevector k_x has to satisfy

$$k_i^2 = k_x^2 + k_y^2 + k_z^2 \quad 2.3$$

Where $|k|_i = 2\pi/\lambda_i = n_i|k_0|$, where λ_i is the wavelength in medium i , and n_i is the refractive index.

In classical optics, the free propagation waves are closely related to the diffraction limit in the far-field region. A wavevector, k -vector has three real-value components, which determines the character of free propagation. So, according to equation (2.3), k_i is always larger than each of the components k_x , k_y and k_z . The minimum cross-section of a freely propagating beam is hence

$$\Delta x > \frac{1}{k_x} = \frac{\lambda_i}{2\pi} \quad 2.4$$

Which is very similar to the well-known formula for the Rayleigh criterion, which describes the smallest resolvable distance for a focusing objective

$$CD = 0.61 \frac{\lambda}{N.A.} \quad 2.5$$

Where λ and N.A. represent the wavelength and numerical aperture. This fundamental limit confines the resolution of images from optical system, such as microscopes, cameras and telescopes.

2.2 Super-resolution with near-field optics

The light emitted or scattered from an object contains not only propagating waves but also evanescent waves. The effect of diffraction limit could be reduced or even eliminated when evanescent waves become significant. The amplitudes of evanescent waves, which are carrying the sub-diffraction-limited information, fade away rapidly in at least one direction in space. According to equation (2.3), if the respective component k_z is imaginary, the residual component k_x , therefore, can be larger than k_i in absolute value. As a result, it makes Δx become smaller. Evanescent waves are electromagnetic waves those can be excited

preferentially (though not exclusively) when light waves traveling from optical dense medium to optical sparse medium undergo total internal reflection. Its amplitude attenuates exponentially with distance from the interface of two different media. Therefore, the good fidelity is lost in far-field image plane and the use of evanescent waves in near-field becomes more important. A well-known example employ evanescent signal is near-field scanning optical microscope, which has remarkable resolution of 12 nm as reported[1].

2.3 Super-resolution techniques

2.3.1 Near-field Scanning Optical Microscope (NSOM or SNOM)

The development of near-field scanning optical microscope (NSOM or SNOM) opens the door to super-resolution research. It uses a tiny tip positioned close to an object's surface to collect evanescent waves in the near field. Scanning the sample generates a super-resolution image whose resolution is determined by tip aperture diameter instead of wavelength of incident light.

The idea of NSOM appeared in 1928 by Synge[17]. He proposed an imaging method to break diffraction limit. In the scheme, he suggested that by employing a strong light source behind a thin metal film with tiny aperture and sub-wavelength sample at 100nm distance from light source could be detected and imaged by point-by-point scanning. He believed, this technique could be a breakthrough in field of imaging research, but practical difficulties of precisely scanning aperture within a wavelength distance stemmed its further development until 1980's. Thanks to the development of nano-fabrication technology to fabricate a subwavelength size probe tip, the precision control of probe tips, and computer-aided image processing techniques transferred from Scanning tunnelling microscope (STM) and Atomic force microscopy (AFM), the first modern NSOM instrumental setup with single molecular detection performance was demonstrated by Betzig's group[1].

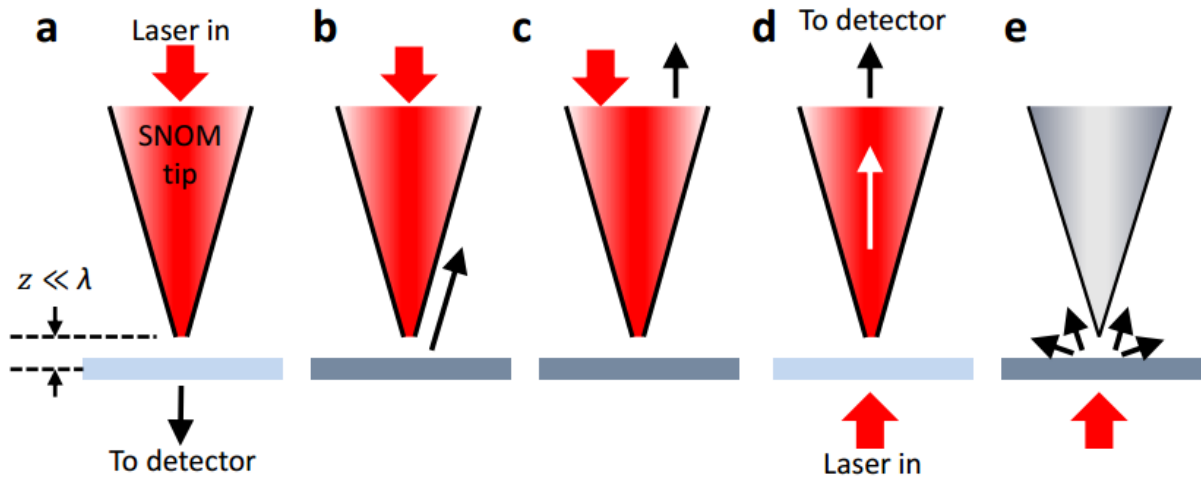


Figure 2.1 Modes of NSOM. (a-d) Aperture mode, and (e) apertureless mode. (a) Apertured tip generates illumination and transmitted signal is collected by external detector, (b) scattered signal collection by the tip, (c) reflected signal collection by the tip, and (d) external illumination and collection by the tip. (e) Illumination from external source and collection by an apertureless NSOM tip[18].

In general, there are two operation modes of near-field imaging in NSOM. They are aperture mode and apertureless mode showing in Figure 2.1. In the aperture mode of NSOM operation (Figure 2.1 a-d), a subwavelength aperture with diameter of 20nm to 100nm is used at the metal-coated tapered fibre tip. The apertured tip operates as either generation of subwavelength point illumination or collection of reflected or transmitted signal. On the other hand, the apertureless mode uses very sharp contour and non-metal-coated tip as a small scatterer and signal transmitted or reflected from the sample is scattered by the tip, then collected by a large external detector.

In order to achieve high resolution and artifact free images, it is necessary to maintain a constant distance of a few nanometres between sample and probe tip. There are two feedback mechanisms usually used in NSOM system: (1) Constant force feedback, which is similar to the feedback mechanism in atomic force microscopy (AFM), measuring the tip deflection during constant force applied. (2) Shear force feedback where a tuning fork is mounted alongside the tip. Its oscillation amplitude reveals the distance from the sample.

In 1984, the aperture mode NSOM reached resolution of $\lambda/20$ reported by Pohl. Few years later, Betzig et al. reported a resolution of 12nm ($\lambda/43$)[19]. More recent paper has reported that the apertureless NSOM can achieve less than 10nm resolution[20]–[22]. The advent of

NSOM brought effective way to determine the nanoscopic and mesoscopic structures. It is widely used in applications across branches of biology, chemistry and physics. Nevertheless, some limitations also exist. Firstly, it need long scan time for large area high resolution imaging. Second, it is limited to surface and subsurface investigation. Any further information at deep structure cannot be captured due to its extremely shallow depth of field. Third, the tip is not robust and easily damaged.

2.3.2 Metal-based Metamaterial Superlens and Hyperlens (M-MSH)

Metamaterial concept was initially proposed by British scientist John Pendry in 2000[2]. It is an intentionally-made artificial material, which employs periodical structure on a scale much smaller than wavelength. Such emerging material exhibits negative index of refraction and, therefore, possesses unprecedented extraordinary optical properties, where NIM (negative-index material) is able to restore the phase of propagating wave and enhance amplitude of evanescent wave. Therefore, a perfect fidelity image can be reconstructed without the constraints imposed by diffraction limit.

Mechanism comparison of various optical lenses is briefly illustrated in Figure 2.2. Wave vectors scattered from an object comprise both propagating waves and evanescent waves. The propagating waves containing large feature information can be deliver to far-field, while evanescent waves possess sub-diffraction information are only confined in the near-field zone. The conventional optical lens can only collect far-field propagating waves and lose the evanescent waves, resulting diffraction-limited resolution (Figure 2.2 a). The near-field superlens, which employs NIM close to object, is able to enhance to evanescent waves and contribute to a sub-diffraction-limit image (Figure 2.2 b). By adding nanoscale corrugations on top surface of superlens, evanescent waves are coupled to propagating waves, thus make information be detectable in far-field (Figure 2.2 c). The hyperlens using multilayer design as a strongly anisotropic metamaterial can transfer the deep subwavelength information into far-field (Figure 2.2 d).

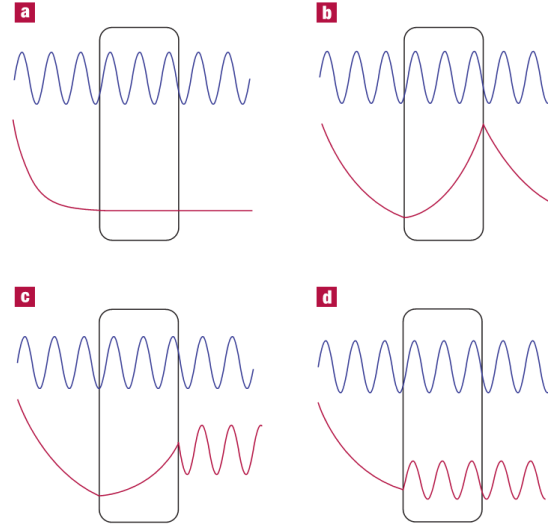


Figure 2.2 Comparison of various types of optical lenses. Blue and red curves are the propagating and the evanescent waves, respectively. (a) Conventional lens. (b) Near-field superlens. (c) Far-field superlens. (d) Hyperlens. The wavy curves and smooth curves represent propagating waves and evanescent waves, respectively[23].

A number of groups have experimentally demonstrated the sub-diffraction-limited imaging performance of metamaterial near-field superlens. In 2003, Liu et al. and Fang et al. experimentally confirmed silver slab is capable to significantly enhance evanescent waves, which matched Pendry's theory[24], [25]. In 2005, optical superlensing effect was realised and reported 60nm ($\lambda/6$) resolution was obtained by thin silver film superlens (Figure 2.3)[26], [27]. However, there are some challenges. The NIMs are usually thin slabs of metal. As we know, light could be easily absorbed by metal, especially the area carrying the higher-resolution information. Another limitation of superlens is that they are 'near-sighted', which means that they only work in the near-field.

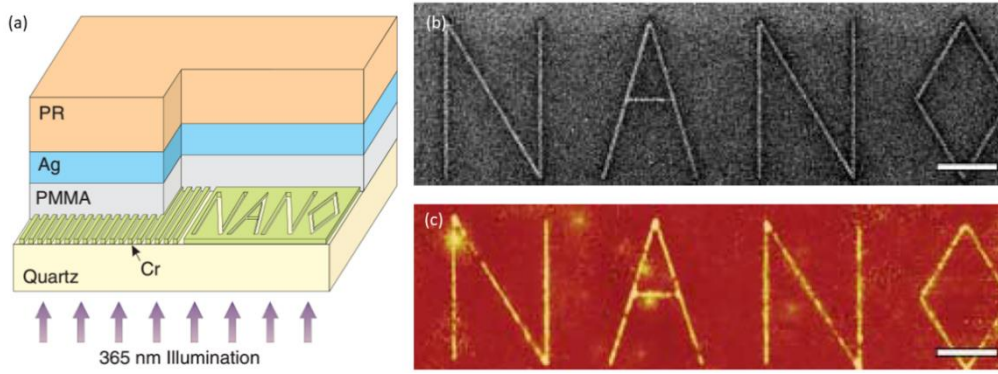


Figure 2.3 (a) schematic configuration for the silver superlens experiment. PR, photoresist layer; PMMA, polymethylmethacrylate. The superlens image was revealed by means of photolithography at wavelength $\lambda = 365$ nm. (b) Focused Ion Beam (FIB) image of the object. The linewidth of the “NANO” object was 40 nm. (c) AFM of the developed image on photoresist with a silver superlens. Scale bar is 2 μ m in (b) and (c) [26].

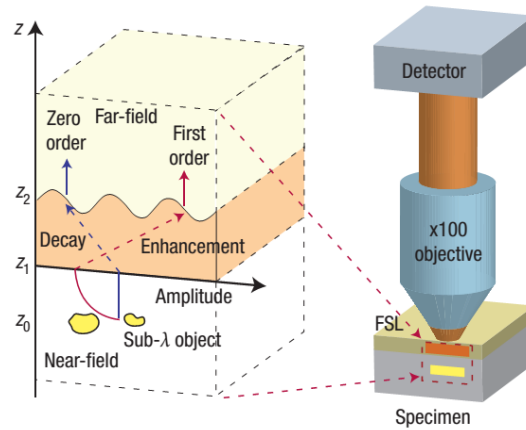


Figure 2.4 Schematic design of far-field superlens (FSL). A FSL is constructed by adding a subwavelength grating onto a thin silver slab. A FSL is inserted between the specimen and objective of optical microscope to realise far-field super-resolution imaging. [28].

Later, a far-field superlens (FSL) based on silver superlens was proposed to deal with sub-diffraction image transferring to far-field[29]. With nanoscale corrugations as diffraction grating on silver superlens, FSL working under conventional microscope is able to resolve nanowires with 50nm width and 70nm interval clearly, reported by Liu et al.[28], [30]. The schematic design is shown in Figure 2.4. The sub-diffraction-limited image in the far-field is contributed by surface resonance to enhance evanescent wave, and subsequently, conversion from evanescent wave into propagation wave by a designed surface scattering.

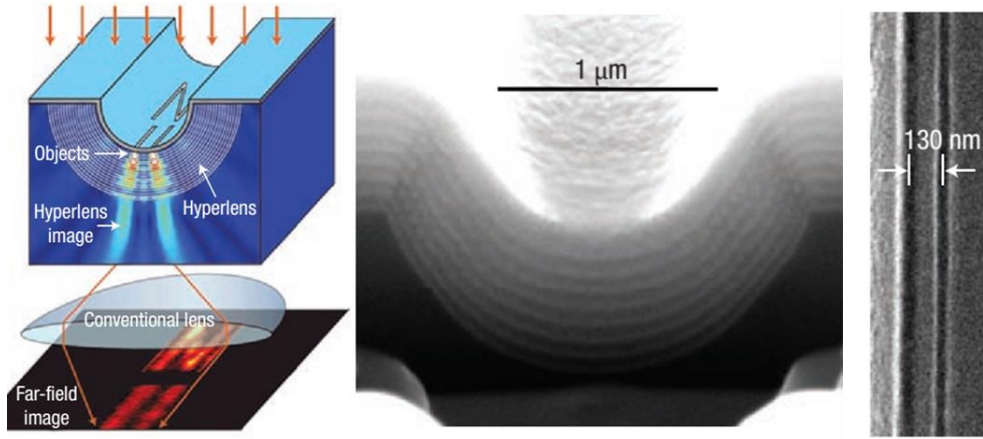


Figure 2.5 (a) Schematic of experimental set-up for optical hyperlens and numerical simulation of sub-diffraction-limit imaging. (b) SEM image of cross-section of a cylindrical hyperlens. (c) SEM image of object with 50 nm linewidth and 80 nm gap[31].

The hyperlens is an alternative magnifying tool which uses cylindrically or spherically curved multilayers as anisotropic medium with characterised hyperbolic dispersion to generate the magnification effect [32]–[34]. The evanescent wave conversion happens instantly at entering such anisotropic media rather than at exit interface. The first optical hyperlens has been demonstrated by [31], consisting of a curved periodic stack of Ag and Al₂O₃ deposited on a semi-cylindrical cavity substrate and has one dimensional magnification of three times with a resolution of 130 nm. Figure 2.5 demonstrates the mechanism of the cylindrical hyperlens. The two-dimensional magnification at visible frequency was obtained from spherical hyperlens by Rho et al [35]. Because of the difficulties of nanofabrication and fundamental surface plasmon polaritons (SPPs) energy loss, the resolution of the superlens and hyperlens is limited to about $\lambda/3$ to $\lambda/7$ in the visible spectrum. Furthermore, a typical laser source is required, meaning it cannot function under a broadband frequency.

2.3.3 Super-Oscillation Lenses

Super-oscillation is of particular important for researches of quantum mechanics, signal processing and optics. In 1943, Schelkunoff proposed a design of super-directive antennas for microwave community, which applied an antenna array of limited size for generating a narrow beam beyond diffraction limit [36]. In 1952, Torraldo di Francia applied this concept to optical instruments to increase resolution, which is realised by specially designed optical pupil filters [37]. Later, Bucklew and Saleh devised an imaging system with ideal band-limited

function which could achieve arbitrary fast Fourier components and it is regarded as superposition of low frequency beam, so that they can transfer high frequency information further than the several wavelengths[38]. Since the inspiration from weak quantum mechanical measurements by Aharonov[39], Berry et al. firstly proposed concept of super-oscillation and linked it to optical imaging[40]. It has been theoretically demonstrated that a precisely designed mask such as multiple concentric rings could form subdiffractional spatial energy localisations which does not require near-field evanescent mechanism.

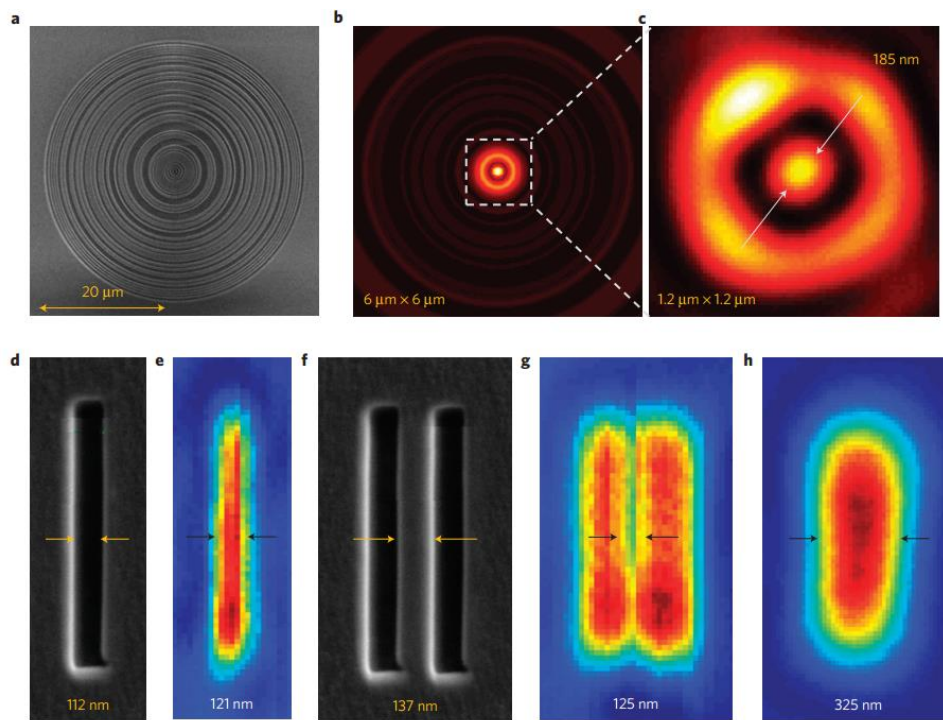


Figure 2.6 Subwavelength imaging with a super-oscillatory lens. (a) SEM image of the super-oscillation lens. (b) Calculated energy distribution of the super-oscillatory lens at 10.3 μm from the lens. (c) The actual focal point, $\lambda=640\text{nm}$. (d) SEM image of a 112 nm slit and (e) its super-oscillatory lens image; (f) a double slit and (g) its super-oscillatory lens image. (h) The image of the same double slit is not resolved using a conventional lens of $\text{NA}=1.4$ [6].

Recently, Zheludev's group in Southampton has theoretically[5] and experimentally[6] demonstrated super-resolution imaging of multiple points or slits by using a mask with quasi-periodic nanostructured array. Figure 2.6 demonstrates a concentric rings super-oscillation lens design with a resolution better than diffraction limit. Another possible solution of super-oscillation optical needle has been proposed for generating a sub-diffractive localised hotspot for illuminating samples and hence offering a scanning process of sample imaging[41]. The localised hotspot requires continuous mask and the fabrication is limited by current

technology. Although they have claimed that this super-resolution technique can provide infinitesimal resolution and does not require near-field evanescent wave collection, its disadvantages are also obvious, including difficulties of mask fabrication and the appearance of high intensity sidelobes near the central spot simultaneously created by interference, which seriously affect the practical application.

2.3.4 Structured Illumination Microscopy (SIM)

In 1966, Lukosz suggested that the use of gratings for the illumination and/or the detection pathway should improve the resolution in reflection imaging[42]. This concept was recently further advanced as Structured Illumination Microscopy (SIM)[43]. In SIM technique, objects are illuminated by multiple-structured illumination with different phases and orientations to reconstruct information of high-frequency components into detectable Moiré patterns. Consequently, the resolution can be boosted by a factor of two at most in this method. Figure 2.7 (a-c) illustrates the principle of resolution enhancement by SIM. However, this technique requires intensive computation for image reconstruction. And imaging resolution is limited to 2-fold of the diffraction limit.

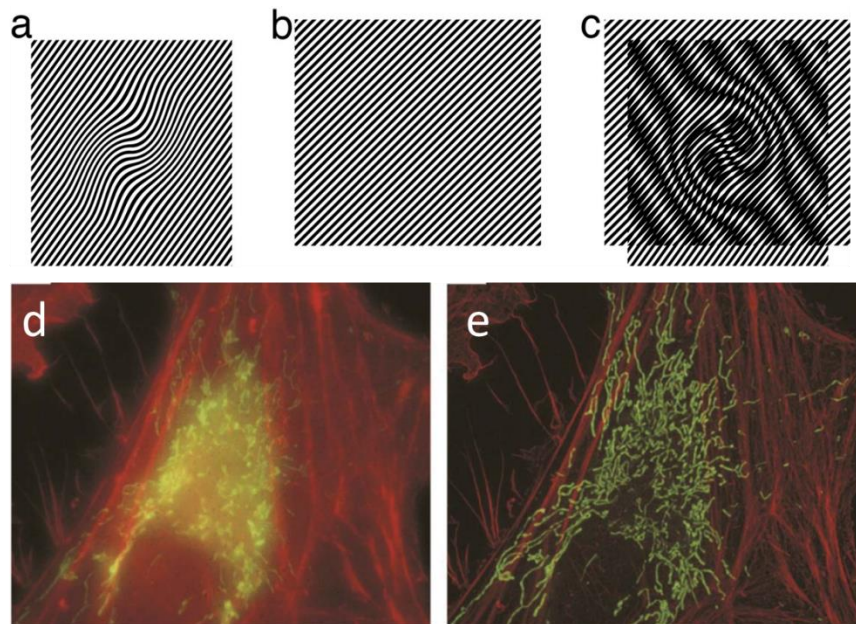


Figure 2.7 (a-c)Schematic of structured illumination microscopy. Comparison of (d) conventional microscopy image and (e) structured illumination microscopy image of mitochondrial and actin cytoskeleton[44].

2.3.5 Super-resolution Fluorescent Microscopy

Fluorescence microscopy is the most popular tool for observing biological specimens. It is a technique provides high-resolution with aid of fluorescence effect. As a result, it can provide visualisation and analysis of real-time dynamic of living organisms. There are two categories among general fluorescence microscopy: wide-field microscopy and laser scanning microscopy. The difference between two techniques is the mechanism of collecting fluorescent signal. Nevertheless, both microscopies suffer the classical optical diffraction limitation. The super-resolution fluorescence microscopy techniques were developed to overcome diffraction limit and have achieved great success. Nowadays, they can be classified into two main categories: spatially patterned excitation method (STED, RESOLFTs, SSIM) and single -molecule localisation method (STORM, PALM, FPALM)[3].

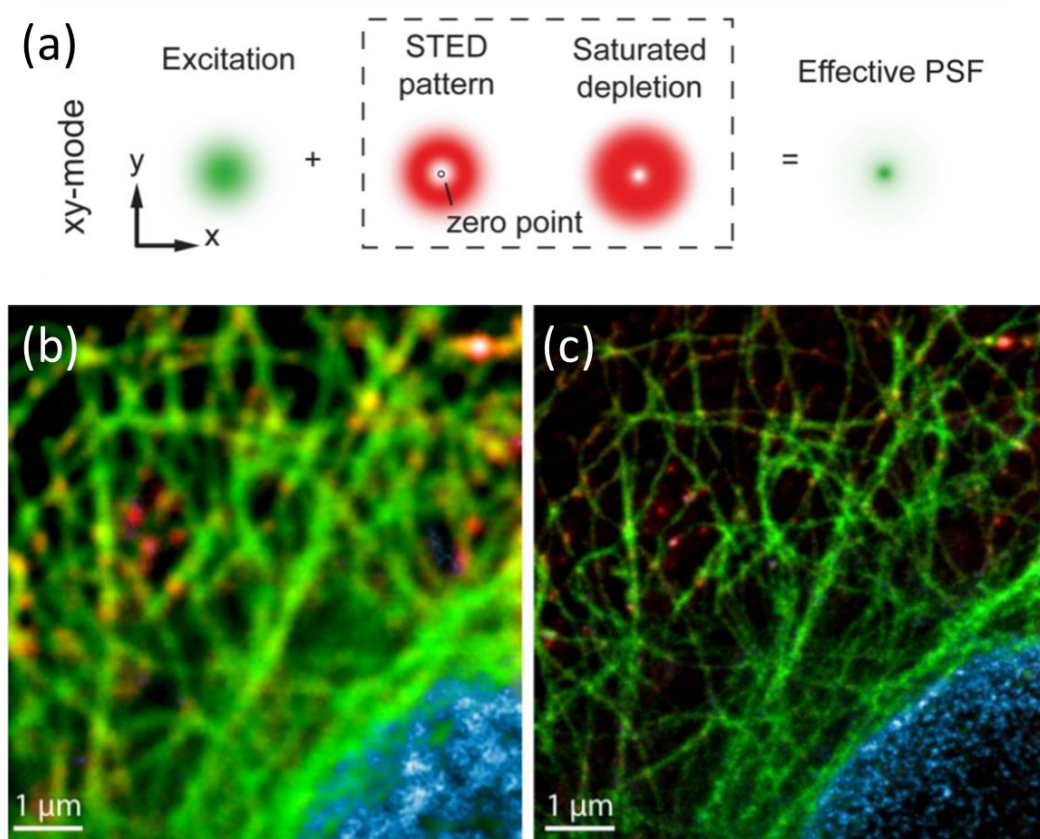


Figure 2.8 (a) Mechanism of STED microscopy. Combined beam from excitation and depletion in STED microscopy. (b) Conventional confocal microscope image of lamin and tubulin sample and (c) STED microscope image of same sample[45].

The representative product for spatially patterned excitation method is stimulated emission depletion microscopy (STED)[45]. It attains sub-diffraction image by minimising excitation area on staining sample. In addition to a focused laser beam to excite a fluorescent dye, a second doughnut-shaped laser beam is applied to suppress emission from the doughnut region, leaving the small central position to be detected (Figure 2.8 a). By increasing intensity of doughnut beam, the doughnut width increases, subsequently resulting sub-diffraction scale in central portion. STED microscope has spatial resolution of below 10 nm, reported by Hell et al. in 2009[45].

Differing to above, single-molecule localisation method requires photo-switchable fluorescent probes and computation algorithms to precisely determine the position of each molecule. In this approach, individual fluorescent labels on the sample can be precisely localised by single laser illumination and then final images are reconstructed by stacking thousands of images with different illuminations [Figure 2.9 (a)]. This idea of photo-switchable imaging was first used in photoactivation localisation microscopy (PALM)[46] and stochastic optical reconstruction microscopy (STORM)[45]. Each activated molecule exhibits blurred Airy pattern with Gaussian shape whose width is the same as diffraction limit. Through computational algorithms, the centre of the molecule can be determined. In theory, the resolution is not limited by diffraction, but rather by the precision of molecular positions can be measured. This could be affected by the distance between two adjuncts excited molecules in single illumination. If two fluorophores locate within a distance smaller than Airy width, they cannot be optically distinguished due to the overlapped intensity distributions. Therefore, it is important to control the density of photon switchable probes and it can be achieved by applying variety of fluorophores with organic molecules and fluorescent proteins. As a consequence, this technique requires many cycles of imaging processes and it is not fast imaging approach.

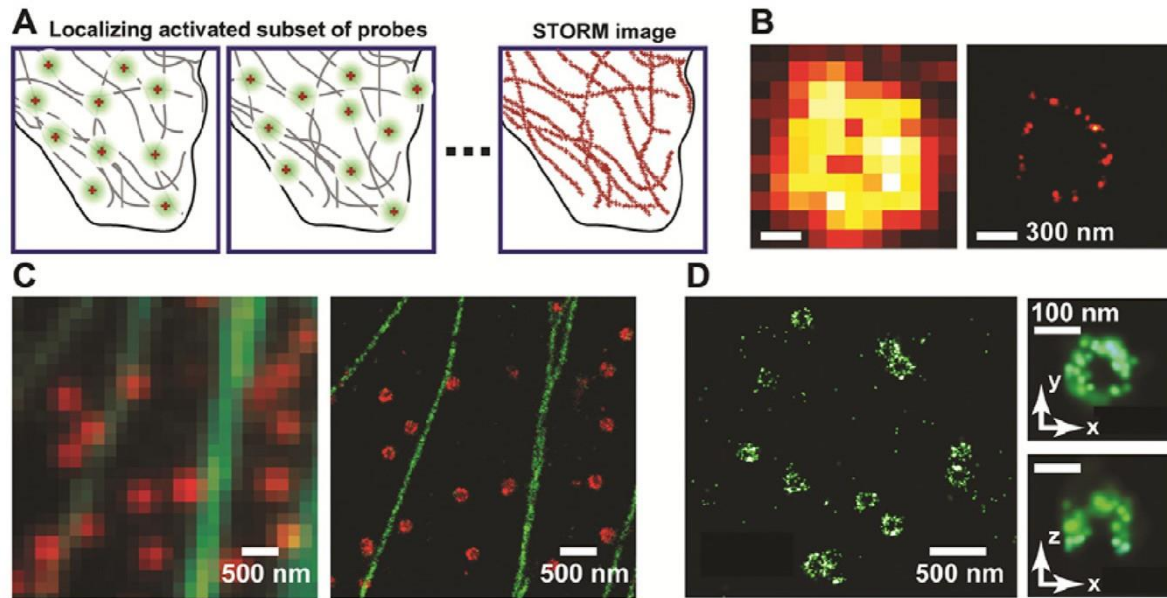


Figure 2.9 Super-resolution imaging by single-molecule localisation method. (A) At any time, only a sparse set of fluorophores decorating the sample are switched ON (green circles), and their positions are determined (crosses). Over time, many molecules have been localized, and their positions are plotted to create the STORM image. (B) Comparison of conventional (left) and STORM (right) images of a circular RecA filament. (C) Comparison of conventional (left) and two-color STORM (right) images of microtubules (green) and clathrin (red) in a cell. (D) (Left) XY-cross-section of a 3D STORM image of clathrin-coated pits in a cell. (Right) Magnified image of a single coated pit. Upper panel: an XY cross-section of the pit. Lower panel: an XZ cross-section of the pit[47].

2.3.6 Other techniques

- **Scattering Superlens Technique**

According to classic diffraction limit established by Ernst Abbe, the optical resolution is affected by the size of numerical aperture (NA). The NA of lens defines the ability of coupling the incident light. A greater NA can contribute to minimising the resolution limit. Recently, it has been proved that scattering superlens technique is able to effectively increase the NA of an imaging system, hence enhances the resolution. This approach utilises a strongly disordered scattering layer combined with high-refractive-index homogeneous slab to couple the incident light to all propagating waves. Disordered intensity pattern created by internal multiple-scattering, however, cannot be directly used for imaging. By controlling the phase of incident wavefront, a sharp optical focus is generated in the object plane[48]. A similar work was presented by Park et al.[49]. They used turbid media consisting of random nanoparticles to couple sub-wavelength information in near-field to the far-field. Figure shows the principle

and imaging performance of scattering superlens[50]. Scattering superlens provides sub-diffraction imaging in wide field of view, however the drawbacks are also obvious, it requires long pre-processing and precise control of distance condition of sample and disordered media.

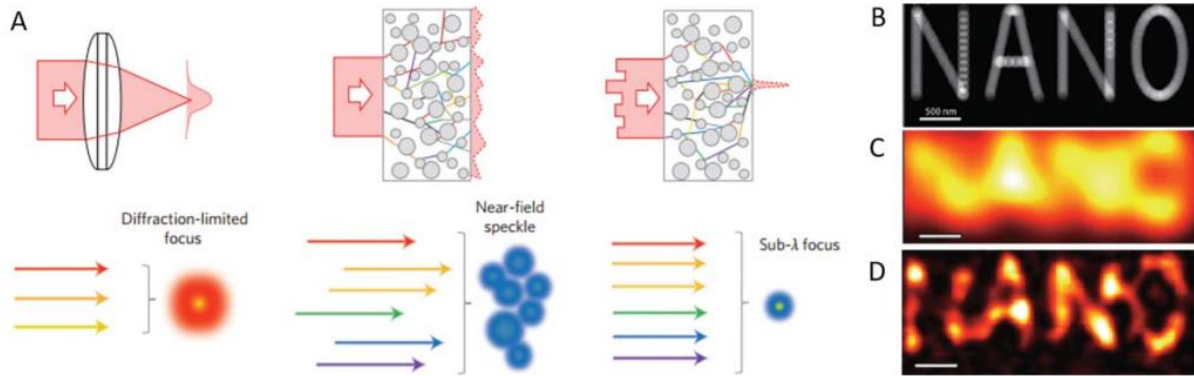


Figure 2.10 Schematic of scattering superlens principle. (A) light focusing comparison of conventional lens, random nanoparticle media layer and incident wavefront control. conventional lens cannot focus beyond diffraction limit due to the lack of high transverse wave vector (left). In random nanoparticle media, incident waves are scattered inside media and coupled to propagating waves via speckle waves (middle), and due to the wavefront control (right), phase-matched light is focused in sub-wavelength scale. (B–D) Image reconstruction through random media. (B) The movement of the tip apertures, (C) convolution of the tip movement, and (D) final reconstructed images by near-field transfer matrix of random particle, indicating sub-wavelength imaging[49], [50].

• 4Pi Lens Technique

A conventional microscope always generates a focal spot with an elongated shape which results lower axial resolution. This is due to the fact that an objective lens only produces a segment of a spherical wavefront in a single direction. In principle, a full spherical wavefront of a solid angle of 4π can create spherical focal spot, hence enhance the spatial resolution in z-direction. The 4Pi microscope based on the principle of interference is an extension of confocal and two-photon microscopy. The idea behind the 4Pi microscope is to create a spherical focusing spot onto a sample by using two opposing high objective lenses coherently[51]. A confocal laser scanning 4Pi microscopy can achieve an axial optical resolution down to 100 nm regime which is 5-7-fold improvement to conventional confocal laser scanning microscope[52].

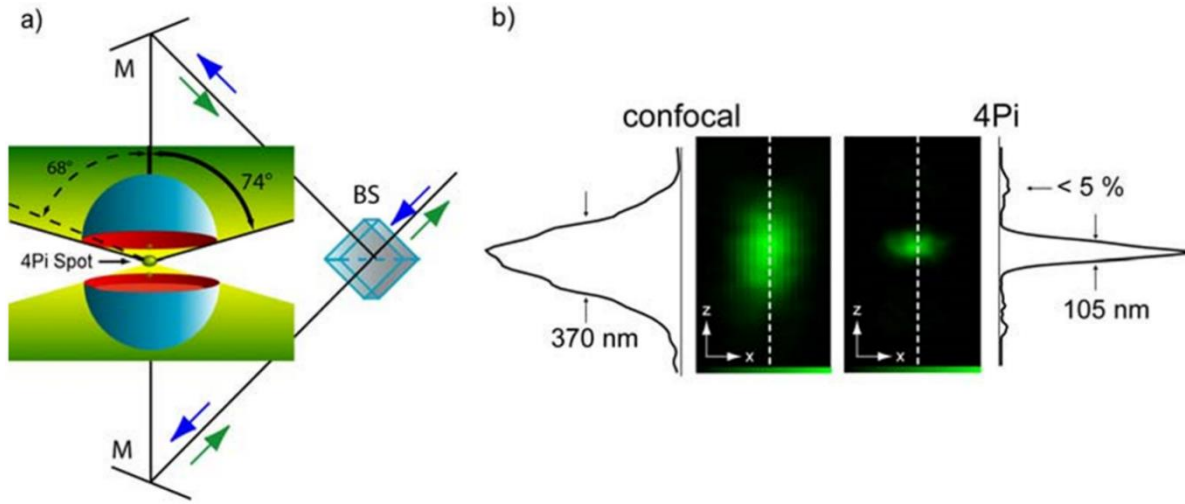


Figure 2.11 Schematic of 4Pi microscopy (a) a laser light is split into two beams that focus onto a sample through two opposing lenses converting the partial wavefront into spherical wavefront. (b) imaging performance comparison of a conventional confocal microscope and 4Pi microscope[53].

2.4 Microsphere super-resolution imaging technique

2.4.1 Photonic nanojet

Recently, microspheres can function as optical superlenses for nanoscale super-resolution imaging. Unlike metamaterial superlens and hyperlens, which use metal to amplify evanescent waves to achieve super-resolution, the mechanism was discovered that super-resolution focusing can be achieved by a phenomenon called ‘photonic nanojet (PNJ)’ from microsphere light scattering. This effect was firstly discovered by Lu and Luk’aynchuk et al. in 2000[8]. They demonstrated a 500-nm silica sphere was able to enhance optical near-field for subwavelength surface structuring. This near-field focusing effect by microsphere has attracted enormous attention and many progresses have been made. In 2004, Chen et al. proposed a new term ‘photonic nanojet’ which is widely known in optics community for dielectric particle super-resolution focusing at the shadow side of particle[7].

Important properties of PNJ summarised in reference [52] and [53] are following, firstly the lateral resolution of PNJ can reach $\lambda/2n$, where λ is the light wavelength and n is the refractive index of particle. Secondly, PNJ is a narrow, high intensity and non-evanescent light beam. And it is a non-resonant phenomenon which can appear for a certain range of diameter of the microcylinder or microsphere from 2λ to 40λ when the refractive index contrast relative to the background medium is less than about 2:1.

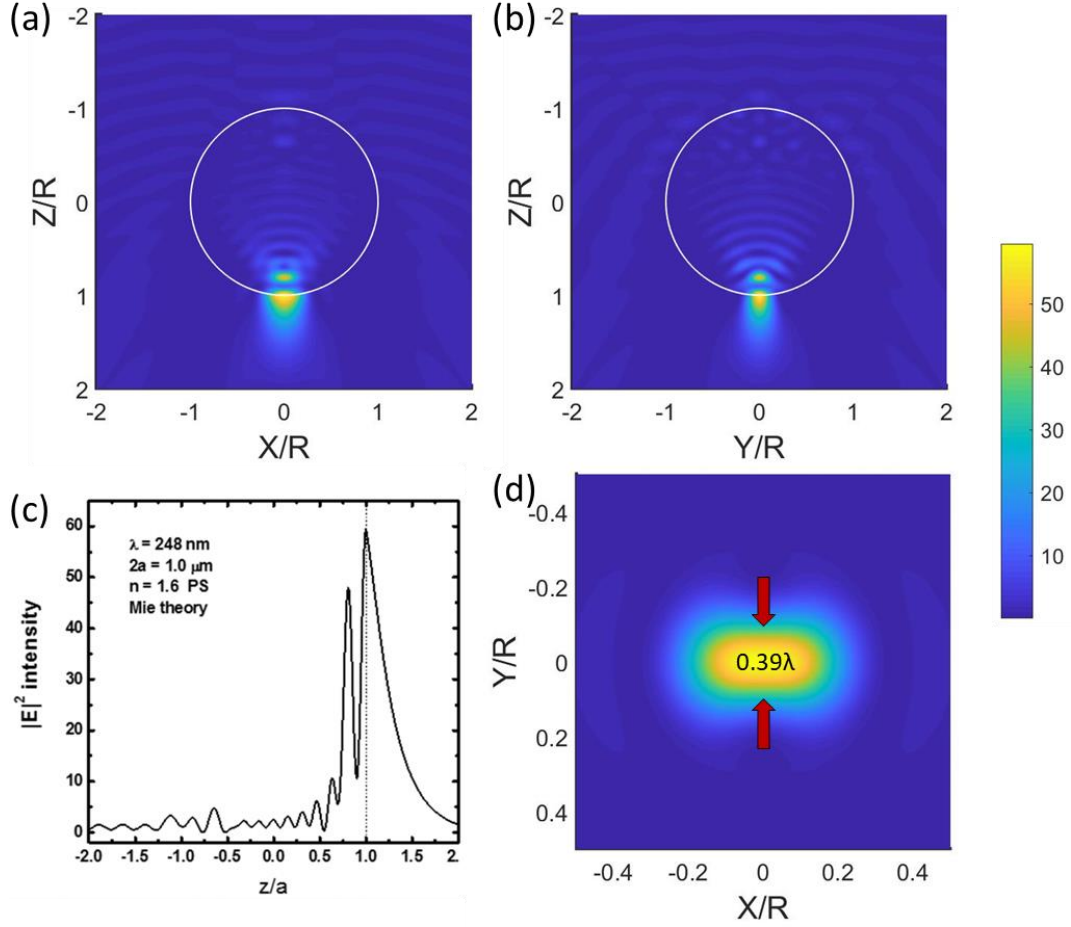


Figure 2.12 An example of PNJ generated by $1\mu\text{m}$ PS ($n=1.6$) microsphere. Illuminated by a laser at $\lambda=248\text{nm}$. (a) electric field intensity distribution, $|E|^2$, at XZ-plane (parallel to polarisation) and (b) YZ-plane (perpendicular to polarisation). (c) shows the intensity along Z-axis (propagation direction). (d) lateral field distribution (XY-plane) of focal spot under the microsphere ($z=a$). The maximum intensity enhancement is about 60 times and minimum lateral focus size is 0.39λ .

An example of near-field distribution calculated by Mie theory is illustrated in Figure 2.12. A $1.0 \mu\text{m}$ diameter polystyrene (PS) microsphere ($n=1.6$) is illuminated by a laser beam with 248 nm wavelength. As can be seen from the figures, the electric field is dramatically enhanced 59.6 times in the near-field zone under the microsphere ($z=a$, where a is particle radius), then decreases rapidly to 1.57 at $z=2a$. The photonic nanojet exhibits an elliptical profile in lateral (XY-plane) and has a waist of 0.39λ within the cross direction of incident polarisation, which is below the diffraction limit, 0.61λ (Rayleigh criteria) or 0.5λ (Sparrow criteria). This unique characteristic of PNJ can contribute to effectively shrink the full width at half maximum (FWHM), hence it has a wide variety of applications, including sub-wavelength nanopatterning, nanolithography, optical storage and spectroscopy[8], [10], [56]–[65].

On the other hand, as a result of the reciprocity principle[66], super-resolution imaging can be realised by reversing PNJ mechanism. When an object is placed close to or in contact with microsphere, evanescent waves scattered by sub-wavelength samples are coupled into microsphere. Then evanescent waves are converted into propagating waves inside a microlens due to the reciprocity principle, the subwavelength information of the object is magnified and transferred to the far-field region. The following sections will discuss some development of super-resolution imaging via microsphere superlens techniques.

2.4.2 Wide-field microsphere superlens

In 2011, Wang et.al proposed ‘microsphere nanoscopy’ technique that uses optically transparent SiO_2 microsphere with 2-9 μm diameter as superlens to resolve nano-feature down to 50 nm under a standard white-light illumination[67]. Schematic diagram and imaging performance are illustrated in Figure 2.13.

This technique is easily achieved by simply depositing microsphere on top of the sample surface via self-assembly method. An ordinary microscope with halogen illumination source is used. These microspheres function as superlenses that collect and magnify the underlying near-field object information into a magnified far-field virtual image, which can be captured by a conventional microscope objective. Therefore, microsphere superlens technique requires the combination of microsphere superlens and microscope objective.

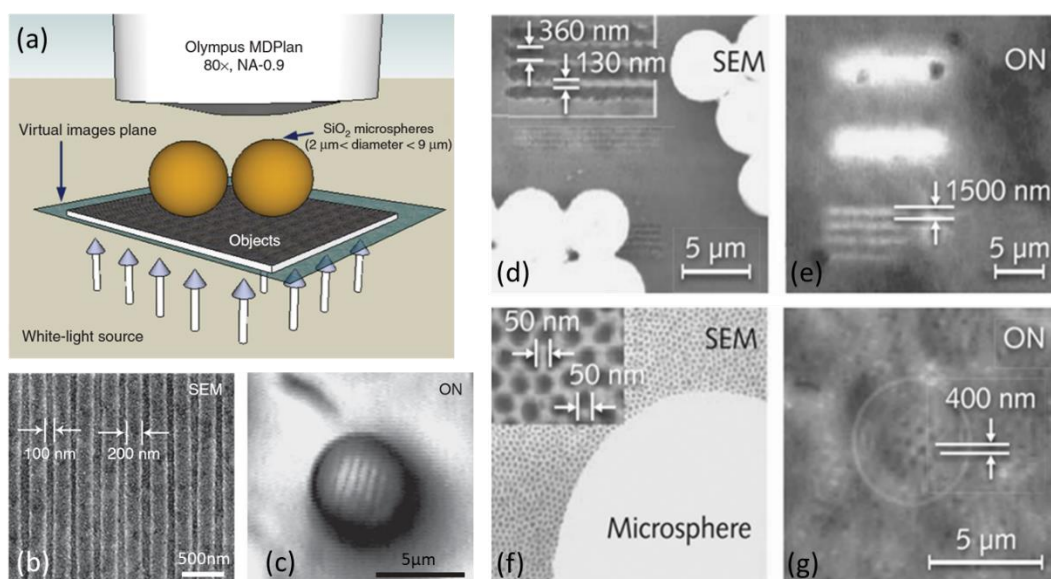


Figure 2.13 Schematic diagram and imaging performance of SiO_2 microsphere superlens.

(a) Experimental configuration of microsphere superlens integrated with a classical optical microscope. (b-g) Experimental results for microsphere superlens imaging. (b) SEM image of a Blu-ray DVD disc (200 nm lines and 100 nm grooves). (c) Optical imaging by microsphere in reflection mode. (d) shows SEM image of a diffraction grating with 300 nm wide lines spaced 130 nm apart. (e) shows the lines are clear resolved by microsphere with a 4.17X magnification in transmission mode. (f) shows the SEM image of a gold-coated fishnet membrane sample with 50 nm pores spaced 50 nm apart. (g) shows the optical image by microsphere superlens with 8X magnification in transmission mode[14].

In Figure 2.13 (b-g), it is demonstrated that objects with sub-diffraction-limited features are clearly imaged by microsphere nanoscope in either transmission or reflection illuminations. Figure 2.13 (b and c) reveals that a Blu-ray DVD disc with 200-nm-wide lines and 100-nm-wide grooves are clearly imaged by a 4.7 μm microsphere in reflection mode. In another sample, (see Figure 2.13 d and e) diffraction gratings with 360-nm-wide lines and 130 nm space are imaged in transmission mode. It is noted that nano-patterns without microsphere are merged into a single bright spot which means unresolvable by conventional microscope. In addition, super-resolution capability of microsphere in resolving 50 nm was also reported in Figure 2.13 (f and g). In this case, the microsphere nanoscope resolves 50 nm pores well beyond the diffraction limit with a resolution of $\lambda/8$ - $\lambda/14$ in the visible band and corresponding magnification of 8X.

Apart from above, many studies have demonstrated super-resolution imaging performance by different types of microspheres. Large diameter (30–100 μm) polystyrene microspheres (refractive index of the particle: $n_p = 1.59$) were also reported for the super-resolution imaging of a Blue-ray disc in an air atmosphere, achieving a resolution of 120 nm[68]. When SiO_2 spheres were semi-immersed in a thin layer of ethanol or SU-8 resist[12], [9]. the imaging contrast could be strongly strengthened. Darafsheh et al. found that when BaTiO_3 ($n_p = 1.9$) glass spheres were totally submerged in a liquid of isopropyl alcohol[69], the small spheres (diameter = 4.2 μm) were able to discern features as small as 75 nm ($\lambda/7$), while for large microspheres (50 μm < diameter < 220 μm), the resolved feature sizes were only $\lambda/4$. Li et al. reported water submerged BaTiO_3 (diameter = 100 μm) for the imaging of an adenovirus with a resolution of 75 nm[10].

2.4.3 Confocal microsphere superlens

Some studies have reported that a combination of microsphere superlens and scanning laser confocal microscope offers improvements in resolution. As shown in Figure 2.14 (a), a scanning laser confocal microsphere can increase optical resolution and contrast by employing a laser beam as illumination and collecting the reflected light via a pinhole-coupled photomultiplier. Therefore, out-of-focus light is eliminated and only object illuminated at focal plane can be detected. Due to the sample is illuminated one point at a time, scanning laser beam across the object horizontally and vertically enables reconstruct a 2-dimensional or 3-dimensional image. The resolution limit of a confocal microscope is about $0.4\lambda/NA$ [70].

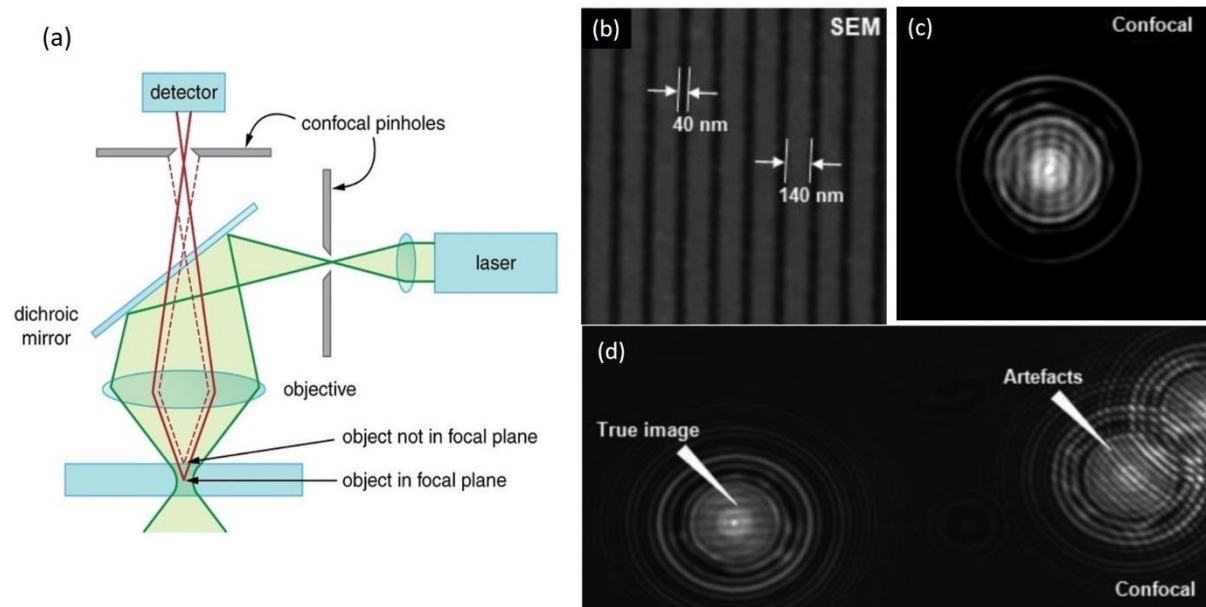


Figure 2.14 (a) Schematic of scanning laser confocal microscope. (b) SEM image of nano-feature sample with 40-nm-wide lines and 140 nm spacing. (c) Corresponding microsphere laser confocal microscope image, taken by LEXT4100 laser confocal microscope with 405 nm laser illumination, 50x NA0.95 objective lens. (d) Artefacts due to neighbouring microsphere interference versus true pattern under single microsphere[71].

Figure 2.14 (b-d) shows the achieved super-resolution imaging far beyond diffraction limit by coupling a scanning laser confocal microscope with microsphere superlens. Nano-structure sample with 40-nm-wide lines and 140 nm spacing is clearly discerned by 3.3 μm silica microsphere under confocal mode[71]. It is noteworthy that multiple concentric rings appear in the confocal imaging. This may be caused by near-field interactions of particle and substrate under a coherent laser illumination. Moreover, coherent light interference between

neighbouring microspheres leads to strong grating artefacts which are not representing real features under microspheres [an example was illustrated in Figure 2.14 (d) right part]. In contrast, isolated microsphere can still provide true detail of underlying sub-diffractive structure.

This combination approach was also reported by other researchers. Yan et al. revealed that 25 nm lateral resolution was achieved by combining fused silica and polystyrene microsphere with a conventional scanning laser confocal microscope[72]. Darafsheh et al. reported that liquid-immersed BTG microspheres were able to discern 50-60 nm features under confocal mode[13].

2.4.4 Scanning microsphere superlens

Although microsphere superlens has greatly improved resolution, ordinary microsphere technique suffers from small imaging window and poor processability which prevent it being compatible to variable samples and make them less attraction in practical application. Controlling the position of the microspheres is required for generating a complete image of sample. There are a few demonstrations in the literature. Krivitsky et al. attached a fine glass micropipette to the microsphere lens to scan the particle[73]. This method allows precisely controlling the microsphere position in three dimensions. Figure 2.15 shows its experimental setup.

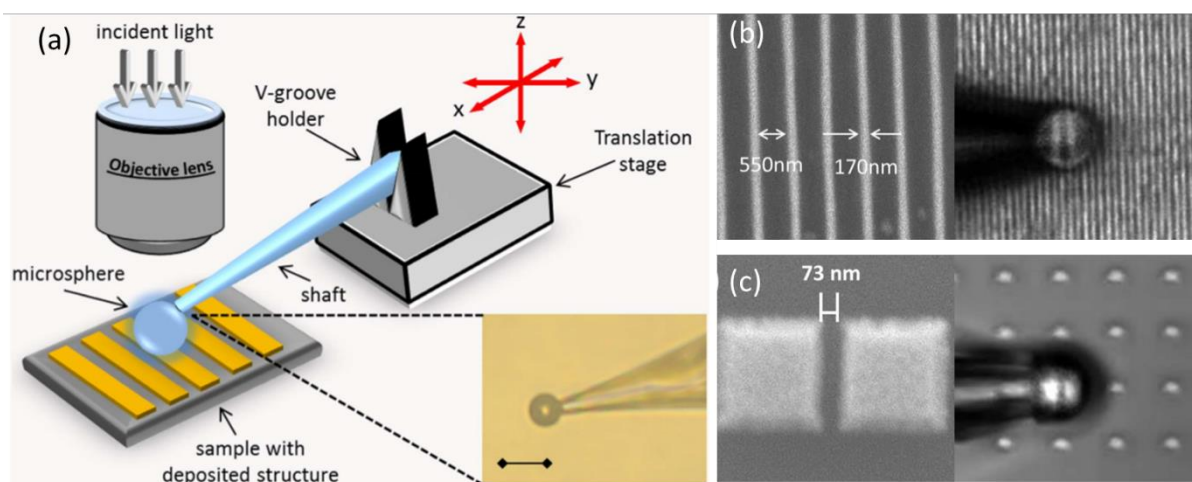


Figure 2.15 (a) Experiment layout of micropipette attached microsphere superlens scanning imaging. (b) 170 nm stripes with 550 nm gaps are imaged by microsphere lens. (c) squares of 500x500 nm² separated by a 73 nm gap are imaged by microsphere lens[73].

In another group, Li et al. designed a “swimming lens” technique in which the microsphere lens was propelled and scanned across the sample surface by chemical reaction force in a liquid[74]. This approach enables large-area, parallel and non-destructive scanning with sub-diffraction resolution. Figure 2.16 illustrates the schematic diagram and scanning imaging process.

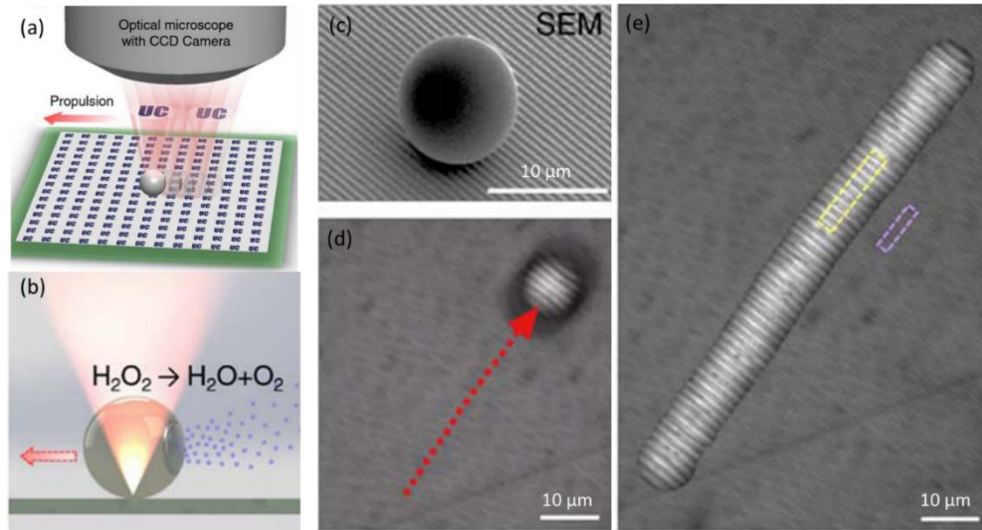


Figure 2.16 Swimming lens design. (a) Schematic illustration. (b) Schematic illustration of the chemically powered propulsion and light illumination through the microsphere. (c) SEM of 10 μm PS microsphere on a 320 nm grating structure. (d) Microsphere imaging and arrow shows the scanning motion. (e) Reconstructed image by stitching from individual video frame[74].

Most recently, Wang et al. introduced a non-invasive, environmentally compatible and high-throughput imaging technique called scanning superlens microscopy (SSUM), which applying the AFM principle by attaching microsphere onto AFM tip for scanning imaging (Figure 2.17)[75]. This system has high precision in maintaining distance between microsphere and the objects. It has capabilities of operating in contact scanning mode and constant-height scanning mode, therefore variety of samples such as stiff sample and sensitive specimens can be efficiently imaged.

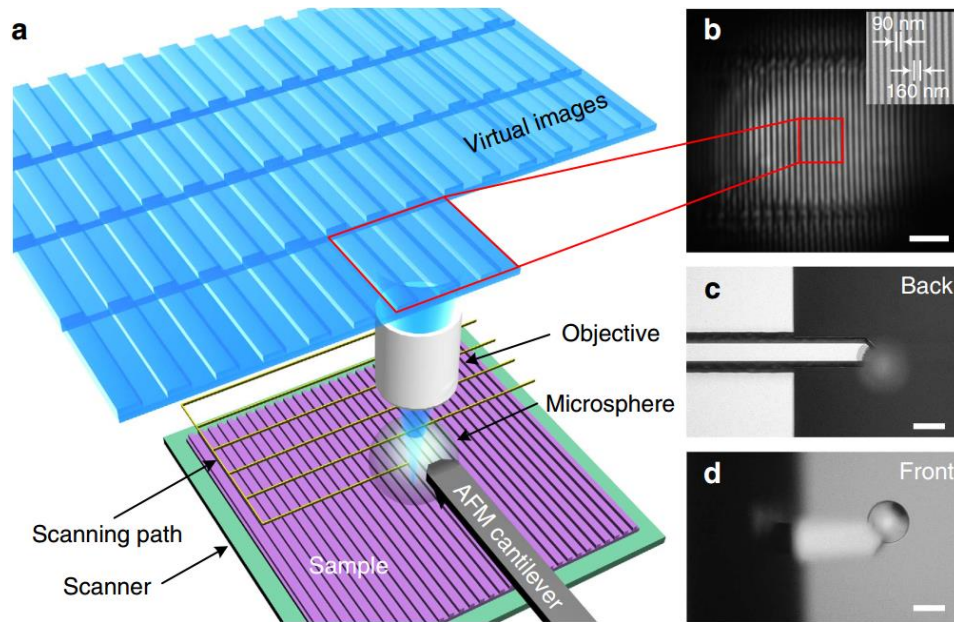


Figure 2.17 Microsphere-based scanning superlens microscopy (SSUM). (a) Schematic of the construction of a microsphere-based SSUM that integrates a microsphere superlens into an AFM scanning system by attaching the microsphere to an AFM cantilever. The objective picks up the virtual images containing sub-diffraction-limited object information and simultaneously focuses and collects the laser beam used in the cantilever deflection detection system. (b) An original virtual image observed using the microsphere superlens. The inset shows an SEM image. (c, d) Backside and frontside images, respectively, of the AFM cantilever with an attached microsphere superlens. Scale bars, 2 μm (b); 50 μm (c, d)[75].

2.4.5 Other developments

Due to the tiny scale of microsphere superlens, it has advantage of being integrated in other microsystems, such as microfluidics and optical fibre system, to form a multifunctional on-chip device. An example of microlens-based trapping and detection device was reported by Yuchao Li et al.[76]–[78]. In their work, microsphere lenses were attached on an optical fibre probe in order to generate photonic nanojet for performing manipulation and detection sub-100-nm objects, for instance nanoparticles and biomolecules.

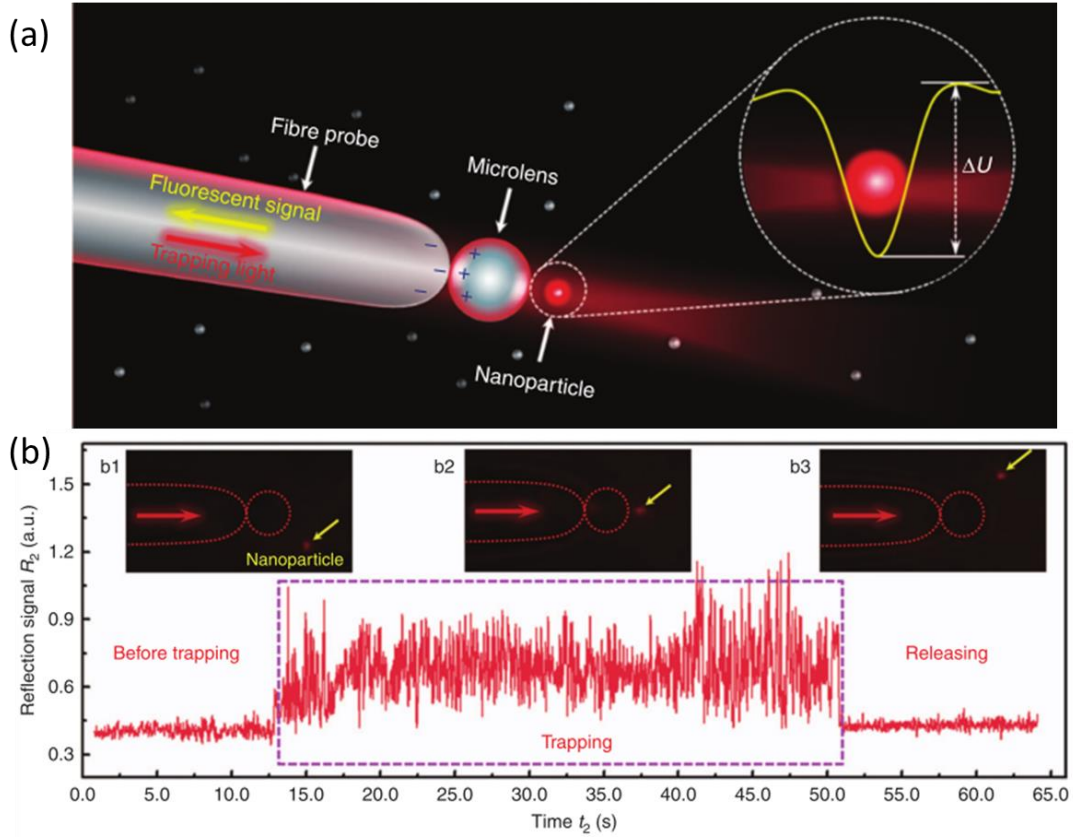


Figure 2.18 (a) Experimental schematic illustration of manipulation and detection of a single nanoparticle by nanojet generated from microlens binding on the fibre probe. (b) The real-time trace of the reflected 808-nm signal in the trapping process of an 85-nm fluorescent PS nanoparticle. The insets show the fluorescent images b1 before trapping, b2 during trapping and b3 in the release[77].

In addition, Hui Yang et al. revealed that when a microsphere-lens-array was integrated with a microfluidic channel, photonic-nanojet-array was formed to expose the content within the channel. Flowing particles such as Au nanoparticles with size of 50 nm and fluorescent nanoparticle down to 20 nm were able to be stimulated by photonic-nanojet-array and became detectable[79].

Previously, our group proposed a coverslip superlens by encapsulating high-index microspheres (BaTiO_3 or TiO_2) inside a transparent host material (such as PMMA and PDMS)[80]. The microsphere was completely immersed inside the encapsulation material with its bottom touching the coverslip surface. This concept was also explored by Darafsheh and Astratov et al. in the U.S.[13], [69]. The coverslip superlens are reusable and can be manually manipulated in a way similar to a classical coverslip, offering the freedom to position the particle lens at a desired location. At the same time, higher resolution can be achieved

due to the contribution of solid immersion mechanism, as the working wavelength in the near-field zone is scaled down by a factor of n (refractive index of surrounding material). Moreover, this design makes the microsphere lens less sensitive to the ambient working condition. In other words, it provides a more reliable solution for super-resolution imaging and has great commercial potential. In this thesis, further developments of superlensing nanoscopy based on coverslip superlens will be present in later chapters.

Besides, researchers from National University of Singapore discovered that by fabricating functional microstructures or depositing metal cover on surface of microsphere, the photonic nanojet can be effectively modified and super-resolution was achieved[81], [82].

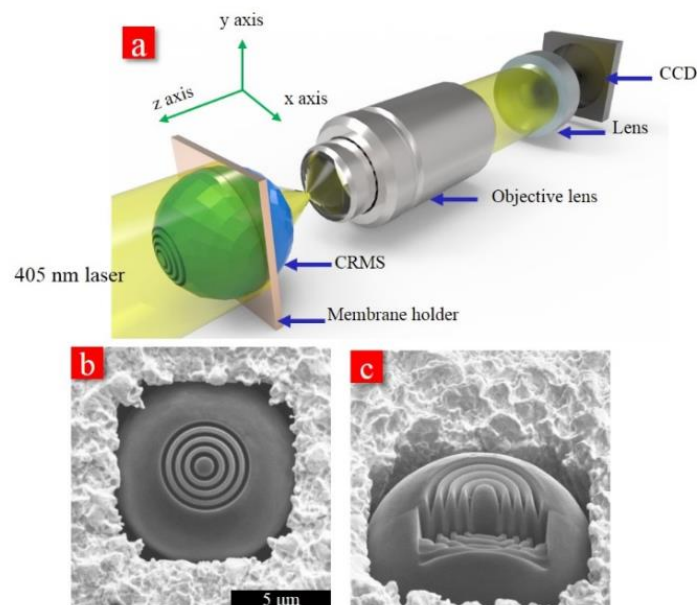


Figure 2.19 Microsphere decorated with concentric rings. (a) Schematic of observing PNJ by an optical microscope. The lens located between the objective lens and CCD represents for the focusing lenses in the optical microscope. (b) top and (c) side views[82].

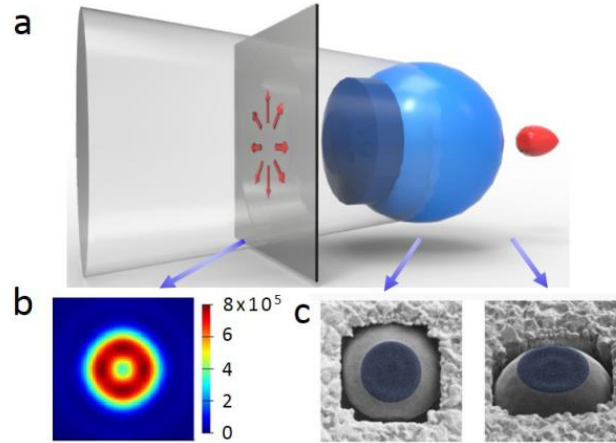


Figure 2.20 Design of the center-covered engineered microsphere for super-focusing of radial polarized beam[81].

2.5 Theoretical methods for super-resolution simulation

Optics describes the behaviour of interaction between incident light and objects. There are two main branches in optics: geometrical optics and wave optics. In geometric optics, light is considered as a collection of rays and travels in straight lines. According to Snell's law, light bends when passing through a media and reflects at interface. It provides a simple way for analysing optical lens focusing properties in macroscopic case which object is much larger than incident wavelength ($a \gg \lambda$). On the other hands, wave optics is more comprehensive model of light. It is considered as a propagational wave and is applied in the phenomena such as interference, polarisation and diffraction.

In the near-field, cases are always considered to a region with size in nanoscopic or mesoscopic scales ($a \ll \lambda$). In this situation, evanescent electromagnetic waves become significant due to the typical size of the objects is comparable to λ and the decay of evanescent waves occurs within a range given by the wavelength and the angle of incident. Unlike macroscopic (described by Kirchhoff theory) and microscopic system, near-field optics requires the detailed solution of the full set of Maxwell equations. In order to ensure the simulate accuracy, two main types of simulation methods, which are analytical and numerical, are used in this project.

2.5.1 Mie theory

Mie theory was proposed by Gustav Mie 1908[83]. It describes the exact solution of light incident, scattering and internal field of a homogeneous sphere with arbitrary radius and refractive index under a plane electromagnetic wave. The theory expressions take the form of an infinite series expansion of vector spherical harmonics (VSWF) from which cross-section, efficiency factor and intensity distribution on a particle can be derived. Particle structural feature affecting particle resonances is of particular interest, including incident light wavelength (λ), refractive index of particle (n_p), refractive index of medium (n_m) and particle size (a). As summarised, it can be defined as two independent input parameters, size parameter ($q = 2\pi a/\lambda$) and refractive index of particle (n_p). Hence, this theoretical study is conducive to investigations of;

- The morphology-dependent resonance (MDR) of a Mie resonator
- Validity of the Rayleigh approximation applying to latex, gold and silver particles
- A straightforward calculation of optical field and force.
- Distribution of the intensity over a cross section of an illuminated particle which is useful for applications in laser patterning, fluorescence and Raman sensing.
- Comparison of MDR for plane wave and evanescent wave excitation.

When the light is incident on a small particle, the oscillations of electrical charges of electrons and protons are induced by optical electric field. As a consequence, one fraction of incident beam is absorbed and other is scattered. The electric and magnetic fields inside and outside the sphere satisfy the vector Helmholtz equation [83]:

$$\nabla^2 \mathbf{E} + k^2 \mathbf{E} = 0, \nabla^2 \mathbf{H} + k^2 \mathbf{H} = 0, \quad 2.6$$

where $k = \frac{\omega}{c} \sqrt{\epsilon}$ is the wave vector and ∇ is the Laplacian.

In Mie theory, the incident plane wave is rewritten as a superposition of spherical waves and boundary conditions are imposed to obtain the coefficients of the development. The electric

field and magnetic field of scattered and internal can be written in the spherical coordinate system $\{r, \theta, \varphi\}$ as equation 2.7 and 2.8.

$$\begin{aligned}
E_r^{(s)} &= \frac{\cos \varphi}{(k_m r)^2} \sum_{\ell=1}^{\infty} i^{\ell+1} (2\ell+1) a_{\ell} \zeta_{\ell}(k_m r) P_{\ell}^{(1)}(\cos \theta) \\
E_{\theta}^{(s)} &= -\frac{\cos \varphi}{k_m r} \sum_{\ell=1}^{\infty} i^{\ell+1} \frac{2\ell+1}{\ell(\ell+1)} \left[a_{\ell} \zeta'_{\ell}(k_m r) P_{\ell}^{(1)'}(\cos \theta) \sin \theta - b_{\ell} i \zeta_{\ell}(k_m r) \frac{P_{\ell}^{(1)}(\cos \theta)}{\sin \theta} \right] \\
E_{\varphi}^{(s)} &= -\frac{\sin \varphi}{k_m r} \sum_{\ell=1}^{\infty} i^{\ell+1} \frac{2\ell+1}{\ell(\ell+1)} \left[a_{\ell} \zeta'_{\ell}(k_m r) \frac{P_{\ell}^{(1)'}(\cos \theta)}{\sin \theta} - b_{\ell} i \zeta_{\ell}(k_m r) P_{\ell}^{(1)'}(\cos \theta) \sin \theta \right] \\
H_r^{(s)} &= \frac{\sqrt{\epsilon_m} \sin \varphi}{k_m r} \sum_{\ell=1}^{\infty} i^{\ell+1} (2\ell+1) b_{\ell} \zeta_{\ell}(k_m r) P_{\ell}^{(1)}(\cos \theta) \\
H_{\theta}^{(s)} &= i \frac{\sin \varphi}{k_0 r} \sum_{\ell=1}^{\infty} i^{\ell+1} \frac{2\ell+1}{\ell(\ell+1)} \left[a_{\ell} \zeta_{\ell}(k_m r) \frac{P_{\ell}^{(1)}(\cos \theta)}{\sin \theta} + i b_{\ell} \zeta'_{\ell}(k_m r) P_{\ell}^{(1)'}(\cos \theta) \sin \theta \right] \\
H_{\varphi}^{(s)} &= -i \frac{\cos \varphi}{k_0 r} \sum_{\ell=1}^{\infty} i^{\ell+1} \frac{2\ell+1}{\ell(\ell+1)} \left[a_{\ell} \zeta_{\ell}(k_m r) P_{\ell}^{(1)'}(\cos \theta) \sin \theta + i b_{\ell} \zeta'_{\ell}(k_m r) \frac{P_{\ell}^{(1)}(\cos \theta)}{\sin \theta} \right] \quad 2.7
\end{aligned}$$

$$\begin{aligned}
E_r^{(a)} &= \frac{\cos \varphi}{(k_p r)^2} \sum_{\ell=1}^{\infty} i^{\ell+1} (2\ell+1) c_{\ell} \psi_{\ell}(k_p r) P_{\ell}^{(1)}(\cos \theta) \\
E_{\theta}^{(a)} &= -\frac{\cos \varphi}{k_p r} \sum_{\ell=1}^{\infty} i^{\ell+1} \frac{2\ell+1}{\ell(\ell+1)} \left[c_{\ell} \psi'_{\ell}(k_p r) P_{\ell}^{(1)'}(\cos \theta) \sin \theta - i d_{\ell} \psi_{\ell}(k_p r) \frac{P_{\ell}^{(1)}(\cos \theta)}{\sin \theta} \right] \\
E_{\varphi}^{(a)} &= -\frac{\sin \varphi}{k_p r} \sum_{\ell=1}^{\infty} i^{\ell+1} \frac{2\ell+1}{\ell(\ell+1)} \left[c_{\ell} \psi'_{\ell}(k_p r) \frac{P_{\ell}^{(1)'}(\cos \theta)}{\sin \theta} - i d_{\ell} \psi_{\ell}(k_p r) P_{\ell}^{(1)'}(\cos \theta) \sin \theta \right] \\
H_r^{(a)} &= \frac{\sqrt{\epsilon_m} \sin \varphi}{k_m r} \sum_{\ell=1}^{\infty} i^{\ell+1} (2\ell+1) d_{\ell} \psi_{\ell}(k_p r) P_{\ell}^{(1)}(\cos \theta) \\
H_{\theta}^{(a)} &= i \frac{\sin \varphi}{k_0 r} \sum_{\ell=1}^{\infty} i^{\ell+1} \frac{2\ell+1}{\ell(\ell+1)} \left[c_{\ell} \psi_{\ell}(k_p r) \frac{P_{\ell}^{(1)}(\cos \theta)}{\sin \theta} + i d_{\ell} \psi'_{\ell}(k_p r) P_{\ell}^{(1)'}(\cos \theta) \sin \theta \right] \\
H_{\varphi}^{(a)} &= -i \frac{\cos \varphi}{k_0 r} \sum_{\ell=1}^{\infty} i^{\ell+1} \frac{2\ell+1}{\ell(\ell+1)} \left[c_{\ell} \psi_{\ell}(k_p r) P_{\ell}^{(1)'}(\cos \theta) \sin \theta + i d_{\ell} \psi'_{\ell}(k_p r) \frac{P_{\ell}^{(1)}(\cos \theta)}{\sin \theta} \right] \quad 2.8
\end{aligned}$$

Where the P_{ℓ}^m are the associated Legendre functions and ζ_{ℓ} and ψ_{ℓ} are the spherical Bessel functions. a_{ℓ} and b_{ℓ} are scattering wave coefficient, c_{ℓ} and d_{ℓ} are internal wave coefficient.

In this project, Mie theory was implemented for studying the cross section, intensity distribution and focusing effects of small sphere as describes in **Chapter 4**. The morphology-dependent resonance (MDR) effect is fully investigated and, hence providing principles of

field-invariant scaling of the Mie parameters which is important for experimental scaling of the super-resolution designs.

In case of non-magnetic particles, there are four general input parameters: incident wavelength of light (λ); medium refractive index (n_m) particle radius (a) and particle refractive index (n_p). These parameters can be reduced to two independent size parameters (q_p, q_m), defined as:

$$\text{Size parameter: } q_0 = \frac{2\pi a}{\lambda}; \quad 2.9$$

$$\text{Particle size parameter: } q_p = q_0 n_p = \frac{2\pi a}{\lambda} \cdot n_p; \quad 2.10$$

$$\text{Medium size parameter: } q_m = q_0 n_m = \frac{2\pi a}{\lambda} \cdot n_m \quad 2.11$$

The near-field profiles are fundamentally determined by the scattering wave coefficients (a_ℓ, b_ℓ) and internal wave coefficients (c_ℓ, d_ℓ). For the convenience of parameter scaling discussion in following **Chapter 4**, both coefficients are re-presented here:

$$a_\ell = \frac{q_p \psi'_\ell(q_m) \psi_\ell(q_p) - q_m \psi_\ell(q_m) \psi'_\ell(q_p)}{q_p \zeta'_\ell(q_m) \psi_\ell(q_p) - q_m \psi'_\ell(q_m) \zeta_\ell(q_p)} \quad 2.12$$

$$b_\ell = \frac{q_p \psi'_\ell(q_p) \psi_\ell(q_m) - q_m \psi_\ell(q_p) \psi'_\ell(q_m)}{q_p \psi'_\ell(q_p) \zeta_\ell(q_m) - q_m \psi_\ell(q_p) \zeta'_\ell(q_m)} \quad 2.13$$

$$c_\ell = \frac{q_p \zeta'_\ell(q_m) \psi'_\ell(q_m) - q_p \zeta'_\ell(q_m) \psi_\ell(q_m)}{q_p \zeta'_\ell(q_m) \psi_\ell(q_p) - q_m \psi'_\ell(q_p) \zeta_\ell(q_m)} \quad 2.14$$

$$d_\ell = \frac{q_p \zeta'_\ell(q_m) \psi_\ell(q_m) - q_p \zeta_\ell(q_m) \psi'_\ell(q_m)}{q_p \psi'_\ell(q_p) \zeta_\ell(q_m) - q_m \psi_\ell(q_p) \zeta'_\ell(q_m)} \quad 2.15$$

As it will be shown below in Chapter 4, (q_p, q_m) parameters can be equivalently expressed using (q_0, n_p) parameters, so that there is a freedom to choose using either (q_p, q_m) or (q_0, n_p) . In this study, we will assign Mie parameter using (q_0, n_p) .

2.5.2 Numerical methods

Although analytical method can give most accurate and reliable result, it is dramatically difficult to obtain focusing properties when particles with arbitrary geometry, different degree of aggregation and complex external dielectric environment effects. Therefore, Mie theory cannot be taken in account and we seek numerical solutions. Several numerical calculation methods have been developed in order to solve electromagnetic problems for complex models. They include finite element method (FEM)[84], finite difference time domain (FDTD) technique[85], and Finite Integral Technique (FIT)[86].

2.5.2.1 Finite-element method (FEM)

The FEM initially worked for solving problems of complex elasticity and structural analysis in typical topics. It is widely used in almost all branches of science and engineering topics. A variation formulation or weak formulation of the wave equation plays a vital role in FEM method.

$$\int_{\Omega} \left[\nabla \left(\frac{1}{\varepsilon_r} \nabla H_z \right) + \frac{\omega^2}{c^2} H_z \right] v d\Omega = 0 \quad 2.16$$

Equation 2.16 is the projection of the solution on the basis of test functions v , where v is the test function defined on domain Ω . The integral enables the computation model as a union of N subdomains. Solutions of individual element can be accumulated to generate global solution. In the simulation of near-field model, FEM is a frequency domain method; therefore, the program can use experimental values to set arbitrary dielectric constants. It is noted that the self-adaptive mesh refinement scheme is one key to determine the accuracy in FEM modelling [84].

2.5.2.2 Finite difference in time domain (FDTD)

FDTD method was established by Yee in 1966 and now is widely used for solving electromagnetic problems. It is a grid-based differential time-domain numerical modelling method. The core idea of FDTD is to transform the curl-Maxwell equation with time variable into the differential form, and then the time-domain response between electronic pulse and conductor can be simulated. Partial differential equation and boundary conditions are discretized using central-difference approximations. With a spatial discretization x and a temporal discretization t , one can obtain the standard recursion equations in a non-dispersive and non-magnetic medium for the electric and magnetic fields for a 2D p-polarization incidence wave (H_z , E_x , E_y)

$$H_z|_{i,j}^{n+1/2} = H_z|_{i,j}^{n-1/2} + \frac{\Delta t}{\mu_0 \Delta x} (E_x|_{i,j+1}^n - E_x|_{i,j}^n + E_y|_{i,j}^n - E_y|_{i+1,j}^n) \quad 2.17$$

$$E_x|_{i,j}^{n+1} = E_x|_{i,j}^n + \frac{\Delta t}{\varepsilon_0 \varepsilon_{i,j} \Delta x} (H_z|_{i,j}^{n+1/2} - H_z|_{i,j-1}^{n+1/2}) \quad 2.18$$

$$E_y|_{i,j}^{n+1} = E_y|_{i,j}^n + \frac{\Delta t}{\varepsilon_0 \varepsilon_{i,j} \Delta x} (H_z|_{i-1,j}^{n+1/2} - H_z|_{i,j}^{n+1/2}) \quad 2.19$$

where ε_0 and μ_0 are the permittivity and permeability of free space, and $\varepsilon_{i,j}$ is the relative permittivity at position $x = i\Delta x$, $y = j\Delta y$, any field U (either H or E) at position $x = i\Delta x$ and for the instant $t = n\Delta t$ being represented by $U|_i^n$. The upper limit for Δt is given by the Courant time step $t_c = \Delta x/(c\sqrt{N})$, and N is the dimension of the problem. It has advantage of using less space in computing and storage. In FDTD solutions, a wide range of frequency can be covered in a single simulation and the nonlinear material properties can be treated in a natural way. FDTD method has a wide range of application. However, the accuracy of material dispersions still needs to be improved[85].

2.5.2.3 Finite integral technique (FIT)

The FIT technique was proposed by Weiland in 1977[86]. Unlike FDTD and FEM, the Maxwell's equation is discretized into an integral form by FIT. Varieties of electromagnetic problems whether in time or frequency domain can be solved by a universal spatial discretization method which is provided by FIT. Moreover, FIT is flexible to adapt with other methods. The formulation of FIT can be adapted with FDTD method in the case of Cartesian grids. For the triangular grids, the FIT is closely related to FEM in Whitney formulation. In a non-strict sense, FIT technique is known as a hybrid combination of FDTD and FEM techniques.

Chapter 3. Research Methodology

3.1 Introduction

This chapter describes the theoretical and experimental methods for investigation and development of optical super-resolution lenses. The first half of this chapter details the simulation methods of investigating the optical properties of microspheres, and then proposes several designs that effectively improve the resolution. The latter half describes experimental methods for manufacturing and processing different kinds of superlenses. Instruments of manufacturing and imaging characterisation are given.

Most of the simulation, fabrication and characterisation were undertaken in the School of Electronic Engineering at Bangor University. Chemical synthesis of nanoparticle-derived superlens and high-index hybrid superlens were conducted at Fudan University (China). Fabrication of microfluidic chip and optical imaging of biological samples were undertaken in Institute of Life Science at Swansea University.

3.2 Theoretical works

3.2.1 Calculation of near-field focusing of dielectric microsphere

This section introduces the simulation tool and simulation conditions which are connected to **Chapter 4**. In order to investigate focusing characteristics of single homogeneous dielectric micro/nano spherical particle, an analytical simulation software, DSI Mie was used to calculate field enhancement, focal length and focal size. Simulation conditions are given in this section.

3.2.1.1 DSI Mie

DSI Mie, a simulation software developed by Zengbo Wang and Boris Luk'yanchuk, is based on Mie theory for simulating the field distribution inside and outside a single microsphere[54]. This program offers simulations including scattering on a single particle, far-field effects and particle on surface (POS) calculations, and meanwhile provides fast calculations and accurate

results. By defining parameters of particle and incident light, the exact values of electric intensity and Poynting intensity distribution can be plotted and generated. Figure 3.1 shows the functions and user interface of DSI Mie software.

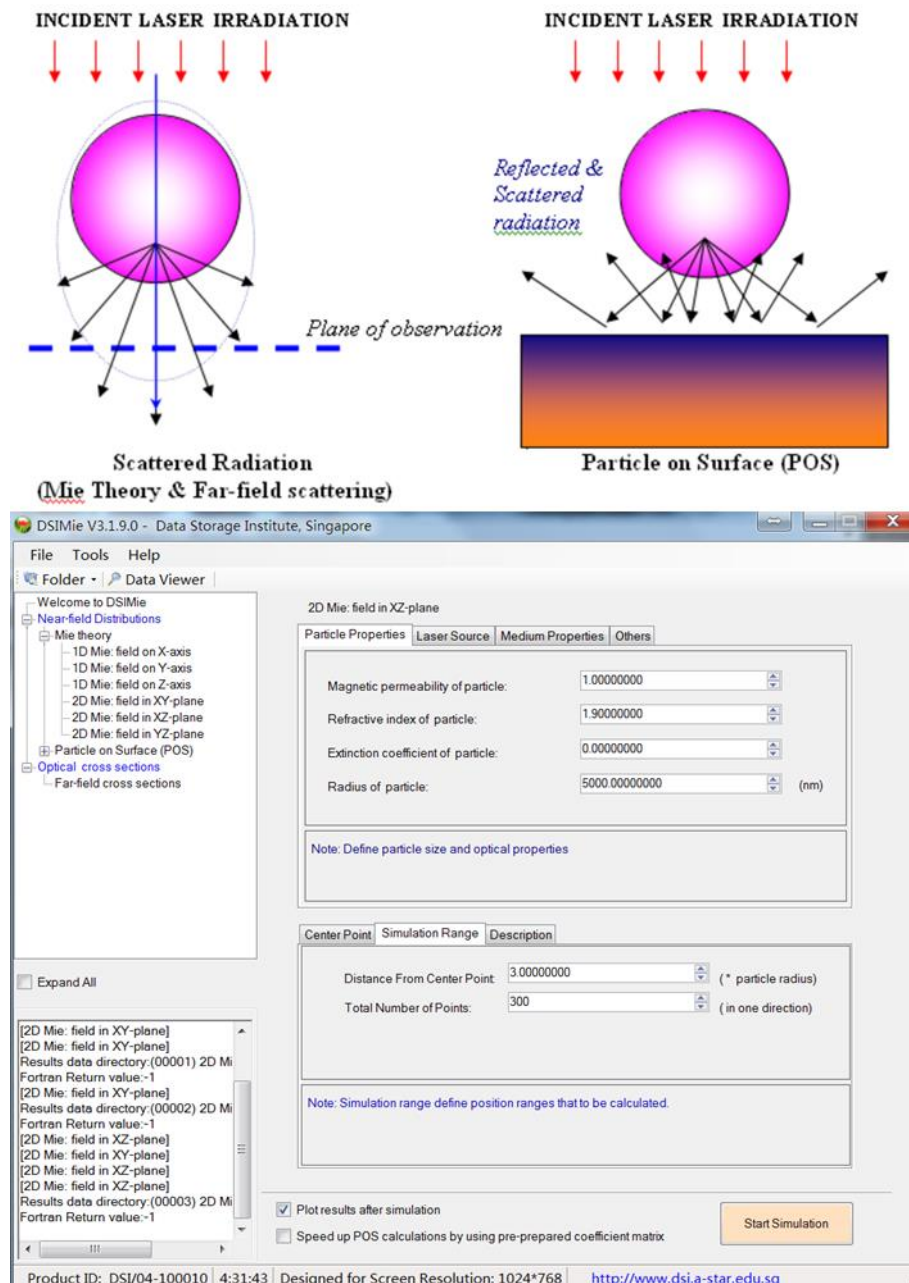


Figure 3.1 User interface of DSI Mie software.

3.2.1.2 Simulation conditions

DIS Mie software was used for simulating the field distribution inside and outside a single microsphere. To simplify the calculation, following assumptions were made for the super-resolution focusing study in Section 3: $n_p=1.6$ (fixed), $n_m=1.0$ (fixed), size parameter q_0 varies from π to 20π (i.e., $\pi \leq q_0 \leq 20\pi$) with step resolution of 0.02. To find the particle focus, we calculate the $|E|^2$ values along a line across the particle centre from $-5a$ to $5a$ following the incident direction. Five thousand points were sampled in the calculation window, thus the result resolution is 500 points per particle radius. The focus size was measured as FWHM (Full Width at Half Maximum).

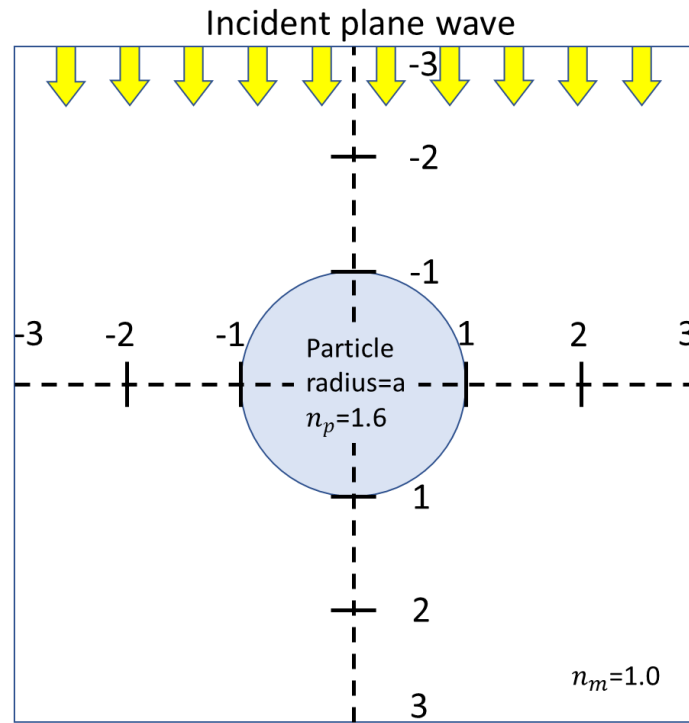


Figure 3.2 Example of simulation condition. Scale is normalised with respect to the particle radius, a .

Note that all results presented in the Chapter 4 the length value, including position value and FWHM, was normalised with respect to the particle radius, for example position $=1$ means focus is at the bottom of particle while for position $=-1$ the focus is at the top of particle. To compare our results with the diffraction limit, we can re-format the Rayleigh formula as the function of size parameter q_0 , by

$$q_0 = \frac{2\pi a}{\lambda} \Rightarrow \lambda = \frac{2\pi a}{q_0} \quad 3.1$$

$$\frac{D_{Rayleigh}}{a} = \frac{0.61\lambda}{n \times a} = 0.61 \frac{2\pi}{n \times q_0} = \frac{1.22\pi}{n \times q_0} \quad 3.2$$

Where n is refracted by focus position, when focus is inside sphere body, $n_p=1.6$ is considered, whereas $n_m=1.0$ is considered. The diffraction limit curve following Equation (3.2) can then be plotted on the same figure with our program outputs for a direct comparison of the calculated focus size with Rayleigh limit.

3.2.2 Engineered microsphere: design and optimisation

Ability to precisely control of focusing properties is highly desired for microsphere-based technologies. In this thesis, we developed new techniques that can control the near-field focusing of a microsphere lens in flexible and easy-to-implement ways, and optical resolution was greatly enhanced via these designs. This section proposes several superlens designs and provides the simulation methods for achieving super-resolution which relates to **Chapter 5**.

3.2.2.1 CST Microwave Studio

CST Microwave Studio was employed for geometrically complicated microsphere superlens designs, where the superlens are no longer just single sphere consisting homogenous material but in forms of combination with pupil mask, composite materials or close stacked nanoparticles. The CST was based on Finite Integration Technique (FIT) technique. FIT provides a universal spatial discretization scheme applicable to various electromagnetic problems, ranging from static field calculations to high frequency applications in time or frequency domain. Unlike most numerical methods, FIT discretizes Maxwell's equation in an integral form rather than the differential ones. In this study we have used triangular meshes in the simulation; it is naturally conformal to the circular boundary of a sphere, and have tight links with finite element methods (FEM) formulated in Whitney forms. Following modelling and simulations were undertaken in CST Microwave Studio software.

3.2.2.2 Pupil mask and composite microsphere designs and simulation conditions

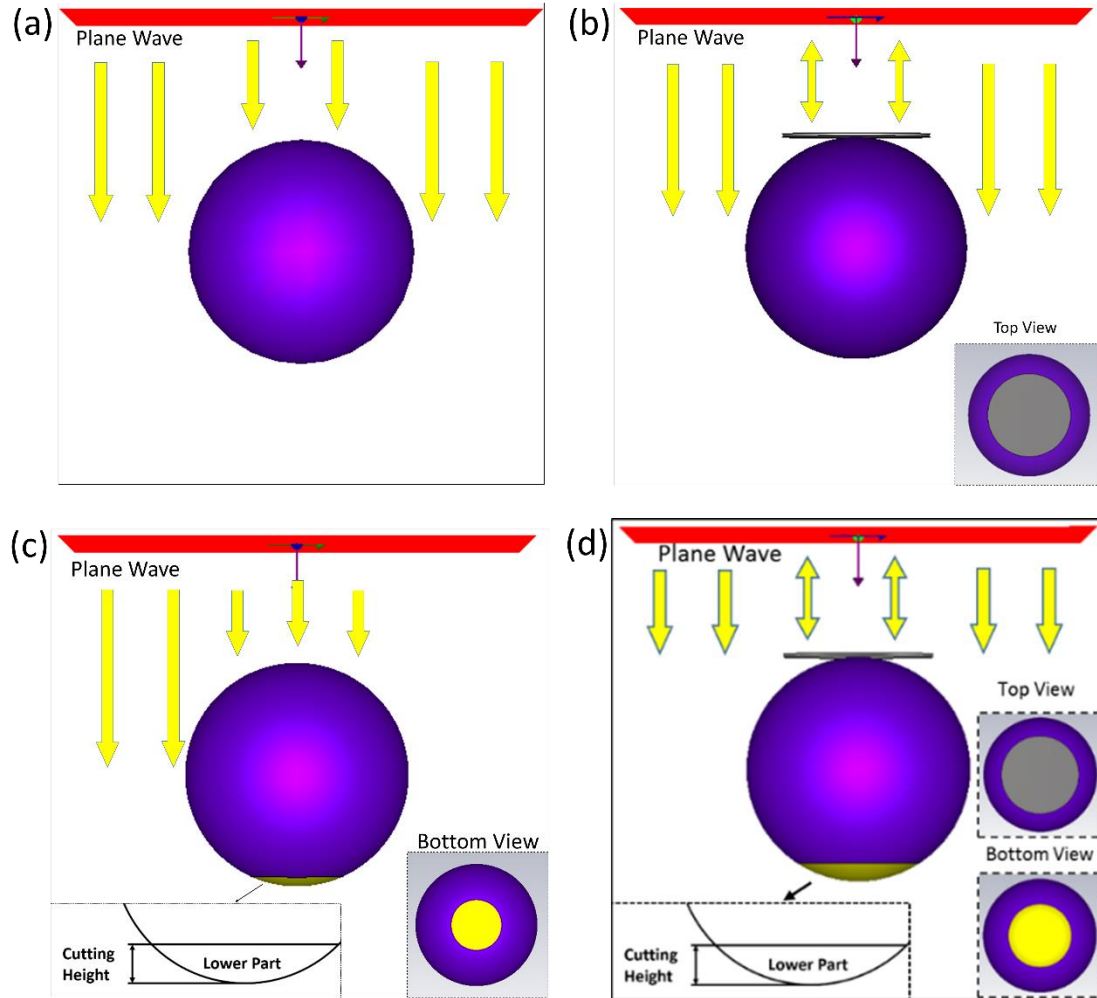


Figure 3.3 Schematic diagram of engineered microspheres. (a) Referencing design of single homogeneous microsphere. (b) Pupil mask assisted microsphere. (c) Composited material in microsphere with higher refractive index located at bottom portion. (d) Combination of pupil mask and composite design.

Binary phase mask is a technique commonly used to enhance resolution in conventional lens system. Meanwhile, solid immersion mechanism by increasing refractive index of surrounding medium also helps resolution improvement. We integrated either and both concepts into our new microsphere superlens designs, which are schematically illustrated in Figure 3.3. It shall be noted we are dealing with near-field problems here, in which the focus is located very close to particle surface and evanescent wave components could be involved. This demands a full wave numerical simulation to include both propagating and evanescent wave modes. A

commercial FIT software package (CST MICROWAVE STUDIO) was used. For better accuracy on simulation results, we have chosen to use triangular grids thus a FEM-like method in simulation, which are naturally conformal to the circular boundary of a sphere. The computation was run on a personal computer with Intel i5-4570 3.20GHz CPU, 32GB RAM.

In simulation, the particle was discretized by tetrahedral meshes at a mesh density of $\lambda/4$, where λ is incident wavelength. The incident wave is a linearly polarised plane wave with electric vector polarized along the x-axis. The desired linear equation system solver accuracy in terms of the relative residual norm was set as 10^{-6} , which enforce a termination criterion for the solver. The retardation effect and contributions from all necessary orders of partial waves dipole, quadruple, etc. are inheritably considered in our modelling. Due to limitation of computation resources, the studied particle diameter was limited to 3 μm and below.

In the pupil mask design (Figure 3.3 b), the mask is a circular disk positioned right on top of the particle, with diameter 2 μm . Apart from particle and mask size parameters, other parameters were kept fixed in this research: refractive index of microsphere = 1.46 (SiO_2); background medium refractive index = 1 (air); incident wavelength = 600 nm, x-polarised, propagates along z-axis; pupil mask material = PEC (perfect electric conductor) which provides 100% blocking of incident light. It shall be noted that the optical resolution (Full Width of Half Maximum - FWHM value of minimum spot size) were measured using electric intensity field distributions ($|E|^2$) in YZ cross-sectional planes. This is because near-field focusing of microsphere lenses is generally elongated along incident polarisation direction (x-axis) and minimum spot size (i.e. best resolution) is found on the Y-direction.

In the composite design (Figure 3.3 c), the sphere was cut into two parts, which consist of a high-index material in lower part and lower-index material in upper part (fixed at $n_{p1}=1.46$). The high-index material allows new lens accessing contribution from solid immersion mechanism. In the calculation, the refractive index of bottom material n_{p2} was set from 1.76 to 2.66, with a linear increasing of 0.1 each step. The cutting height of bottom part was varied from 10 nm to 200 nm with 10 nm step and this interval was minimised to 1 nm in the range in order to investigate where optimized super-resolution occurs. Other simulation conditions were kept the same as previous design.

In the third design (Figure 3.3 d), above two concepts were combined. The simulation environment was set same to the optimised result from second design. Circular mask with variety of diameters were employed on such chosen composited microsphere. Comparison of optical focusing properties between three designs was presented.

3.2.2.3 All-dielectric nanoparticle-based metamaterial superlens

In order to increase view window while enhance super-resolution, a new concept of using nanoparticles as building block to construct a dielectric metamaterial superlens was proposed. To understand how nanoparticles block interacting with electromagnetic wave, near-field simulation was carried out. The basic simulation structure of the artificial media is a closely stacked 15-nm anatase TiO_2 nanoparticle ($n=2.55$) composite, in which tiny air gaps between the particles exist, resulting in a dense scattering media. To simplify the model, seven layers of TiO_2 nanoparticles were arranged in hexagonally close-packed form, as shown in Figure 3.4 (a). A plane wave illumination at a wavelength of 550 nm from far field was applied. The particle was discretized by tetrahedral meshes at a mesh density of $\lambda/4$, where λ is incident wavelength. The incident wave is a linearly polarized plane wave with electric vector polarised along the x-axis. The frequency domain solver (FIT method) in CST Microwave Studio simulation software was used. The computation was run on a server with 16x 2.4GHz CPU, 128GB memory.

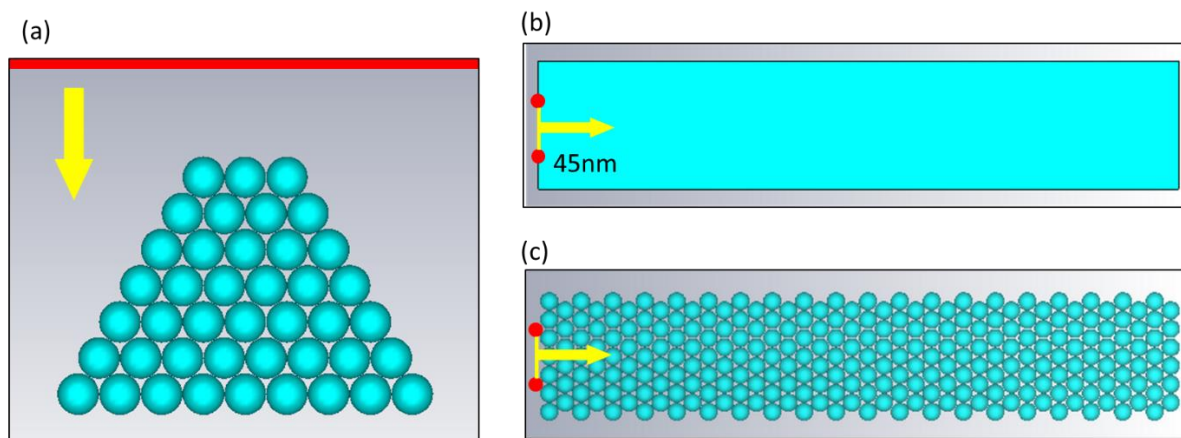


Figure 3.4 Simulation schematic of nanoparticle-based dielectric metamaterial. (a) 15-nm anatase TiO_2 nanoparticles ($n=2.55$) arranged in hexagonally close-packed form under a 550 nm wavelength plane wave illumination. Two incoherent point sources (45 nm separation) illuminating from boundary of (b) homogeneous ($n=2.55$) and (c) nanoparticle composite material.

On the other hand, according to the reciprocal principle[66], the conversion process in nanoparticles composited media from propagating waves to evanescent waves can be optically reversed. In simulation, a monolayer of close-packed nanoparticles with 40 layers in light propagation direction (z-direction) was built, as shown in Figure 3.4 (c). Two incoherence point sources (y-polarised, perpendicular to XZ-plane, set using 1nm x 1nm rectangular waveguide port in software) including all evanescent wave components were placed 45 nm away illuminating from boundary of composited media, and a convergence accuracy of $1e-4$ was used. Periodic boundary conditions were applied in both x- and y-directions. In order to evaluate the evanescent waves coupling and convertibility by nanoparticle metamaterial media, the averaged electric fields at different z-planes were obtained using the post-processing functions built in the software. Comparison study was made between homogeneous media [Figure 3.4 (b)] and nanoparticles composited media.

3.3 Experimental works

3.3.1 limitations of ordinary microsphere superlens

The advent of microsphere superlens provides an inherently simple process for achieving super-resolution real time imaging. This technique is label-free and has been further advanced by a number of groups across the world, for example, the development of confocal microsphere nanoscopy[87], [72] solid immersion microsphere nanoscopy[13], [69], [87], microfiber nanoscopy[88], subsurface nano-imaging[89], [90], and new microsphere superlens designs[91], [92]. However, practical limitations impose restrictions on ease of installation and use.

- 1. Microspheres are randomly distributed on substrate, hence the area to be tested may not be covered by microsphere.**
- 2. Deposited microspheres need to be carefully protected during working due to their sensitivity to surrounding environment and they are very perishable. Such a subtle change of surrounding medium can lead to change in imaging quality.**
- 3. The non-reusable disadvantage reveals that microsphere superlens is not suitable for commercial and industrial production.**

It is very necessary for some real innovations to drive the technology forward. Following sections propose methods of improving microsphere superlens in the ways of resolution enhancement, ease of use and reliability in practical applications.

3.3.2 Procedures for fabricating coverslip microsphere superlens (CMS)

As the name indicating, the coverslip microsphere superlens (CMS) is presented as a form of traditional coverslip, but moreover it provides super-resolution capability. It is realised by applying transparent host medium to encapsulate microspheres. The host medium can be Polydimethylsiloxane (PDMS) or polymethyl methacrylate (PMMA) due to their appropriate optical, chemical and mechanical properties. These two materials exhibit as liquid state before polymerisation. The high liquidity enables them to spread over substrate surface which contains microspheres. Two-dimensional and three-dimensional structure can be constructed. After polymerisation, PDMS exhibits a flexible solid form and highly adhesive capacity, therefore this is conducive to embed micro-particles and easily attach to arbitrary surface. While PMMA performs the same function but it becomes tough as general plastic after polymerisation. It could be considered in the application of aqueous sample imaging and nano-scale patterning.

By applying host media, it enables the microsphere to be a reusable, environmental independent, super-resolution and substrate irrespective superlens. The experimental procedure and materials are presented in following sections. Based on CMS's advantages, some expansion on developments including scanning imaging, nano-patterning and microfluidic on-chip superlens will be demonstrated in **Chapter 7 and Chapter 8**.

3.3.2.1 Overview of procedures

The coverslip microsphere superlens (CMS) fabrication consists of four main steps, including substrate cleaning, microsphere deposition, hosting medium deposition and polymerisation, separation and transferring of CMS. Figure 3.5 indicates the fabrication procedures. Noted that the hosting media must be thin enough (about 170 μm , same as general glass coverslip) to insert into a small gap between samples and high magnification microscope objective. However, thin PDMS layer is not easily peeled off from substrate and can be easily torn. This requires a sacrificial layer between PDMS-CMS and substrate for final separation. While,

PMMA layer does not need this process. Detail processes will be presented in following sections.

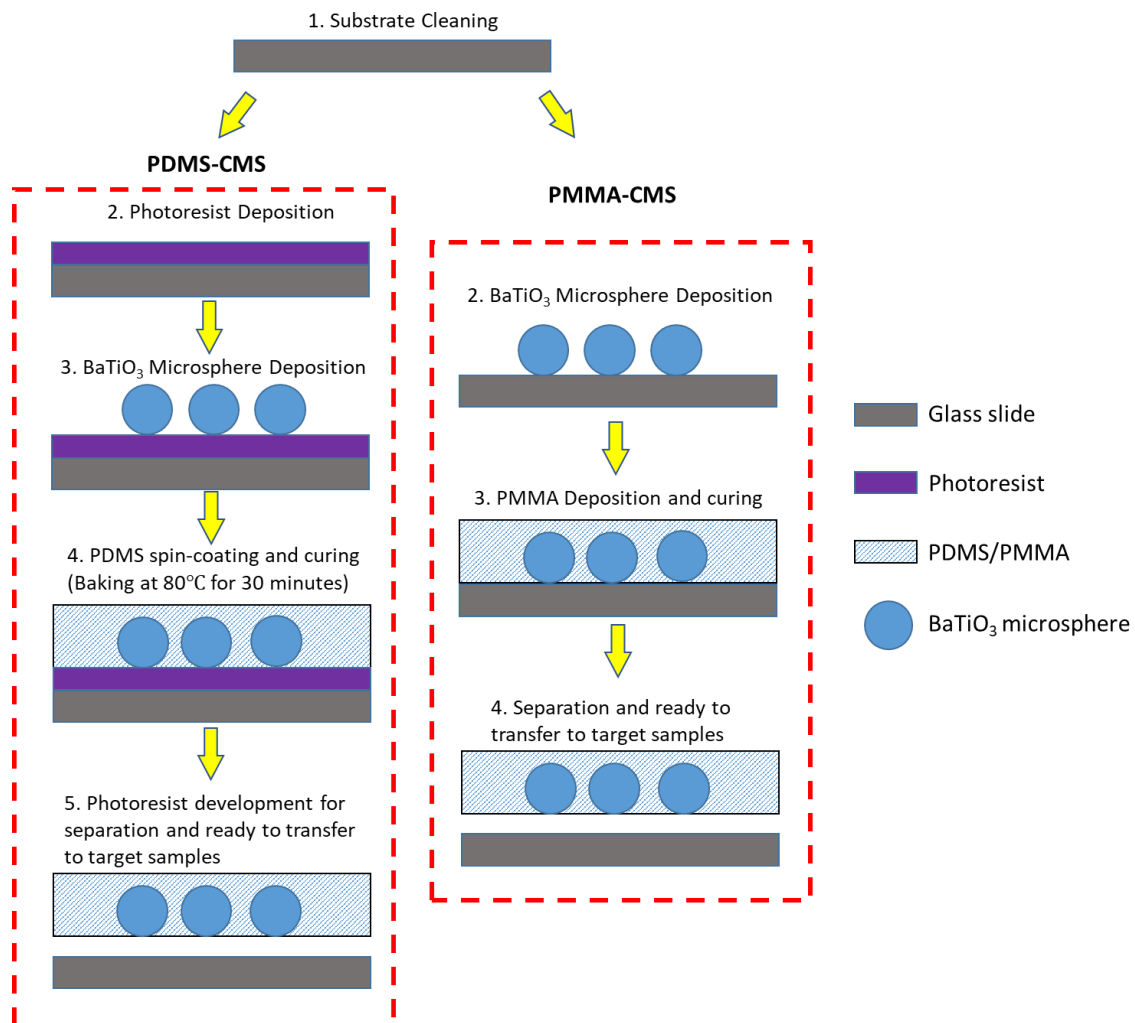


Figure 3.5 Fabrication procedure of coverslip microsphere superlens (CMS).

3.3.2.2 Processes and materials properties

- **Substrate Cleaning**

Microscope glass slides with 25.4 mm x 76.2 mm x 1mm were used. Substrate clean determines the quality of the result. Contamination on the surface can influence the surface smoothness and imaging performance. The substrates were firstly washed by soapy water and Decon 90 detergent, followed by thoroughly washed by deionised water. They were then subjected to sonication in solvents including acetone (99.5%) and isopropanol alcohol (IPA) for 5 minutes each. Finally, they were blown dry and stored in petri dish for later use.

- **Sacrificial Layer Deposition**

In order to help separate the PDMS thin layer from the substrate, a sacrificial layer made of photoresist is necessary. The substrate was spin-coated with a negative photoresist (AZ nlof 2070) at 500 rpm for 10 seconds and 3000 rpm for 40 seconds to give a thickness of $\sim 10\text{ }\mu\text{m}$, after which baked at 100°C for 15 minutes.



Figure 3.6 Spin coater (Model WS-650MZ-8Npp/A1/AR1).

- **Barium Titanate Glass (BTG) Deposition**

Barium Titanate glass (BTG) microspheres are optically transparent and have high refractive index of 1.9, which is capable of imaging under the immersion condition. In our work, BTG microspheres with two size ranges, $3 - 25\text{ }\mu\text{m}$ and $60 - 100\text{ }\mu\text{m}$, were used. For the initial demonstration, microspheres are randomly deposited onto photoresist-coated substrate by using a simple cotton swab, whose fibres is able to wind microspheres and make them drop after slight shaking. The distance between cotton swab and substrate should be over 20 mm to secure even distribution of particles through free-fall, meanwhile avoid spill redundant particles at the same location, in case particle stacking. The property of BTG microsphere is listed in Table 3.1.

Manufacturer	Cospheric
Material	Barium Titanate Glass
Index of Refraction	1.90 – 1.92
Diameter	3 - 25 μm and 60 - 100 μm
Specific Gravity	4.49 +/- 0.01

Table 3.1 Detailed data of BTG microspheres.

- **Polydimethylsiloxane (PDMS) Preparation**

Polydimethylsiloxane (PDMS, Sylgard 184 Silicone Elastomer) was chosen as a hosting medium in this experiment. There are two components, 184 silicone elastomer and curing agent as showing in Figure 3.7. Table 3.2 shows the basic properties of PDMS Sylgard 184 Silicone Elastomer.

Product Name	Sylgard 184 Silicone Elastomer (PDMS)
Manufacturer	Dow Corning
Index of Refraction	1.4
Specific Gravity @ 25C	1.03
Room Temperature Cure-Hours	48 hours
Mix Ratio	10:1 Base to Curing Agent

Table 3.2 PDMS Properties.

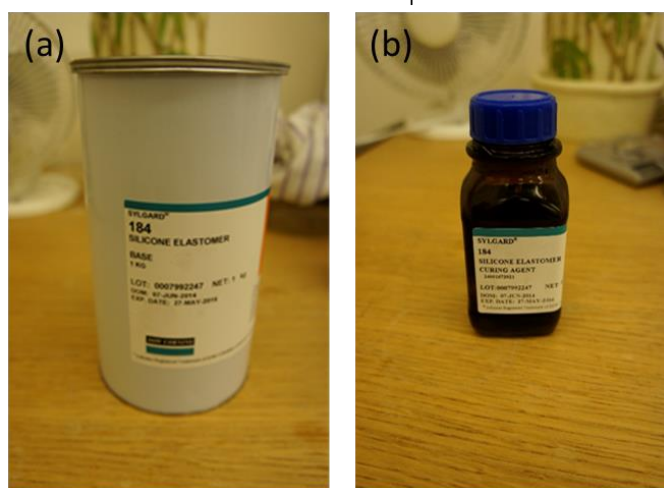


Figure 3.7 Polydimethylsiloxane Sylgard 184 (a) silicone elastomer and (b) curing agent.

The PDMS pre-polymer was prepared via mixing silicone elastomer base and curing agent with ratio of 10:1. These two components were thoroughly mixed by disposable stirring rob.

Air bubbles were produced while stirring, and in order to obtain good transparency, they must be removed before polymerisation occurs. Vacuum desiccator was used to remove air bubbles. Then the degassed PDMS pre-polymer liquid was carefully and slowly poured over the surface of photoresist-coated substrate which contains BTG microspheres.



Figure 3.8 Vacuum desiccator.

In order to achieve uniform thin PDMS layer, spin coater is used. Substrate with microspheres was spin-coated with PDMS at 500 rpm for 45 seconds to give a thickness of $\sim 170 \mu\text{m}$. Then, it was baked at 80°C for 30 minutes to become elastic solid.

- **Polymethyl methacrylate (PMMA) Preparation**

Polymethyl methacrylate (PMMA) is another candidate for encapsulating microspheres and that was prepared by solution polymerisation of methyl methacrylate (MMA) and initiator Benzoyl peroxide (BPO) (properties of both chemicals are listed in Table 3.3 and Table 3.4).

Product Name	Methyl methacrylate
Manufacturer	Sigma-Aldrich
Index of Refraction	1.412-1.416
Appearance (From)	Liquid
Formula	$\text{C}_5\text{H}_8\text{O}_2$
Formula Weight	100.12 g/mol

Table 3.3 MMA properties.

Product Name	Benzoyl peroxide
Manufacturer	Aladdin
Appearance (From)	Granular powder
Formula	C ₁₄ H ₁₀ O ₄
Formula Weight	242.2 AWU

Table 3.4 BPO properties.

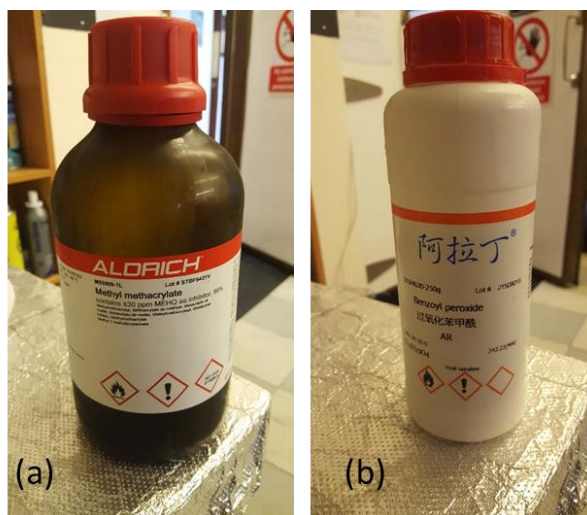


Figure 3.9 Chemicals for preparing PMMA, (a) MMA and (b) BPO.

The PMMA preparation includes three steps which are pre-polymerisation, casting and polymerisation. 100 mg BPO initiator was dissolved in 100 ml MMA solution. Mixture solution was contained in glass vial and placed in a water bath operating at 70-80°C. The level of the water should be slightly higher than MMA level. After about one hour, the contents became viscous as glycerine which was considered completion of pre-polymerisation. Then viscous solution was pour directly onto flat glass substrate and baked at 40 °C for 24 hours. Transparent and flat solid PMMA layer was eventually formed. The thickness of PMMA was controlled by applying volume.

- **CMS Separation and Transferring**

After host media are cured, CMS were peeled off from substrate. It should be noted that the average thickness of CMS is about few hundreds of microns, hence careful operation is required. For separating the PDMS-CMS, sample was completely immersed in acetone (99.5%) for 5 minutes. Since the photoresist layer between substrate and PDMS was dissolved by

acetone, PDMS-CMS was successfully detached from substrate without damage. For separating the PMMA-CMS, sample was heated up to 100°C and immediately cooled down in fridge. Because of much larger coefficient of thermal expansion (CTE) of PMMA (68-75) than glass (5.9), the PMMA shrunk faster than glass, resulting relative displacement between two layers so that PMMA is detached.

The final form of CMS is illustrated in Figure 3.10. As it shown, BTG microspheres were encapsulated in hosting materials. The PDMS-CMS exhibits flexible property which contributes to attaching on a curved surface. Moreover, it can be manipulated similarly to classical coverslip, offering the freedom to position particle lens at desired location. While PMMA-CMS performs the same function, but it becomes tough as general plastic when completing polymerisation. It could be considered in the application of aqueous sample imaging and nano-scale patterning.

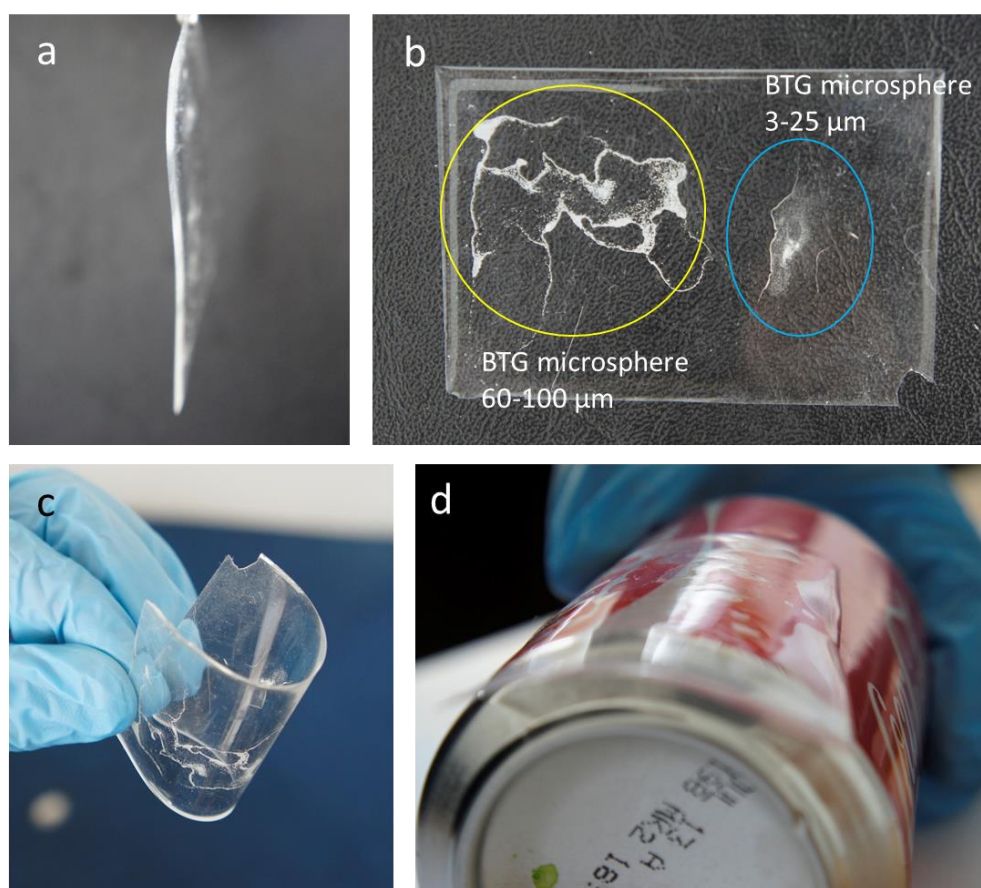


Figure 3.10 The CMS peel-off and transfer onto samples. (a) The side view showing the thickness. (b) Top view. The particles in yellow circle is large (60~100μm) microspheres, while particles in blue circle is small (3~25μm) microspheres. (c) and (d) show that CMS exhibits flexible body and can strongly adhere on curved surface.

3.3.3 Manufacturing of superlensing microsphere objective lens

The imaging window of a microsphere lens is often very small, typically a few micrometres only. This requires a scanning operation of the microsphere superlens to generate a complete image of a sample. In the previous sections, a coverslip superlens was proposed by encapsulating high-index microspheres (BaTiO_3) inside a transparent host material (such as PMMA and PDMS). Scanning of microsphere superlens, however, requires synchronization with microscope objective for full super-resolution image construction. This is difficult to achieve with existing design of coverslip superlens which is separated from objective lens. In this thesis, we propose an improved design which solves the synchronization problem between coverslip superlens and objective lens. The idea is simple but effective, using a custom-made lens adaptor to integrate these two lenses to form a superlensing microscope objective lens. Imaging performance and nano-patterning results can be found in **Chapter 7**.

3.3.3.1 Fabrication procedures

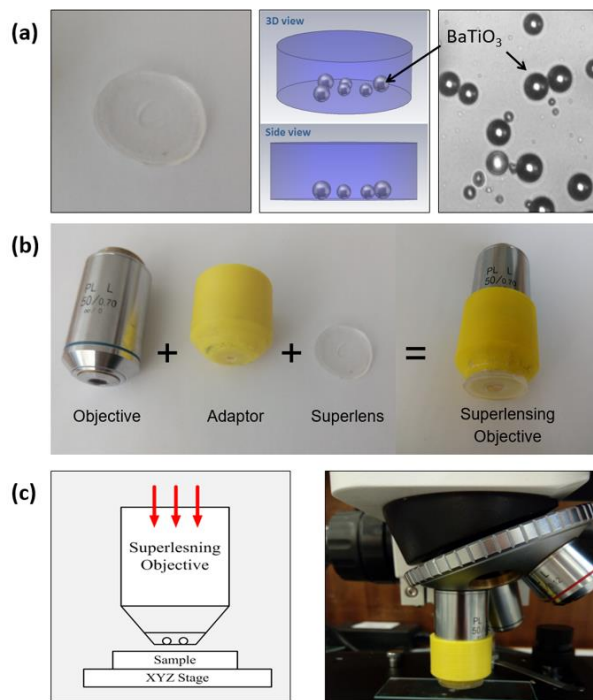


Figure 3.11 Superlensing objective lens. (a) The BaTiO_3 superlens was fabricated by encapsulating a monolayer of BaTiO_3 microsphere inside a PDMS material. (b) the super objective was made by integrating a conventional microscope objective lens (e.g. 50x, NA: 0.70, or 100x, NA:0.95) with a BaTiO_3 microsphere superlens using a 3D printed adaptor (c) Experimental configuration for super-resolution imaging using developed objective which was fitted onto a standard white light optical microscope.

The key concept and design of superlensing microscope objective is illustrated in Figure 3.11(b) and (c). A conventional microscope objective (OB) lens with magnification factor between 50x and 100x, NA between 0.7 and 0.95 was selected. A lens adaptor was designed in Solidworks and then printed with a 3D plastic printer (model: Prusia I5). The adaptor has a tube size fit to the objective lens tube, with reasonable friction allowing up-down adjustment. A CMS (Figure 3.11(a)) was bounded to the bottom end of the adaptor using high-adhesive glue. This results in an integrated objective lens consisting of conventional OB and a Coverslip Microsphere Superlens (CMS). The imaging resolution will be determined by the CMS while the conventional objective lens provides necessary condition for illumination. The obtained superlensing lens can be easily fitted to any existing conventional microscopes; in this study, we used two brands of optical microscopes to prove the lens's flexibility (Olympus BX60 and a low-cost ICM100 microscope) in usage.

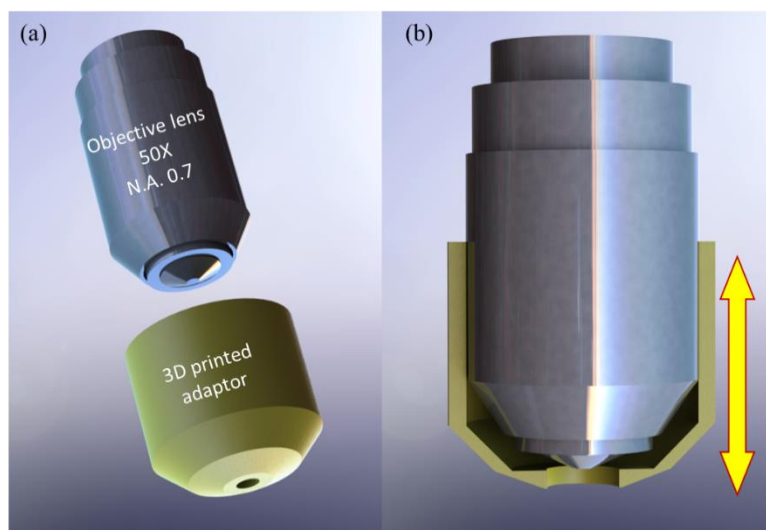


Figure 3.12 3D design of adaptor by Solidworks. The adaptor has a tube size fitting to the objective lens tube. (b) shows cross-section of lens adaptor. It can be adjusted vertically to reach best focus position.

This design can operate in either static imaging and scanning imaging. The scanning was performed using a high-resolution nano-stage (model: PI P-611.3 Nanocube), with 1 nm resolution in XYZ direction, travel range 100 μm . In experiments, the superlensing objective lens was fixed on microscope and kept static, the underlying nano-stage moved and scanned the samples across the objective lens. The imaging process was video recorded using a high-

resolution camera (ToupCAM UCMOS 14000KPA). The video was then analysed, and frames were used to generate a stitched image of the sample.

3.3.4 Methods for preparing ordered array of microsphere superlens

Many applications in optics and nanotechnology require ordered arrays of spherical particles[76], [93]–[98]. Various technologies were invented to fabricate tailored arrays for multiple sized and shaped particles. For small particle with dimension of nano-scale or few microns, self-assembly is common methods to obtain their regular arrangement. However, when particles size increase, gravity is much bigger than the floating force and becomes dominated. Unlike small particles, the big particles sink rapidly after being dissolved in DI water. It is hard to collect the solution with microspheres inside. The self-assembly, which is commonly used for small particle monolayer fabrication, is not suitable for big microspheres. Another technique is optical trapping or optical tweezers, which can capture and move single or multiple particles by an attractive or repulsive force from a highly focused laser beam or micro optical fibre[99], [100]. However, observation and laser aiming for optical trapping are time-consuming, and regarding particle moving is individually performed, which results in size limitation of processing area. Besides, fast arrangement of particles over large-area is also challenging for mechanical positioning methods which typically use atomic force microscopy (AFM) probe, a fine glass micropipette or piezo-based robotic manipulator to push particles to targeted positions[101], [102].

In this thesis, method for rapidly generating large-area microsphere arrays were demonstrated. Approach utilised photolithography technique to form a template with micro-well arrays. Thereby, microspheres were trapped by micro-well. The final sample made by this approach was attached onto 3D printed lens adaptor and incorporated with laser system for nano-scale patterning (presented in **Chapter 7.5**).

- **Overview of Procedures**

Photolithography is a useful technique in micro- and nano-fabrication, for example complex integrated circuits, CMOS wafer and microfluidic channels. It applies photomask to project geometric patterns onto a light-sensitive material ‘photoresist’. After series chemical treatment, exposed areas are either remained or removed. In this section, a micro-pillar array

template was fabricated by photolithography method. Then template texture was transferred into PDMS substrate to create micro-wells structure, thus microspheres were easily trapped. Figure 3.13 shows the procedure to make micro-well structure for aligning microspheres in array.

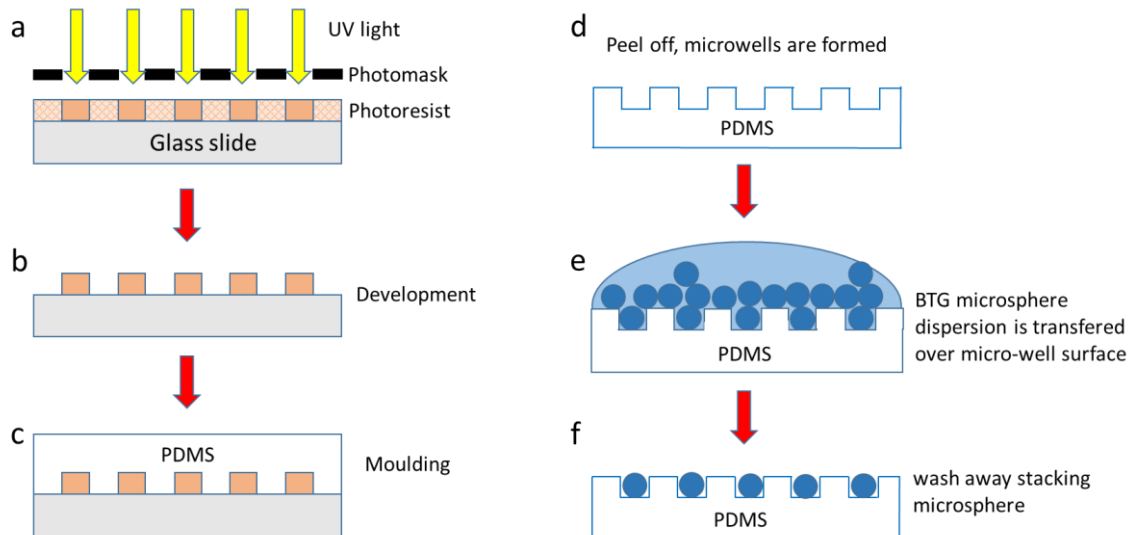


Figure 3.13 Template prepared by photolithography and PDMS moulding transfer micro-structure from template. (a) Negative photoresist is deposited on glass substrate and exposed by UV light. (b) unexposed area is developed by AZ 726 MF developer. (c) PDMS solution is deposited onto micro-structured surface and (d) duplicating opposite micro-structure. (e) BTG microsphere dispersion droplet is spread across surface and micro-well structure helps to trap them. (f) stacking particles are washed away and remaining particles in micro-wells.

• Template preparation

A cross-linking negative photoresist AZ® 125 nXT (MicroChemicals) was used to generate micro-pillar array on glass substrate (figure 2.10(a)). A film photomask with 20 μm and 30 μm circular transparent holes array was designed and requested from JD Photo Data. In order to efficiently trap 3-20 μm BTG sphere, thin film photoresist need to be coated by Model WS-650MZ-8NPP Spin Coater (Laurell Technologies) (Figure 3.14(c)). Then AZ® 125 nXT negative photoresist solution was carefully drop onto clean glass substrate. To achieve uniform 30 μm thick layer, two steps spinning program were set. Step 1: 500 rpm, 500 accelerations, 10 seconds. Step 2: 2000 rpm, 500 accelerations, 30 seconds. Low speed spinning in first step was for the purpose of initially spreading photoresist drop across entire substrate.



Figure 3.14 Photolithography chemicals and equipment. (a) A cross-linking negative photoresist AZ® 125 nXT (MicroChemicals), (b) AZ 726 MIF developer, (c) Model WS-650MZ-8NPP Spin Coater (Laurell Technologies), (d) Suss MicroTec MA8 contact mask aligner.

After uniform photoresist layer being formed, it was baked on a hotplate with starting temperature at 90°C and followed by 10°C rise every 30 seconds until 140°C. Sample was kept at 140°C for 17 minutes. Afterwards, designed photomask and sample were placed into Suss MicroTec MA8 contact mask aligner for UV (365nm) exposure at 1500mJ/cm² (Figure 3.14(d)). The photomask with transparent holes array let UV light transfer and expose on photoresist, thus exposed area was insoluble to development solution. Last, UV light processed sample was fully submerged into AZ 726 MIF developer (Figure 3.14 (b)) for 1 minute. Unexposed part was dissolved in development solution. Finished structures are presented (in Figure 3.15) matrix arrangement (a-c) with approximate 27 μm diameter pillar and 100 μm spacing; and (d-f) approximate 16 μm diameter pillar and 100 μm spacing. The actual sizes of the circular pillars (27 μm and 16 μm) are relative smaller than mask design. This may be caused by longer time photoresist development.

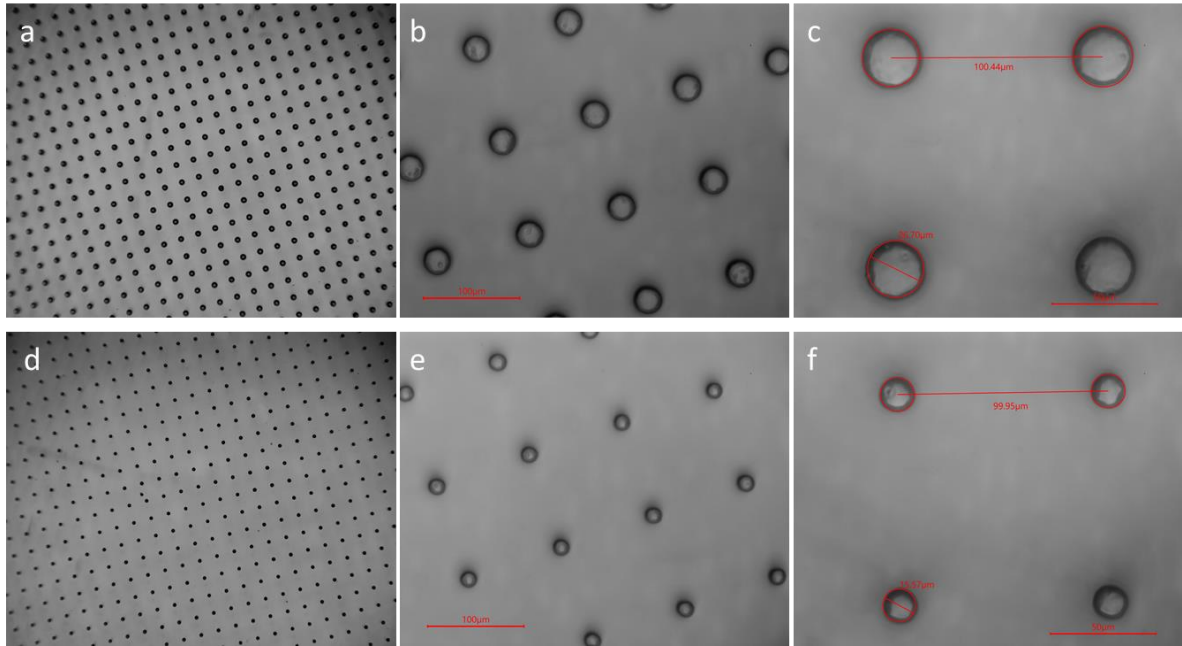


Figure 3.15 Photoresist template of micro-pillar array with (a-c) approximate 27 μm diameter and 100 μm spacing and (d-f) approximate 16 μm diameter and 100 μm spacing.

- **PDMS Moulding**

After micro-structured template being prepared, transparent PDMS solution was poured over the template surface and baked at 80°C for 30 minutes for solidification. PDMS was easily peeled off and micro-structured array was oppositely replicated on PDMS, thereby micro-well array was generated (Figure 3.16). The micro-well array consists of (a-c) 31 μm diameter wells with 98 μm spacing, and (d-f) 18 μm diameter wells with 98 μm spacing. It is noted that the diameters of micro-wells are slight bigger than sizes of pillars from template. this can be explained by the well-known PDMS shrinkage due to curing of PDMS at elevated temperature[103], [104].

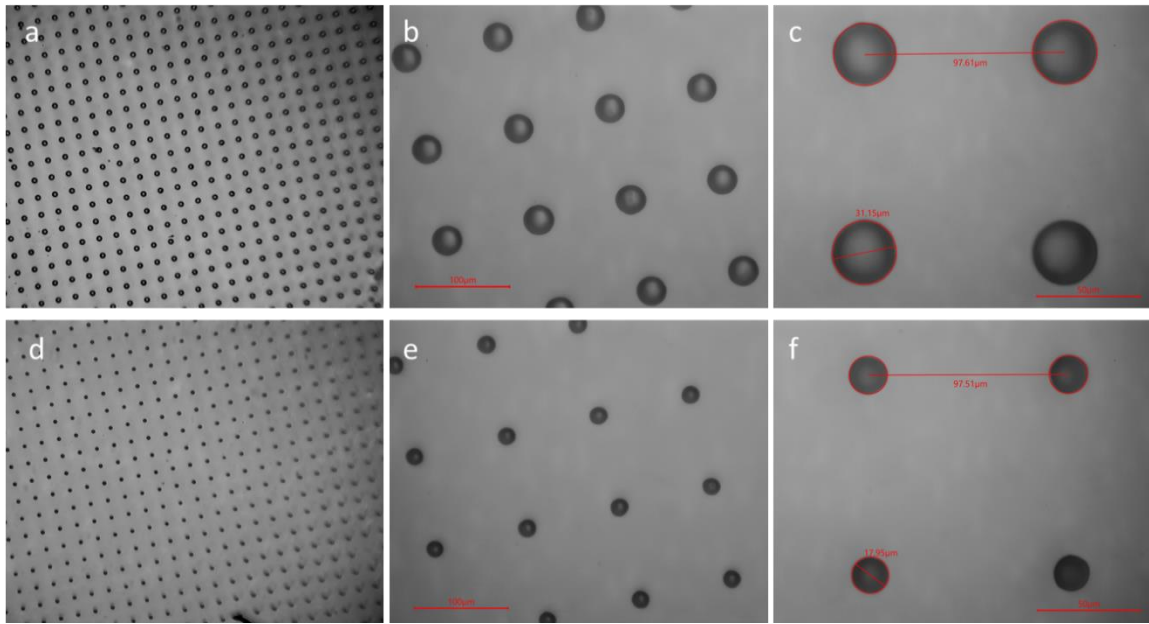


Figure 3.16 Replication of micro-structure onto PDMS to form micro-well arrays with (a-c) approximate 31 μm diameter and 98 μm spacing and (d-f) approximate 18 μm diameter and 98 μm spacing.

- **Microsphere Deposition**

Isopropyl alcohol (IPA) solution containing BTG microspheres dispersion (3-20 μm) was transferred onto PDMS surface and microspheres situating in the location of micro-well cavities were completely submerged. The remaining microspheres which stacked at non-structured area were easily washed away by IPA solution. Figure 3.17 shows the microspheres were trapped by well array. Due to high refractive index of BTG microsphere, illumination in microscope reflection mode can be strongly scattered and reflected by BTG microspheres. Therefore, particles can be clearly distinguished. In the case of 31 μm diameter Figure 3.17(a, b), multiple microspheres located inside the micro-well structure. On the other hand, 18 μm diameter structure was able to trap single particle Figure 3.17(c, d).

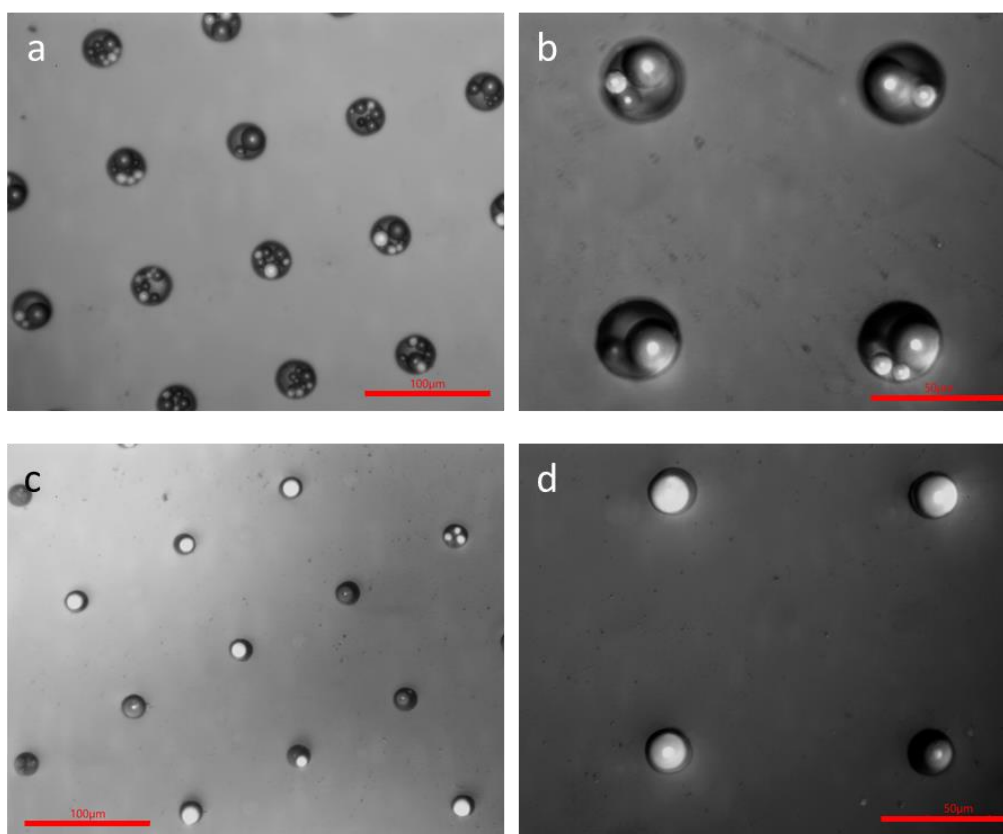


Figure 3.17 Particles trapping by micro-wells (a, b) 31 μm wells (a, b) 18 μm wells.

By this technique, microspheres were efficiently trapped in micro-structured PDMS thin sheet. With good ordered microstructure, microspheres can be arranged nicely. Moreover, due to flexible morphology of PDMS, the arranged microsphere can be manipulated on various of samples. This is conducive to potential applications, including nano-patterning, sensing and large area imaging.

3.3.5 Method for fabricating hemi-sphere metamaterial solid immersion lens (mSIL)

Titanium dioxide (TiO_2) is one of the few high refractive index materials ($n \geq 2.5$), and optical transparency to visible light, thus could be an ideal candidate for all-dielectric metamaterial superlens. However, it remains a great technical challenge to manipulate this type of rigid inorganic materials into desired shapes. In this thesis, we develop a 'nano-solid-fluid assembly' (NSFA) method using TiO_2 nanoparticles as the building blocks to successfully fabricate TiO_2 hemispheres with width up to 20 μm .

- **Procedure overview**

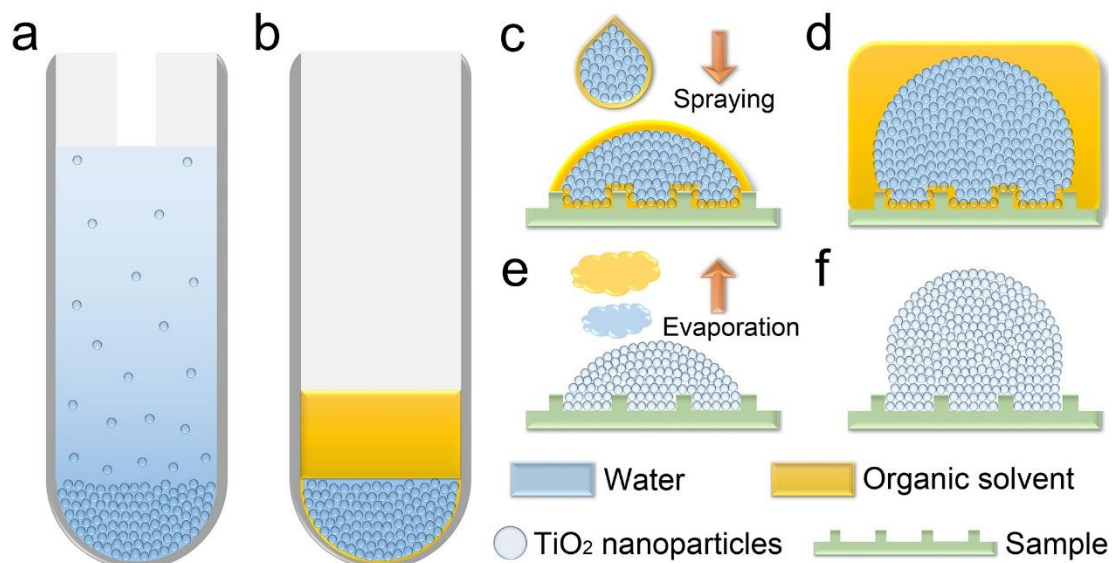


Figure 3.18 Fabrication procedure of TiO₂ nanoparticles-based hemispherical or super-hemispherical mSILs.

Figure 3.18 illustrates NSFA method for fabrication of TiO₂ nanoparticles-based hemispherical or super-hemispherical mSILs. The experimental steps are briefly listed as follow:

- 1) 15 nm anatase TiO₂ nanoparticles were centrifuged from aqueous sol and compressed into a tightly packed precipitate.
- 2) The supernatant was completely removed from the precipitate and replaced by an organic solvent mixture consisting of hexane and tetrachloroethylene to form a TiO₂ nano-solid-fluid.
- 3) To prepare hemispherical mSILs, the precipitate was directly sprayed onto the surface of test sample by a syringe, then the dispersed water-in-oil droplets of TiO₂ nanoparticles penetrated the texturing surface under the effect of oil/water interfacial tension.
- 4) To prepare super-hemispherical mSILs, the precipitate was sprayed onto the sample surface covered by a thin layer of organic solvent mixture which should help to float the nanoparticles droplets.
- 5) During or after evaporation of the organic solvent mixture, the nanoparticles droplets underwent a jamming transition due to further evaporation of interparticle water, causing a more densely packed structure of nanoparticles.

- **Preparation of TiO₂ nano-solid-fluid**

To remove possible aggregates in TiO₂ aqueous sol (VK-TA33, Hangzhou Wanjing New Material Co., Ltd., China), 35 mL 15 wt% anatase TiO₂ sol with a peak number-average size of 15 nm (Zetasizer Nano ZS90, Malvern instruments Ltd., UK) was centrifuged in a 50 mL centrifuge tube at 35,000 g for 20 min at 10 °C (GL-21M refrigerated centrifuge, Xiangyi Centrifuge Instrument Co., Ltd., China). Then, 35 ml of the unprecipitated suspension was collected and further centrifuged at 35,000 g for 60 min at 10 °C (Figure 3.18 a). The supernatant was completely removed from the translucent precipitate and then added by 10 mL organic solvent mixture consisting of hexane and tetrachloroethylene with a volume ratio of 1:2 to further wash away the residual aqueous layer adhered to the surface of the precipitate by a Pasteur pipette (Figure 3.18 b).

- **Self-assembly of TiO₂ mSILs**

A small amount of TiO₂ precipitate suspended in the organic solvent mixture was loaded into a 25 G syringe needle fitted with a stainless-steel tube with the exposed part of the tube removed. To prepare hemispherical mSILs, the TiO₂ precipitate was directly sprayed onto the surfaces of the observed samples via a 1 mL syringe, and the residual solvents were left to evaporate at ambient pressure and temperature (1 atm, 20 °C) for 3 min (Figure 3.18 c). To prepare super-hemispherical mSILs, the drops of organic solvent were spread over the surfaces of the observed samples, then the TiO₂ precipitate was sprayed onto these surfaces. After 30 seconds, the excess organic solvent was removed by touching the edge of the sample with a piece of filter paper, and left for evaporation of residual solvents (Figure 3.18 d).

This organic solvent mixture has a substantial influence on the formation of hemispherical or super-hemispherical mSILs:

- **First, after centrifugation, TiO₂ nanoparticles were compressed into a tightly packed precipitate which yet still has some residual water filling the gap between nanoparticles. The residual water allowed the precipitate to keep a very low but acceptable fluidity, which is very critical to make the TiO₂ nanoparticle-based hemispheres as fluids penetrate into the hyperfine surface texture of the target**

sample to cause an intimate contact between hemispheres and the observed samples. Remarkably, it is the organic solvent mixture which is surrounding the precipitate and immiscible with water, and the presence of high boiling point tetrachloroethylene (121.1 °C) as a protective layer, that prevents the further loss of the residual water during assembly process. Moreover, after evaporation of the organic solvent, these nanoparticles were expected to undergo a jamming transition [105], [106] (the phase transition from a fluid-like to a solid-like state) arising from the interparticle capillary condensation due to further evaporation of the residual water, thus forming an even more densely packed structure of nanoparticles and correspondingly higher refractive index of hemispherical or super-hemispherical mSILs. Without suspension of nanoparticles precipitate in organic solvent, the precipitate would be rapidly dehydrated in air and lose its fluidity.

- Second, owing to the low surface tension of hexane (18.4 mN/m at 25°C), the organic solvent could readily wet the various surfaces of the observed samples, which would further enhance the filling of nanoscale surface features by TiO₂ nanoparticles and thereby maximize the collection of the near field evanescent waves. Without the aid of hexane, the nanoparticles droplets only formed pale hemispheres on observed samples, probably because the presence of air gaps between hemispheres and sample surfaces would cause strong scattering of light (Figure 3.19 a).
- Third, the hydrophobic effect of organic solvent mixture can drive the droplets of hydrophilic TiO₂ nanoparticles to minimize the oil/water interfacial free energy by minimizing their exposed surface areas, producing curved shapes with regular and smooth surfaces.
- Fourth, the pre-coated thin layer of organic solvent can be used to control the types of mSILs as shown in Figure 3.20(a-f): Without this layer of organic solvent onto the sample surface, TiO₂ hemispherical mSILs were obtained due to a compromise between two opposing tendencies, namely the collapse of nanoparticles droplets under gravity and the resistance to collapse owing to the closely stacked structure of nanoparticles (Figure 3.20(a-c)). Use of a thin layer of

organic solvent on sample surface would serve to float and support the nanoparticles droplets, producing TiO₂ super-hemispherical mSILs (Figure 3.20 d-f).

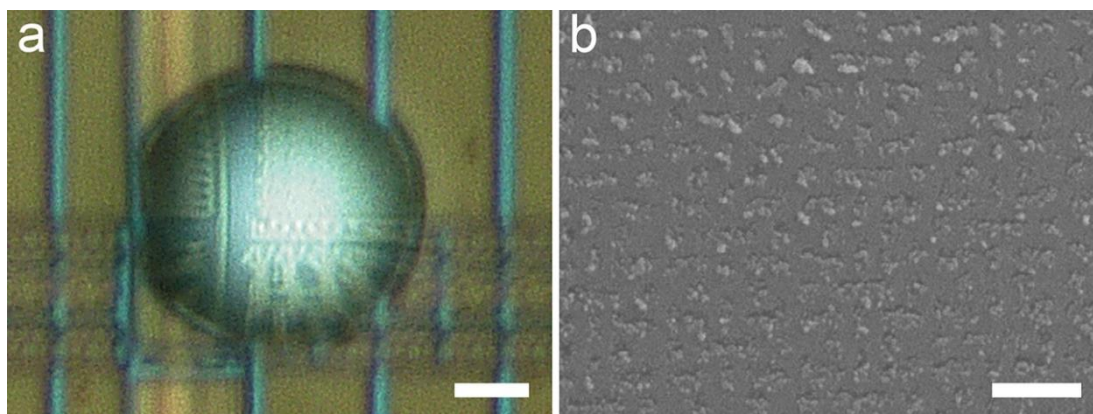


Figure 3.19 Forming of TiO₂ hemispheres without the aid of hexane. (a) The optical micrograph shows that the TiO₂ nanoparticles droplets suspended only in tetrachloroethylene would form pale hemispheres on a wafer pattern with 50 nm features. (b) Corresponding SEM image of the bottom surface of a hemisphere previously located on the water pattern. The results indicate that the relatively high surface tension of tetrachloroethylene (31.7 mN/m at 20 °C) may not fully wet the sample surface and is not effective in improving the penetration of TiO₂ nanoparticles into the nanoscale surface texture on the observed sample, and the resulting air gaps between hemisphere and sample would prevent the collection and propagation of light. Scale bars, 5 μ m in (a) and 500 nm in (b).

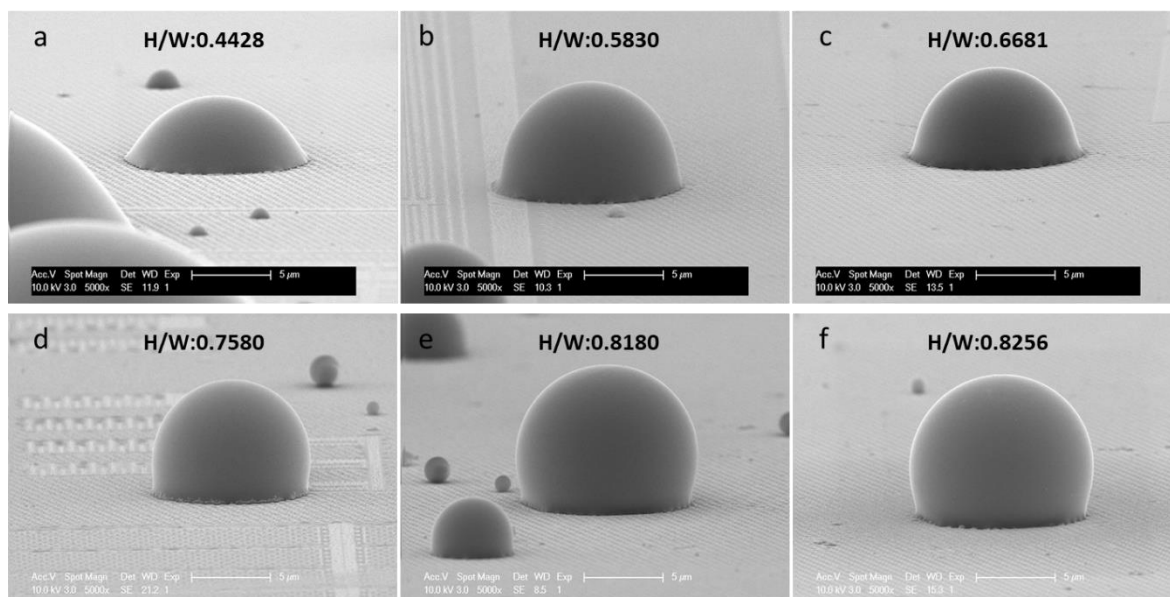


Figure 3.20 Hemispheres (a-c) were prepared without thin layer of organic solvent and super-hemispheres (d-f) were prepared with pre-coated thin layer of organic solvent. The height-to-width ratio are (a) 0.4428, (b) 0.5830, (c) 0.6681, (d) 0.7580, (e) 0.8180, (f) 0.8256.

The detail information regarding to optical mechanism and super-resolution imaging performance will be demonstrated and discussed in **chapter 5.5 and 6.2**.

3.3.6 Fabrication of hybrid microsphere superlens

In this section, a detailed method for preparing optical transparent and high refractive index ZrO_2/PS nanohybrid colloidal microspheres is presented. A facial suspension polymerization method used here can fabricate spheres with controllable refractive index ($n_p = 1.590\text{--}1.685$). In **chapter 6.3**, these hybrid microspheres were used for optical super-resolution imaging and features as small as 50–60 nm was clearly resolved.

- **Materials**

All materials for preparing hybrid microsphere are listed in Table 3.5. Styrene was distilled under reduced pressure to remove the inhibitor hydroquinone, which was then stored in a refrigerator at 4°C.

Chemical	Company
Zirconium(IV) isopropoxide–isopropanol complex (99.9%)	Sigma-Aldrich
Anhydrous benzyl alcohol (99.8%)	Aladdin Reagent Co., Ltd (China)
3-(trimethoxysilyl) propyl methacrylate (MPS, 97%)	Aladdin Reagent Co., Ltd (China)
styrene (S, 99%)	Aladdin Reagent Co., Ltd (China)
oleic acid (OA)	Aladdin Reagent Co., Ltd (China)
lauroyl peroxide (98%)	Aladdin Reagent Co., Ltd (China)
divinylbenzene (DVB, 80%)	Aladdin Reagent Co., Ltd (China)
cedarwood-oil	Aladdin Reagent Co., Ltd (China)
Polyvinyl alcohol (PVA1788)	Sinopharm Chemical Reagent Corp (China)
tetrahydrofuran (THF, Z99.5%)	Sinopharm Chemical Reagent Corp (China)
anhydrous methanol (Z99.5%)	Sinopharm Chemical Reagent Corp (China)
anhydrous ethanol (Z99.7%)	Sinopharm Chemical Reagent Corp (China)
dimethyl-silicone	Sinopharm Chemical Reagent Corp (China)

Table 3.5 Materials for fabricating hybrid microsphere.

- **Synthesis of ZrO_2 nanoparticles**

Firstly, ZrO₂ nanoparticles were synthesised according to a method described elsewhere[107]. Briefly, zirconium(IV) isopropoxide–isopropanol complex (6.25 g) and benzyl alcohol (60 mL) were charged into a 100 mL Teflon-lined autoclave. This Teflon-lined autoclave was sealed and placed into an oven at a temperature of 240 °C. After 4 days, the reaction mixture was allowed to cool down, and a white turbid suspension was obtained.

- **Modification of ZrO₂ nanoparticles**

The as-synthesized ZrO₂ nanoparticle suspension was centrifuged to obtain a white precipitate and then washed by three cycles of sonication and centrifugation with ethanol. The wet ZrO₂ nanoparticles were dispersed in the pre-made THF/MPS solution based on a molar ratio of 0.4:1 for MPS-to-ZrO₂ and 1.22 wt% of ZrO₂. The dispersion was sonicated for 30 minutes at room temperature, and then oleic acid (OA, 500 mL) was added and the mixture was sonicated for another 30 minutes. The transparent dispersion was placed into an oven at a temperature of 60 °C for 20 hours and at 80 °C for another 3 hours. The dispersion was centrifuged at 7000 rpm for 10 minutes to remove the possible aggregates and then concentrated by a rotary evaporator to remove most of the THF. The concentrated MPS and oleic acid modified ZrO₂ nanoparticles slurry was precipitated and washed by two cycles of sonication and centrifugation in ethanol. The purified MPS/OA/ZrO₂ nanoparticles were added into a styrene monomer to obtain a yellowish transparent solution upon ultrasonication, which was then stored in a refrigerator.

- **Preparation of ZrO₂/PS nanohybrid colloidal microspheres**

Suspension polymerisation was used to synthesise the ZrO₂/PS nanohybrid colloidal microspheres. In detail, polyvinyl alcohol was added into deionised water and heated at 60 °C for 20 minutes to obtain a 0.175 wt% of PVA aqueous solution, and then it was allowed to cool. Various amounts of MPS/OA/ZrO₂ nanoparticles dispersed in styrene, 10 wt% of DVB in terms of S and 4 wt% of lauroyl peroxide in terms of S as the initiator were mixed and then poured into a PVA aqueous solution, and emulsified with a homogeniser at 6000 rpm for 3 min. The emulsified dispersion was then poured into a 250 mL four-neck round-bottom flask equipped with a mechanical stirrer, a reflux condenser, a thermocouple, and a nitrogen gas inlet. The system was degassed with nitrogen for 30 minutes to remove oxygen in the reactor, which was heated to 70 °C for polymerisation at 250 rpm for 12 hours under a nitrogen

atmosphere. The products were labelled as M1, M2, M3, M4, and M5, corresponding to 10.5, 23.5, 30.3, 38.2, and 50.8 wt% of ZrO_2 incorporated microspheres based on TGA analysis. As a control, bare polymer microsphere M0 was prepared in the same way but without ZrO_2 nanoparticles. The as-synthesized microspheres were obtained by centrifugation and washing by three cycles of sonication and centrifugation with ethanol, and then dried under vacuum for characterisation.

- **Super-resolution imaging by composite microspheres**

To demonstrate the super-resolution property of the microspheres, the as-synthesized nanohybrid colloidal microspheres were observed with an Olympus optical microscope (BX63) under an objective lens of 100X with a numerical aperture of 0.8 and reflective mode illumination with a halogen light source for the optical imaging. The sub-diffraction-limited objects used in the experiment were semiconductor chips with nano-patterned structures of 75 nm and 60 nm gaps between specific stripes with widths of 145 nm and 115 nm, respectively. For imaging the 75 nm gaps, the microspheres were first spread on the surfaces of the sub-diffraction-limited objects through the evaporation of ethanol drops; subsequently, dimethyl-silicone (refractive index of the medium is $n_m = 1.400$) was dropped onto the substrates to make the microspheres be semi-immersed in silicon oil after spin-coating at a speed of 3000 rpm for 5 min. For imaging the 60 nm gaps, the microspheres were semi-immersed in cedarwood oil ($n_m = 1.515$) through spin-coating in the same way as dimethyl-silicone; then, most of the cedarwood-oil was washed away by tetrachloroethylene to reduce the accumulation of oil around the spheres. The sub-diffraction virtual images of the nano-patterned surfaces were acquired by focusing through the microspheres into the substrates. In addition, more complicated structures of the chips with 50 nm gaps were also imaged by coupling the dimethyl-silicone semi-immersed microspheres with an Olympus LEXT OLS4100 scanning laser confocal microscope under reflection mode laser illumination at $\lambda = 405$ nm. Super-resolution images were acquired by a 100X and NA = 0.95 objective lens.

3.3.7 Spider Silk Superlens Preparation

Figure 3.21 shows the spider, its silk and the corresponding imaging experimental setup. The silk used in our experiments were Minor Ampullate glands filaments reeled directly from *Nephila edulis* spiders (Figure 3.21 a) which was provided by Professor Fritz Vollrath and his

research team from the Oxford Silk Group, Department of Zoology, University of Oxford. In this study, the spun silk filament had a diameter of $6.8\ \mu\text{m}$ and refractive index of 1.55[108]. To facilitate manipulation and precision positioning of the silk at desired location, the silk was top-encapsulated using a transparent cellulose-based tape and directly placed on top of the imaging sample surface. Isopropyl alcohol (IPA, $\text{RI}=1.377$) was then injected to fill the gap of silk and sample surface (Figure 3.21 b), as to improve the sample-silk contact and imaging constant. In **Chapter 8**, the sample systems were examined in reflection mode under a white light microscope equipped with a halogen lamp with peak wavelength at 600 nm (Olympus BX60). Two imaging samples were used: a semiconductor chip with features about 400-500 nm (above diffraction limit), and a commercial Blu-ray disc with 100/200nm features (below diffraction limit).

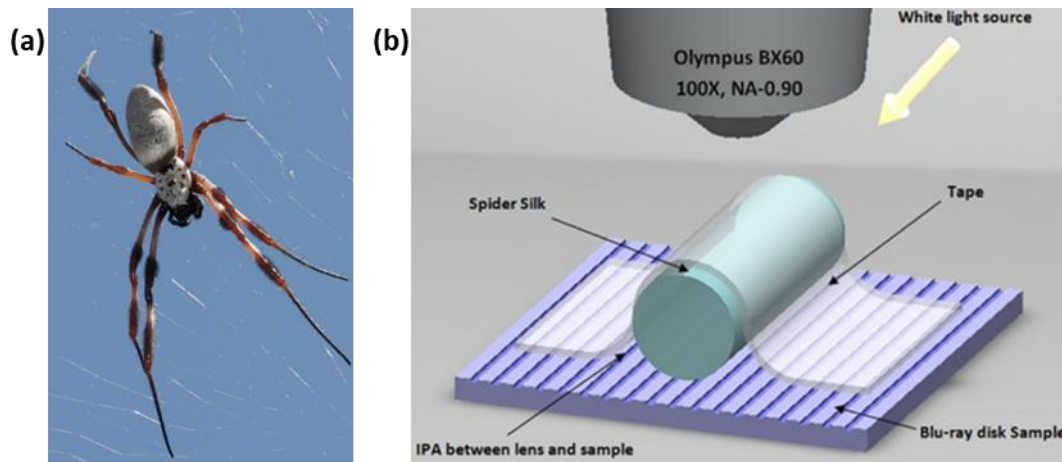


Figure 3.21 (a) *Nephila edulis* spider, (b) schematic drawing of reflection mode silk bio-superlens imaging. The spider silk was placed directly on top of the sample surface by using a transparent cellulose-based tape. The gaps between silk and sample was filled with IPA which improves imaging contrast. The silk lens collects the underlying near-field object information and projects a magnified virtual image into a conventional objective lens (100x, NA:0.9).

3.3.8 On-chip Microfluidic Superlens Fabrication

Microfluidics is an advantage tool for solving biology and chemistry issues in the form of manipulation fluids behaviour in micro-scale. A microfluidic chip incorporates designed micro-channels fabricated into a material (glass, silicon or polymer) offering the possibility of desired features of mixture, pumping, sorting, trapping or controlling the biochemical environment[109]. In our experiment, a coverslip microsphere superlens CMS (high-index

BaTiO₃ microsphere encapsulated in PDMS, introduced in previous section) was aligned and bonded right on top of the microfluidic channels where cells and viruses pass by through the channels. Figure 3.22 illustrates the fabrication procedure of microfluidic superlens.

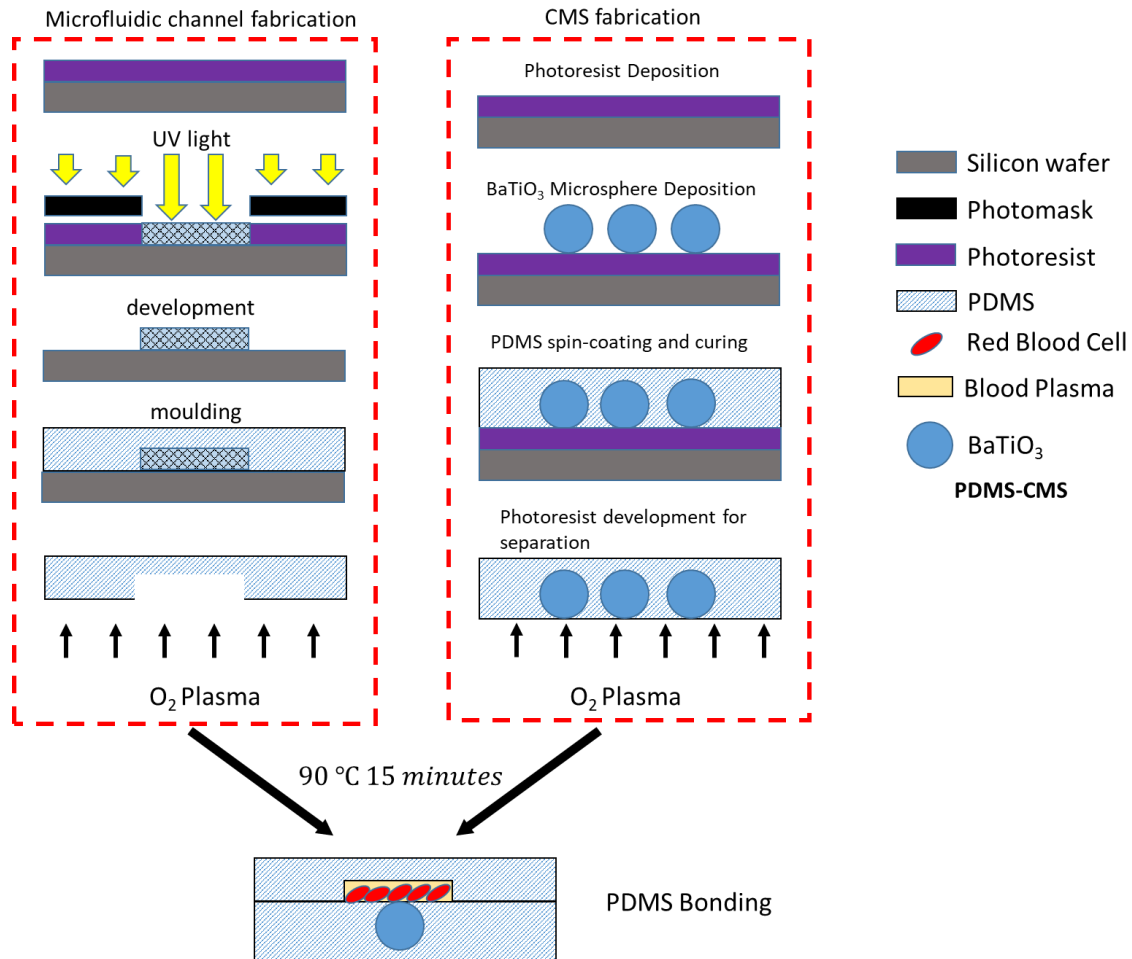


Figure 3.22 Fabrication Procedure of integration of microfluidics channel and microsphere lens.

- **Fabrication of Microfluidic Channel Template**

The microfluidic channel design was provided by Owen Guy's group from Swansea University. Photolithography technique was applied in the experiment for microfluidic channel template manufacturing. SU-8 2075 negative photoresist was spin-coated onto silicon wafer at 3000 rpm for 40 seconds to given ~100 μm thickness. Through a series of processes including 15 minutes 100°C soft-baking; 500mJ UV exposure; 2 minutes 110°C post-baking; and SU-8 development, an inverted micro-channel pattern was formed on substrate.

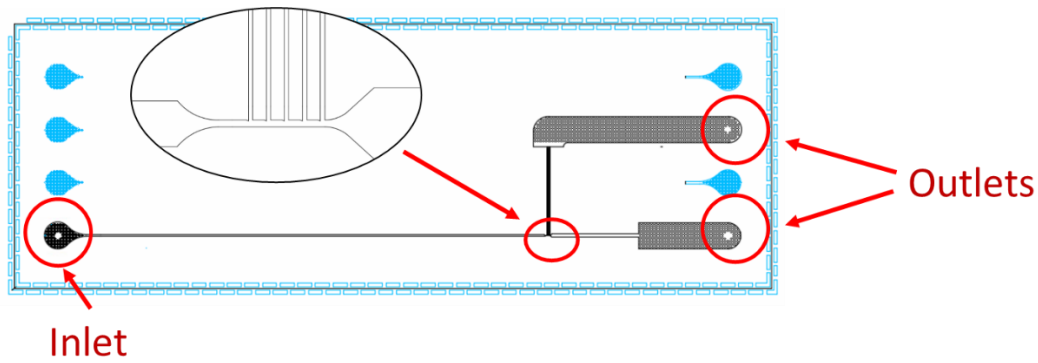


Figure 3.23 Microfluidic chip design.

- **PDMS Moulding**

Prepared PDMS pre-polymer was carefully poured onto silicon wafer template until reaching 3 mm thick in order to obtain easy usability and strong support. Then, it was baked at 80°C for 2 hours to ensure fully solidification. After peeling off from substrate, an inverted structure consisted of micro-channel was formed on substrate.

- **CMS Superlens Fabrication and Bonding onto Microfluidic Channel**

Another PDMS layer which consists of BaTiO₃ microsphere (60-90 μm) coverslip microsphere superlens (CMS) was prepared by following the procedure in **chapter 3.3.2**. Then, O₂ plasma etching (Oxford Plasmalab 80Plus RIE) was employed for oxidising the surfaces of both PDMS samples that enabled the strong bonding between the two surfaces (Figure 3.24). The setting parameters for treating PDMS surfaces are shown in right figure: Oxygen with 20 sccm was applied during processing; chamber pressure was set to 75 mTorr; RF generator power was set to 40 watts; and the process ran for 25 seconds. After O₂ plasma etching, two PDMS layers were attached with alignment of microspheres and channel. By heated at 90°C for 15minutes, two pieces are secured bonded.

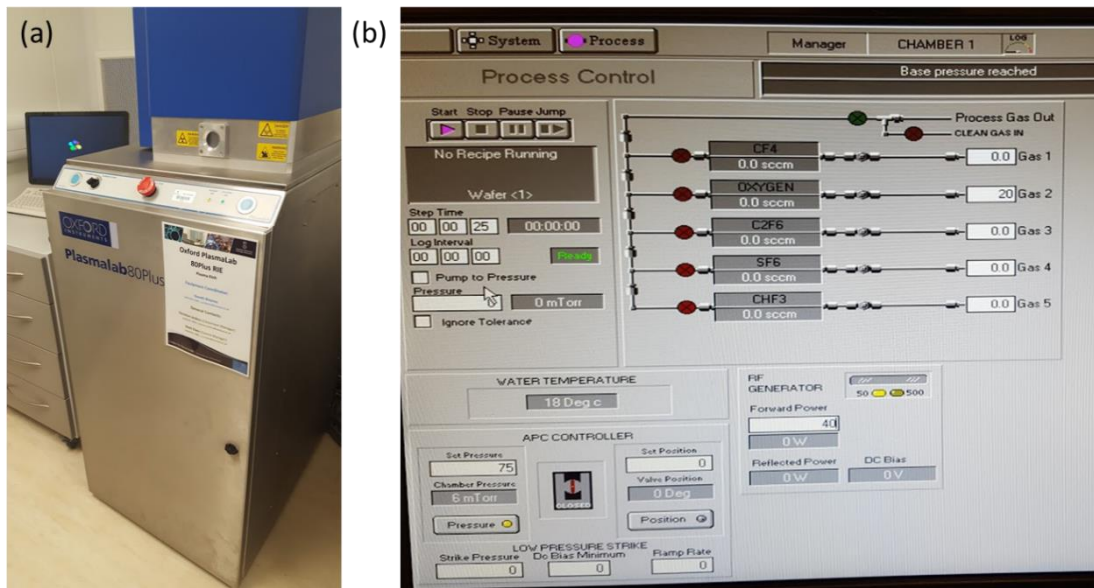


Figure 3.24 (a) Plasma etcher (Oxford Plasmalab 80Plus RIE) for oxidising PDMS surfaces. (b) Corresponding setting parameters.

- **Microfluidics Setup**

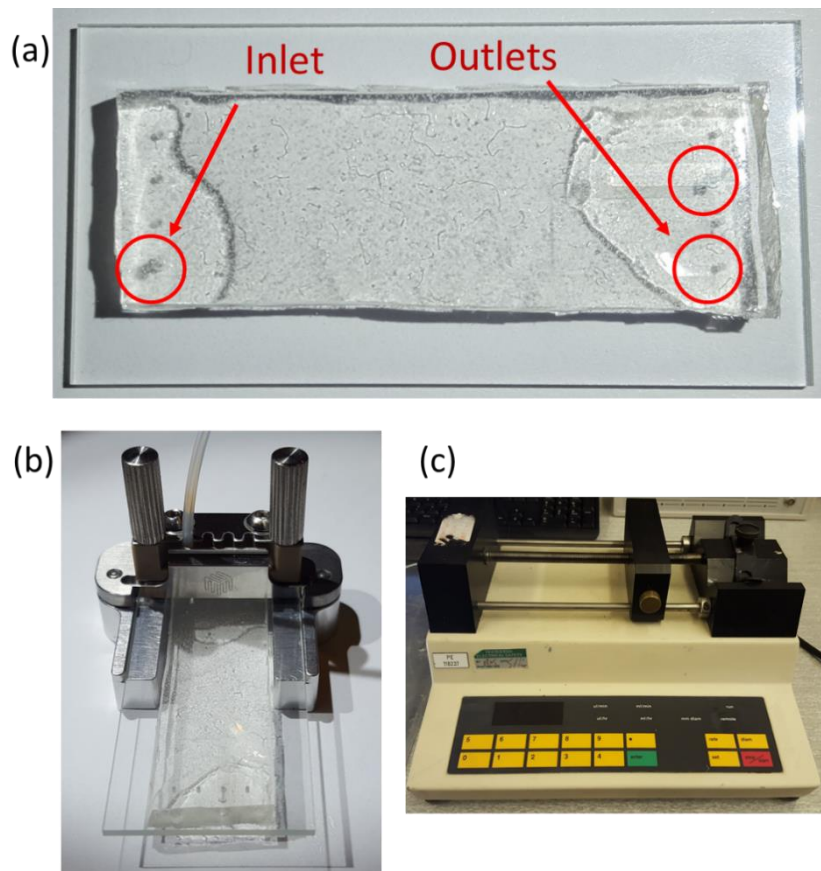


Figure 3.25 (a) Completed microfluidic chip with integration of CMS and micro-channel. (b) microfluidic chip interface and connector (c) syringe infusion pump.

Figure 3.25 (a) is the completed microfluidic chip with integration of micro-channel and CMS. This chip was then attached to microfluidics connection kit (Dolomite Microfluidics) to build up a connection to syringe pump (Harvard Apparatus 22 Syringe Infusion Pump), shown in Figure 3.25 (b and c). In **Chapter 8**, various biological samples including red blood cells (RBC), trypanosome and adenoviruses were injected into microfluidic superlens to evaluate its imaging performance.

3.3.9 Characterisation equipment

Optical super-resolution imaging

Hirox KH-7700 light microscope (Hirox Co., Ltd., Japan) equipped with a 2.11-megapixel CCD camera, a MX-10C co-axial vertical lighting zoom lens and an OL-700II objective lens (numerical aperture NA=0.8) at a total magnification of 2,100× in reflection mode.

Olympus BX63 microscope (Olympus Corporation, Tokyo, Japan) equipped with a 5-megapixel CCD camera (Olympus, DP26) and a 100× objective lens (Olympus, LMPlanFL N, NA=0.80) in reflection.

Olympus BX60 microscope (Olympus Corporation, Tokyo, Japan) equipped with a 5-megapixel CCD camera (ToupCAM UCMOS 14000KPA) and a 100× objective lens (Olympus, LMPlan FI-BD, NA=0.90) in reflection mode.

ICM100 microscope equipped with a 5-megapixel CCD camera (ToupCAM UCMOS 14000KPA) and a 50x (NA=0.70) objective lens in reflection mode.

Scanning laser confocal microscopy (Olympus OLS4100 LEXT) with a 100x and NA = 0.95 objective lens at the laser illumination of $\lambda = 405$ nm was used to characterise the geometry profiles of the oil immersed in the microsphere lenses and achieve higher resolution imaging.

Inverted microscope (Carl Zeiss Primovert) equipped with a 40x (NA=0.50) and an 80x (NA=0.80) objective lenses in transmission mode is incorporated with the on-chip microfluidic superlens for biological sample imaging.

SEM observation AFM observations

The original nanoscale patterns on a recordable Blu-ray disc or a semiconductor wafer were observed on a Philips XL30 SEM operating at an accelerating voltage of 10 kV without gold coating. The wafer pattern with 45 nm features was obtained by gold sputter coating the sample at a current of 30 mA for 180 seconds (Baltec SCD005, Liechtenstein). SEM images of the mSILs located on the observed samples were taken after gold-sputter coating. AFM images were taken on a Bruker MultiMode 8 AFM (Veeco Instruments, USA) in tapping mode.

Other characterisations

Thermogravimetric analysis (TGA) was carried out using a Perkin Elmer TGA-7 instrument (USA) at a heating rate of 10 °C/minute from room temperature to 800 °C in air. Fourier transform infrared spectra (FTIR) were acquired with a Nicolet Nexus 470 spectrometer (USA). High resolution transmission electron microscopy (HRTEM) was performed on a Tecnai G2 F20 S-Twin field emission transmission electron microscope (USA). The ZrO₂/PS nanohybrid colloidal microspheres were embedded in epoxy resin and ultramicrotomed into 70 nm thick slices for HRTEM measurements. The chemical composition and distribution of the composite microspheres were characterized by a Zeiss Ultra 55 field-emission scanning electron microscope (Germany) equipped with an X-ray energy dispersive spectroscope (EDS) for elemental area analysis (SEM mapping) and elemental line analysis (SEM linescan).

Chapter 4. Near-field Super-Resolution

Focusing of Microsphere Lens

4.1 Introduction

Optical near-field of small dielectric particles are of importance and interests for nanoscale optical engineering. Investigating the interaction between light and pure-dielectric micro and nano spheres in near-field helps us to understand focusing properties which are important to super-resolution applications including field localization, fabrication, characterisation, sensing and imaging. In 2000, Lu and Luk'yanchuk et al. firstly discovered dielectric silica particle with dimension of 500 nm can enhance optical intensity at near-field meanwhile provided super-resolution structuring[8]. Four years later this phenomenon was also realised by Chen et al.[7] and coined a new term 'photonic nanojet' which is widely used in the field[64], [110]–[116]. They reported super-resolution of this localised nanojet is on sub-wavelength scale of $\lambda/2n$ [117], where the λ is incident light wavelength and n is the refractive index of particle. However, previous studies evaluated focus properties on particular cases, wide-ranging analysis, internal focus properties and full-wave simulation still have not been explored. In this chapter, a systematic investigation on focusing characteristics such as field enhancement, focal length and focal size is represented.

This chapter is organized as follows. Section 2 presents key results on super-resolution focusing characteristics including focal length, field enhancement and spot size analysis. Section 3 calculates the microsphere focusing under a full-wave condition which considers a wide-band visible spectrum as incident source and it describes focusing properties related to reality. Section 4 is the conclusion.

4.2 Near-fields of a dielectric sphere: focal length and super-resolution

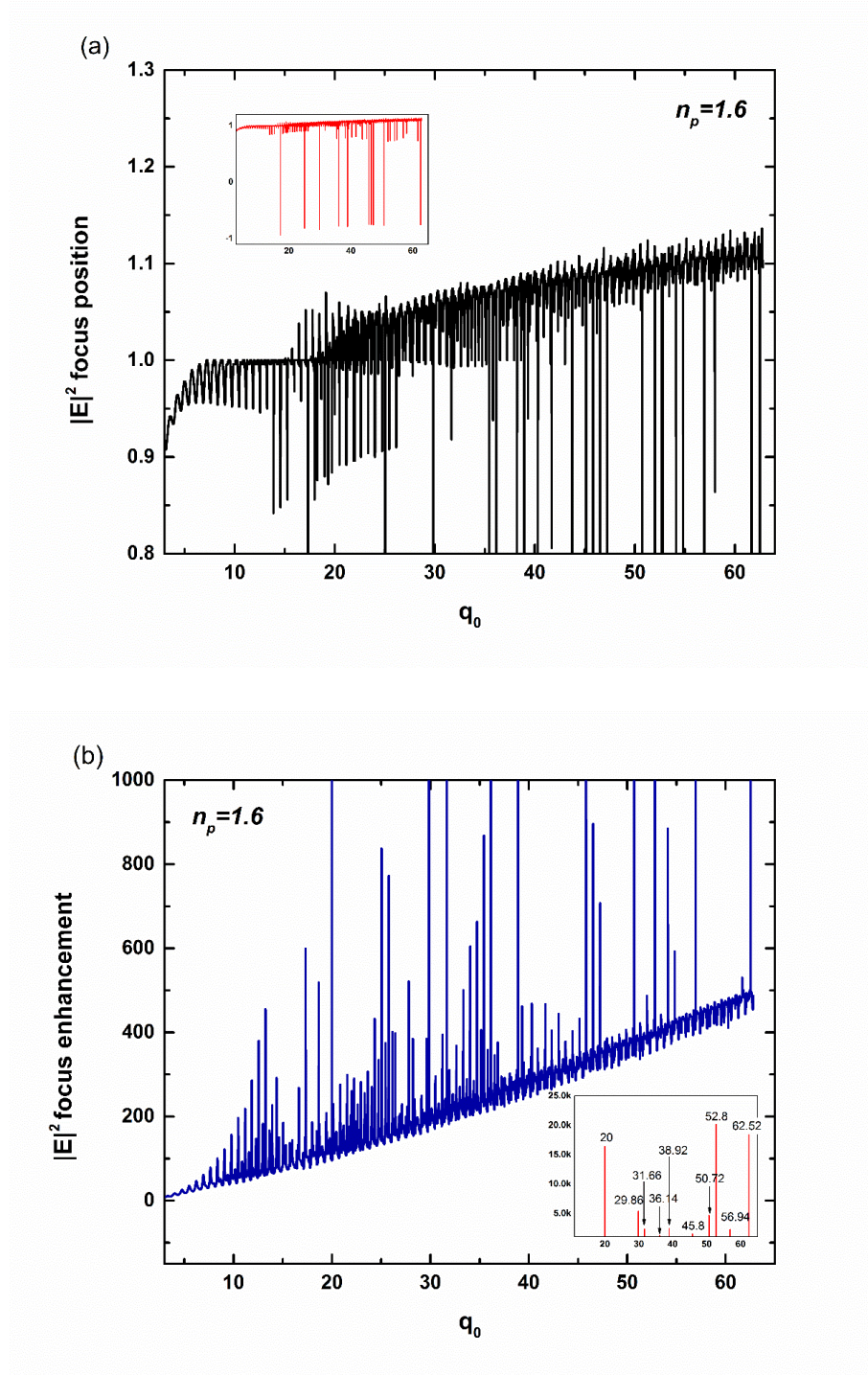


Figure 4.1 (a) Normalized focus position of $|E|^2$ field as a function of size parameter q_0 . The inset shows the overall view including the negative focal length. (b) Corresponding field enhancement factor. Note y scales are different in both plots and insets.

Figure 4.1(a) shows the dependence of particle focus position of the $|E|^2$ field on varying size parameters. The focus position for size parameters within the investigated range $\pi \leq q_0 \leq 20\pi$ shows an increasing tendency, but with highly oscillating values between 0.8 and 1.15 which means the area close to bottom boundary. These oscillations are a typical result of the optical resonance within the spherical cavities. Such problem was discussed in Ref[118]. For some size parameters, the focal length can be negative-valued which suggests focusing near the top side of particle (see Figure 4.1(a) inset) instead of the usual bottom side. It appears to be an indication of extraordinary sharp focusing as shown below. Figure 4.1(b) shows the corresponding focus enhancement factor as a function of size parameter. Similar to Figure 4.1(a), the focus enhancement curve also manifests a general increasing tendency but with strong oscillations. Again, this is due to the high sensitivity of optical resonance inside the spherical cavities on the size parameter. It is surprising to see the giant field enhancements. Figure 4.1(b) inset shows the ten size parameters that produce field enhancement larger than 1k. In fact, three of them, $q_0 = 20, 52.8, 62.52$, produce enhancement larger than 10k. This is a surprising result in terms of its strength for dielectric particle focusing which would be of particular interests for those working in the field of nonlinear optics.

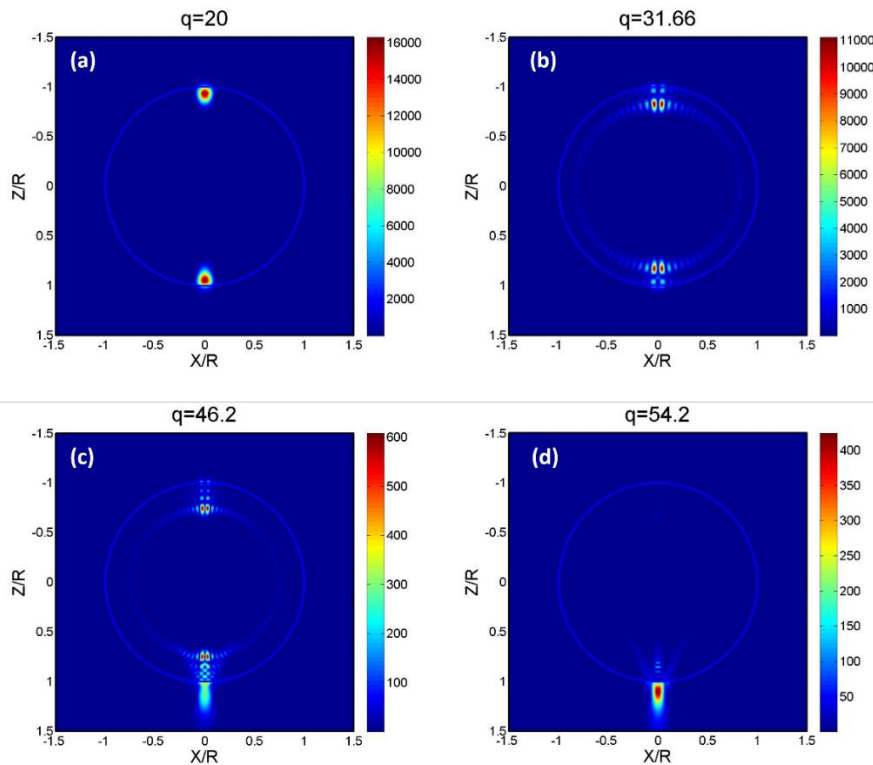


Figure 4.2 Four representative $|E|^2$ field intensity distributions across investigation range $\pi \leq q_0 \leq 20\pi$. (a) $q_0 = 20$ and (b) $q_0 = 31.66$ (c) $q_0 = 46.2$ (d) $q_0 = 54.2$.

Within the investigated range $\pi \leq q_0 \leq 20\pi$, focusing characters of particles can be summarised into four typical types. Figure 4.2 shows four representative $|E|^2$ near-field distributions for the typical size parameters $q_0=20, 31.66, 46.2$ and 54.2 . In the first type, for example Figure 4.2(a) $q_0=20$, highly focused and nearly -symmetric foci are exhibited on both top and bottom sides of the particle. It is noted that the near-fields at out-of-focus regions are weak and almost negligible as compared to the peak focus. Same phenomenon also happens at, for instance, $q_0=52.8$ and 62.52 . In Figure 4.2(b), $|E|^2$ field distribution performs an annular focusing effect along inner boundary of sphere. Meanwhile, it is accompanied by two highly enhanced hot spots on top and bottom. Figure 4.2(c) presents whispering-gallery-mode like field distribution as Figure 4.2(b), and moreover, an additional external focus at backside. Besides, the photonic nanojet generated at backside of particle is mainly happened in investigated range as shown in Figure 4.2(d). The underlying physics for these foci relates to the singularities associated with internal wave coefficients (c_1, d_1) in Equations (2.7) and (2.8), and is still under investigation.

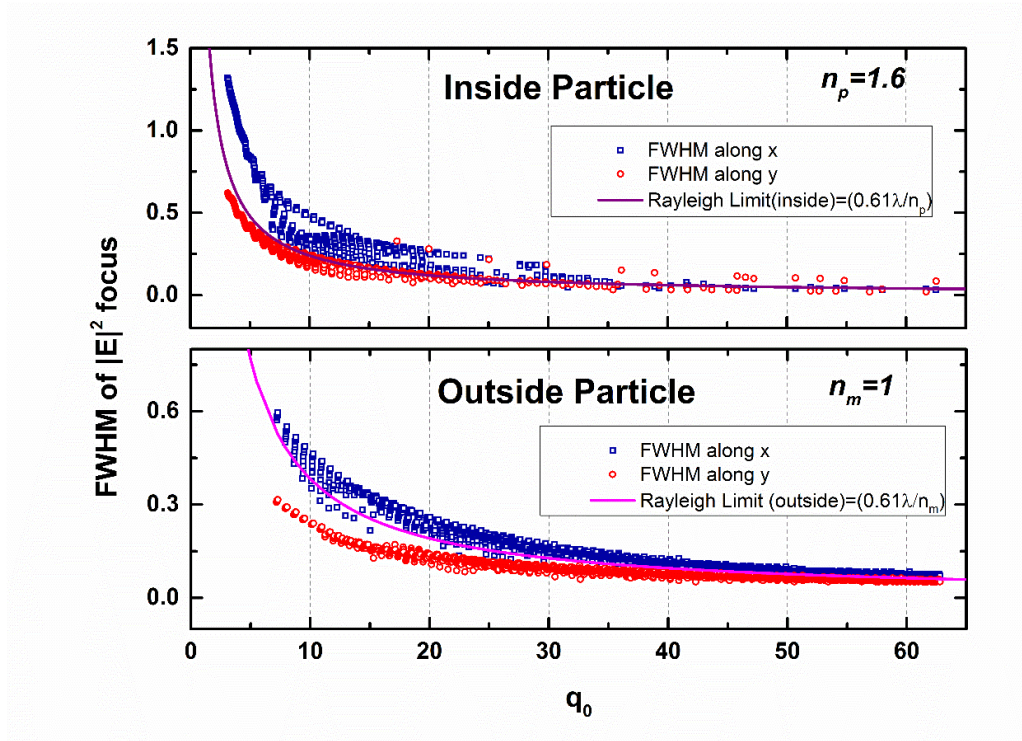


Figure 4.3 Lateral FWHM of $|E|^2$ focus as a function of size parameter q_0 , the size of FWHM was normalised to particle radius. Comparisons of FWHM sizes in x and y direction with respect to (a) focus inside particle and (b) focus outside particle.

Figure 4.3 shows calculated normalised FWHM size in x- and y-direction within the cut-plane that across focus plane as in Figure 4.1(a). Because of focus alternatively occurring at either internal or external of particle, both inside and outside cases which influence focus properties must to be considered. Blue squares and red circles indicate FWHM along x-direction and y-direction respectively. The continuous curves in both plots are Rayleigh criteria at internal ($0.61\lambda/n_p$) and external conditions ($0.61\lambda/n_m$). In both cases of focus at inside and outside, the focus FWHM along y-direction (incident field polarized at x-direction) is always smaller than or very close to that along x-direction, meaning an elliptical spot profile in lateral. Meanwhile, the FWHM in y-direction is also generally smaller (i.e., y-direction super-resolution) than or close to the Rayleigh diffraction limit, and in contrast, FWHM in x-direction is generally above the Rayleigh limit values. These findings indicate that the polarization property of the incident beam plays a role on the focus size of the electric field: the focus is prolonged at the polarisation direction and shortened at cross direction.

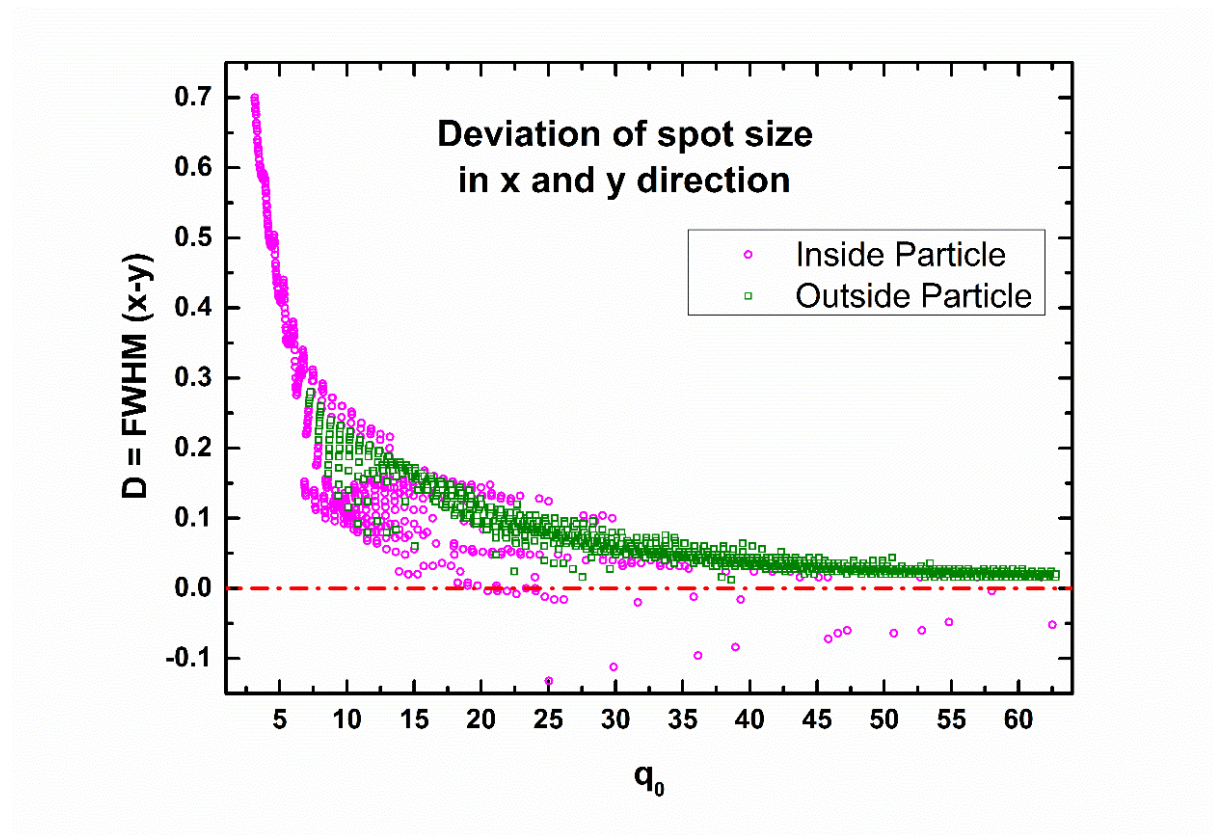


Figure 4.4 Difference of focus size along x-direction and y-direction (Deviation factor value), which produces an elliptical focus.

In Figure 4.4, the focus shape deviation factor D , defined by the difference of focus size along x and y direction was shown. The pink dots and green dots are the focus FWHM deviation value inside and outside particles respectively. As Figure 4.4, the deviation reduces with size parameter q_0 increasing. Besides, pink dots mainly concentrate at $q_0 < 15$, meanwhile, more green dots appear when $q_0 > 15$. This implies big particles have rounder lateral focus profile than small particles. Moreover, focus position of small particle is likely happened inside particle, in contrast, it tends to shift out with increase in size.

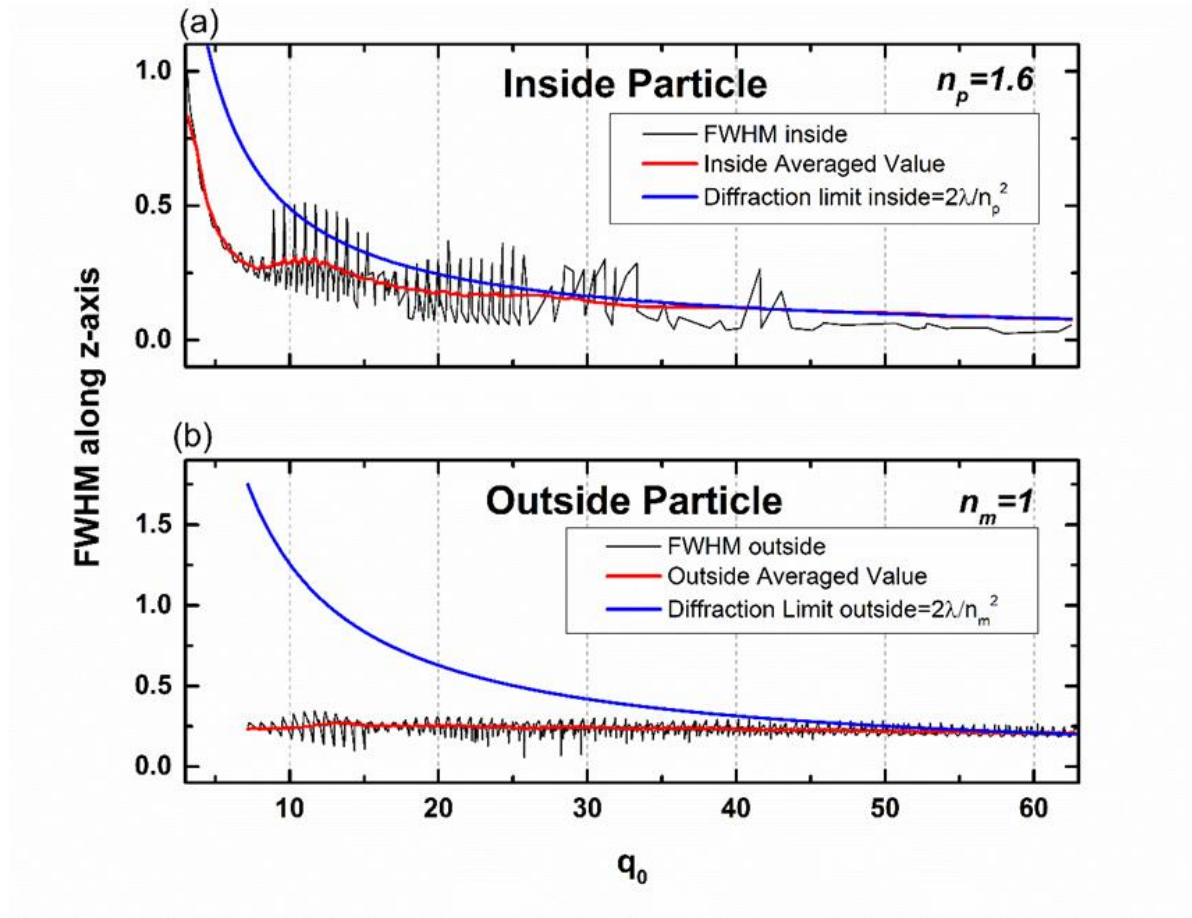


Figure 4.5 Axial FWHM of $|E|^2$ focus as a function of size parameter q_0 , the size of FWHM was normalised to particle radius.

Axial resolution achieved by spherical particle with varying parameter size is revealed in Figure 4.5. The diffraction limit along z axis is defined as $D_z = 2\lambda/n^2$. In both inside and outside focusing conditions, $\text{FWHM}(z)$ curves have obviously oscillating characteristic. We define FWHM averaged values by

$$FWHM = \frac{1}{2\ell} \int_{q_0-\ell}^{q_0+\ell} FWHM dq_0 \quad 4.1$$

This averaging smear out the resonance oscillation and clearly manifests the tendency. The ℓ is characteristic interval for averaging. It is interesting to note that in the range of $q_0 < 30$ the averaged value of internal focus is lower than diffraction limit. Then, two curves become merged. While the average value of external focus is nearly constant.

A real super-resolution spot requires both values for FWHM in x and y directions below the Rayleigh limit curve. To find these super-resolutions spots, a new figure derived from Figure 4.3 results was presented in Figure 4.6. It shows the values of FWHM along x-direction, namely FWHM(x), minus Rayleigh limit and FWHM along y-direction, namely FWHM(y), minus Rayleigh limit. Negative values represent super-resolution in that direction and real super-resolutions spots are seen for those size parameters that have both negative value in x and y direction. A lot of these super-resolution cases can be seen in Figure 4.6.

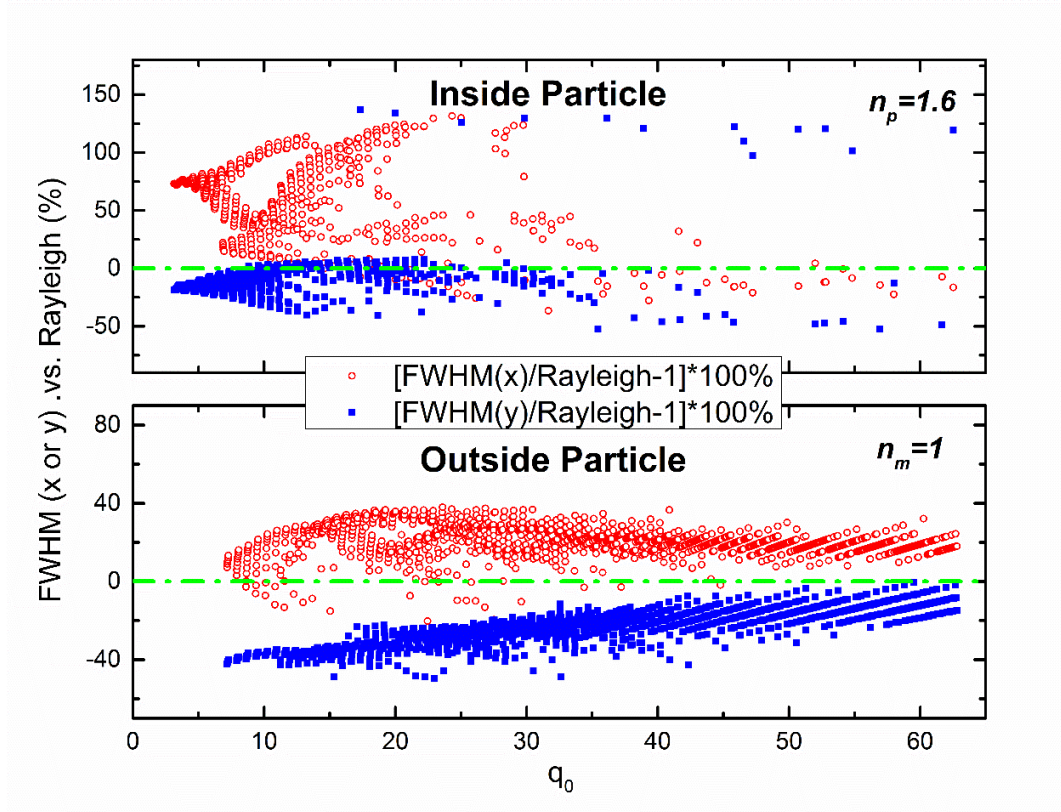


Figure 4.6 FWHM(x) minus Rayleigh (dot) and FWHM(y) minus Rayleigh (square) as a function of size parameter q_0 . Both inside and outside cases are present. Negative values represent super-resolution.

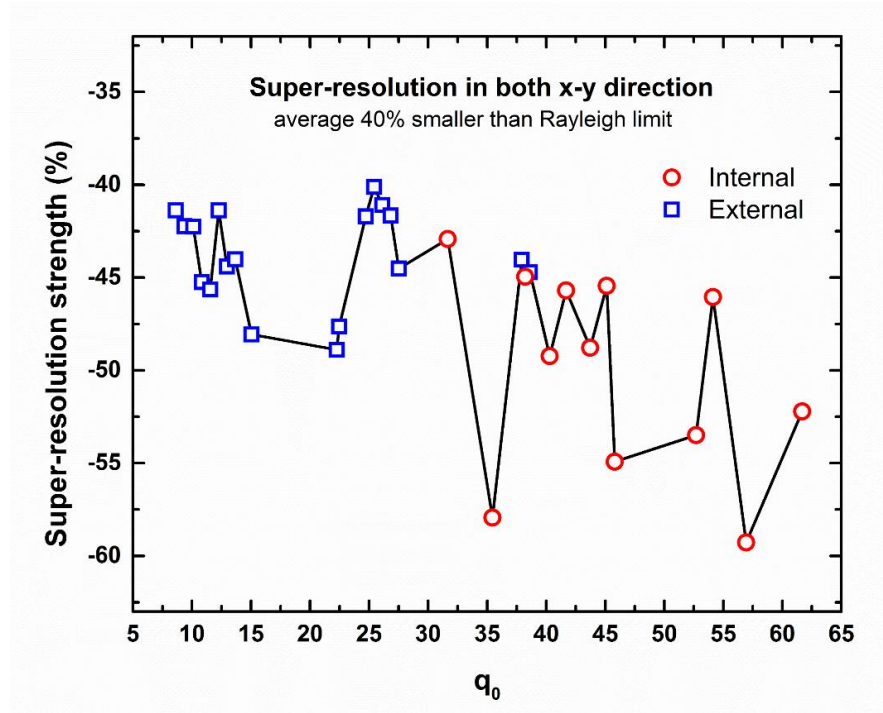


Figure 4.7 Super-resolution electric field intensity ($|E|^2$) spots within size parameter range $\pi \leq q_0 \leq 20\pi$ with refractive index $n_p=1.6$ and $n_m=1.0$. Blue squares indicate external focus and red circles indicate internal focus.

Within them, we have identified 30 ‘extreme’ super-resolution spots whose average spot size are at least 40% smaller than the diffraction limit, as shown in Figure 4.7 and tabulated in Table 4.1. In Figure 4.7, the blue squares indicate external focus and red circles indicate internal focus. The best super-resolution conditions of external and internal are seen for $q_0=22.26$ and $q_0=56.94$ respectively. Together with the results of $|E|^2$ field intensity distribution showing in Figure 4.8, a more comprehensive understanding of their focusing properties are provided. In the condition of best external resolution ($q_0=22.26$), the focus is located on the boundary ($z=1$) of shadow side, with an intensity enhancement of 239, as shown in Figure 4.8 (c). Its focal spot size in y-direction is 48.87% below the diffraction limit, corresponding to resolution of $0.312\lambda \approx \lambda/3.2$. Due to an elliptical shape nature of the focus, the resolution in x-direction is slightly bigger, almost equivalent to the diffraction limit. The averaged spot size for this case, calculated as $\sqrt{FWHM(x) \times FWHM(y)}$, is about $0.436\lambda \approx \lambda/2.3$. In the case of $q_0=56.94$, the maximum intensity is observed inside particle at $z=0.786$, with a huge enhancement factor of 2251, as indicated in Figure 4.8 (f). Its focal spot size in y-direction is 52.44% below the diffraction limit, corresponding to resolution of $0.181\lambda \approx$

$\lambda/5.5$. The resolution in x-direction is still below the diffraction limit by 14.38%. The averaged spot size for this case is about $0.243\lambda \approx \lambda/4.1$. Moreover, by looking at the 2D field distribution in XZ and YZ-plane [Figure 4.8 (a, b, d and e)], we found some interesting phenomena. In addition to the highest peak at bottom side of particle, a relatively weaker internal hotspot is generated near top boundary in XZ-plane in both cases, meanwhile, along with an annular focusing effect along inner boundary that are observed in YZ-plane.

Size parameter q_0	rx= [FWHM(x)/Rayleigh-1]*100%	ry= [FWHM(y)/Rayleigh-1]*100%	Super-resolution= [FWHM(x)*FWHM(y)/Rayleigh ² -1]*100%	Spot size in unit of λ
8.62	-2.7921%	-39.6951%	-41.3789%	0.467
9.36	-6.1752%	-38.4275%	-42.2297%	0.463
10.1	-7.1943%	-37.7780%	-42.2545%	0.463
10.82	-11.8764%	-37.8615%	-45.2413%	0.451
11.54	-13.2421%	-37.3416%	-45.6389%	0.450
12.26	-6.5490%	-37.2726%	-41.3807%	0.467
12.96	-10.6860%	-37.7509%	-44.4028%	0.455
13.66	-8.7146%	-38.6676%	-44.0125%	0.456
15.04	-15.1968%	-38.7533%	-48.0608%	0.439
<u>22.26</u>	<u>-0.0543%</u>	<u>-48.8650%</u>	<u>-48.8928%</u>	<u>0.436</u>
22.46	-20.2631%	-34.3343%	-47.6403%	0.441
24.72	-9.6586%	-35.4704%	-41.7030%	0.466
25.42	-9.7546%	-33.6431%	-40.1160%	0.472
26.12	-9.9969%	-34.5432%	-41.0868%	0.468
26.82	-13.1858%	-32.7890%	-41.6513%	0.466
27.52	-19.5406%	-31.0348%	-44.5110%	0.454
31.66	-36.5279%	-10.0812%	-42.9267%	0.288
35.44	-11.1872%	-52.6332%	-57.9322%	0.247
37.92	-16.8508%	-32.6887%	-44.0312%	0.456
38.22	-4.2205%	-42.5323%	-44.9578%	0.283
38.62	-19.3484%	-31.4462%	-44.7103%	0.453
40.3	-5.7408%	-46.1376%	-49.2298%	0.272
41.68	-2.5131%	-44.2932%	-45.6932%	0.281
43.72	-12.3500%	-41.5667%	-48.7832%	0.273
45.12	-9.5433%	-39.6955%	-45.4506%	0.281
45.8	-15.8317%	-46.4383%	-54.9181%	0.256
52.7	-11.9557%	-47.1734%	-53.4892%	0.260
54.12	-0.5417%	-45.7500%	-46.0439%	0.280
<u>56.94</u>	<u>-14.3849%</u>	<u>-52.4360%</u>	<u>-59.2781%</u>	<u>0.243</u>
61.68	-7.2578%	-48.4766%	-52.2160%	0.263

Table 4.1 'Extreme' super-resolution foci for $n=1.6$ microsphere.

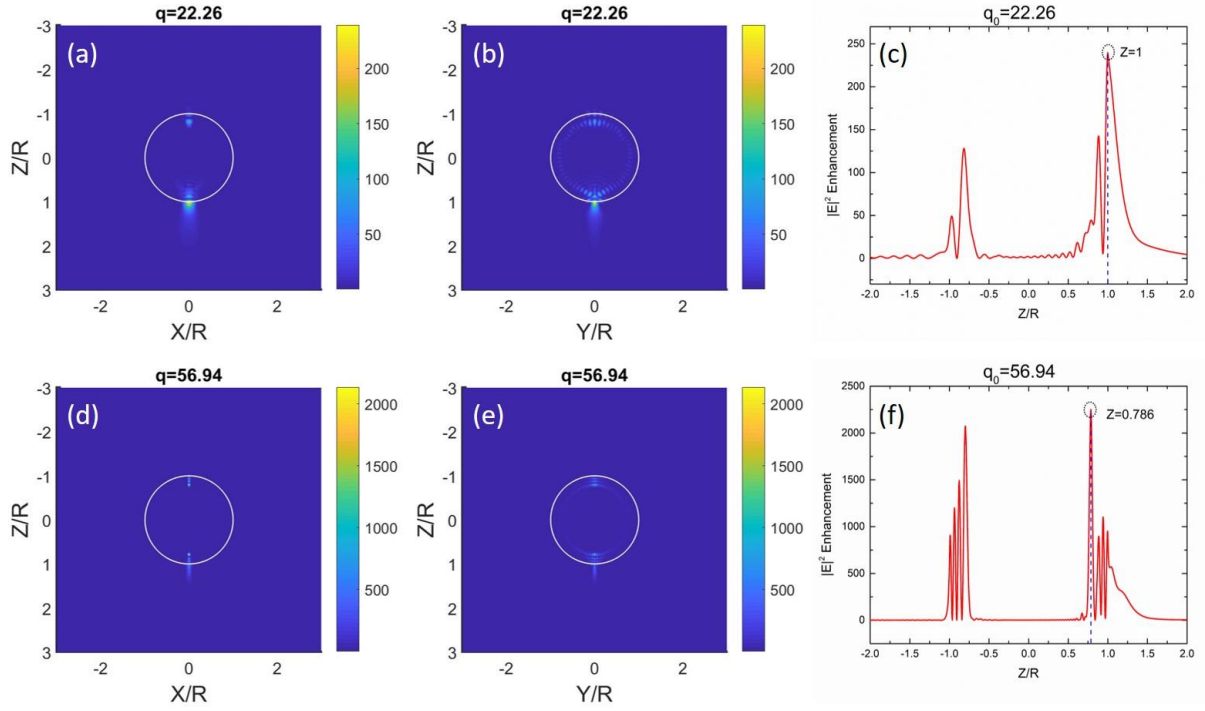


Figure 4.8 The $|E|^2$ intensity distribution of best super-resolution of external, $q_0=22.26$, and internal, $q_0=56.94$, respectively. (a) and (b) are field distribution of $q_0=22.26$ in XZ and YZ-plane. (c) indicates that the focus is located on the boundary of particle ($z=1$). (d) and (e) are field distribution of $q_0=56.94$ in XZ and YZ-plane. (f) indicates that the highest peak is generated inside particle (at $z=0.786$).

Once the super-resolution conditions were identified, it is natural to consider its scalability in different environments. For example, if the particle size was fixed, how the other Mie theory input parameters, such as light wavelength, should be scaled such that the final super-resolution foci remains unchanged. Such consideration is particularly important for experimental design and parameters selection for super-resolution applications. Here, we provided an example to illustrate that how the best external focus can be obtained in practical situation. A microsphere with $n_p=1.6$ and $5\ \mu\text{m}$ diameter in air was selected. Figure 4.9 shows the simulation results of external focal spot size within wavelength range from 250 nm to 2200 nm. As can be seen from the figure, the FWHM in both x- and y-direction have a rising trend with wavelength increasing. FWHM along y-direction are always below diffraction limit, while most FWHM along x-direction are higher than diffraction limit. As the wavelength increasing, the deviation between x and y-direction become more obvious, which means more elliptical shape focus spot in transverse. This phenomenon is same as previously seen in Figure 4.3. The best super-resolution of the given microsphere condition was achieved by

a 705.7 nm incident wavelength, in which $q_0=22.26$. In this case, the FWHM is 430 nm in x-direction and 220 nm in y-direction, while the Rayleigh diffraction is 430.5 nm.

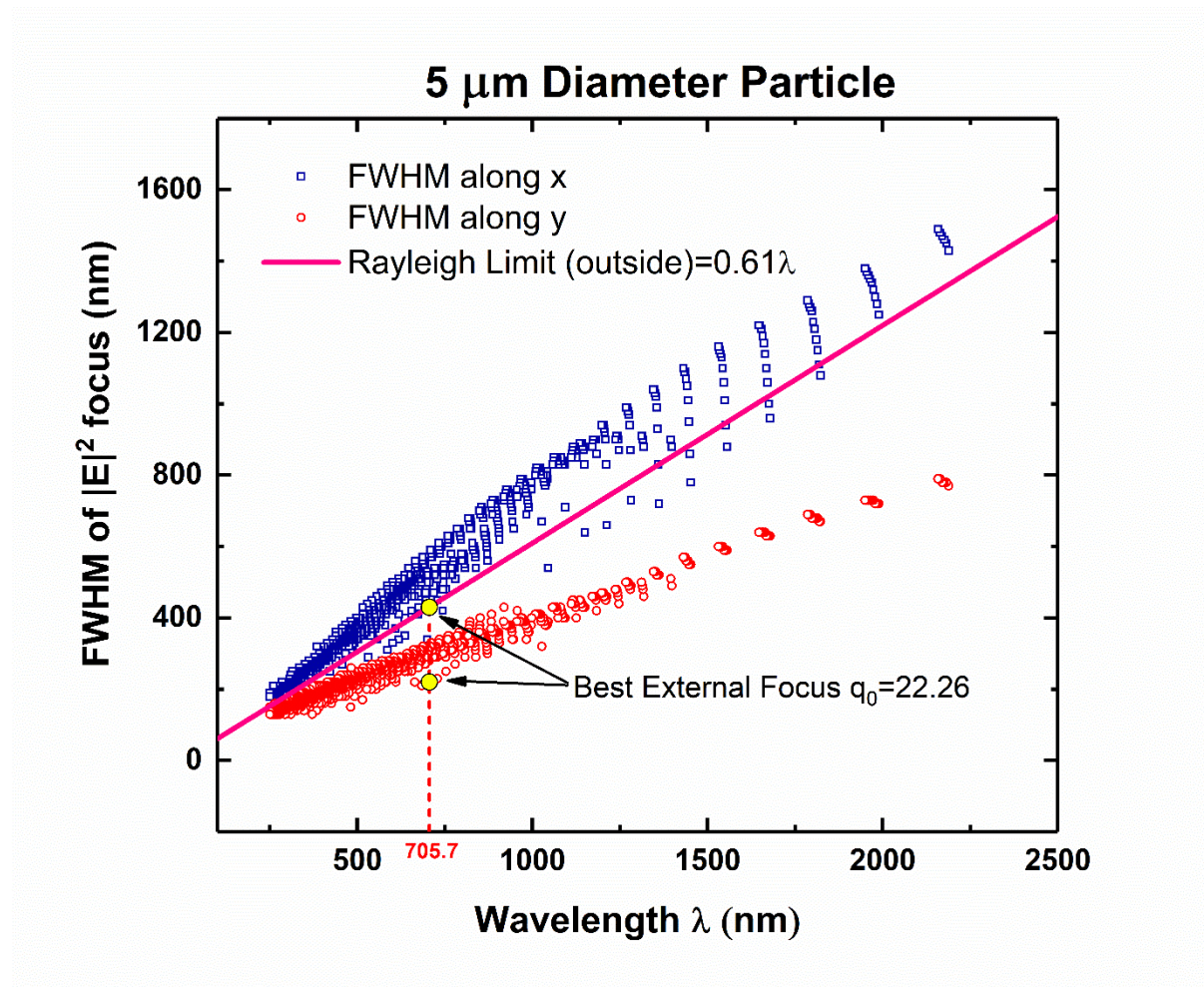


Figure 4.9 An example of external resolution obtained by a 5 μm diameter $n_p=1.6$ microsphere. The best external super-resolution was achieved by a 705.7 nm incident wavelength, which $q_0=22.26$.

4.3 Full-wave white-light spectral analysis of microsphere focusing characteristics

Previous works based on small particles focusing properties. They provide detailed descriptions of super-resolution, field enhancement and focal length in circumstance of single incident wavelength. However, realistic situation often occupies wide range of electromagnetic waves which work simultaneously in many practical applications such as optical imaging, and analysis of single wavelength is incapable of explaining practical complication. The microsphere nanoscopy can work under visible light whose wavelength is

range of 390 nm to 700 nm. Therefore, a comprehensive consideration with respect of full-wave investigation of particle focusing is necessary.

In this section, three different incident light sources which are monochromatic (600 nm), uniform polychromatic (intensity=1) and Quartz Tungsten-Halogen lamp (THORLABS, QTH10) (Figure 4.10) were employed in the simulation. Here, the electric field of 5 μm microsphere ($n_p=1.6$, $n_m=1$) was investigated by calculation of integral intensity in a wide wavelength range from 390 nm to 700 nm (visible band), and regarding results of optical focusing properties of each case were generated and comparison between three cases were made.

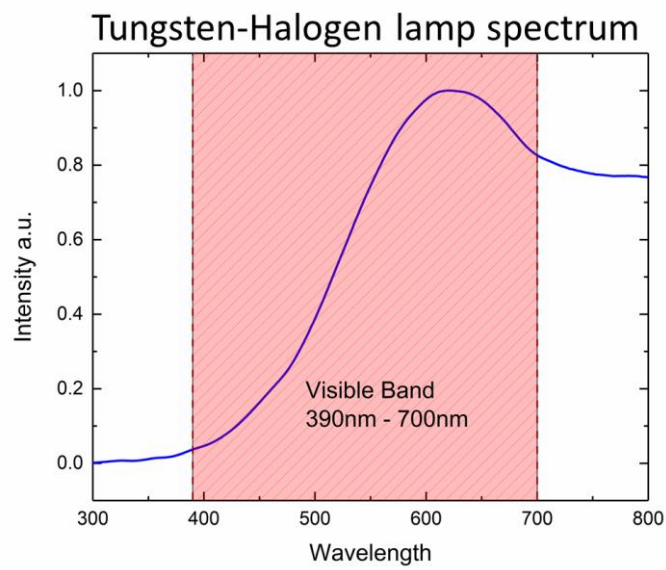


Figure 4.10 Spectrum of Tungsten-Halogen lamp (THORLABS, QTH10).

The electric field intensity $|E|^2$ of each radiation wavelength was simulated individually by DSIMie software. Then final integration plotting results were calculated using Matlab program. In order to easily compare field distribution among various incident cases, the field intensity was calculated as,

$$|E|^2 = \int_{\lambda_1}^{\lambda_2} E(\lambda)S(\lambda)d\lambda / \int_{\lambda_1}^{\lambda_2} S(\lambda)d\lambda \quad 4.2$$

where the $E(\lambda)$ is the enhancement factor of the microsphere at various wavelength and the $S(\lambda)$ is a curve to characterise the change of incident source intensity at various wavelength,

for example Figure 4.10. Figure 4.11 illustrates the normalized electric field enhancements along propagating axis. Each curve exhibits similarity of two main peaks locating at top and bottom boundaries of microsphere, but with slight differences in position and value. The monochromatic 600nm wavelength generates top side focus with weaker enhancement (about 20) and more internal position than Tungsten-Halogen and uniform incidents results who have about 70 and 50 enhancements respectively. At shadow side, all cases present large field enhancement of approximate 160 to 190 times. It is noted that an observable dip occurs at inner boundary, resulting two peaks at inside and outside. The insert shows the zoom-in curve profiles. The single wavelength and uniform-intensity polychromatic light source produce higher focus intensity at external. In contrast, larger internal peak is induced by the Tungsten-Halogen light.

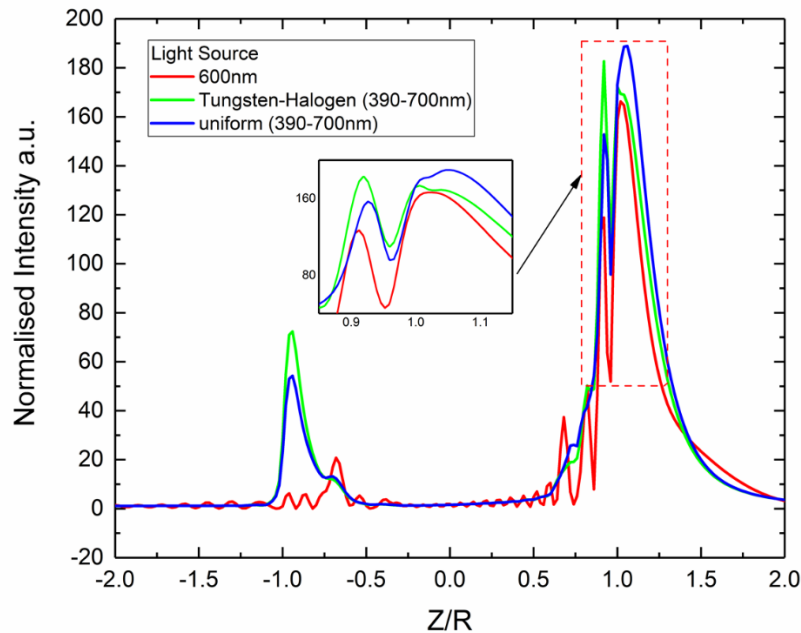


Figure 4.11 Normalised field intensity of 5 μm microsphere under three incident sources along propagational direction z-axis. The insert is zoom-in of peak area.

Figure 4.12 shows the calculated electric field distributions of 5 μm microsphere in XZ and YZ-plane. It can be clearly identified that a noticeable hot spot at top of microsphere is brighter under wide-band illumination than 600 nm single wavelength result. This could be explained by the special optical resonance phenomena discussed in section 3.3 (Figure 4.1 and Figure 4.2), as contribution of a giant enhancement at top boundary by particular wavelength. In addition, three simulation results reveal the same appearance that bottom hot spots exhibit

narrower waists in YZ-plane. Furthermore, in wide-band simulation results (Figure 4.12 c-f), bottom focuses are always slenderer than monochromatic 600 nm incident (Figure 4.12 a and b). Detail information from Figure 4.11 and Figure 4.12 were summarised in Table 4.2.

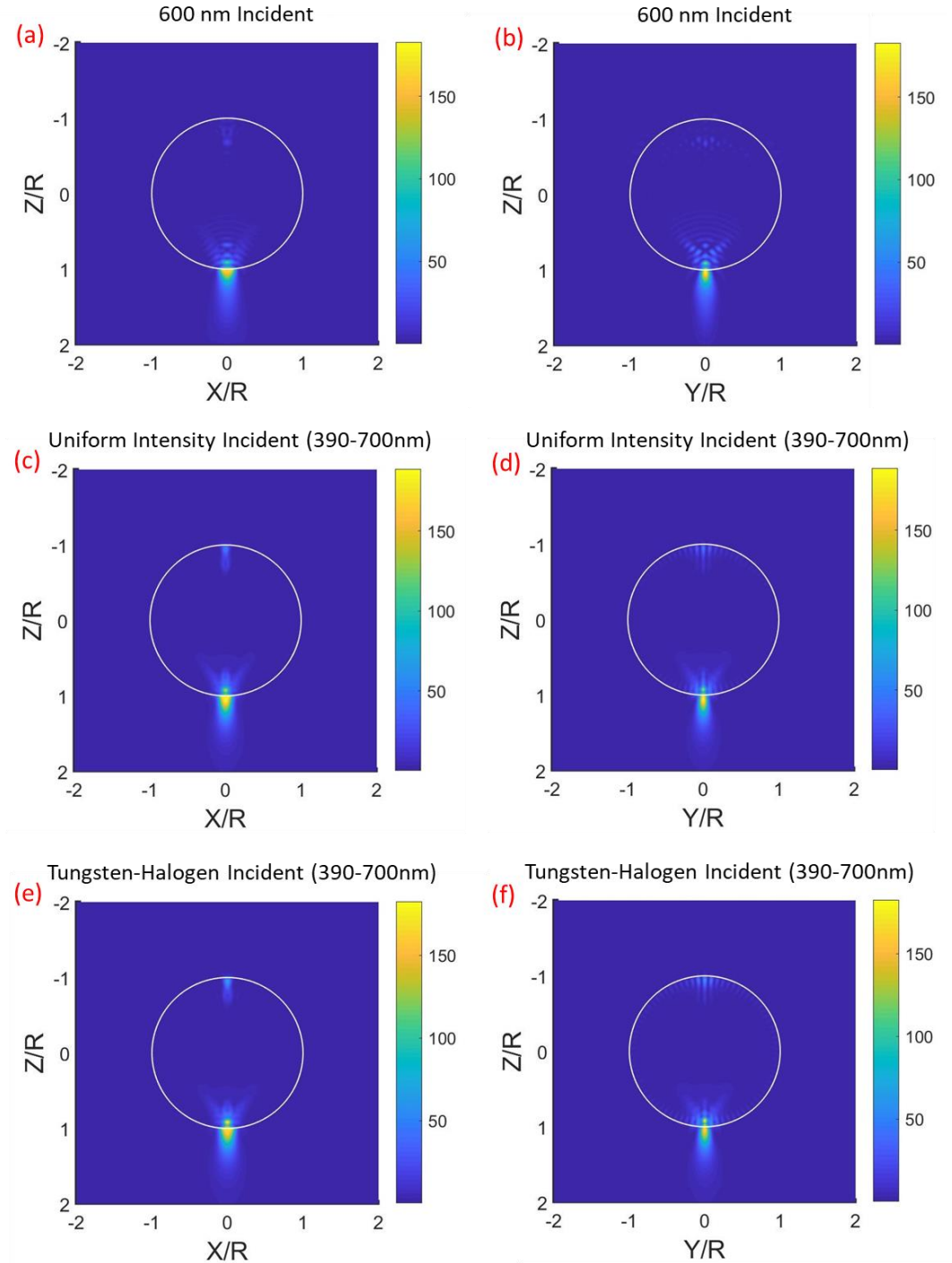


Figure 4.12 Electric field $|E|^2$ distributions of 5 μm microsphere ($n_p=1.6$, $n_m=1$) in (a, c and e) XZ-plane and (b, d and f) YZ-plane by (a, b) monochromatic 600 nm incident, (c, d) uniform intensity incident (390-700 nm) and (e, f) Tungsten-Halogen lamp (390-700 nm).

Incident wave	Focus position (normalised with respect to radius)	xFWHM	yFWHM
600nm	1.0256	492nm	252nm
390-700nm (uniform intensity=1)	1.0512	392nm	236nm
390-700nm (Tungsten- Halogen lamp)	0.9192	240nm	156nm

Table 4.2 Summarised result from Figure 3.11 and Figure 3.12.

4.4 Conclusions

Super-resolution and near-field scaling of a dielectric particle focusing were systematically investigated. It was shown that optical resonances inside microspheres would lead to highly oscillating features of the field focus enhancement and focus position as particle size changes. The super-resolution was observed for particular sets of size parameters and often manifests an elliptical focus shape. Extreme sharp super-resolution foci with resolution of $\lambda/5.5$ has been seen for an $n=1.6$ particle in air. In addition, microsphere focusing under a full-wave visible spectrum condition was simulated. It describes focusing properties closer to reality and may contribute to further understanding of practical application of microsphere super-resolution imaging.

Chapter 5. Design and Optimisation of Engineered Micro-Lens for Enhanced Optical Super-resolution

5.1 Introduction

It has been proven that spherical particle with a size of a few wavelength presents extraordinary capabilities of confining an incident beam to a sub-diffraction focal spot. The appearance of photonic nanojet is one of the most important characteristic. The presence of the photonic nanojet reflects the particle's converging ability such as spatial-resolution and focusing position. The ability to precisely control of the focusing properties is highly desired for microsphere-based technologies. Previous chapter has theoretically discussed that the best focusing of spherical particle can be obtained via controlling particle size, its refractive index with respect to surrounding medium and incident wavelength. literature has also demonstrated theoretical and experimental methods of modulating optical properties of photonic nanojet[36], [55], [90], [113], [119], [120], including changing surrounding material (liquid submerged), varying the illumination condition (wavelength, polarisation and beam shape) and geometric shape (core-shell or hollow structure). However, these conditions could be difficult to meet in reality, since desired microspheres may not be commercially available. It is therefore highly desirable to develop a new technique that can control the near-field focusing of a microsphere lens in a flexible and easy-to-implement way.

In this chapter, we propose several designs to achieve controllability of focusing properties. Binary phase mask is a technique commonly used to enhance resolution in conventional lens system[92]. Meanwhile, solid immersion mechanism also helps resolution improvement. We integrated separately and combine both concepts into our new microsphere superlens designs, which are schematically illustrated in the following sections. In addition, a new concept of using nanoparticle as building block to construct a superlens was proposed for the first time. With near-field evanescent waves interacting with close-packed nanoparticles, a conversion of evanescent wave to propagation wave occurs, resulting sub-diffraction limit

information being discerned. It shall be noted we are dealing with near-field problems here, in which the focus is located very close to particle surface and evanescent wave components could be involved. This demands a full wave numerical simulation to include both propagating and evanescent wave modes. A commercial FIT software package (CST MICROWAVE STUDIO) was used. For better accuracy on simulation results, we have chosen to use triangular meshing grids thus a FEM-like method in simulation, which are naturally conformal to the circular boundary of a sphere. Detail simulation condition can be found in **Chapter 3.2.2**.

The chapter is organized as follows; Section 2 presents a design of pupil mask assisted microsphere; Section 3 presents a composite material microsphere which consists of a higher refractive index material in bottom part and lower refractive index material in upper part; Section 4 presents a design with combination of pupil mask and composite material microsphere; Section 5 present a nanoparticle derived superlens. Simulation results are shown and discussed detail in each section; Section 6 will conclude this chapter work.

5.2 Pupil mask assisted microsphere lens

Paeder et al. studied the effect of annular amplitude and phase masks on far-field microlenses[121]. Sufficient literature with similarities can be found in this regard, with applications in photolithography [122], data storage and confocal scanning microscopy [123], [124] etc. In contrast to this, previous researches on pupil mask assisted optical super-resolution were often focusing on far-field problems where no evanescent waves will be involved, and simplified formulations can be used. In this section, a circular pupil mask made of perfect electric conducting (PEC) material is located above the microsphere for blocking light ray traveling at the centre. It proves the modulation ability of its focusing properties.

Figure 5.1 shows the schematics and corresponding electric intensity field distribution for (a, b) no-mask and (c, d) with mask case. The particle diameter was 3 μm in both cases. The pupil mask is a circular disk positioned right on top of the particle, with diameter 2 μm . Apart from particle and mask size parameters, other parameters were kept fixed in this research: refractive index of microsphere =1.46 (SiO_2); background medium refractive index = 1 (air); incident wavelength = 600 nm, x-polarised, propagates along z-axis; pupil mask material = PEC (perfect electric conductor) which provides 100% blocking of incident light. It shall be noted

that the optical resolution (Full Width of Half Maximum - FWHM value of minimum spot size) were measured using electric intensity field distributions ($|E|^2$) in YZ cross-sectional planes. This is because near-field focusing of microsphere lenses is generally elongated along incident polarisation direction (x-axis) and minimum spot size (i.e. best resolution) is found on the Y-direction. Unlike far-field lenses, near-field microsphere lens could generate internal focus inside the microsphere as well. Here we skipped analysis of such internal focuses but chose to use the exterior highest intensity position as resolution measurement position. This is because all existing demonstrated microsphere super-resolution applications are relying on the fields outside of microspheres. However, we believe new applications based on internal focusing fields will be developed in the future. An example of comparison between Figure 5.1(b) and (d) clearly illustrates that with mask the focus spot become smaller in both y and z directions. This means an improved lateral and axial resolution have been simultaneously achieved by the mask. This is an important finding of present study.

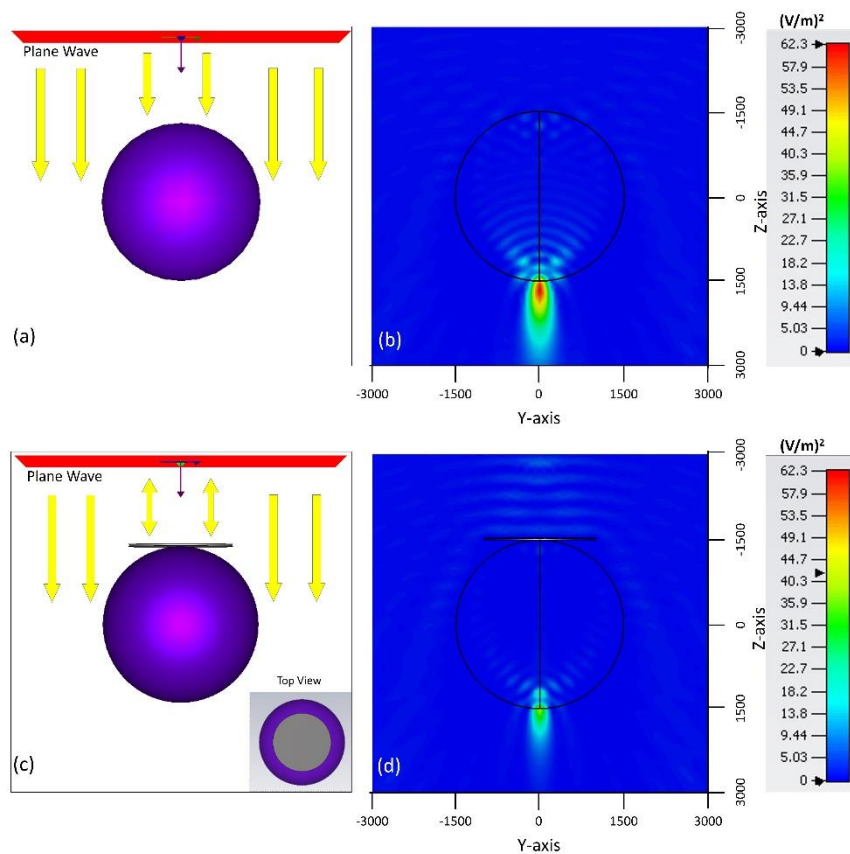


Figure 5.1 Schematic diagrams and $|E|^2$ intensity field distributions for two microsphere systems. (a, b) single microsphere, (c, d) proposed microsphere with pupil mask system. Parameters: wavelength 600nm, microsphere diameter 3 μm , and (c) with mask diameter 2 μm , refractive index (RI) of microsphere is 1.46 and mask material PEC).

Figure 5.2(a) shows 1D intensity field profiles along z axis for a 3 μm microsphere coupled with pupil masks, whose diameter varies from zero (no mask) to 3 μm (same as particle diameter). There are two intensity peaks, one inside and the other outside of particle. The external peak dominates over the internal peak when the mask size is smaller than particle size. It is interesting to note that, when mask size equals to particle size, the light is not fully blocked but still got a weak focusing due to light bending effects occurring in micro domains [125] which cannot be understood using ray optics. A clear tendency in the figure is that the external peak amplitude decreases quickly with mask size and meanwhile, its focus position moves closer to the particle, leading to a shortened focal length. The internal peak, however, has shown much less influenced by the mask; its amplitudes drops much slowly, and its location remains almost unchanged. It should be noted that with the mask area increasing, the enhancement effect is dropping. However, in the case of 3 μm mask, the contrast between peak and non-focus area can be obviously distinguished. In the reality, the intensity can be strengthened by applying higher intensity light source. Figure 5.2(b) plots the corresponding intensity profile along the y-axis across external focus position. The resolution is measured using the full-width at half-maximum (FWHM) value of each profile curve in the plot.

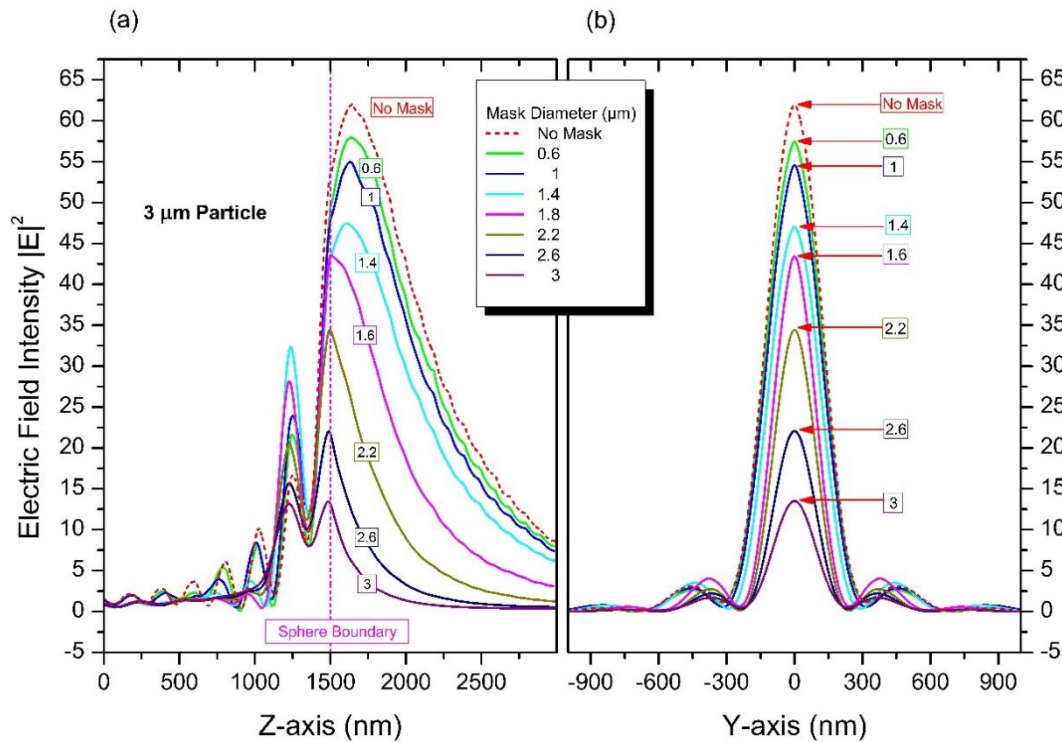


Figure 5.2 (a) $|E|^2$ intensity field distribution along propagation axis z across 3 μm -diameter microsphere centre, with varying pupil mask diameter from 0 to 3 μm (b) corresponding exterior focus field profile along Y-axis which measures focusing resolution.

For the ease of comparison, we retrieved focal length and resolution data for the 3 μm particle from Figure 5.2 and graphed them in Fig.3 as a function of MAP (Masked Area Percentage of particle cross-section), which is defined as:

$$MAP = \frac{\pi \times r^2}{\pi \times R^2} \times 100\% \quad 5.1$$

where r is mask radius and R is particle radius. A higher MAP value means a larger sized mask. As shown in Figure 5.3, at zero MAP (no mask), the focal length is about 1635 nm for the 3 μm microsphere. The focus is outside of sphere since it is larger than the particle radius of 1500 nm. Between 0 and 25% MAP, the focal length decreases slowly with small oscillations, but remains greater than the particle radius. Between 25% MAP and 35% MAP, however, the focal length decreases significantly faster, dropping from about 1600 nm to about 1500 nm. When MAP is above 35%, the focus position is relatively steady which remains close to the particle bottom surface, moving from outside to inside of the particle with less than 25 nm variations. At 100% MAP, the main focus is located inside the particle, about 15 nm away from the boundary. These results confirm the flexibility of using pupil mask to precisely control the focus position in optical near-fields, movable from outside particle zone to internal particle zone.

Figure 5.3(b) shows corresponding resolution curve measured as a function of MAP at focus positions outside of particle. Note, this curve is sitting below the classical diffraction limit curves ($\lambda/2$ as shown in the figure) which means it produces a sub-diffraction optical focus to enhance the resolution. The resolution curve evolves in a way similar to the focal length curve in Figure 5.3(a). At zero MAP (no mask), the focus FWHM size is about 274.56 nm ($=\lambda/2.19$). For MAP smaller than about 12%, the resolution shows small oscillations but keep approximately at same size as no mask case. As MAP increases over 12%, the focus spot size drops quickly, reaching a minimum of 208.93 nm ($=\lambda/2.87$) at 44% MAP. This is the best resolution we can achieve for the discussed system, which is 76% smaller than the resolution for the reference case (no-mask). At higher MAP, the resolution is slightly lower and is oscillating around 220 nm ($=\lambda/2.73$). The small oscillations in both curves are not caused by numerical accuracy in simulation, but by multi-orders Mie resonances nature in the micro-

sized particles; such oscillations are expected to be reduced in larger sized particles[83]. Due to limitation of computing resources, we won't be able to investigate such problem at present but will look into it in the future when resources become available.

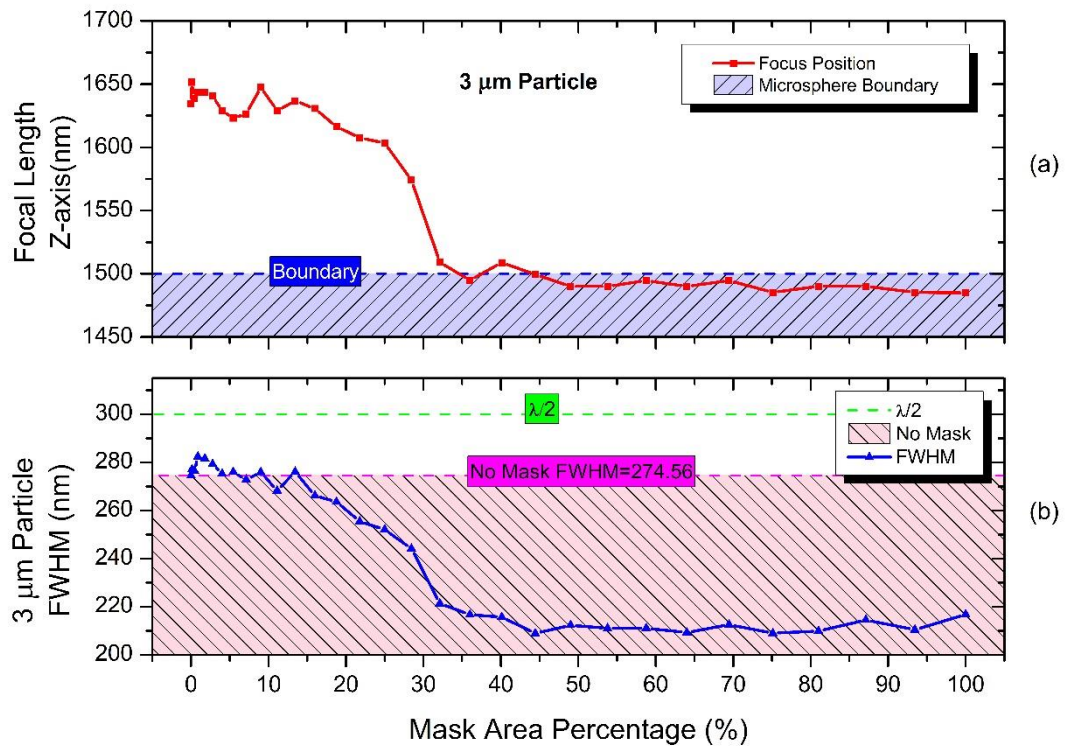


Figure 5.3 Corresponding (a) focal length and (b) focus resolution (FWHM of focus spot) at external peak location as a function of mask area size, derived from Figure 5.3 for 3 μm-diameter microspore lens coupled with varying size pupil masks.

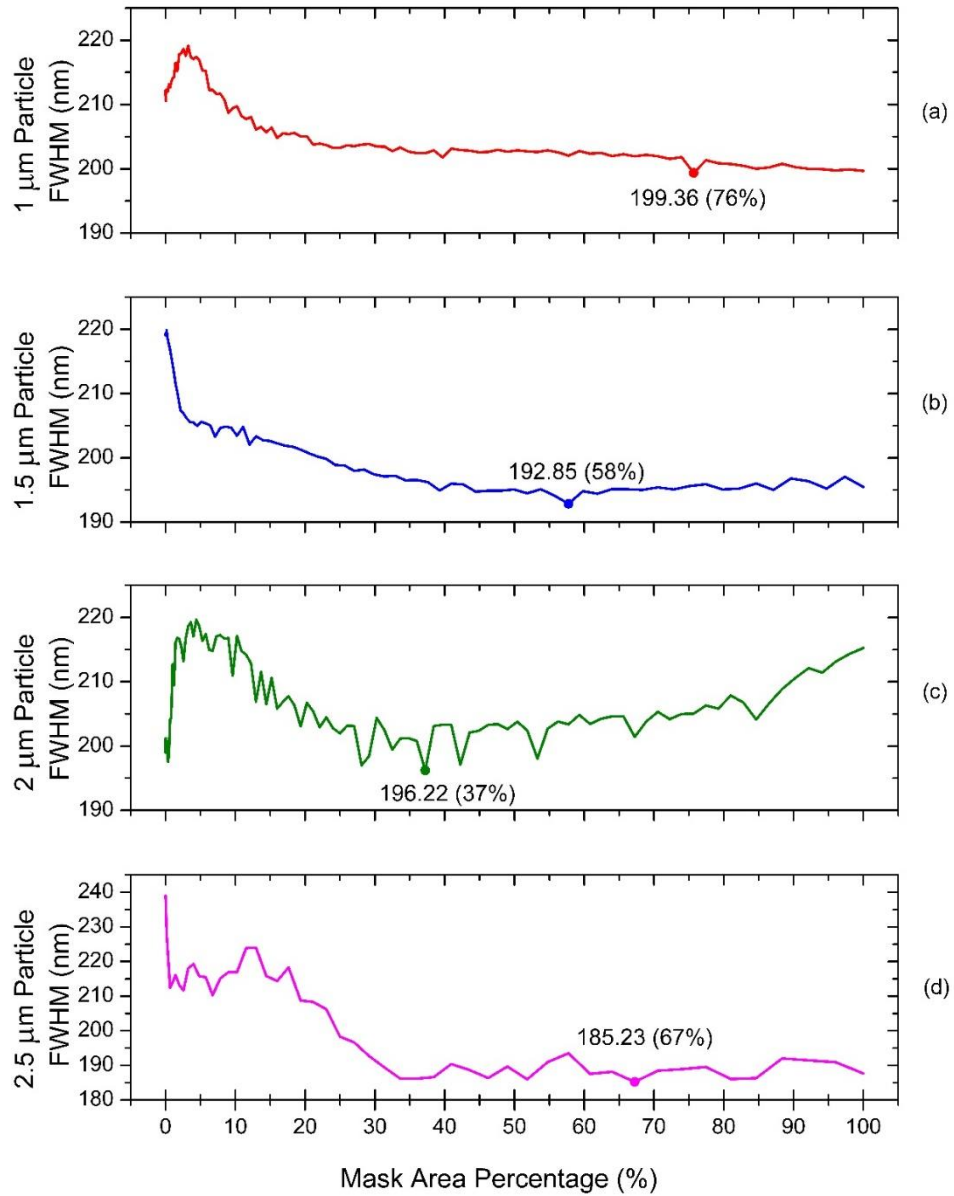


Figure 5.4 Focusing resolution as a function of mask area percentage (MAP) for smaller diameter microsphere lenses: (a) 1.0 μm , (b) 1.5 μm , (c) 2.0 μm and (d) 2.5 μm .

For smaller diameter microspheres, the pupil mask can produce similar super-resolution enhancement effect. Figure 5.4 shows calculated resolution curve as a function of MAP for microsphere lenses with diameter (a) 1.0 μm , (b) 1.5 μm , (c) 2.0 μm and (d) 2.5 μm . Due to Mie-type resonances occurring in wavelength-scale microspheres, the resolution curves are in different evolution profiles. However, a general tendency can be drawn for most particles; as mask size increases, the resolution tends to increase. This happens for particle sizes 1.0, 1.5 and 2.5 μm . However, the 2.0 μm particle seems slightly different, possibly due to the

excitation of internal modes. Nevertheless, all studied particles have shown improved resolutions when the pupil mask was used. The corresponding optimized resolution data was retrieved from Figure 5.3 and Figure 5.4 and results were summarized in Table 5.1. As it can be seen, the best optimized resolution is 199.36 nm ($=\lambda/3$) for 1 μm particle, 192.85 nm ($=\lambda/3.11$) for 1.5 μm particle, 196.22 nm ($=\lambda/3.05$) for 2 μm particle and 185.23 nm ($=\lambda/3.24$) for 2.5 μm particle and 208.93 ($=\lambda/2.87$) for 3 μm particle, respectively. These optimized resolutions are well beyond the classical $\lambda/2$ diffraction limit and most of them have even exceeded the solid immersion resolution limit of $\lambda/2n = \lambda/2.97$ ($n=1.46$). The enhanced super-resolution gained through pupil mask is quite significant and we believe such effect will play a big role in advancing all microsphere-based super-resolution techniques. In reality, the proposed pupil mask could be realised by projecting a millimetre scale mask through demagnification effect, illustrated as Figure 5.5, which is commonly used in photolithography[126].

Microsphere Diameter	FWHM (nm)	Smaller than pure sphere (no mask)	MAP	Resolution in term of λ
1 μm	199.36	94%	76%	$\lambda/3$
1.5 μm	192.85	88%	58%	$\lambda/3.11$
2 μm	196.22	99%	37%	$\lambda/3.05$
2.5 μm	185.23	77%	67%	$\lambda/3.24$
3 μm	208.93	76%	44%	$\lambda/2.87$

Table 5.1 Summarised results from Figure 5.3 and Figure 5.4.

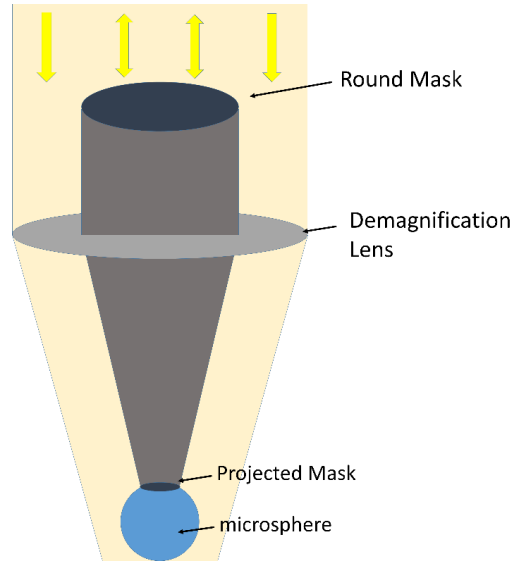


Figure 5.5 Concept of realising the pupil mask by projecting a millimetre scale mask through demagnification effect.

5.3 Composite material microsphere lens

Solid immersion lens (SIL) is a simple but useful tool to yield higher magnification and spatial resolution by increasing surrounding medium refractive index, thus achieving higher numerical aperture (NA). Owing to its advantages, this technique has adopted across a diverse range of applications, including semiconductor integrated-circuit inspection[127]–[130], optical data storage [131]–[134] and photolithography[135], [136]. However, it still remains a great challenge to resolve structures below 130 nm due to the shortage of high refractive index material that is transparent to visible light or the nanoscale separation between the surfaces of the SILs and the investigated substrates.

In this section, the concept of solid immersion mechanism was considered and integrated onto microsphere lens. As can see in Figure 5.6(c), the sphere was cut into two parts, which consist of a high-index material in lower part and lower-index material in upper part (fixed at $n_{p1}=1.46$). The high-index material allows new lens accessing contribution from solid immersion mechanism. in the calculation, the refractive index of bottom material n_{p2} was set from 1.76 to 2.66, with a linear increasing of 0.1 each step. The cutting height of bottom part was varied from 10 nm to 200 nm with 10 nm step and this interval was minimised to 1 nm in

the range in order to investigate where optimized super-resolution occurs. Other simulation conditions were kept the same as previous section.

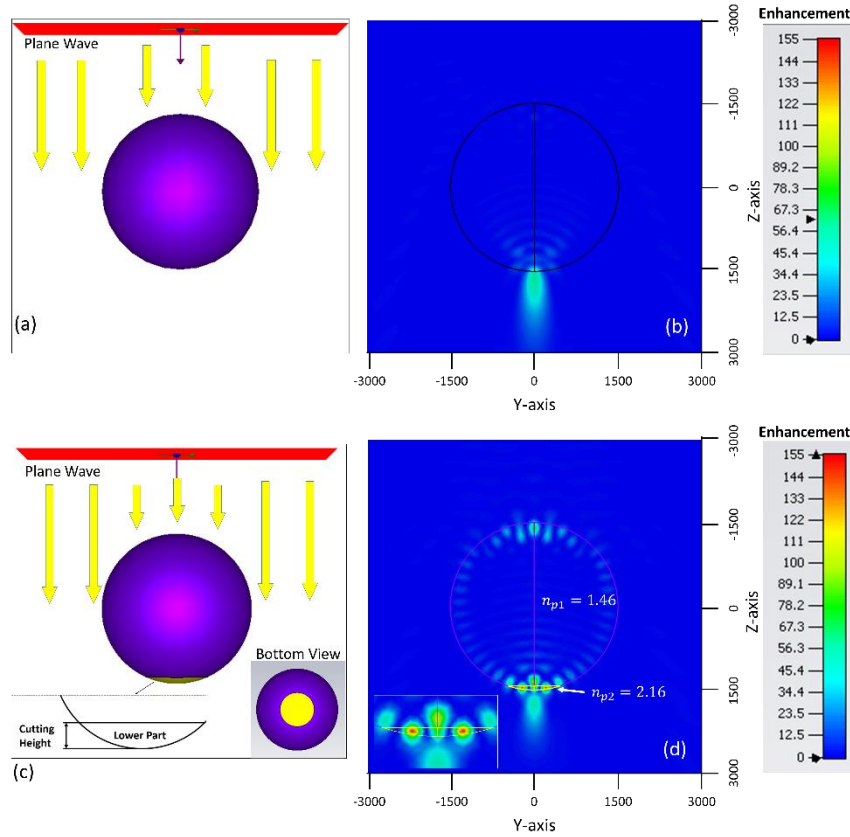


Figure 5.6 Schematic diagrams and $|E|^2$ intensity field distributions for two microsphere systems. (a, b) single microsphere, (c, d) proposed composite material microsphere. Parameters: wavelength 600nm, microsphere diameter 3 μm , and (c) lower part cutting height 75 nm, refractive index (RI) of microsphere is 1.46 and bottom material is 2.16.

Figure 5.6(a, b) show ordinary microsphere with RI=1.46 and Figure 5.6(c, d) are composite microsphere with lower part being replaced by higher-index $n_{p2}=2.16$ and the cutting height is 75 nm. By comparing field distribution of Figure 5.6 (b) and (d), composite microsphere has more converged focus than ordinary microsphere which perform similar function as pupil mask design, and moreover, $|E|^2$ intensity does not drop. Besides, it is noted that multiple localised hot spots are in an annular arrangement across spherical boundary and two highest enhancement appear in both sides of internal high-index material. One possible explanation is the excitation of optical super-oscillation effects, causing by wave interferences at two-material interfaces.

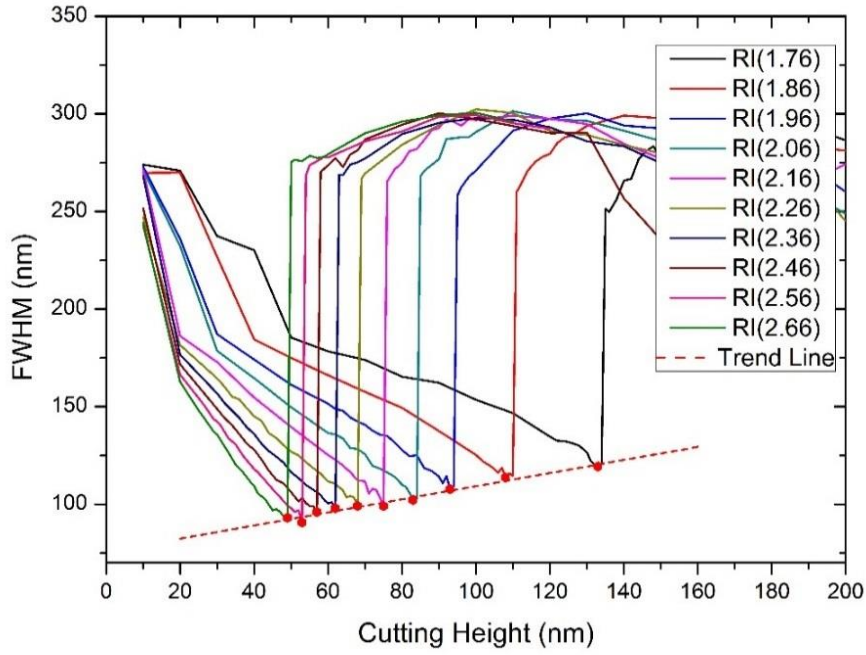


Figure 5.7 Focus resolution FWHM along y-direction at external peak location as a function of cutting height for refractive index $1.76 \leq n_{p2} \leq 2.66$.

Figure 5.7 depicts the external focus FWHM along Y-direction with varies cutting heights and RI (n_{p2}). There is an interesting finding, the focusing sizes follow a similar tendency which declines with cutting height increasing and reaches around 100nm, afterwards climbs dramatically to approximately 300nm within few nanometer heights increasing. In the contrast, obvious difference between these curves is that higher RI leads faster obtain minimum FWHM value, while lower RI need larger volume to reach optimized FWHM. The optimized resolution can be achieved at $\lambda / 6.62$ when bottom RI is 2.56 with 53 nm height. With comparing the best focal size in all parameter sets, although lower RI case generate slight bigger focus, it still reaches $\lambda / 5.03$ which is far smaller than diffraction limit $\lambda / 2$. Meanwhile, it seems that optimized resolutions of different RI conditions can be achieved by some crucial heights of lower part. Table 5.2 summarised the optimized FWHM achieved by critical cutting heights for index range of $1.76 \leq n_{p2} \leq 2.66$.

n_{p2}	Critical Cutting Height (nm)	External focus position (nm)	FWHM (nm)	Resolution in λ
1.76	133	1500	119	$\lambda / 5.03$
1.86	108	1500	114	$\lambda / 5.28$
1.96	93	1500	108	$\lambda / 5.57$
2.06	83	1500	102	$\lambda / 5.87$
2.16	75	1500	99	$\lambda / 6.06$
2.26	68	1500	99	$\lambda / 6.06$
2.36	62	1500	98	$\lambda / 6.13$
2.46	57	1500	96	$\lambda / 6.25$
2.56	53	1500	91	$\lambda / 6.62$
2.66	49	1500	93	$\lambda / 6.45$

Table 5.2 Optimized FWHM with crucial cutting height for $1.76 \leq n_{p2} \leq 2.66$.

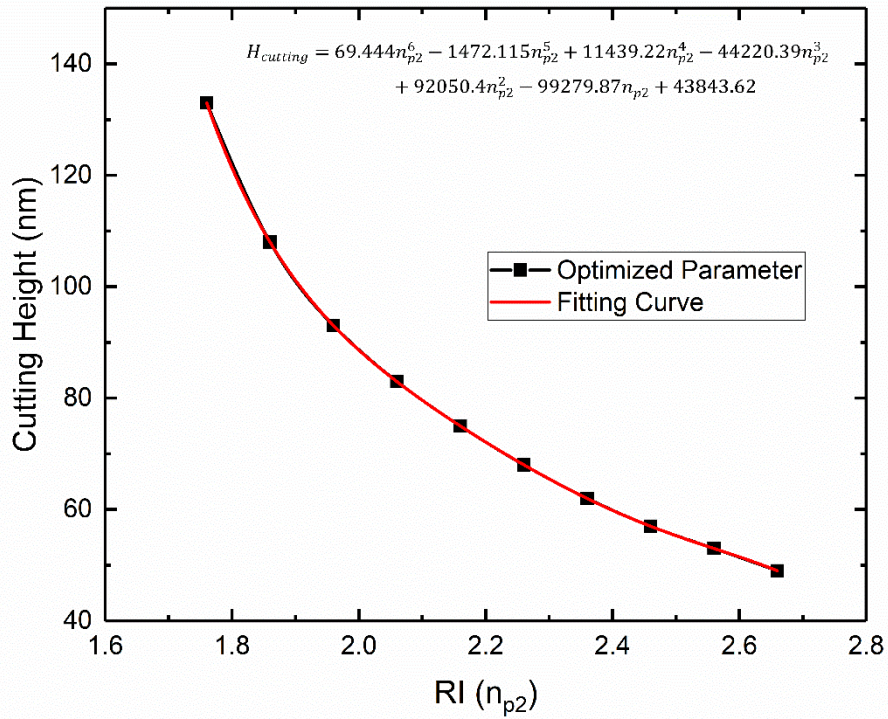


Figure 5.8 Cutting height vs. RI (n_{p2}) to achieve best super-resolution.

This data can be considered as a scaling factor for achieving optimized super-resolution in variable working conditions. In the range of $1.76 \leq n_{p2} \leq 2.66$, the tendency of optimized cutting height can be written as function of n_{p2} in equation 4.1.

$$H_{cutting} = 2.158 \times 10^7 \times \exp(-7.638 \cdot n_{p2}) + 429.8 \times \exp(-0.8194 \cdot n_{p2}) \quad 4.1$$

Therefore, we can calculate best cutting height of a defined lower part refractive index n_{p2} . For example, if the bottom part refractive index is 2, the corresponding cutting height is calculated to be 89 nm for obtaining the best super-resolution in such condition. The simulation result (Figure 5.9) demonstrates that the resolution along y-direction at external peak location for the $n_{p2} = 2$. This curve still follows the similar trend of curves in Figure 5.7. The minimum value is 103 nm at the condition of 90 nm height which roughly complies with our prediction. This consideration is particular important for experimental design and parameter selection of super-resolution applications.

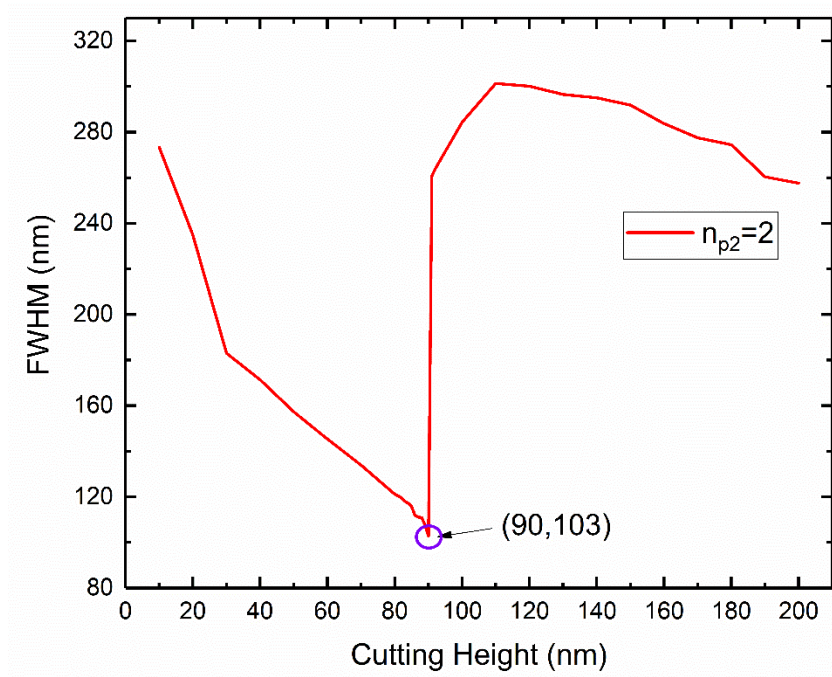


Figure 5.9 Focus resolution FWHM along y-direction at external peak location as a function of cutting height for refractive index $n_{p2} = 2$. The minimum value is 103 nm at cutting height of 90 nm.

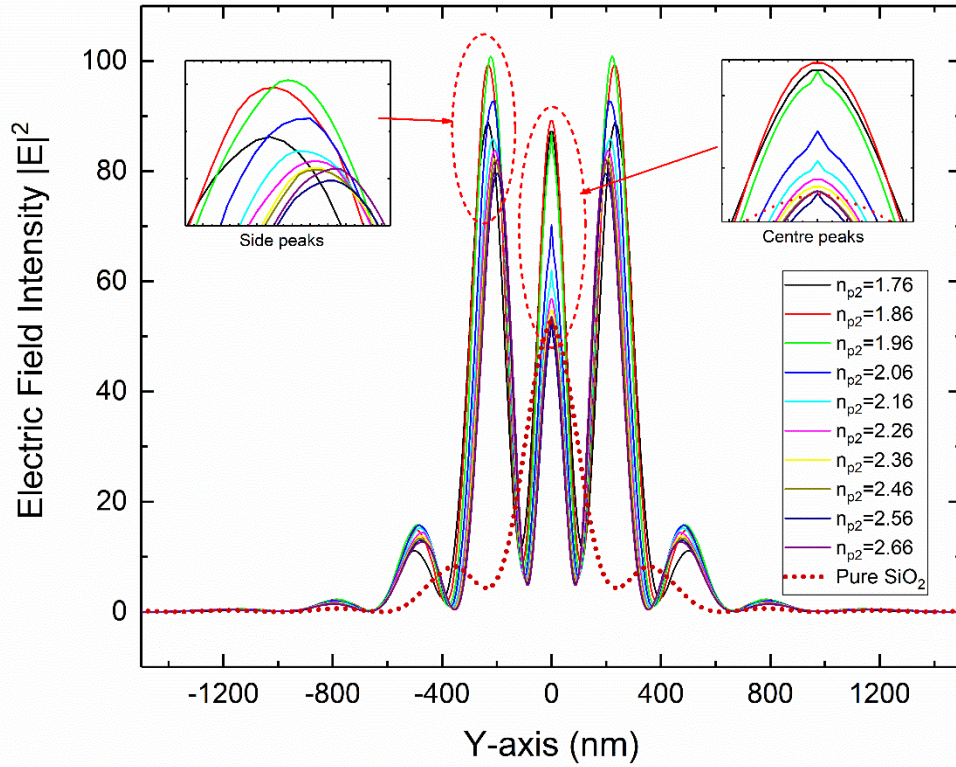


Figure 5.10 $|E|^2$ field distribution along Y-direction at focus position ($z=1500$ nm) of optimized super-resolution focus (solid curves) and ordinary SiO_2 (red dot line).

Although composite microspheres have achieved better super-resolution than pupil mask design, it forms multiple peaks at external focus. Figure 5.10 shows the $|E|^2$ field distribution along Y-direction at focus position ($z=1500$ nm) of optimized super-resolution focus of composite particle and ordinary SiO_2 (dot line). The red dot curve represents the $3\text{ }\mu\text{m}$ homogeneous SiO_2 ($n_p=1.46$) microsphere which has a single intense peak at centre. While there are always three sharp peaks produced by composite material particles. Moreover, their symmetric side peaks are consistently higher than central one, for example in $n_{p2}=2.56$ case, the centre intensity is 52.9 and corresponding side-peaks are 79.5. The central peak size is extremely small, can reach 91 nm which accounts for $\lambda/6.62$. This is an amazing achievement as it goes well beyond the solid immersion resolution limit of $\lambda/2n=\lambda/5.12$. One possible explanation is the excitation of optical super-oscillation effects, causing by wave interferences at two-material interfaces. However, like other super-oscillatory lens it has strong side-lobes which is unfavourable for imaging and other applications.

5.4 Combination design of pupil mask and composite materials onto microsphere lens

Previous two sections discussed the effects of pupil mask and composite material concepts on microsphere focusing. Both of techniques provide significant enhancement on near-field focus resolution to surpass classical diffraction limit and precise controllability of focal length. However, drawbacks also exist in both cases. In pupil mask design, super-resolution was achieved by scarifying light intensity from blocking centre incident beam. Poor focus intensity was presented due to mask area increase (Figure 5.2). While, although composite microsphere design provides significantly enhanced resolution, it suffers obviously unfavourable side-lobe effects which makes it non-preferred for practical applications. In this section, two concepts were simultaneously applied on microsphere to realise superior focusing quality.

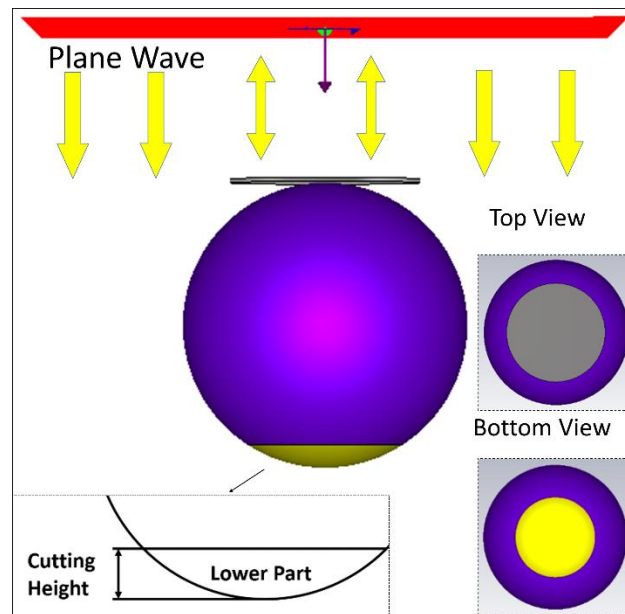


Figure 5.11 Schematic diagrams of combining pupil mask and composited microsphere.

The schematic diagram was presented in Figure 5.11. As previous sections discussed, both pupil mask and composite designs are crucially important to enhance the resolution. Herein, we report a combination of two concepts and an example results demonstrated how those factors can affect focusing properties. Since the best super-resolution was identified to be

91nm which is under the condition of $n_{p2} = 2.56$ and $H_{cutting} = 53nm$, it was selected for comparison. In Figure 5.12, circular mask with variety of diameters were employed on such chosen composited microsphere. The red dotted line represents the field distribution along y-axis at focus of composited microsphere. It is clearly to be observed that the centre peak though is narrow, sidebands intensity is 79.5 which is 50% higher than centre. In contrast, sidebands are obviously restrained by assist of circular mask, and meanwhile centre peaks are effectively enhanced. This phenomenon is summarised in Table 5.3. It is noted that the side enhancement drops correspondingly with mask size increased. In the case of 2 μm mask size, the centre enhancement rises to 290.8 which is highest value among studied cases. On the other hand, the side enhancement is 118.3 which is 59% lower than centre peak. In the same time, its resolution, 112 nm, is still surpass the diffraction limit ($\lambda/2n \approx 117nm$). Furthermore, this circumstance can be considered for adapting to other conditions, $1.76 \leq n_{p2} \leq 2.66$. It is particular important for many practical applications, such as imaging and nano-fabrication.

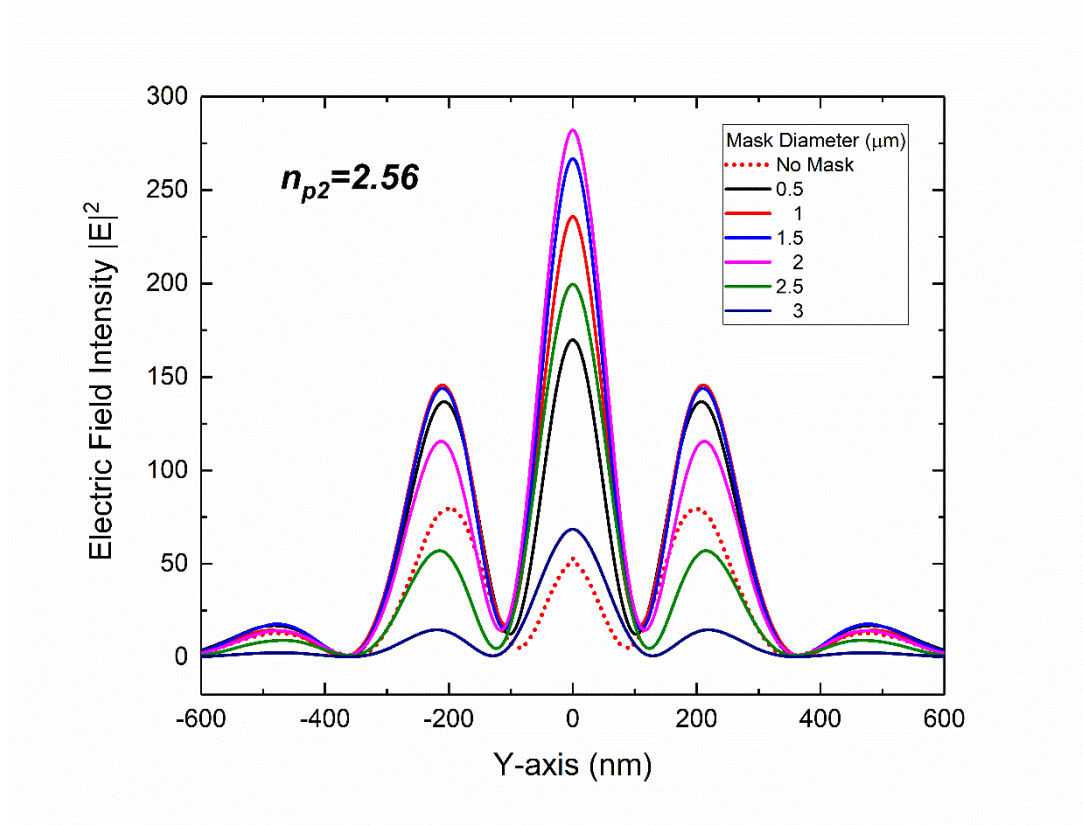


Figure 5.12 Comparison of $|E|^2$ intensity from various mask size on composited microsphere with $n_{p2}=2.56$.

Mask Diameter (μm)	Centre Intensity	Side Intensity	$\frac{(\text{Centre} - \text{side})}{\text{centre}} * 100\%$	FWHM (nm)	Resolution in λ
0	52.9	79.5	-50	91	$\lambda / 6.62$
0.5	171.1	138.7	19	104	$\lambda / 5.76$
1	243.6	148.2	39	107	$\lambda / 5.59$
1.5	274.8	146.8	47	107	$\lambda / 5.59$
2	290.8	118.3	59	112	$\lambda / 5.35$
2.5	200.8	58.3	71	117	$\lambda / 5.14$
3	70.2	15.1	78	118	$\lambda / 5.1$

Table 5.3 Comparisons of centre and side enhancement with various sizes of mask.

Figure 5.13 presents the resolution with varying mask diameter and refractive index n_{p2} . The red dotted curve is diffraction limit, $\lambda/2n_{p2}$, and shadow area means super-resolution. Although composited microsphere has best resolution, it suffers the unfavourable side-lobe effects. The circular pupil mask leads the centre enhancements are significantly increased meanwhile suppresses the sideband. More importantly, most masked composite microspheres can achieve super-resolution.

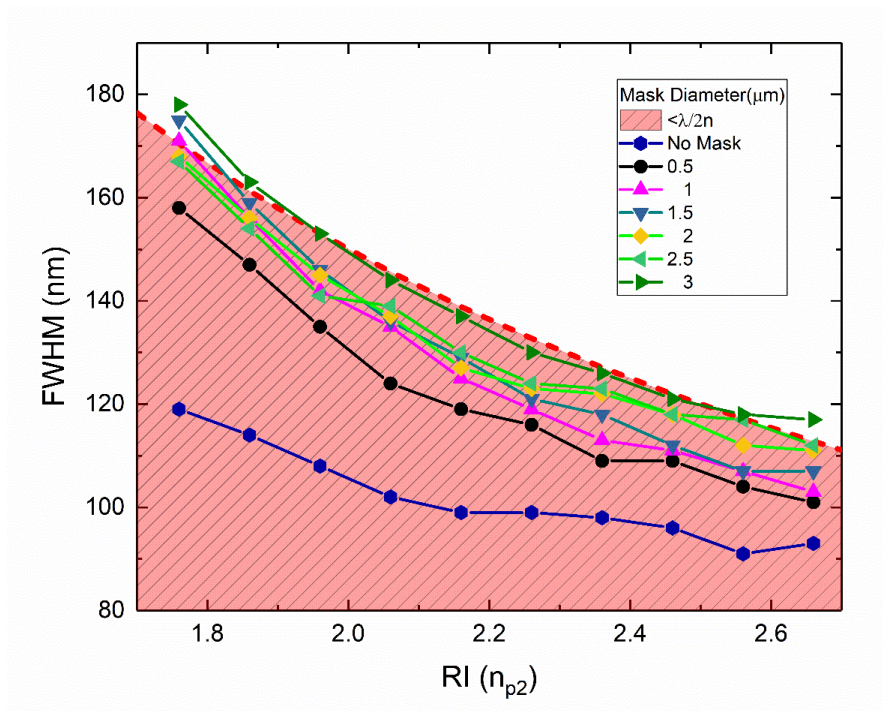


Figure 5.13 Comparison of FWHM with varying mask size and n_{p2} .

5.5 Dielectric nanoparticle-based metamaterial superlens

In this research, we also incorporated the metamaterial concept in our superlens design. Apart from the typical microsphere-based designs, this section proposes a new concept of using dielectric nanoparticles as building block to construct a dielectric metamaterial superlens. As many studies reveal that most metal-based metamaterials suffer from intrinsic loss at high optical frequencies, which cause them to be unfavourable in near-infrared and visible region[137]–[140]. Moreover, metal-based plasmonic components have low transmission efficiency at optical frequencies, thus making them less useful for optical waveguiding over long distances or through bulk three-dimensional (3D) structures[141], [142]. Unlike the metal-based metamaterials, dielectric metamaterials use the near-field coupling between transparent (low absorption), high-refractive index dielectric building blocks, which perform similar optical phenomena to metallic nano-resonators, but with much lower energy dissipation[143]–[146]. Meanwhile, high transmission and diffraction efficiencies of dielectric components make it possible to move optical metamaterials from current 2D metasurfaces or layered metamaterials to truly 3D metamaterials[141].

To explore the optical performance of the nanoparticles composited metamaterial, we performed full-wave 3D simulations of the all-dielectric metamaterial media. The detail simulation setup and conditions were introduced in **Chapter 3.2.2.3**. The basic simulation structure of the artificial media is a closely stacked 15-nm anatase TiO_2 nanoparticle composite, in which tiny air gaps between the particles exist, resulting in a dense scattering media. Figure 5.14 shows the simulation results of electric field distribution in the media when applying a plane wave illumination at a wavelength of 550 nm from the far field. Electric field confinements are observed in the gaps between nanoparticles, indicating the ability of the composited media to modulate and confine visible light at the nanoscale, as shown in Figure 5.14 (A). Since TiO_2 is nearly free of energy dissipation at visible wavelengths, this near-field coupling effect among neighbouring nanoparticles can effectively propagate through the media over long distances, forming an arrayed “patterned illumination” landscape on the surface of an underlying substrate, as shown in Figure 5.14(B). These illumination spots are evanescent in nature, containing high-spatial frequency components. Their sizes are mainly

determined by the size of TiO₂ nanoparticles, having a full width at half maximum (FWHM) resolution of ~8 nm, as shown in Figure 5.14 (C).

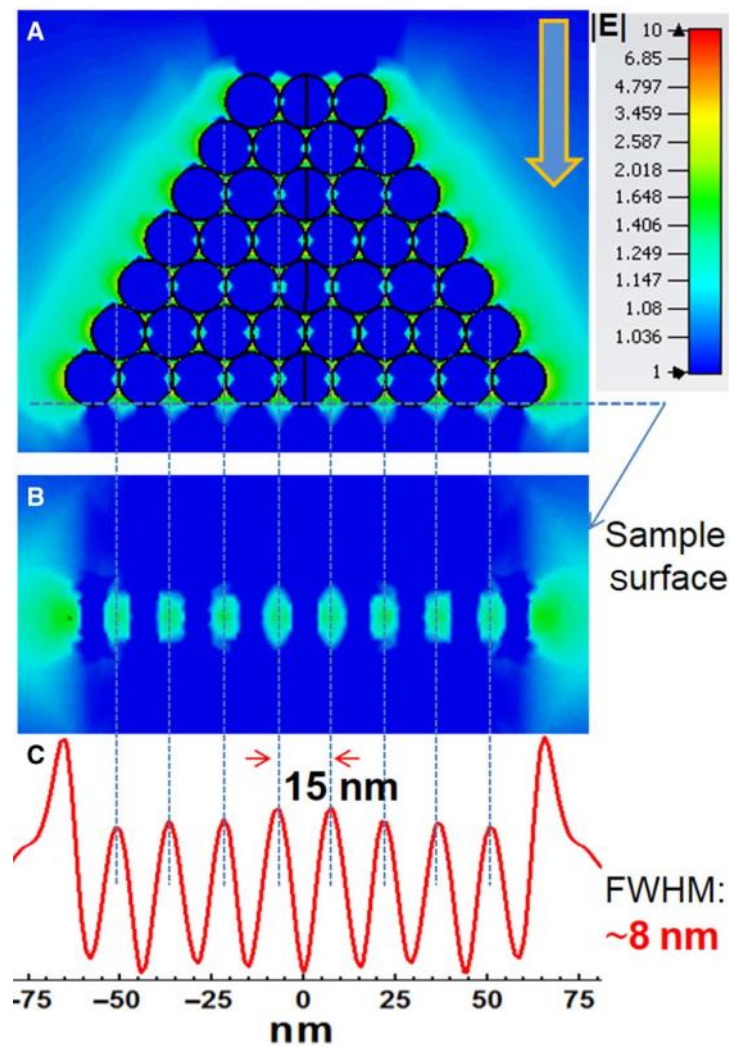


Figure 5.14 Propagating wave scattering by dense all-dielectric nanoparticles medium. (A) Plane wave ($\lambda = 550$ nm) passing through the stacked TiO₂ nanoparticles. Electric field hotspots are generated in the gaps between contacting particles, which guides light to the underlying sample. (B) Large-area nanoscale evanescent wave illumination can be focused onto the sample surface because of the excitation of nanogap mode. (C) The size of the illumination spots is equal to the particle size, having an FWHM resolution of ~8 nm.

Therefore, it is expected that nanoparticle composited media will have the unusual ability to transform the far-field illumination into large-area nanoscale evanescent wave illumination focused on the object surface within the nearfield region. This novel nanophotonic effect is somewhat similar to that of aperture near-field scanning optical microscopy (NSOM), in which evanescent wave illumination is transmitted from the subwavelength aperture at the tip of a metal-coated optical fibre, and the size of the illumination spot is not limited by the incident

wavelength but by the aperture size[19], [147]. However, the single nanoaperture design in NSOM suffers from several limitations, such as low optical throughput, long scanning time, and insufficient contact between aperture probe and object surface [147]. In our design, the array of TiO₂ nanoparticles can act as thousands of near-field probes to simultaneously illuminate the sample surface, and the strength of the focused evanescent wave illumination can be maximised owing to the near perfect solid immersion of imaging object by TiO₂ nanoparticles. Moreover, theoretically, the size of the evanescent wave illumination spots can be further reduced by using smaller anatase TiO₂ nanoparticles or higher refractive index rutile ($n = 2.70$) TiO₂ nanoparticles, and this near-field illumination may also be useful for other applications such as nanoscale light harvesting and sensing.

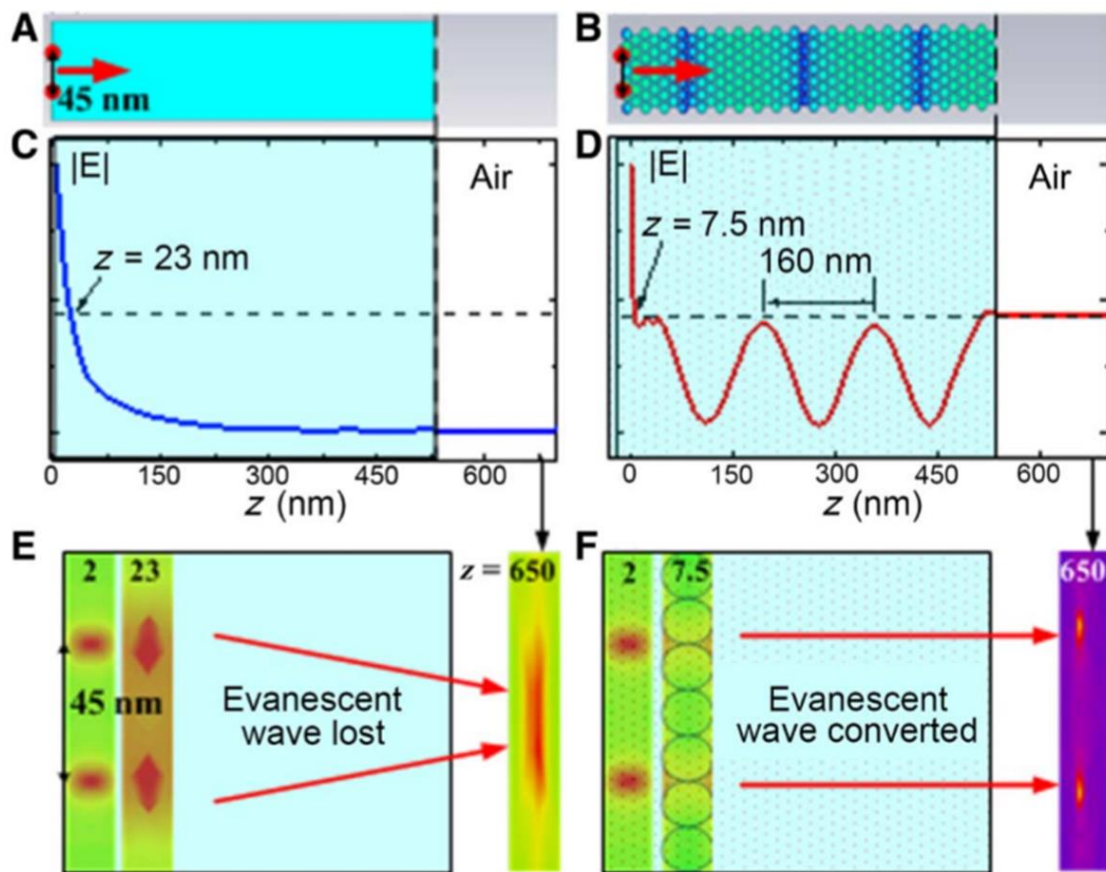


Figure 5.15 Comparisons between homogeneous and nanoparticle composited media. (a) Mean electric field amplitude as a function of distance from point sources (y-polarised, incoherent). The amplitude decays exponentially. Most evanescent wave energy was lost within 50 nm distance. (b) In nanoparticle composited material, evanescent waves interact with TiO₂ nanoparticles and turn into propagation waves which travel outward to far-field. A periodicity of 160 nm was observed. (c-f) Two-point sources (45 nm separation) imaged with (c) homogeneous and (f) composited material, at positions $z=2$ nm (near source), $Z=23$ nm (near-field, inside slab) and $Z=650$ nm (far-field, outside slab). In far-field, (e) the homogenous media fails to resolve the two points while (f) the composited media can successfully resolve them.

According to the reciprocal principle [66], the conversion process in nanoparticle composited media (Figure 5.15) from propagating waves to evanescent waves can be optically reversed. In other words, an array of evanescent wave source located on the bottom surface of the nanoparticles composited media will be converted back into propagating waves by the media. This is confirmed by two-point source calculation—a technique widely used to determine the imaging resolution of an optical system. In simulation, two incoherence point sources (y-polarised, set using 1nm x 1nm rectangular waveguide port in CST software) including all evanescent wave components were placed 45 nm away and a convergence accuracy of $1e-4$ was used. Periodic boundary conditions were applied in both X and Y directions. The averaged electric fields at different z-planes were obtained using the post-processing functions built in the software.

For comparison purposes, both conventional media (homogeneous anatase TiO_2 material) and our metamaterial media (stacked 15 nm anatase TiO_2 nanoparticle) were simulated. Using slab geometry, we demonstrate in Figure 5.15 that evanescent waves behave differently when interacting with conventional media, Figure 5.15 (a), and composited metamaterial media, Figure 5.15 (b and d).

As shown in Figure 5.15 (c), in homogeneous media the evanescent waves decay exponentially as expected when the distance to sources increases. The loss of evanescent waves causes reduced resolution. Figure 5.15 (e) demonstrates the inability of conventional media to resolve two-point sources (separated by 45 nm) in far-field zone (*e.g.* $z=650 \text{ nm} > \lambda=550\text{nm}$). The two points are only resolvable in near-fields when distance to source is extremely small, typically smaller than 50 nm in present case. In nanoparticle composited media, however, the evanescent waves experience strong interaction with TiO_2 nanoparticles, which causes effective conversion of evanescent waves into propagation waves. The converted waves are mainly guided through the gaps between particles. As shown in Figure 5.15 (d), electric field received at far-field region ($z>\lambda$) is about $|E| \sim 0.45$ (since source amplitude $|E|=1$, this corresponds to $|E|^2 = 20\%$ of total evanescent energy), which is comparable to the field strength at $z=7.5\text{nm}$ (near-field). This means near-field energies are indeed converted and transported to the far-field. It is also interesting to notice the periodic modulation effects of E-field inside the composited media, which can be seen as a signature

of this design. Since there is no material loss in composited media, the periodic propagation experiences an un-damped modulation, showing an effective period of 160 nm. These waves propagate outwards from near-fields into far-fields and contribute to super-resolution. In Figure 5.15 (f), it is demonstrated that at far-field (*e.g.* $z=650\text{nm}$), the two-point sources are reconstructed and clearly discernible. Comparing to metal-based superlens and hyperlenses whose resolution is limited by material losses in metal[26], [28], [31], [148], the proposed all-dielectric nanoparticles media is free from loss problems; its resolution is mainly affected by the excitation of evanescent waves and the conversion efficiency of evanescent waves into propagating waves, as well as the effective capture of the subwavelength information in the far field. This makes it possible to design a perfect imaging device using dielectric nanoparticles as building block. In the **Chapter 6**, we will experimentally demonstrate a fabricated TiO_2 nanoparticle-based metamaterial solid immersion lens (mSIL) and its super-resolution imaging performance (45 nm) as predicted by the theory.

5.6 Conclusion

In summary, we have shown that by using circular pupil mask and varying its size, it is possible to precisely tune the focal point of a microsphere lens in near-field zones from external zone to internal body of the microsphere, and meanwhile improve its focusing lateral resolution by more than 30% to close to 80%, leading to an optimised resolution hugely surpassing the classical diffraction limit. Meantime, the composite microsphere with high-index material dominating at bottom can efficiently improve resolution. By varying the volume and RI of lower portion of sphere, it is capable to achieve significant refinement of focal size to $\lambda/6.62$. However, this breakthrough is accompanied by obvious side-effect whose unfavourable side-lobe effects make it non-preferable for practical applications. Therefore, an integration design which couples the pupil mask and composite concept has been proposed to overcome disadvantages of previous designs. The sharp side-peaks exhibited from the composite microsphere are effectively suppressed and meanwhile centre focus intensity is enhanced. Besides, it still able to achieve resolution better than $\lambda/2n$ limit. The work provides a new freedom in controlling super-resolution focusing of microsphere lens and is expected to play a big role in the future of microsphere-based super-resolution techniques. In addition, owing to near-field coupling among neighbouring high RI nanoparticles, this composited man-made

metamaterial superlens can contribute to a unique photophysical properties that are not existing in homogeneous material lens. The simulation results showed that near-field evanescent information consist of 45 nm features can be resolved in far-field zone. This is attributed to the exceptional abilities of the metamaterial media to create an array of evanescent wave illumination focused on the sample surface and to effectively couple the evanescent information into propagating waves. Due to the inherent low loss in the all-dielectric metamaterial, these processes can be carried out in a truly 3D structure and over long distances.

Chapter 6. Superlensing Metamaterial

Solid Immersion Lens (mSIL) and

Nanohybrid Lens

Two types of metamaterial superlenses designs were investigated in this chapter. The first design follows from that presented in **chapter 5.5** –all-dielectric metamaterial superlens derived from 3D stacking of high-index nanoparticle (see fabrication in **chapter 3.3.5**). Hereinafter we refer it as “metamaterial solid immersion lens (mSIL)”. The second metamaterial lens design derives from the concept of hybridization of two nano-materials – “nanohybrid lens”. High-quality microspheres consisting of ZrO_2 /polystyrene elements were synthesised (see **chapter 3.3.6**). The super-resolution imaging performance of these two superlenses were studied in detail in this chapter.

6.1 Introduction

Recently, many researchers found that microspheres can function as optical superlenses for nanoscale super-resolution imaging. The first ‘microsphere nanoscopy’ technique used optically transparent SiO_2 microsphere as superlens to collect and convert the underlying near-field object information into a magnified far-field virtual image, which shows an astonishing super-resolution of 50 nm under a standard white-light illumination[67]. However, due to the limitation of the low refractive index of SiO_2 spheres, the super-resolution window of SiO_2 spheres was confined to the diameter (D) range of 2–9 μm . Silica spheres with diameters larger than 10 μm even failed in 100 nm resolution imaging tests. Large diameter (30–100 μm) polystyrene microspheres (refractive index of the particle: $n_p = 1.59$) were also reported for the super-resolution imaging of a Blu-ray disc in an air atmosphere, achieving a resolution of 120 nm[68]. However, in these cases, the microspheres exposed in an air environment usually resulted in a low imaging contrast. When SiO_2 spheres were semi-immersed in a thin layer of ethanol or SU-8 resist[12], [9], the imaging contrast could be strongly strengthened; however, it was not easy to resolve features below 100nm because of their low refractive index ($n_p = 1.46$). Darafsheh et al. found that when BaTiO_3 (n_p

= 1.9) glass spheres were totally submerged in a liquid of isopropyl alcohol[69], the small spheres (diameter = 4.2 μm) were able to discern features as small as 75 nm ($\lambda/7$), while for large microspheres ($50\text{ }\mu\text{m} < \text{diameter} < 220\text{ }\mu\text{m}$), the resolved feature sizes were only $\lambda/4$. Li et al. reported water submerged BaTiO₃ (diameter = 100 μm) for the imaging of an adenovirus with a resolution of 75 nm[10]. Microspheres coupled to optical super-resolution imaging were focused on commercial SiO₂, PS and high RI BaTiO₃. However, these spheres have either a low refractive index or poor processability, which make them a little less attractive in practical applications. Therefore, there is an urgent need of a new material or method can effectively improve resolution.

Previous chapter provided several possible approaches to enhance resolution, one of which the dielectric nanoparticle-derived metamaterial lens which has exceptional photonic effect. Although all-dielectric metamaterials offer a low-loss alternative to current metal-based metamaterials to manipulate light at the nanoscale and may have important applications, very few have been reported to date owing to the current nanofabrication technologies. Based on this, we urgently hope that it can be realised through experimental methods. In this chapter, we develop a new “nano–solid-fluid assembly” method using 15-nm TiO₂ nanoparticles as building blocks to fabricate the first three-dimensional (3D) all-dielectric metamaterial at visible frequencies. As for its optical transparency, high refractive index, and deep-subwavelength structures, this 3D all-dielectric metamaterial-based solid immersion lens (mSIL) can produce a sharp image with a super-resolution of at least 45 nm under a white-light optical microscope, significantly exceeding the classical diffraction limit and previous near-field imaging techniques.

Another development of superlens is proposed by uniformly distributing high RI ZrO₂ material into polystyrene for synthesising high RI and transparent micro-scale sphere. We demonstrate a nanoparticle-hybrid suspension polymerisation approach to chemically synthesise high-quality microspheres ZrO₂/PS hybrid microspheres that are highly controllable in shape and refractive index. With increasing the refractive index of microspheres can enhance the imaging resolution and quality. A 60 nm resolution has been obtained in the wide-field imaging mode and a 50 nm resolution has been obtained in the confocal mode imaging of semiconductor chip samples.

This chapter is organised as follows; Section 2 discusses the optical imaging performance of a dielectric metamaterial solid immersion lens (mSIL) synthesised by high-index TiO_2 nanoparticles; In section 3, ZrO_2/PS nanohybrid colloidal microspheres with various RI and sizes are evaluated under white light and laser confocal microscopes; Section 4 will conclude this chapter work.

6.2 Dielectric nanoparticles derived metamaterial solid immersion lens (mSIL)

Ordinary microsphere lens technique often sustains poor contrast due to the perceptible inadequate contact between microsphere and sample surface, and the virtual image is restricted to a narrow field-of-view since the super-resolution ability of microsphere lenses is obtainable only for small microspheres. Semi-immersion of the microsphere lens in a liquid layer can increase the field intensity collected by the microsphere and thus enhance the contrast of the virtual image, but it also reduces the magnification factor and super-resolution ability[12], while complete submersion of the microsphere lens in a liquid would easily form concentric interference fringes that disturb the performance of virtual image[10], [149],

It has been theoretically and experimentally demonstrated that high refractive index materials are not always preferred in microsphere superlens[67], [149], yet they are indeed urgently needed in solid immersion lens (SIL)[12], [150], which are expected to combine the desirable properties of a far-field superlens, including significant improvements in field collection efficiency, magnification and spatial resolution[151]. However, the currently available SILs reported so far fail to resolve features below 130 nm under white light illumination due to the shortage of high refractive index material that is transparent to visible light[152]–[154].

In **Chapter 5.5**, a concept which used high RI titanium dioxide (TiO_2 , $n=2.5$) nanoparticles to construct a dense-packed composited metamaterial that can illuminate object surfaces with large-area nanoscale near-field evanescent spots and, inversely, collect and convert the evanescent information into propagating waves. By leveraging the exceptional abilities of dielectric metamaterials into a three-dimensional structure such as sphere or hemisphere, it can produce a sharp-contrast, wide field-of-view virtual image with a super-resolution under

a white-light optical microscope. In this section, we develop a ‘nano-solid-fluid assembly’ (NSFA) method using TiO_2 nanoparticles as the building blocks to successfully fabricate TiO_2 hemispheres with width up to 20 μm . The detail synthesis procedure was mentioned in **Chapter 3.3.5**. In contrast to artificial large size TiO_2 particles and the previously reported other microsphere superlens, the as-fabricated TiO_2 nanoparticles-derived hemispheres are highly transparent to visible light owing to the densely packed structure of nanoparticles and can penetrate into the nanoscale surface textures on different samples due to their small nanoparticles and acceptable fluidity. Of particular interest is the fact that this new class of Metamaterial Solid Immersion Lens (mSIL) can produce a high contrast and wide field of view virtual image with a super-resolution of at least 45 nm under a white-light optical microscope. Our approach opens a new pathway and possibility for the fabrication of nanoparticles-derived hemispheres even other complex structures with high refractive index and optical transparency, which are hardly obtained through the existing strategies.

6.2.1 Investigation of field-of-view and magnification factor of TiO_2 mSIL

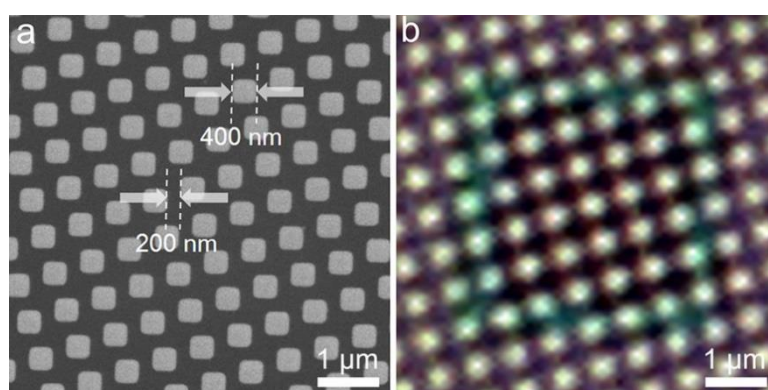


Figure 6.1 Wafer pattern used for evaluating the magnification factor and field of view of TiO_2 mSILs. (a) SEM image of the wafer pattern, which shows 400-nm-wide squares with an interval of 200 nm. (b) Optical micrograph of the wafer pattern at a magnification of $\times 2100$, indicating that the conventional optical microscope would fail to reveal the shape of the squares due to the Abbe diffraction limit. Scale bars, 1 μm in (a) and (b).

To understand the parameters affecting the magnifications and field of view of these TiO_2 nanoparticles-derived hemispheres or super-hemispheres, we compared the white-light optical microscope images of a semiconductor wafer pattern with a lattice spacing of 200 nm observed through these as-fabricated TiO_2 mSILs (Figure 6.1).

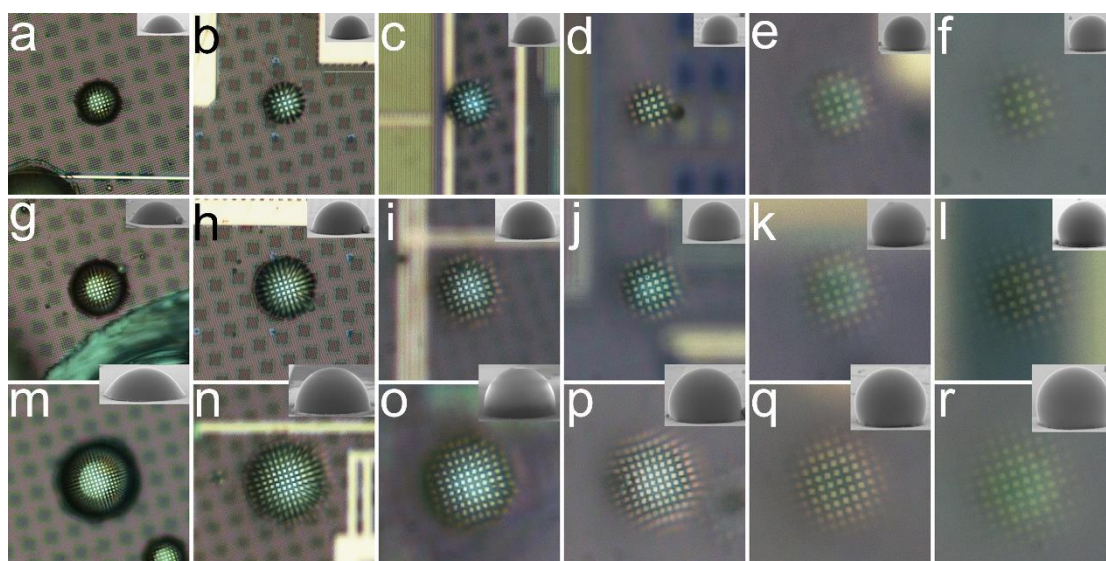


Figure 6.2 Magnification factors and field of view of TiO_2 nanoparticles-based hemispheres or super-hemispheres as mSILs. Optical microscope images of a wafer pattern with a lattice spacing of 200 nm observed through TiO_2 mSILs with widths of about (a-f) 10 μm , (g-l) 15 μm and (m-r) 20 μm , corresponding to an increasing magnification factors of (a, g, m) 1.8, (b, h, n) 2.5, (c, j, o) 3.0, (d, j, p) 3.6, (e, k, q) 4.7, and (f, l, r) 5.3, respectively. Inset: side-view SEM images of the corresponding mSILs located on the pattern.

As shown in Figure 6.2, each group of transverse images has the same widths of mSILs, being around 10, 15 and 20 μm , respectively (see the inserted SEM images). Not surprisingly, as the height of mSILs increases, the increasing magnification factors of around 1.8, 2.5, 3.0, 3.6, 4.7, and 5.3, respectively, are observed. Further analysis indicates that the magnification factor is significantly correlated with the shape (height-to-width ratio) of mSILs, rather than the width of mSILs in the investigated range of 10 to 20 μm . The magnification factor sharply increases with the height-to-width ratio of mSILs is approaching unity (a spherical shape), and reaches 5.3 at the height-to-width ratio of 0.82. With the further increase of this ratio, the contrast of the virtual images gradually decreases.

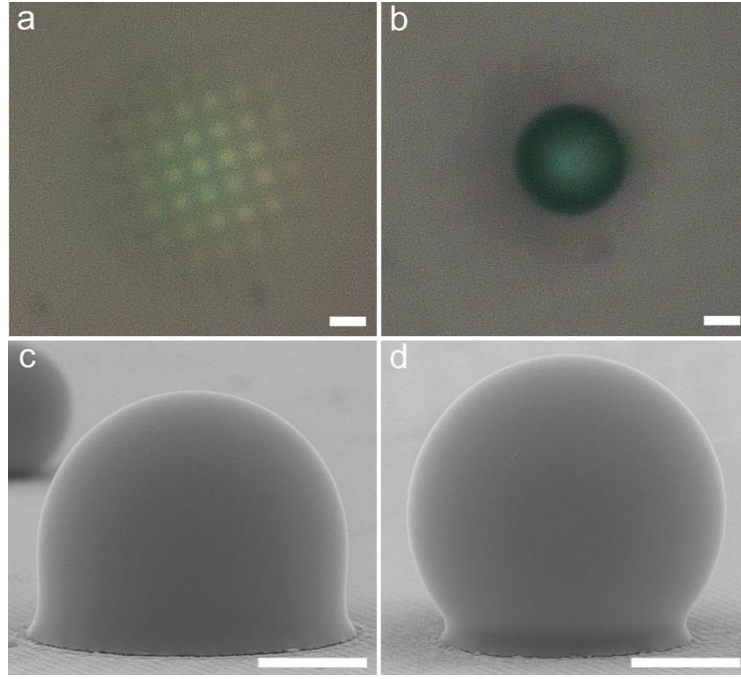


Figure 6.3 Magnification effect of TiO₂ mSILs with higher height-to-width ratios. Optical micrographs of the wafer pattern observed through TiO₂ mSILs with a height-to-width ratio of (a) 0.84 or (b) 0.94, and (c, d) their corresponding SEM images, respectively. The virtual image (a) has a magnification factor of 6.7 but suffers from low contrast. (b) failed to resolve pattern in air condition. The mSILs have widths around 15 μm. Scale bars, 5 μm in (a)-(d).

Although a higher height-to-width ratio of 0.84 could allow a magnification factor of up to 6.7, the contrast was too low to distinguish the details of the virtual image, and the mSIL with a height-to-width ratio of 0.94 would completely fail to create a virtual image in the air (Figure 6.3). Using geometrical optics ray tracing, we theoretically fit the experimental magnification curve and inversely derived the mSIL media has an effective index of ~1.95 (Figure 6.4). On the other hand, the volume fraction of TiO₂ nanoparticles can be calculated as follow equation[155].

$$n_{SIL} = n_{air} \times V_{air} + n_{particles} \times V_{particles} \quad 6.1$$

where n_{SIL} is effective refractive index of mSIL, n_{air} and $n_{particles}$ are respectively refractive index of air and TiO₂ nanoparticles, V_{air} and $V_{particles}$ are the volume fraction of air and TiO₂ nanoparticles. Therefore, the volume fraction of TiO₂ nanoparticles can be inversely derived as 59.4%.

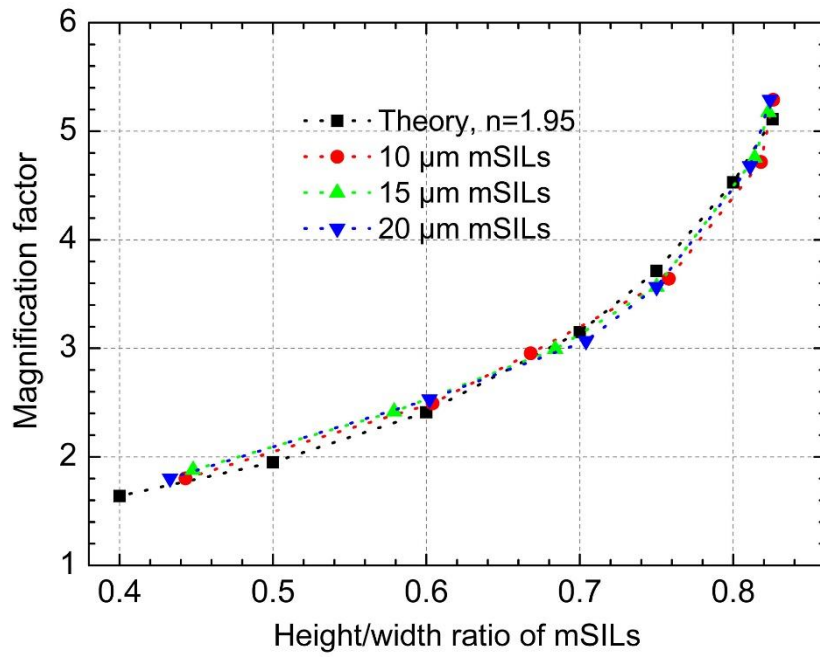


Figure 6.4 Estimation of the effective refractive index of TiO₂ mSILs. The experimentally observed correlation (black) between the magnification factor and the height-to-width ratio for 10 μm mSILs (red), 15 μm mSILs (green) and 20 μm mSILs (blue) in Fig. 3. Theoretical curve was obtained using geometry optics analysis with an effective index of 1.95.

Moreover, in contrast to the microsphere-based lens, which usually provides a narrow field of view due to spherical particle focusing, the TiO₂ nanoparticles-derived hemispheres or super-hemispheres as mSILs presented here exhibit a wide field of view, which is approximately linearly proportional to the width of mSILs (Figure 6.5), and less related to the shape of mSILs.

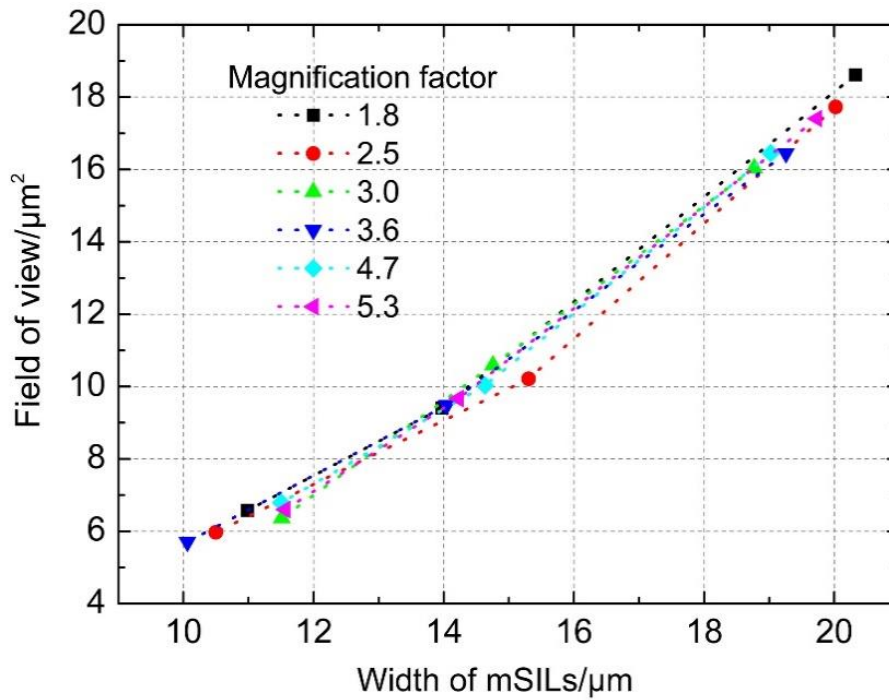


Figure 6.5 Field of view of TiO_2 mSILs. In Figure 6.2, the field of view (undistorted region) of mSILs increases almost linearly with an increase in the width of mSILs from 10 μm to 20 μm , and less related to the magnification factor (height-to-width ratio) of mSILs.

6.2.2 Super-resolution imaging performance of TiO_2 mSIL

Figure 6.6 further presents the white-light optical microscope images of a recordable Blu-ray disc and a semiconductor wafer observed by TiO_2 nanoparticle-based mSILs. Through SEM, the Blu-ray disc contains recording tracks with 200-nm-wide ridges separated by 100-nm-wide grooves (Figure 6.6 a), and the wafer contains parallel line patterns with a pitch of 60 nm (Figure 6.6 (e)) or point and line patterns with a pitch of 50 nm (Figure 6.6 i). Typically, the surface roughness (maximum height of irregularities) on the wafer surface is below 5 nm (Figure 6.6 f, j). Interestingly, the SEM images of bottom surfaces of mSILs detached from the test samples, as shown in Figure 6.6 (b, c, g and h), indicate that the nano-solid-fluids consisting of 15 nm nanoparticles have indeed penetrated into different nanopatterns with a feature size down to a few tens of nanometres owing to their small size and liquidity.

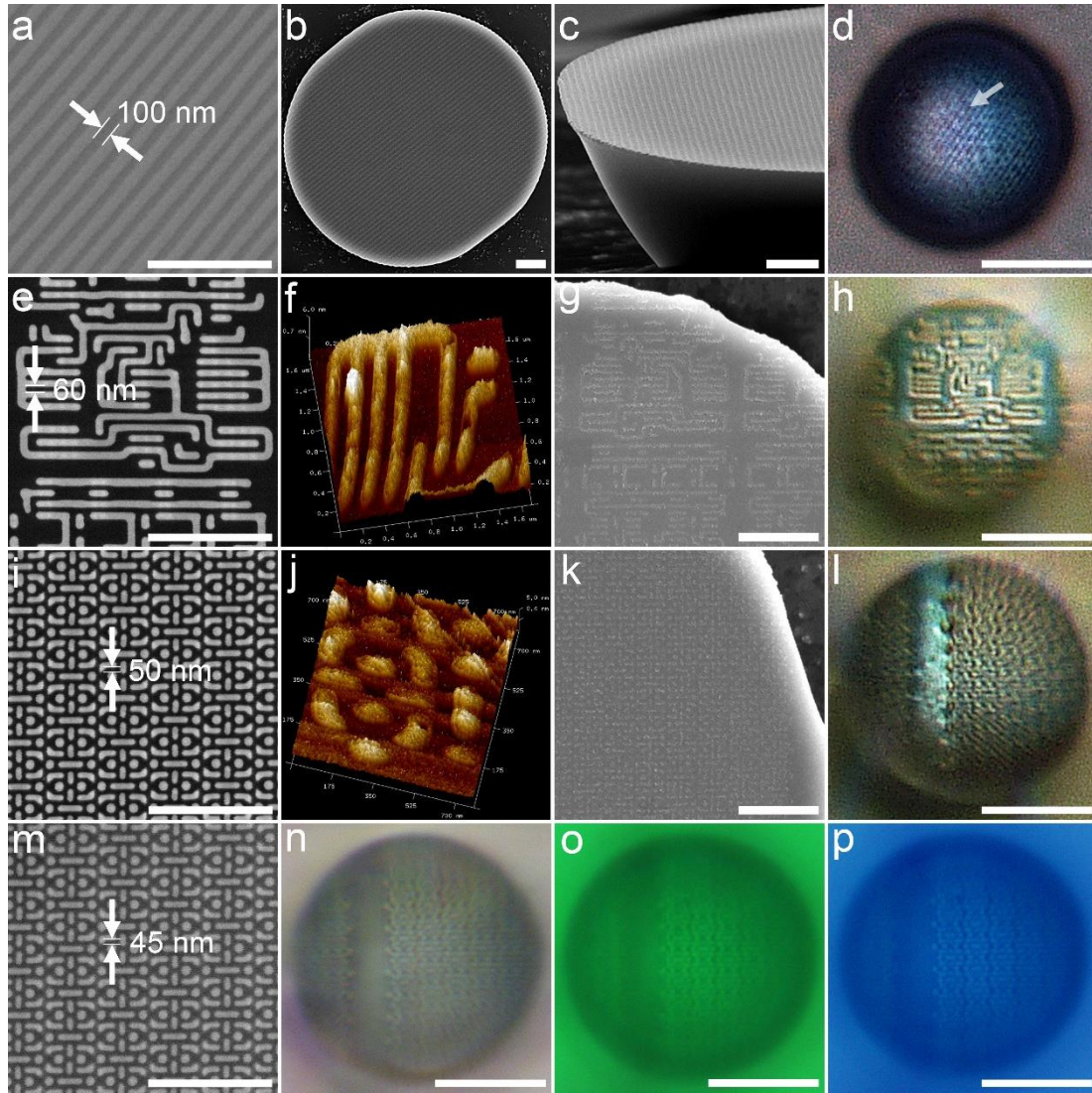


Figure 6.6 Super-resolution imaging through TiO_2 mSILs. SEM images of (a) a Blu-ray disc containing 100-nm-wide grooves, and the wafer patterns with (e) 60 nm pitches, (i) 50 nm pitches or (m) 45 nm pitches after gold coating of sample (i), and (b)-(c), (g) and (k) the bottom surfaces of mSILs detached from the surface of samples (a), (e) and (i), respectively. AFM images of the wafer patterns with (f) 60 nm pitches or (j) 50 nm pitches, respectively. Optical microscope images of TiO_2 mSILs focused on the surface of (d) Blu-ray disc, wafer patterns with (h) 60 nm pitches, (l) 50 nm pitches or (n)-(p) 45 nm pitches, with a magnification factor of 1.8, 3.1, 3.0 and 3.1, respectively. The last mSIL was illuminated under (n) white light, (o) green light ($\lambda \sim 540$ nm) or (p) blue light ($\lambda \sim 470$ nm), respectively. The mSILs had widths of about 20 μm . Scale bars, 2 μm for SEM images and 10 μm for optical images.

As shown in Figure 6.6(d), the 100-nm-wide grooves on the Blu-ray disc surface, are clearly visible through the 1.8 times magnified virtual image created by mSIL hemisphere. The mSIL also enables direct observation of the recorded data that are stored in the grooves as the difference in reflectivity, as indicated by the arrows in Figure 6.6(d), which even cannot be detected by SEM. Moreover, it is interesting to find that the hemispherical mSIL was formed

into a semi-ellipsoid shape with its long axis parallel to the tracks on the disk, as shown in Figure 6.6 (b-d). This indicates that the TiO_2 nano-solid-fluid could plastically deform and flow along the grooves and ridges on the disk during assembly process. Furthermore, after dehydration of interparticle water, the assembled morphology of TiO_2 nanoparticles could be maintained and even reinforced due to the strong capillary attraction between particles.

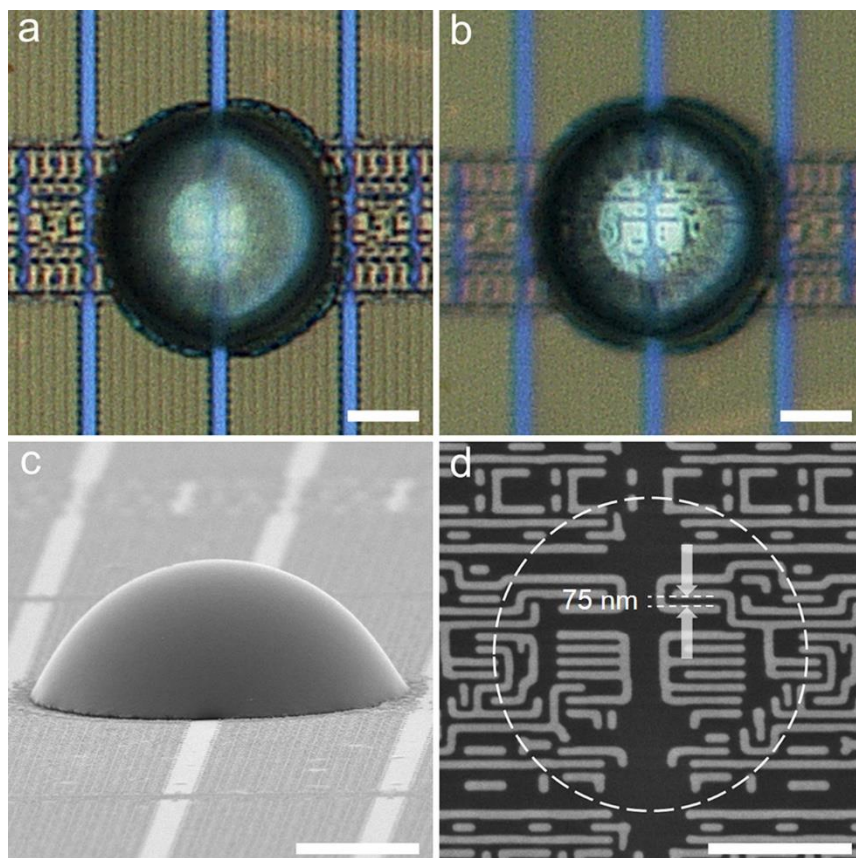


Figure 6.7 The limiting resolution obtained with a TiO_2 hemispherical mSIL. Optical micrographs focused on (a) the wafer pattern, and (b) the 1.8 times magnified virtual image created by a TiO_2 hemispherical mSIL. The corresponding SEM images of (c) the hemispherical mSIL and (d) the wafer pattern with 75 nm features, the dashed circle in (d) represents the field of view seen in (b). The hemispherical mSIL has a width of 15 μm . The results indicate that the hemispherical mSIL with a magnification factor of 1.8 is insufficient to resolve the features below 75 nm. Scale bars, 5 μm in (a)-(c) and 2 μm in (d).

Nonetheless, this low height-to-width ratio hemispherical mSIL cannot intelligibly resolve the wafer pattern with 75 nm features (Figure 6.7). However, when the TiO_2 nanoparticle-based super-hemisphere as the mSIL located on the pattern, 60 nm pitch can be clearly observed through the magnified virtual image with a higher magnification factor of 3.1 (Figure 6.6 h). This super-hemispherical mSIL can be further used to image more complex structure with 50

nm features (Figure 6.6 l). By using optical microscope equipped with a higher resolution CCD camera, we could more clearly capture the subwavelength details of the target sample (Figure 6.8), even 45 nm (Figure 6.6 m), the dots in the 3.1 times magnified virtual image were clearly distinguished from the lines under an illumination of white light, green light ($\lambda \sim 540$ nm) or blue light ($\lambda \sim 470$ nm), respectively (Figure 6.6 n-p). It is also noteworthy that the best super-resolution performance was achieved under the illumination of short-wavelength blue light. This suggests that the as-fabricated TiO_2 nanoparticle-based super hemisphere mSIL can be used for the observation of sub-50 nm features, in agreement with the theoretical predicts in Chapter 5.5.

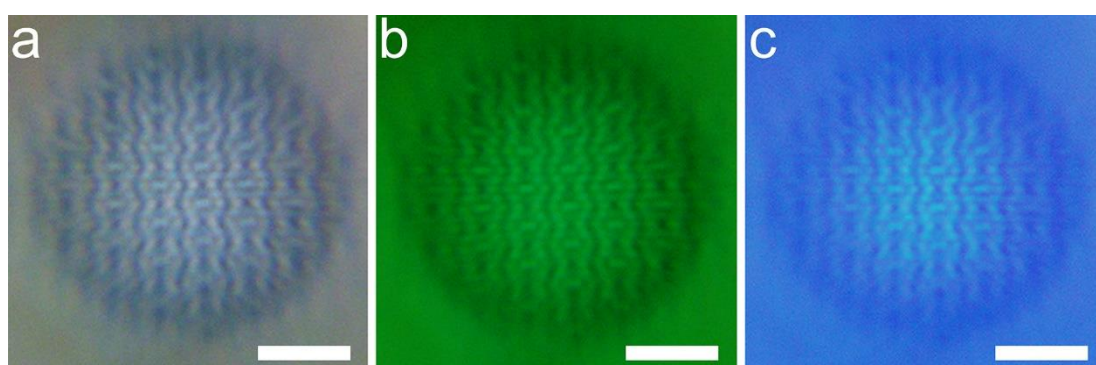


Figure 6.8 The super-resolution images obtained with a TiO_2 super-hemispherical mSIL. Optical micrographs of a TiO_2 super-hemispherical mSIL focused on the surface of a wafer pattern with 50 nm features (without gold coating) under an illumination of (a) white light, (b) green light ($\lambda \sim 540$ nm) or (c) blue light ($\lambda \sim 470$ nm), respectively. The super-hemispherical mSIL has a magnification factor of 3.0 and a width of 15 μm . The optical micrographs were taken using an Olympus BX63 light microscope. Scale bars, 5 μm in (a)-(c).

Arguably, the particle size of TiO_2 nanoparticles should have a profound influence on the performance of the as-fabricated TiO_2 mSILs. When 45 nm anatase TiO_2 nanoparticles were used as the building blocks, the TiO_2 nanoparticles-based transparent hemispherical mSIL revealed worse contrast and resolution than that from 15 nm TiO_2 , as shown in Figure 6.9 (b). This means that the smaller the nanoparticle size, the higher the super-resolution of the TiO_2 nanoparticle-derived mSIL is. This should be attributed to a couple of main reasons:

- **one is the nano-solid-fluid with smaller TiO_2 nanoparticles has better ability to infiltrate the smaller nano-patterns on the surfaces of the observed samples;**
- **The other is the hemispherical and super-hemispherical mSILs with smaller TiO_2 nanoparticles have higher refractive index of mSILs due to smaller air gaps inside.**

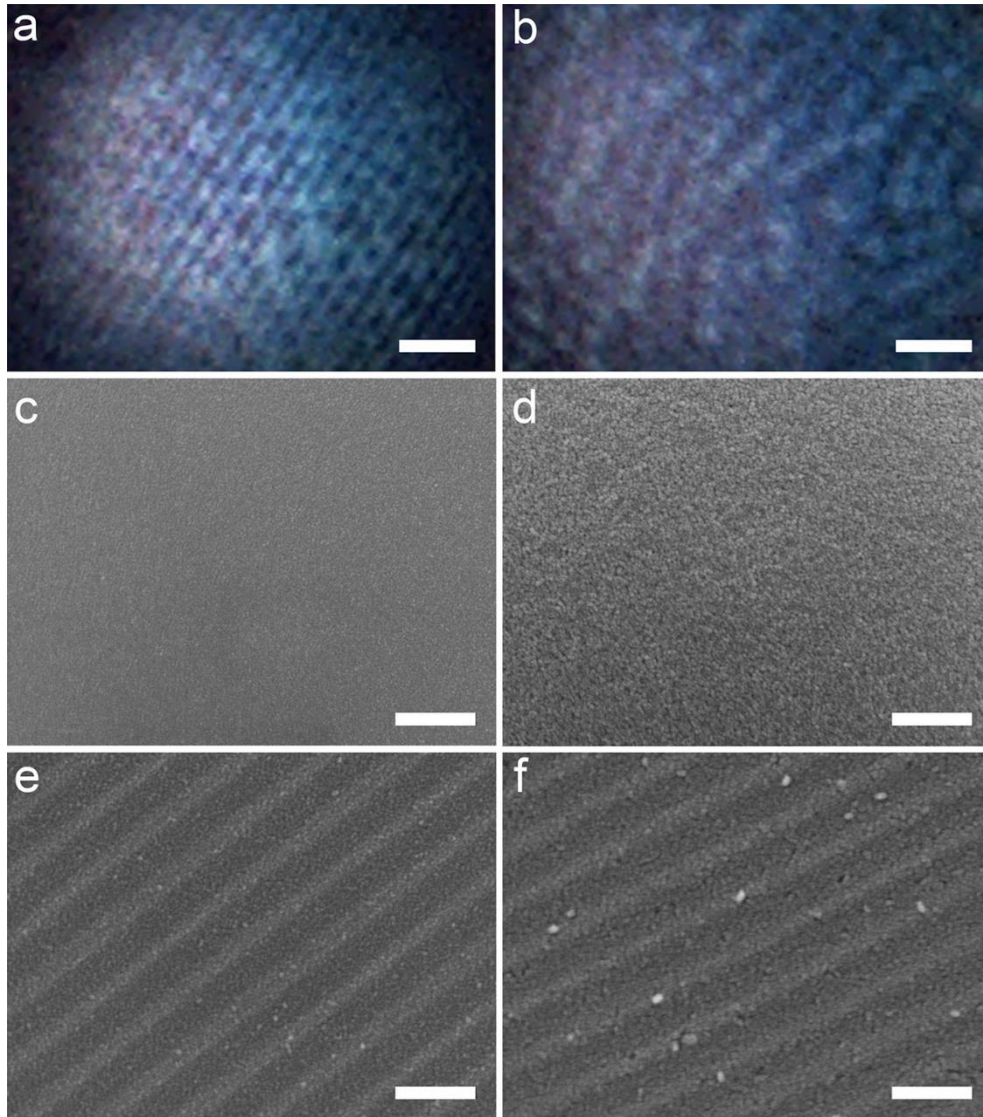


Figure 6.9 Comparisons of TiO_2 hemispherical mSILs assembled from 15 nm or 45 nm anatase TiO_2 nanoparticles. Optical micrographs of a Blu-ray disc observed through hemispherical mSILs composed of (a) 15 nm or (b) 45 nm anatase TiO_2 nanoparticles, respectively. High magnification SEM images of (c), (d) the top surfaces, and (e), (f) the bottom surfaces of the hemispherical mSILs composed of 15 nm or 45 nm TiO_2 nanoparticles, respectively. Scale bars, 2 μm in (a), (b) and 500 nm in (c)-(f).

6.3 ZrO_2/PS nanohybrid microsphere superlens

To date, microspheres coupled to optical super-resolution imaging were focused on commercial SiO_2 , PS and high RI BaTiO_3 . However, these spheres have either a low refractive index or poor processability, which make them little less attractive in practical applications. The imaging performance of microsphere superlens is mainly affected by the size and refractive index of the microsphere and surrounding medium, this was theoretically discussed

in **Chapter 4**. Precise control of these parameters is a challenging task but of fundamental importance to the further development of the technique. Introducing high RI inorganic nanoparticles into a polymer matrix may be a promising strategy to obtain high refractive index nanocomposites, which combine the advantages of an organic matrix (low weight, good impact resistance and excellent processability) and inorganic materials (high RI and good thermal stability)[156]. In fact, the high RI nanocomposite films[157]–[159] or bulk nanocomposites[160] have already been reported by some researchers. However, due to the arguable difficulty, the fabrication of high RI nanocomposite microspheres with high optical transparency for the super-resolution imaging has barely been reported to the best of our knowledge. In **Chapter 3.3.6**, a facial suspension polymerisation method for the preparation of optically transparent and high RI ZrO_2/PS nanohybrid colloidal microspheres was introduced. Compared with the femtosecond laser direct writing method, which is usually applied to the fabrication of lenses composed of low refractive index photosensitive molecules, the suspension polymerization method used here can fabricate spheres with high and controllable refractive index. Herein, as high as 50.8 wt% of ZrO_2 nanoparticles can be uniformly distributed in the final composite microspheres, which makes these colloidal microspheres have a controllable refractive index ($n_p = 1.590\text{--}1.685$). These microspheres were used for optical super-resolution imaging and features as small as 50–60 nm were clearly resolved.

6.3.1 Morphology and structure of the MPS/OA/ ZrO_2 nanocrystals and $\text{ZrO}_2/\text{Poly}(\text{St-co-DVB})$ composite microspheres

Figure 6.10 demonstrates the typical TEM images of the MPS/OA/ ZrO_2 nanoparticles. The sample was dispersed well in THF with a uniform crystal size of about 3.5 nm (Figure 6.10a). The high crystalline lattice of the nanoparticles, as shown in Figure 6.10 (b), belongs to the cubic phase (JCPDS: 27-991)[107].

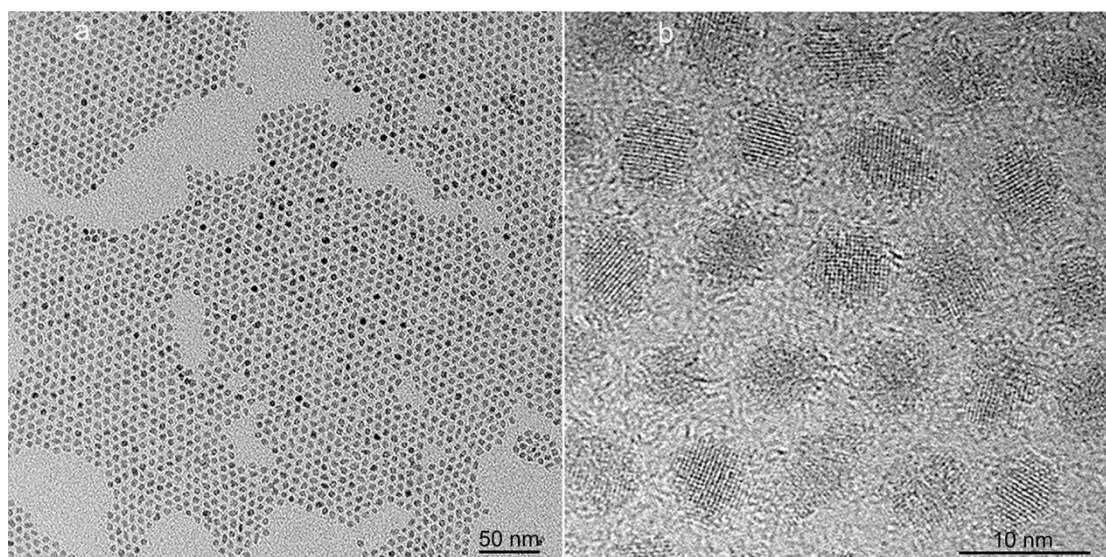


Figure 6.10 (a, b) TEM images of MPS/OA/ ZrO_2 nanoparticle under low and high magnifications.

The FTIR spectrum of MPS/OA/ ZrO_2 nanoparticles shows the absorption peaks at 500–700 cm^{-1} and 800–1100 cm^{-1} assigned to Zr-O and Si-O-Zr vibrations (Figure 6.11a), respectively, indicating that MPS has been chemically bonded to the ZrO_2 nanoparticles. The peaks at 1547 and 1460 cm^{-1} belong to the characteristic absorption of $-\text{COO}^-$ groups, meaning that OA has been chemically absorbed to the surface of ZrO_2 nanoparticles as well. The absorption peaks at 1719 cm^{-1} , 2923 cm^{-1} and 2852 cm^{-1} are attributed to carbonyl vibration, C-H vibration in $-\text{CH}_3$ and $-\text{CH}_2$, respectively. All these results unveil the successful modification of both MPS and OA on the surface of the ZrO_2 nanoparticles. The FTIR spectrum of ZrO_2 /PS nanohybrid microspheres (Figure 6.11 b) shows absorption peaks at 500–700 cm^{-1} for the Zr-O vibration, at 1451 cm^{-1} and 1492 cm^{-1} for the characteristic peaks of phenyl stretching vibration and at 757 cm^{-1} and 700 cm^{-1} for flexural vibration ($\delta_{\text{C-H}}$) of the benzene ring, which demonstrates the successful encapsulation of ZrO_2 in the hybrid microspheres.

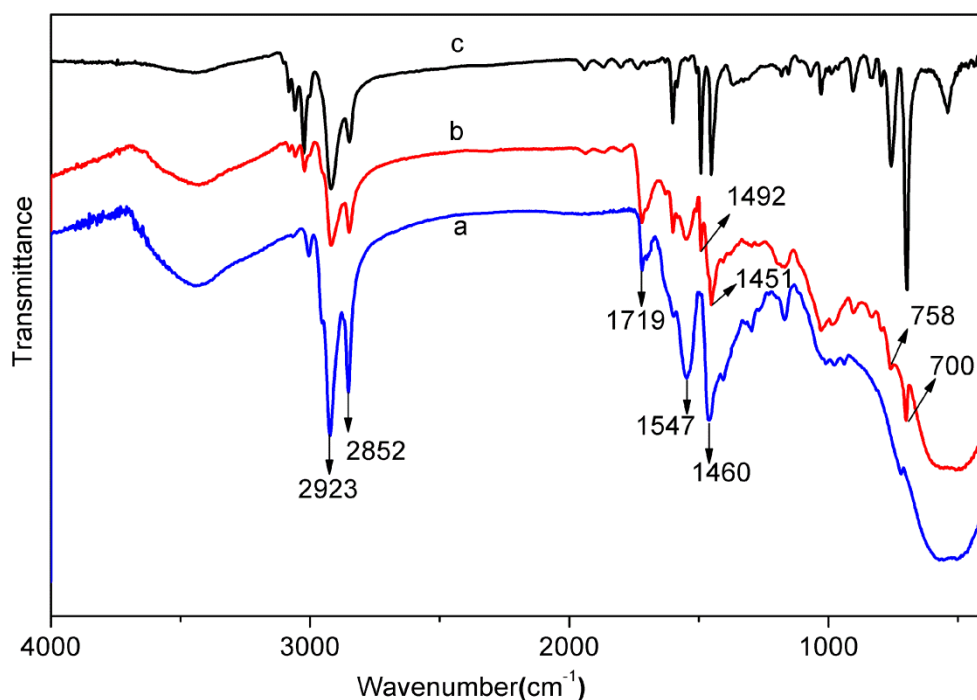


Figure 6.11 FTIR spectrum of (a) MPS/OA/ZrO₂ nanoparticles, (b) ZrO₂/PS nanohybrid colloidal microspheres and (c) pure PS microspheres.

Figure 6.12 (a-c) present the typical SEM images of the ZrO₂/PS nanohybrid colloidal microspheres M1, M3 and M5, which have a smooth spherical surface morphology. All the samples from M1 to M5 have smooth surfaces even at a high ZrO₂ content of 50.8 wt%, which can be further seen from their high magnification SEM images. The TEM images of the ultrathin sections, as shown in Figure 6.12 (d-i), further display that ZrO₂ nanoparticles are uniformly distributed at their primary size (~3.5nm) in the polymer matrix, even at as high as 50.8wt% of ZrO₂ content. This can ensure that the nanohybrid microspheres are highly transparent to visible light, which is necessary for microsphere superlenses to improve the resolution of optical microscopy.

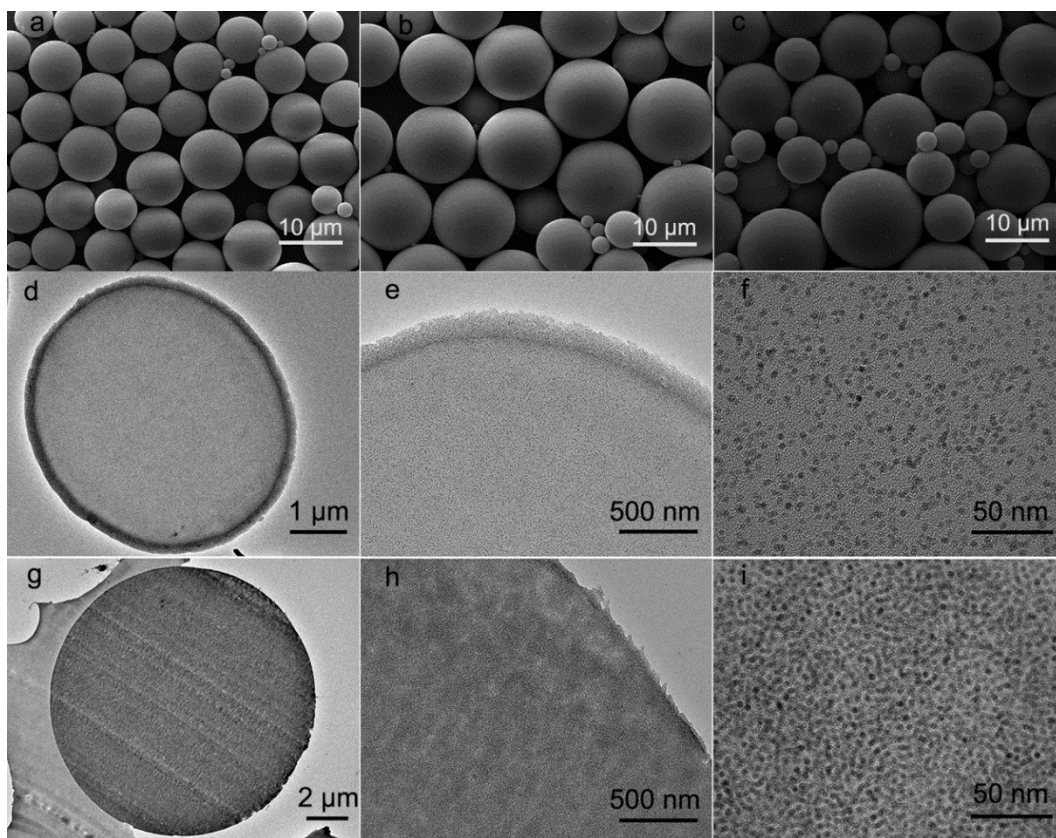


Figure 6.12 SEM images of ZrO_2/PS nanohybrid colloidal microspheres; (a)M1, (b)M3, (c)M5; TEM images of ultrathin sections of M1(d, e, f) and M5(g, h, i)

Typical SEM mapping graphs of the nanohybrid colloidal microsphere clearly reveal the existence of Zr, C, and O elements in hybrid microspheres (Figure 6.13 a–d), with well-defined spherical structure. A SEM linescan of the individual microsphere further demonstrates the uniform distribution of Zr in the microsphere (Figure 6.13 e). From the corresponding linescan spectrum in Figure 6.13 (f), the relative weight contents of Zr, C, and O are found to be 36.0%, 49.6%, and 14.4%, respectively. The composition of samples M1–M4 were also analysed by SEM linescan analysis. All the samples show uniform distribution of Zr, C, and O in the hybrid microspheres, and their relative weight contents of Zr, O, and C are summarized in Table 6.1.

Sample code	Zr (wt%)	O (wt%)	C (wt%)
M1	5.79%	4.64%	89.57%
M2	14.95%	6.88%	78.17%
M3	19.26%	10.12%	70.62%
M4	27.35%	11.57%	61.08%
M5	35.99%	14.40%	49.61%

Table 6.1 SEM linescan results of Zr, O, and C content in M1~M5.

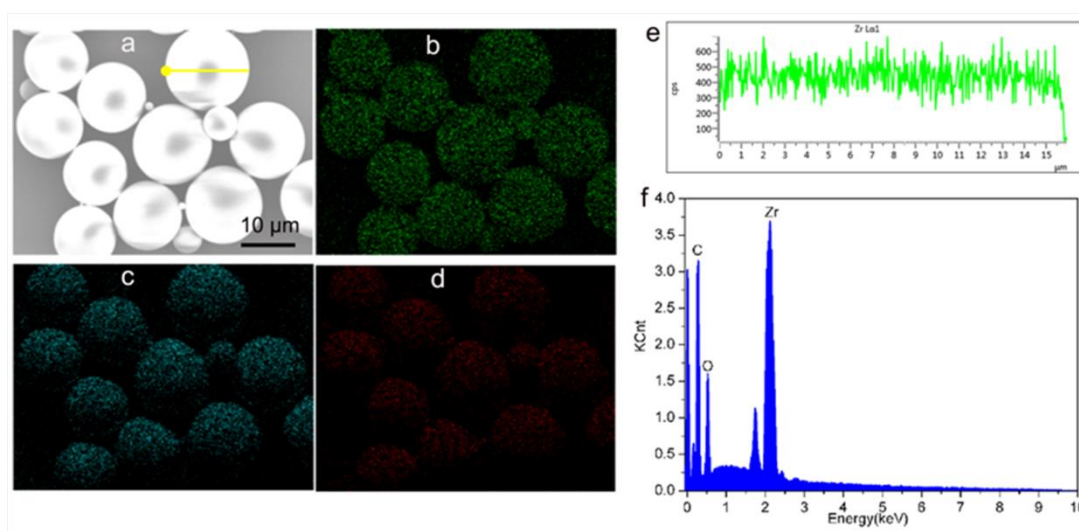


Figure 6.13 SEM image (a) and SEM mapping photographs of Zr (b), C (c) and O (d) in the nanohybrid microspheres M5; a yellow line is stretched across a selected microsphere in the top left SEM image for SEM linescan element analysis. (e) SEM linescan element distribution of Zr in the selected microsphere of M5. (f) The corresponding linescan EDX spectrum of the microsphere.

Figure 6.14 shows the thermogravimetric analysis (TGA) results of the modified ZrO_2 nanoparticles and ZrO_2/PS composite microspheres M1–M5. The weight loss of the modified nanoparticles below 200 °C is 1 wt%, which is attributed to the loss of physically absorbed water and organic solvent. The weight loss between 200 and 800 °C is 25 wt%, corresponding to the chemically bonded OA and MPS on the ZrO_2 nanoparticles. The residual inorganic substances are about 10.5, 23.5, 30.3, 38.2 and 50.8 wt% for samples M1, M2, M3, M4, and M5, respectively, and are mainly composed of ZrO_2 .

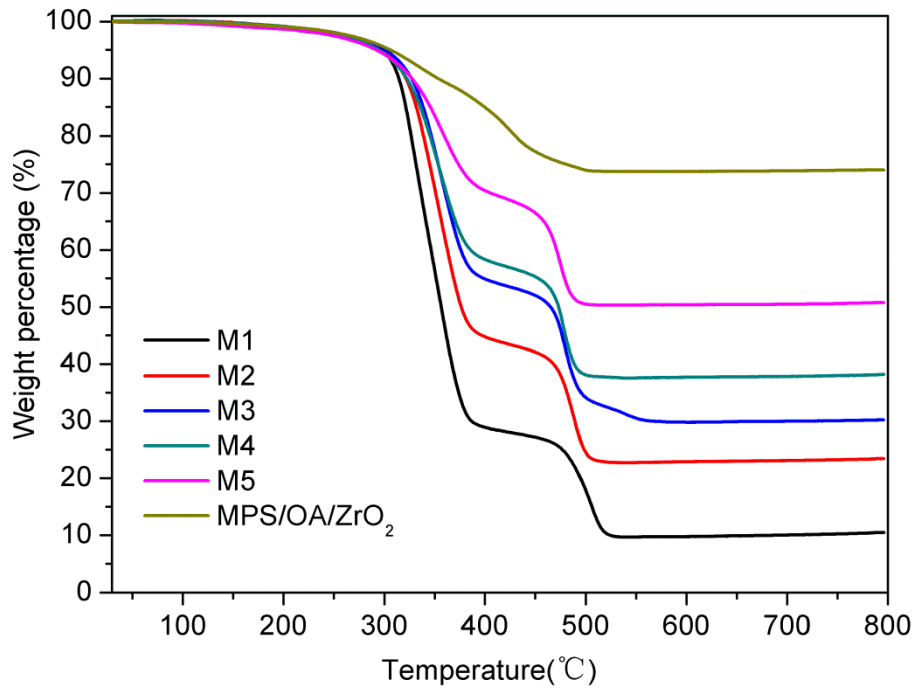


Figure 6.14 TGA curves of MPS/OA/ZrO₂ nanoparticles and ZrO₂/PS nanohybrid colloidal microspheres M1-M5.

The refractive index of M0–M5 could be theoretically estimated according to the following formula:

$$n_p = n_{org} \times V_{org} + n_{ZrO_2} \times V_{ZrO_2} \quad 6.1$$

where n_{org} and n_{ZrO_2} are the refractive indices of polymer ($n_{org} \approx 1.59$) and ZrO₂ nanoparticles ($n_{ZrO_2} \approx 2.2$). V_{org} and V_{ZrO_2} are the volume fractions of polymer and ZrO₂ in the microspheres. Based on the TGA analysis, the theoretical refractive indices were calculated to be 1.590, 1.600, 1.622, 1.634, 1.651 and 1.685 for samples M0–M5, respectively.

Sample code	M0	M1	M2	M3	M4	M5
theoretical refractive index	1.590	1.600	1.622	1.634	1.651	1.685

Table 6.2 Theoretical refractive index of M0~M5.

6.3.2 Super-resolution imaging: wide-field mode and white light illumination

The experimental configuration of microsphere nanoscope under white light illumination is shown in Figure 6.15 (a). The semi-immersed microspheres collect the underlying near-field information of the substrate, magnify it and form a magnified virtual image located at certain position below the surface of the substrate which can be picked up by a 100x objective lens (NA=0.8, Olympus BX63). Dimethyl silicone is used as the medium to reinforce the imaging contrast. Compared with liquid solvents such as ethanol or isopropyl alcohol, it is less volatile and can easily spread on the substrate. The distribution of dimethyl silicone around the microsphere is shown in the three-dimensional picture in Figure 6.15 (b). The substrate is an IC chip with nano-patterned structures of 60 nm and 75 nm gaps between specific stripes with widths of 115 nm and 145 nm respectively, which are indicated by the arrows in the SEM image in Figure 6.15 (c).

According to the diffraction limit, $d=0.5\lambda/NA$, in which λ is the illumination wavelength and NA is the numerical aperture of the objective lens. The resolution limit is 344 nm under white-light illumination, which peaked at $\lambda= 550$ nm and $NA = 0.8$ for the optical microscopy used here. Obviously, this microscopy cannot resolve the nanoscale surface features of the chip. However, when the dimethyl-silicone semi-immersed microspheres (diameter = 10 μm) are used as a superlens, the imaging resolutions of the microscope are obviously improved. Nonetheless, the pure polymer microspheres M0 ($n_p=1.590$) and hybrid microsphere M1 ($n_p = 1.600$) still cannot resolve 75 nm gaps (indicated by the arrows in Figure 6.15 d and e). With the increase in refractive index of the microspheres, 75 nm gaps between three stripes with a width of 145 nm can be clearly discerned (Figure 6.15 f and g). As the diameter of the nanocomposite microsphere is increased, with the sample M5 as an example, not only can the 75 nm features be observed, but the imaging windows significantly increase, as shown in Figure 6.15 (h–k). The only drawback is that the dimethyl-silicone semi-immersed microspheres still cannot image the texturing structure with 60 nm gaps.

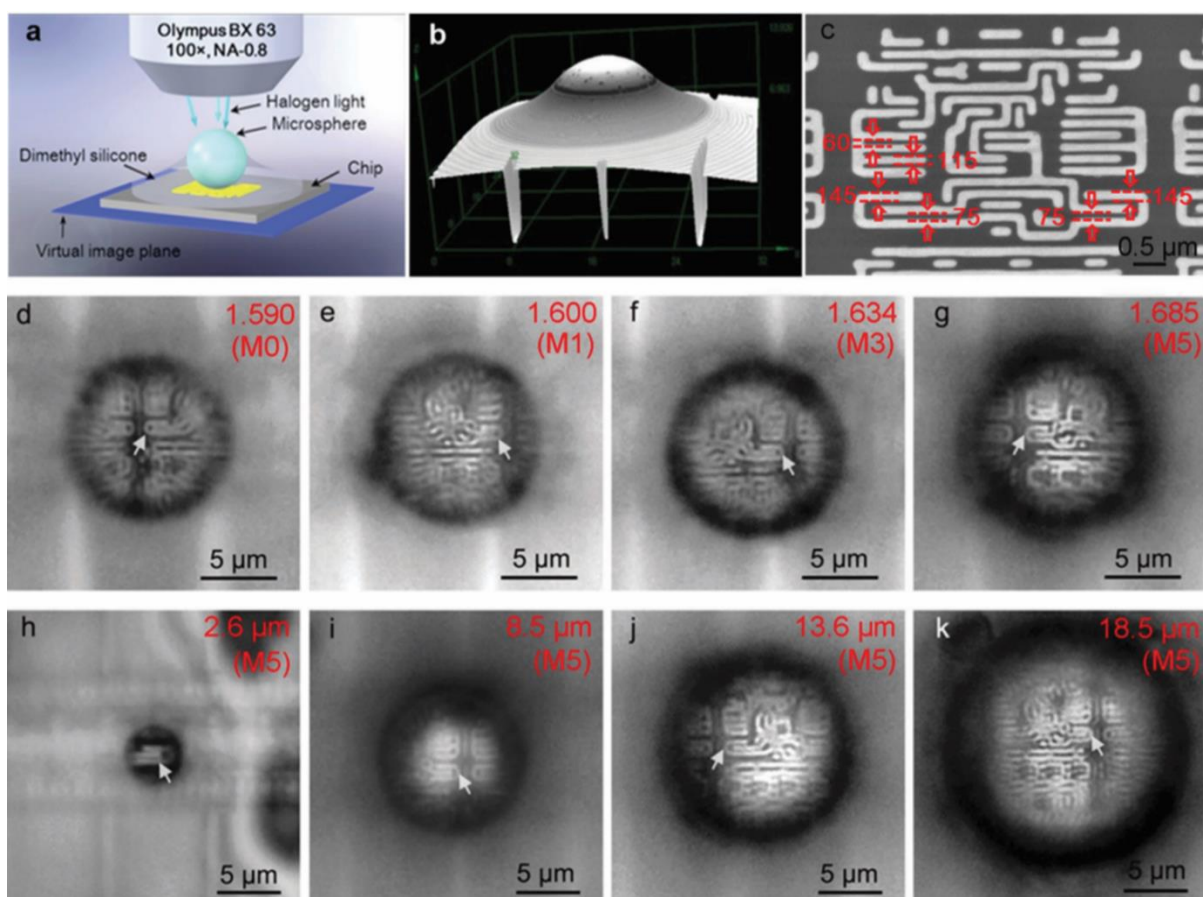


Figure 6.15 (a) Schematic of the dimethyl-silicone semi-immersed microsphere for super-resolution imaging under white-light illumination; (b) three dimensional image showing the distribution of dimethyl-silicone around the sphere; (c) SEM image of the nano-patterned chips with 75 nm and 60 nm gaps between 145 nm and 115 nm wide stripes; (d–g) optical super-resolution imaging of nano-patterned chips by M0 (1.590), M1 (1.600), M3 (1.634), and M5 (1.685) in the same diameters of 10 μm ; (h–k) optical super-resolution imaging of the chips by M5 with different diameters of 2.6 μm , 8.5 μm , 13.6 μm , and 18.5 μm , the corresponding imaging magnifications of these pictures are x2.41, x2.31, x2.10, and x2.08, respectively. The white arrows in (d–k) indicate the location of the structure containing 75 nm gaps in the image.

To further improve the image resolution, cedarwood-oil was used as the immersion medium instead of dimethyl-silicone for observing the chips with 60 nm gaps between four 115 nm wide stripes (Figure 6.16 a). The three-dimensional images of the microspheres semi-immersed in cedarwood-oil are shown in Figure 6.16 (b). All the microspheres M0, M1, M3, and M5 have almost the same diameter of $\sim 13 \mu\text{m}$ and can resolve the 75 nm gaps between three 145 nm wide stripes of the chips (Figure 6.16 c–e), but only the microsphere M5 with the highest refractive index can resolve the 60 nm gaps of the chip (Figure 6.16 f). These results further demonstrate that the microspheres with higher refractive index produce

higher resolution and imaging quality compared to those with low refractive index microspheres. The reason is explained below.

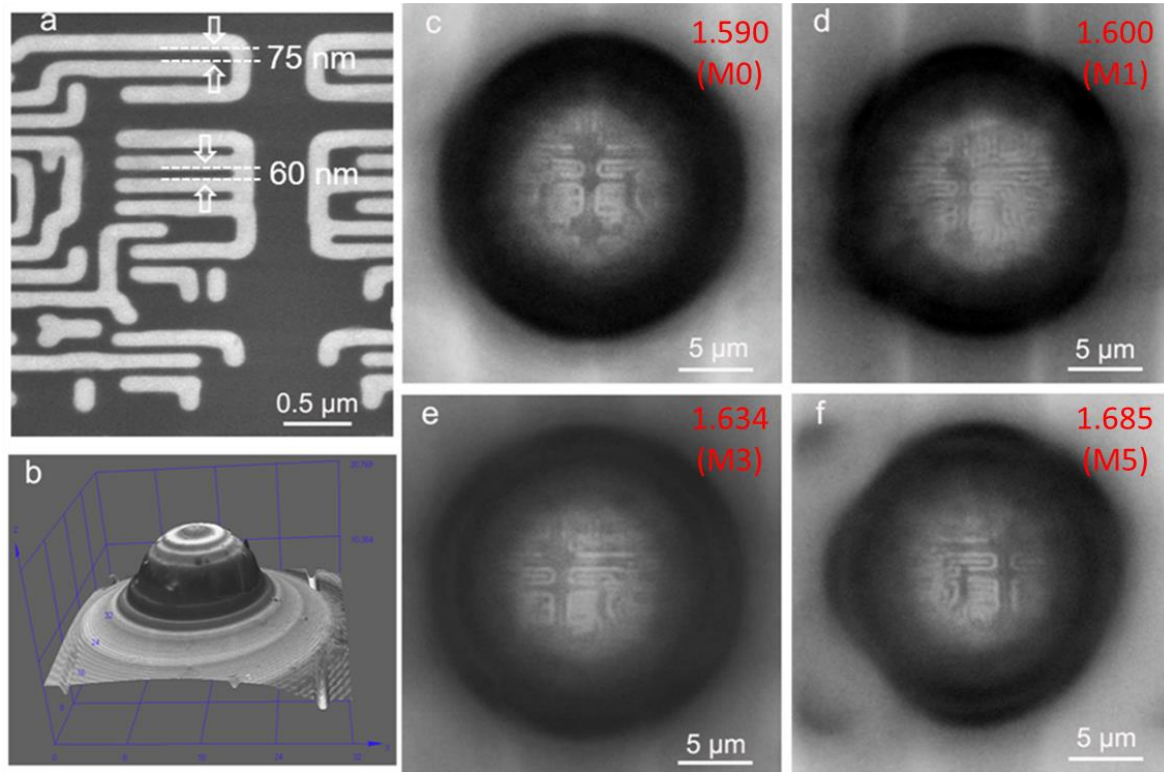


Figure 6.16 (a) SEM image of the nano-patterned chips with 60 nm gaps between four 115 nm wide stripes; (b) three dimensional image showing the distribution of cedarwood-oil around the sphere; (c-f) optical super-resolution imaging of the chips by M0, M1, M3, and M5, respectively, the dotted bordered rectangles in these pictures indicate locations of the structure containing 75 nm and 60 nm gaps between 145 nm wide stripes (upper three stripes) and 115 nm stripes (lower four stripes).

6.3.3 Super-resolution imaging: confocal mode and laser illumination

Furthermore, we investigated the imaging behaviour of the microsphere coupled confocal microscopy. As shown in Figure 6.17 (a), the chip has a periodic structure with minimum gaps of 50 nm. This nanotexturing cannot be resolved by confocal microscopy (Olympus OLS4100 LEXT) with a 100x and NA = 0.95 objective at the laser illumination of $\lambda = 405$ nm (Figure 6.17 b). However, when the dimethyl silicone semi-immersed microspheres M1, M3, and M5 with almost the same diameters of 13.3 mm were placed on top of the chips, the 50 nm gaps can be resolved (Figure 6.17 c-e). As the refractive index of the microsphere increased from 1.600 to 1.634 and 1.685 for spheres of M1, M3 and M5, the corresponding image magnifications

increased from 1.50 to 1.81 and 2.05, respectively, indicating that microspheres with higher refractive index can produce better super-resolution imaging.

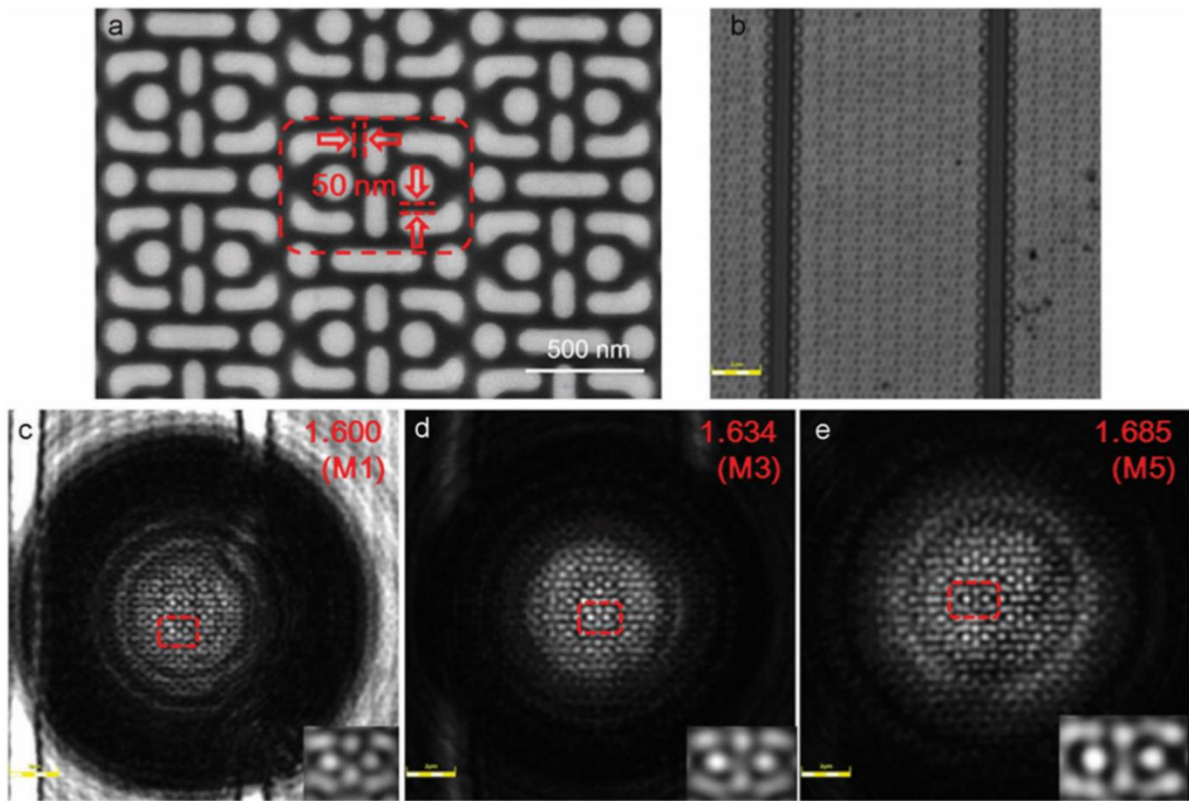


Figure 6.17 (a) SEM image of the chip with periodic structures containing 50 nm gaps; (b) confocal image at $\lambda = 405$ nm of the same chip in (a); (c-e) imaging of the chips at $\lambda = 405$ nm through 13.3 mm spheres of M1, M3, and M5, respectively; the dotted bordered rectangles in these images indicate locations of the structure containing 50 nm gaps that are resolved by these spheres, the corresponding magnified images are shown in the bottom right corners. The parameters of the objective lens are 100x, NA = 0.95, and the bars are 2 mm in (b–e).

6.4 Conclusion

Based on the results above and discussion, we have shown, for the first time, TiO_2 nanoparticles can be used to assemble low-loss all-dielectric metamaterials working over the entire visible spectrum. Owing to the densely packed structure of deep-subwavelength-sized TiO_2 nanoparticles, the metamaterial can achieve both high refractive index and high transparency. The nano-solid-fluid assembly method is a simple and versatile way to assemble TiO_2 nanoparticles or even other dielectric nanoparticles into arbitrarily shaped metamaterial-based photonic devices. The increase in the height-to-width ratio of TiO_2 mSILs can enhance the magnification factor but weaken the contrast of the virtual image. The field

of view of the virtual image is found to be linearly proportional to the width of mSILs. Using a standard white light illumination microscope, the super-hemispherical mSILs can realize a super-resolution of 45 nm. Furthermore, it can provide a significantly widened field of view compared to the microsphere-based lens.

The super-resolution of mSILs is readily expected to be further improved by increasing the refractive index of nanoparticles, for example, by using rutile TiO_2 nanoparticles ($n=2.7$) or smaller anatase TiO_2 nanoparticles. Moreover, combined with some modern microscopy techniques, such as scanning laser confocal microscopy[72] and super-resolution fluorescence microscopy, the as-fabricated TiO_2 mSILs may realize the optical observation of sub-10-nm objects, such as DNA and proteins. Thus, the TiO_2 nanoparticle-based mSILs presented here are useful for bio-imaging, near-field lithography, whispering gallery mode microcavity, high-density optical data storage and enhanced fluorescence detection[161], [162]. The NSFA we have described is simple and versatile, and can be readily extended to assemble other inorganic or organic nanoparticles into transparent hemispheres and super-hemispheres with various refractive indexes or functionalities for optical microscopes or other devices. Finally, in addition to transparent hemispheres, arbitrarily shaped structures, *e.g.* transparent spheres, transparent wires, bowls, etc., can also be fabricated (see Supplementary), suggesting potential applications in optical nanoscopy, optical fibres, etc.

In addition, a novel type of nanohybrid colloidal microspheres with high refractive index and optical transparency have been successfully synthesised through suspension polymerisation of MPS and OA modified ZrO_2 nanoparticles with styrene. Because these modified ZrO_2 nanoparticles have very good compatibility and reactivity with the monomers, as high as 50.8 wt% of ZrO_2 nanoparticle can be homogeneously dispersed in the hybrid microspheres. When this new class of high refractive index and optically transparent ZrO_2/PS hybrid microspheres are used as a superlens, the dimethyl-silicone oil semi-immersed microspheres can discern surface features at 75 nm, and the cedarwood-oil semi-immersed microspheres can reach a super-resolution imaging of 60 nm under white-light microscopy. Under laser illumination at $\lambda=405$ nm, these microspheres can even resolve more complicated structures with 50 nm gaps. The synthesis of hybrid microspheres is feasible, easily repeatable and designable in shape, size and refractive index. Accordingly, the approach that we have described here is quite general, and can be readily extended to prepare a series of hybrid microspheres with

various refractive index and optical transparency, by changing the types of polymers and nanoparticles. The as-synthesized nanohybrid colloidal microspheres can be used not only in optical nanoscopes for super-resolution imaging with visible frequency, but also in some potential fields of nanolithography, optical memory storage, and optical nano-sensing.

Chapter 7. Superlensing Microscope

Objective Lens

To improve the usability of superlens, we present in this chapter an innovative design that integrate the conventional objective lens with microsphere superlens, and demonstrates its application in scanning imaging of different samples in super-resolution. The new integrated superlens was also used for nano-patterning applications.

7.1 Introduction

The imaging window of a microsphere lens is often very small, typically a few micrometres only. This requires a scanning operation of the microsphere superlens to generate a complete image of a sample. There are a few demonstrations in the literature. Krivitsk et al. attached a fine glass micropipette to the microsphere lens to scan the particle[73]. Li et al. designed ‘swimming lens’ technique in which microsphere lens was propelled and scanned across sample surface by chemical reaction force in a liquid[74]. We proposed a coverslip superlens by encapsulating high-index microspheres (BaTiO_3) inside a transparent host material (such as PMMA and PDMS) [80], detail fabrication procedure can be referred to **chapter 3.3.2**. This concept was also explored extensively by Darafsheh and Astratov et al. in the US [13], [163], [164]. The coverslip superlens can be manually manipulated in a way similar to classical coverslip, offering the freedom to position particle lens at desired location. Scanning of microsphere superlens, however, requires synchronisation with microscope objective for full super-resolution image construction. This is difficult to achieve with existing design of coverslip superlens which is separated from objective lens. In this chapter, we propose an improved design which solves the synchronisation problem between coverslip superlens and objective lens. The idea is simple yet effective, using a custom-made lens adaptor to integrate these two lenses to form a superlensing microscope objective lens. Meanwhile, apart from its use in imaging, possibility of other application was proposed. This new design is easy to be adapted to a laser marker system, thus offering a new potential near-field approach for arbitrary shape nano-patterning.

This chapter is organised as follow; Section 2 illustrates the superlensing microscope objective and its working conditions; Section 3 demonstrates its imaging performance under both static and scanning modes; Section 4 discusses the mechanism; Section 5 presents its potential abilities for arbitrary shape nano-scale patterning with assist of laser maker; And section 6 will conclude this chapter work.

7.2 Superlensing microscope objective

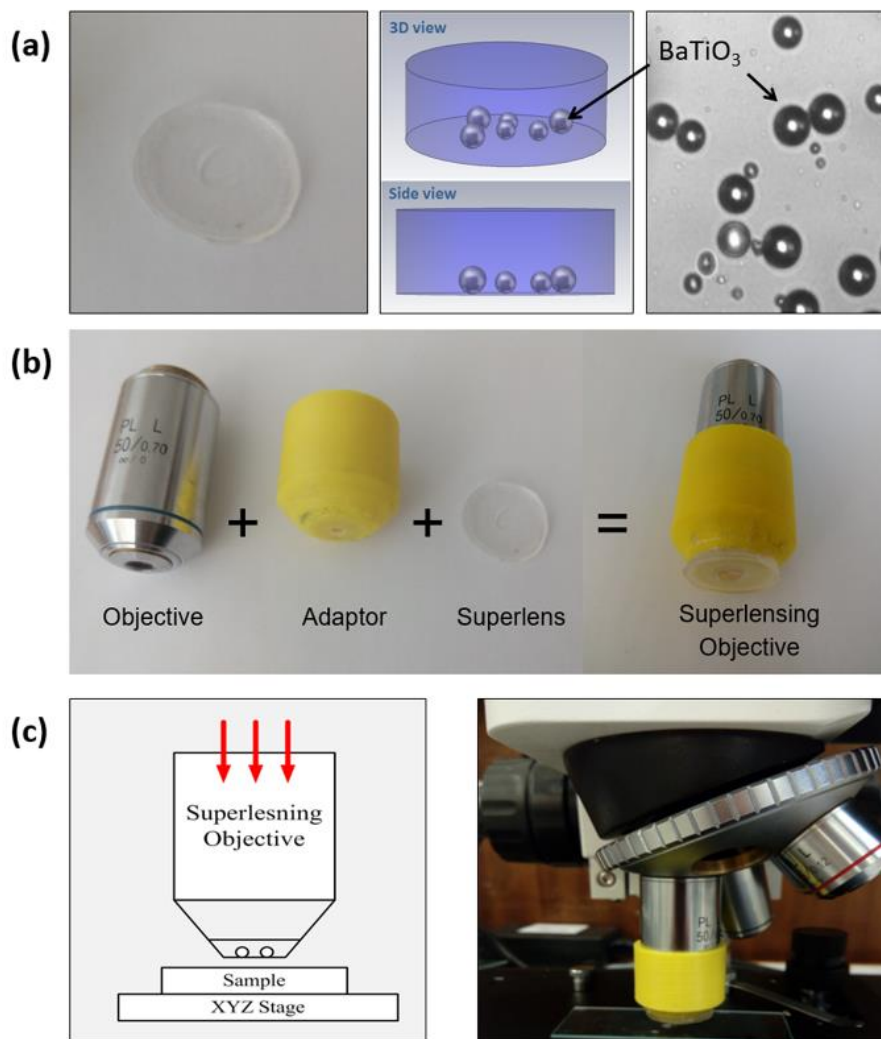


Figure 7.1 Superlensing objective lens. (a) The BaTiO₃ superlens was fabricated by encapsulating a monolayer of BaTiO₃ microsphere (3-80 μm diameter) inside a PDMS material. (b) the super objective was made by integrating a conventional microscope objective lens (e.g. 50x, NA: 0.70, or 100x, NA:0.95) with a BaTiO₃ microsphere superlens using a 3D printed adaptor (c) Experimental configuration for super-resolution imaging using developed objective which was fitted onto a standard white light optical microscope.

The key concept and design of superlensing microscope objective is illustrated in Figure 7.1(b) and (c). A conventional microscope objective (OB) lens with magnification factor between 40x and 100x, NA between 0.7 and 0.95 was selected. A lens adaptor was designed in CAD software (e.g. Solidworks) and then printed with a 3D plastic printer (model: Prusia I5). The adaptor has a tube size fit to the objective lens tube, with reasonable friction allowing up-down adjustment. A coverslip superlens (Figure 7.1a) was bounded to the bottom end of the adaptor using high-adhesive glue. This results in an integrated objective lens consisting of conventional OB and a Coverslip Microsphere Superlens (CMS). The imaging resolution will be determined by the coverslip superlens while the conventional objective lens provides necessary condition for illumination. The obtained superlensing lens can be easily fitted to any existing conventional microscopes; in this study, we used two brands of optical microscopes to prove the lens's flexibility (Olympus BX60 and a low-cost ICM100 microscope) in usage.

The scanning was performed using a high-resolution nano-stage (model: PI P-611.3 Nanocube), with 1 nm resolution in XYZ direction, travel range 100 μm . Samples (Blu-ray disc, semiconductor chip, virus on glass slider) were firmly bonded to the nano-stage using high-strength double-side sticking tape. In experiments, the superlensing objective lens was kept static and the underlying nano-stage moves and scans the samples across the objective lens. The imaging process was video recorded using a high-resolution camera (ToupCAM UCMOS 14000KPA). The video was then analysed, and frames were used to generate a stitched image of the sample. The focusing properties of developed superlens were analysed using classical Mie theory.

7.3 Superlensing objective lens in static and scanning imaging performance

7.3.1 Static Imaging

The superlensing objective lens was carefully adjusted to maximum imaging contrast and image quality. The main adjustments include the followings: (1) the lens adaptor was adjusted so that the top objective lens will pick up virtual image generated by the bottom coverslip microsphere superlens. (2) Light illumination angle was adjusted, roughly an angle between

10-40 degree will produce enhancement in image quality, this is because the magnification factor is increasing with incident angles and there is a compromise between image quality and magnification factor[165]. Best imaging resolution is obtained in contacting mode where lens and samples contact with each other. The resolution was found to decrease rapidly when lens move away from the sample surface, at about wavelength distance (~ 600 nm) away the super-resolution was completely lost (due to loss of evanescent wave contribution) which indicates the near-field nature of the technique. This inversely poses a technical challenge in scanning imaging as will discussed below.

In contacting mode, we carried out super-resolution imaging of several different samples, including Blu-ray disc with 100nm/200nm features and adenoviruses (replication deficient human adenovirus serotype 5 vector) with size about 90-100 nm. Noting superlensing objective lens in these tests could be slightly different from each other, with aim of demonstrating the ability of achieving super-resolution with different lens configurations. As previously mentioned, the overall resolution is determined by Coverslip Microsphere Superlens (CMS) which consists of BaTiO_3 microsphere (3-100 μm) inside PDMS sheet. Figure 7.2(a-c) demonstrate Blu-ray disc imaging using the developed superlensing objectives. In Figure 7.2(a), the SEM image reveals the disc consists of 200 nm gratings separated 100 nm away. Figure 7.2(b-c) show the images obtained using Olympus BX60 microscope equipped with developed superlensing objective lenses with following parameters: Figure 7.2(b) with OB (100x, NA 0.90) + CMS (67 μm BaTiO_3 in PDMS) and Figure 7.2(c) with OB (100x, NA 0.90) + CMS (22 μm BaTiO_3 in PDMS). As can be seen, both lenses can clearly resolve the 100 nm features, which is beyond the classical diffraction limit of 300 nm. The smaller diameter BaTiO_3 superlens in Figure 7.2(c) offers a larger magnification factor ($M \approx 6\times$) over the larger size BaTiO_3 superlens ($M \approx 2\times$) in Figure 7.2(b). This is caused by the shorter focal length of a smaller sized microsphere lens in virtual imaging mode [12]. The central zone of the resulting image appears a bit over-exposed in Figure 7.2(b) due to reflected beam by the Blu-ray substrate. This phenomenon is less obvious in smaller particles (Figure 7.2(c)). In microsphere superlens imaging, artificial images are always an issue and one should pay particular attention to it. The artificial images can be excluded by rotating the imaging samples.

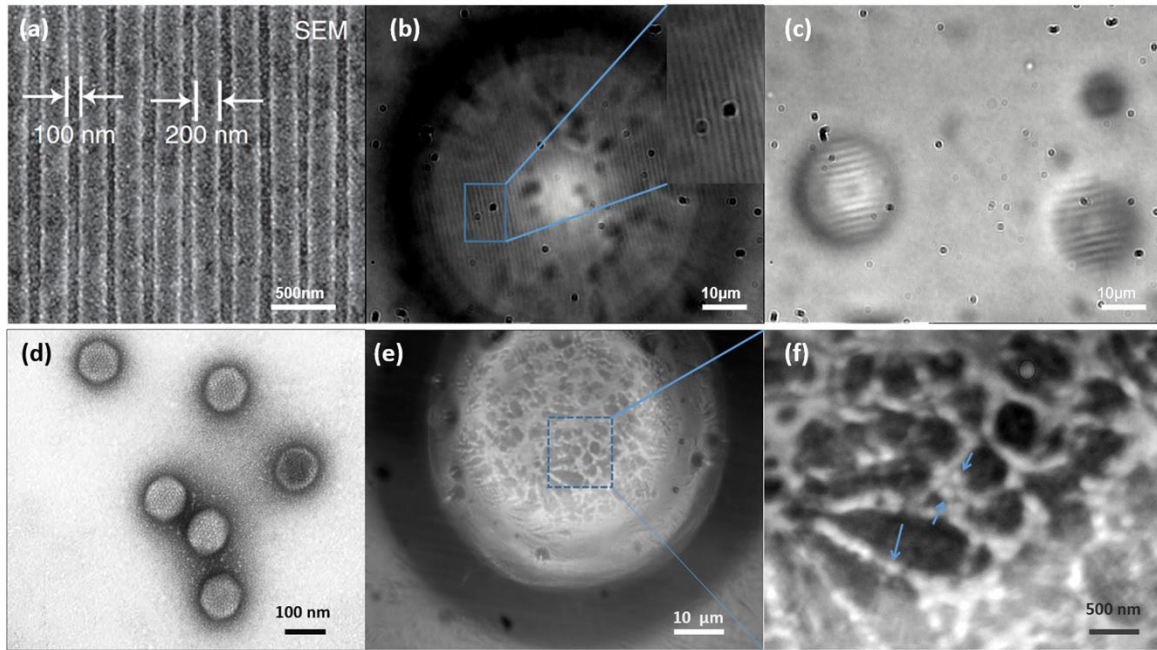


Figure 7.2 Static super-resolution imaging of Blu-ray and virus by superlensing objective lens. (a) SEM image of Blu-ray disc. (b) 67 μm BaTiO₃ superlens imaging. (c) 18 μm BaTiO₃ superlens imaging. (d) SEM of adenovirus. (e) 70 μm BaTiO₃ superlens imaging of virus cluster. (f) Enlarged view of section of (e).

Let's turn our eye on another sample, the adenoviruses sample. These virus particles are nearly spherical in shape with diameter around 90-100 nm (Figure 7.2 d), and they are sub-diffraction-limited and is difficult to be observed using conventional microscopes. Figure 7.2(e) shows super-resolution image obtained using a superlensing objective lens formed by 80x, NA 0.90 objective and 70 μm BaTiO₃ microsphere. The viruses are aggregated in clusters in our sample, but it was possible to isolate them by zoom in the image. The magnified particle size is about 200 nm in Figure 7.2(f), which means the real virus size is around 100 nm since the 70 μm BaTiO₃ superlens offers a magnification factor around 2 under experimental condition. Comparing to Figure 7.2(b), here the central zone doesn't have a bright spot due to reflection by underlying substrate, this is because virus particles are deposited on a glass slider which is transparent, and has much less reflection compared to Blu-ray disc.

7.3.2 Scanning Imaging and Image Stitch

In our superlensing objective lens, the microsphere superlens is synchronized with objective lens. During scanning operation, both parts of the lens will move together and simultaneously, their relative position is kept constant. This is beneficial to scanning imaging since it was ensured same particle lens was used in imaging. It is also possible to have multiple particle lenses in parallel for simultaneously scanning imaging. In experiments, we evaluated scanning imaging of different samples, including the adenovirus samples. However, due to lens-sample contacting requirements, we have met some difficulty in scanning imaging of virus samples, since the virus particles were dragged by the lens during scanning. This is due to the virus particles are not well fixed onto the glass slides. This may not be the case for cell sample which could be immobilized on glass slides and is the plan of our next step experiments. In this study, we have used a simple well-structured semiconductor IC chip to demonstrate the feasibility of scanning imaging using developed superlensing objective lens. This was shown in Figure 7.3. To reduce the friction between lens and sample, we evaluated different lubricant medium including DI water, IPA, silicone oil, and WD40. WD40 produces best lubrication effect so that it was used in Figure 7.3 scanning experiments. The IC chip in Figure 7.3(b) has features of 200 nm and 400 nm, which are easy to be observed using the new lens. The scanning process was video recorded (video at: <https://www.youtube.com/watch?v=GoS7JVNFLpk>). Comparing Figure 7.3(c-e), we can see the scanning takes place along the indicated scanning direction in Figure 7.3(c), and high-resolution images were taken at different spatial positions. Stitching images produces a larger-sized picture covering scanned sample regions of interests following the scanning path (see demonstration in insets of Figure 7.3(d,e)). The in-house developed image stitching code based on MATLAB language works automatically for a sequence of frames with moderate movement between adjacent frames. The location and size of a superlens imaging region in the first image frame are specified. In the subsequent frames, the location can change gradually. To compensate for this, with the assumption that superlens imaging regions are in focus and thus contain more image features, the algorithm searches in the neighbourhood of the location from the previous frame to find the region with most significant total edge strengths. For each extracted region, radial distortion correction is applied. The correction parameter is estimated based on images with regular grid structure (e.g. an image on the IC chip). From the first extracted region, the images are stitched

sequentially, and the optimal offset between adjacent extracted regions is calculated based on maximizing the normalized cross correlation. This criterion works more effectively than e.g. sum of squared differences because it copes with variation of image brightness better. The stitched images are obtained by integrating pixels from all the extracted regions with corresponding offsets applied. To avoid visible boundaries between regions from different frames, alpha blending is used such that for the stitched image pixels where multiple source regions overlap, a combination of their contributions is used. Similar scanning experiments also were performed with a Blu-ray disc sample (Figure 7.3 f) where the stitched image was shown in Figure 7.3(g).

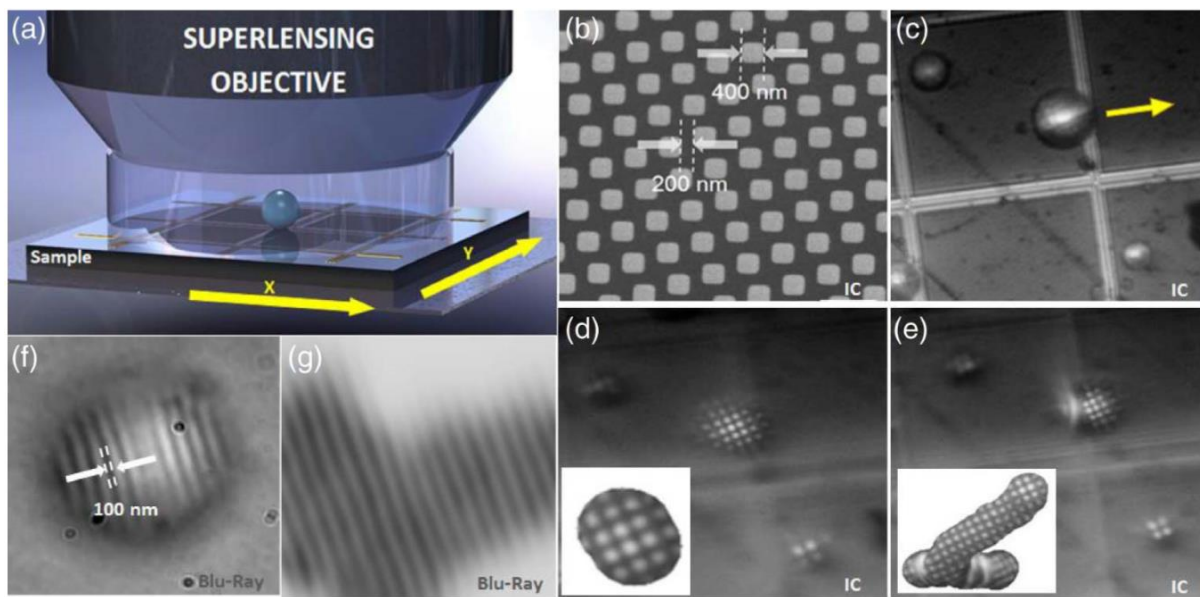


Figure 7.3 Scanning super-resolution imaging and image stitch. (a) Scanning schematics. (b) Scanning direction of IC chip sample (c) SEM of IC chip. (d) IC scanning image position 1. (e) IC scanning position 2. Insets show stitched image following scanning paths. (f) Blu-ray sample imaged by microsphere. (g) Stitched image of Blu-ray scanning.

7.4 Mechanism and discussion

Light interaction with spherical particles can be simulated using the classical Mie theory. Figure 7.4 shows examples of calculated electric field intensity $|E|^2$ distribution across a cross-sectional plane of an 18 μm and a 67 μm BaTiO₃ microsphere ($n=1.90$) embedded in PDMS ($n=1.40$) under different illumination wavelengths, covering the 400 nm to 700 nm spectrum range of a typical white lighting source. The corresponding size parameter for each case, defined as $q=\pi D/\lambda$, where D is the particle diameter and λ the wavelength, was also indicated

in the figure. A video was provided (see <https://www.youtube.com/watch?v=Xu4xzRRSYDY>) that offers a systematic view of the evolution of field distribution for size parameters $0.1 \leq q \leq 628$, with a step accuracy of $\Delta q = 0.1$. From Figure 7.4 we can see, in addition to the well-known photonic nanojet-focusing modes by microspheres (Figure 7.4 a, c, d, f), strong internal focusing modes featuring hugely enhanced intensity peaks inside the particle could be excited at particular wavelengths (Figure 7.4 b and e). All these modes will play a role in super-resolution image formation.

The imaging sample in contact with microsphere is illuminated by the microsphere lens; super-resolution arises from the strong near-field interaction between the microsphere lens and the underlying nano-objects, which leads to the conversion of surface-bounded high spatial frequency evanescent waves into propagating waves[87], [166]. Such an interaction process is quite complex and is out of the scope of Mie theory. An example calculation for the coupled microsphere-substrate system was demonstrated in a previous publication [87] using a full-wave simulation approach. It was noted that such a conversion process is sensitive to the substrate properties and the gap distance between lens and object. The technique requires a gap distance below the wavelength scale and, ideally, a zero-distance gap is desired [87].

Besides the substrate effect, other factors such as different NA illumination, the incident illumination angle, and the microscope image plane have been found to also influence the experimental resolution and magnification. These uncertainties are challenges, but also opportunities, for next-generation dielectric superlens development. For example, inspired by enhancing the lens and sample evanescent coupling for a better super-resolution, we previously used a high-index TiO_2 nanoparticle as a building block to form a mouldable micro-sized lens that was deposited on an imaging sample, leading to perfect contacting with an imaging sample and meanwhile supporting extremely high evanescent-to-propagation conversion efficiency. This new superlens design has shown greatly improved imaging contrast and field of view over all previously reported designs, and has a record white light super-resolution of 45 nm[167].

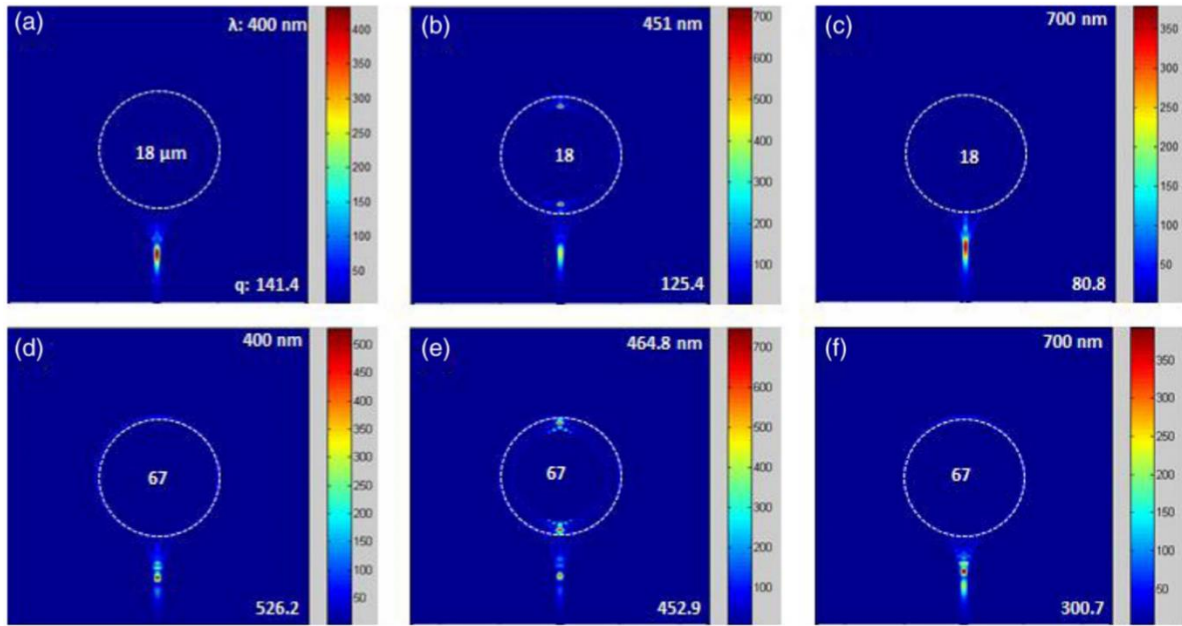


Figure 7.4 Electric field intensity $|E|^2$ distribution in cross sectional plane of 18 μm and 67 μm diameter BaTiO_3 microsphere embedded in PDMS material illuminated by different visible wavelengths. The light is light is incident from top to bottom, with electric field polarised from left to right. q is the size parameter defined as $q=\pi D/\lambda$, where D is the particle diameter and λ the wavelength; see Visualization 2 for the animation of field evolution as a function of size parameter q .

Besides the constant contacting scanning mode, we are currently developing a new “tapping scanning” imaging mode to minimise the friction issues during contacting imaging. Our work reported here laid down a solid foundation for further development of superlensing objective lens technology and it is the first kind of such in the literature. We are expecting the key problem of contacting scanning will be circumvented in future design, and a contactless superlensing objective lens will be developed. This may be achieved by combining optical superoscillatory mask design with existing superlensing objective design.

7.5 Superlensing objective lens in nano-scale laser patterning performance

Due to the near-field sub-diffraction focusing effect by the microspheres and the reversibility principle of light path. A concept has emerged to realise the optical sub-wavelength fabrication. Some literatures have demonstrated near-field writing/patterning techniques including laser-integrated scanning near-field optical microscopy[168]–[170], laser assisted AFM/STM-tip patterning[171]–[173], contacting particle-lens array (CPLA) [174]–[178] and

plasmonic lithography [179], [180] which have the capability of creating features on a surface smaller than diffraction limit. However, these techniques either need high-precision operating system to control the distance and orientation between tip and target surface or suffer from microsphere lens disappearance after single shot utility.

Previous sections discussed the scanning imaging capability by our new designed superlensing objective, this technique, in the meantime, has potential to be operated as near-field patterning lens with the assistance of a general laser maker. Here, the superlensing objective imaging system has been modified to adapt to laser marking system, the experiment setup is illustrated in Figure 7.5. Unlike imaging system, the target sample was remained stationary by a 3D printed holder, and the lens holder with CMS attached was attached onto a high-resolution (1 nm in XYZ) nano-stage (model: PI P-611.3 Nanocube), providing precise movement in three-dimensional space. LMT2010P portable nanosecond pulsed fibre laser making machine (power: 10 W, pulse duration: 100 ns, wavelength: 1064 nm, repetition rate range: 20–200 kHz) was aligned in this system.

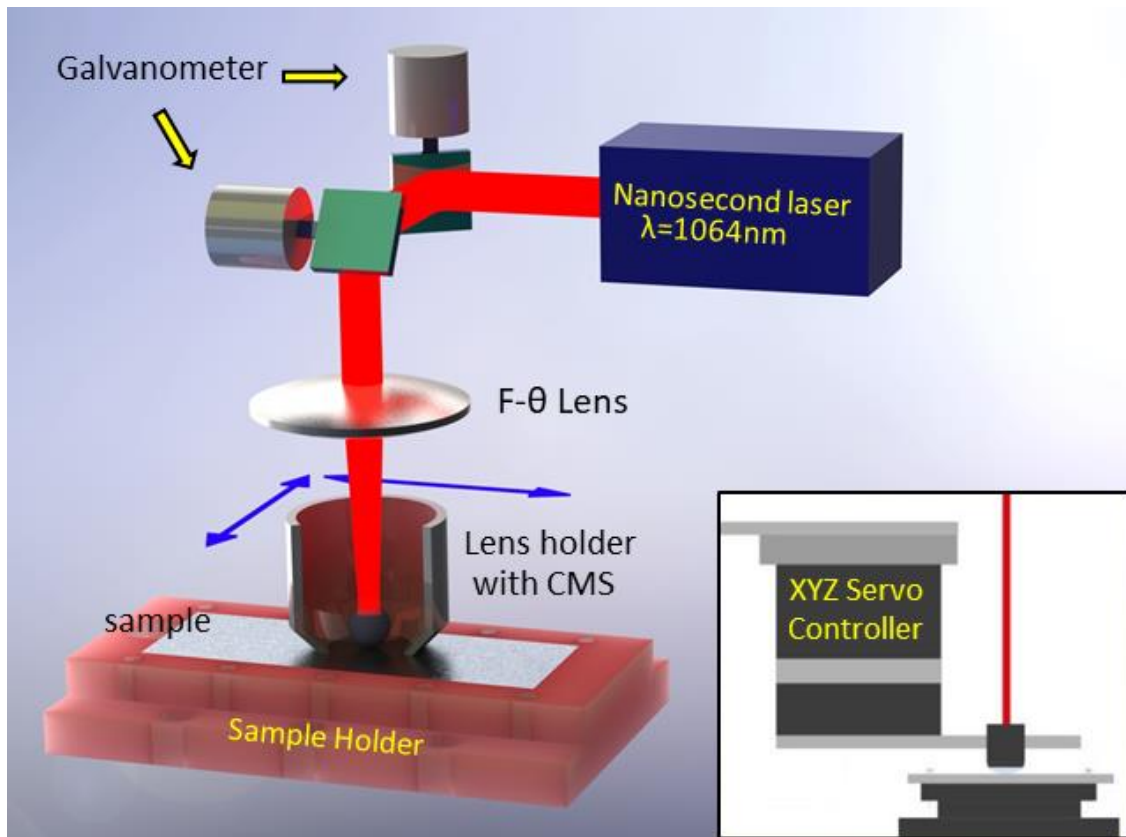


Figure 7.5 Experiment setup of laser-assisted scanning mode nano-patterning. Insert is the XYZ servo nano-stage with CMS lens fixing on it.

In experiment, all results were collected using 1% laser power, 500 mm/s scanning speed and 25 kHz repetition rate. The laser beam size is 50 μm and scanning area is larger than lens adapter holder to ensure laser beam move over each microsphere. 90 nm aluminium coated microscope slide was a target sample for patterning test. Sample was placed 23 mm below laser focus position to be lower the ablation threshold of thin film. Therefore, patterning can only work with the help of microsphere focusing. In order to perform a smooth scanning, WD40 was used to reduce the friction between the superlens and sample.

7.5.1 Patterning resolution analysis

Previous sections have discussed the particle size effect on focal length and magnification. In this experiment, BTG microspheres with size of 3-25 μm was encapsulated in PDMS. To clearly understand the particle size influence on the patterning features, 24.7 μm , 16.6 μm and 7.5 μm microspheres were selected. Figure 7.6 shows the laser processed hole patterns results by three different sizes BTG microspheres. As can be seen, smaller particles can generate finer features. The average patterned hole size is 2.17 μm for 24.7 μm particle, 1.53 μm for 16.6 μm particle and 0.45 μm for 7.5 μm particle. While the diffraction limit of this laser source is $\lambda/2=532\text{nm}$. This means 7.5 μm microsphere is able to produce sub-diffraction feature $\approx\lambda/2.36$. It is noted that the holes are not perfectly round in shape and some of the hole edges are broken. The main reason could be the perturbation of the WD40 liquid solution during the process.

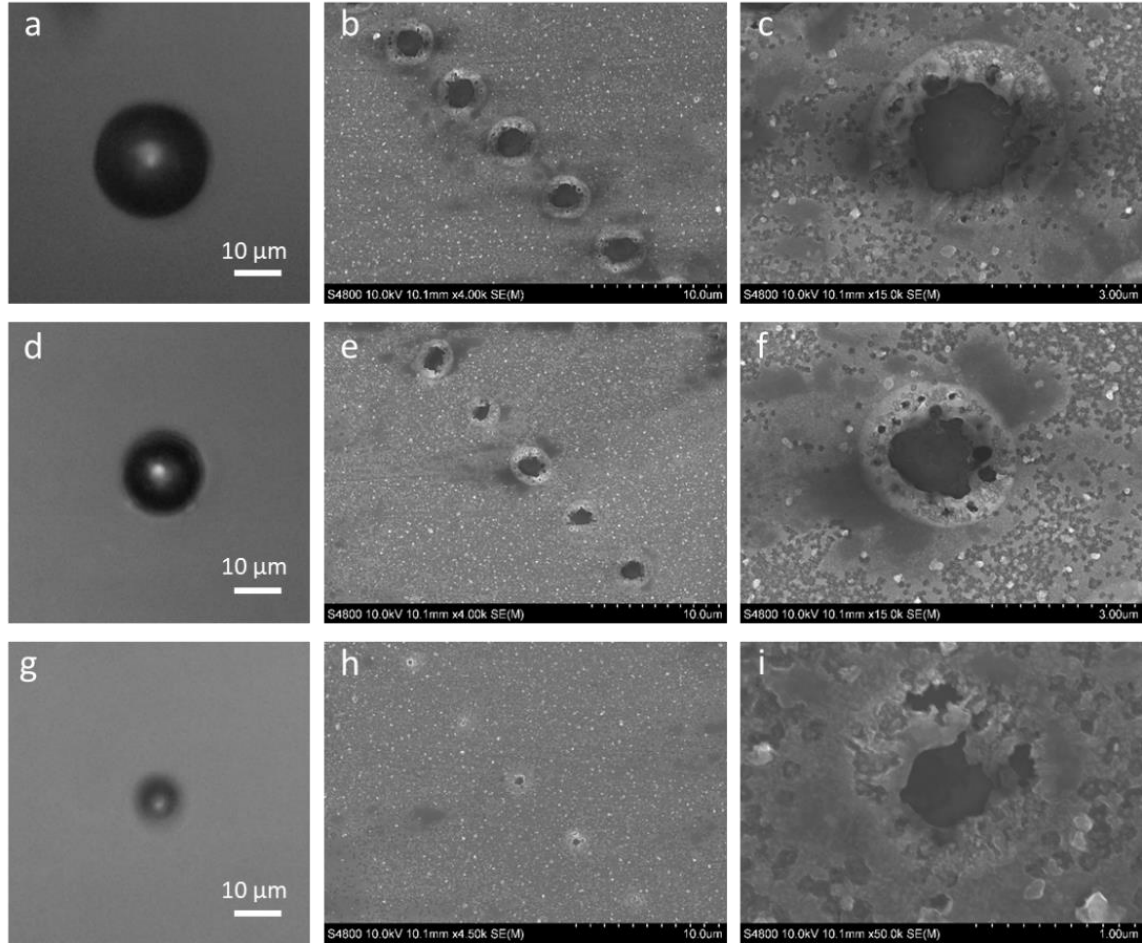


Figure 7.6 Microsphere superlens patterning. SEM images of laser machined hole patterns by (b-c) 24.7 μm microsphere, (e-f) 16.6 μm and (h-i) 7.5 μm . Note scale bar in (i) is 1 μm different from others in the column.

Moreover, we found that when sample was positioned further away from laser focus position, the feature size became smaller. The results shown in Figure 7.6 were obtained at 23 mm below focus. Based on that, the sample was put further away with 2mm-step each time until 31 mm. Figure 7.7 demonstrates the laser processing patterns at positions of 25 mm (a, b), 27 mm (c, d) and 29 mm (e, f) respectively. The left and right columns are patterns generated by 24.7 μm and 26.6 μm microspheres. Due to unresolvable patterns by 7.5 μm particle, only 24.7 μm and 16.6 μm particle cases were discussed. The summarised data was presented in Table 7.1. The machined patterns shrink by increasing the distance from focus. At 29 mm away from focus, the average size was achieved 0.83 μm by 24.7 μm particle, and moreover, a sub-diffraction pattern 0.42 $\mu\text{m} \approx \lambda/2.53$ was found by 16.6 μm particle. After that, there was not resolvable pattern produced on surface. Therefore, a conclusion can be driven from

above results that super-resolution can be occurred in laser patterning by the assistance of cover microsphere superlens (CMS) in either particular particle size or defocus distance.

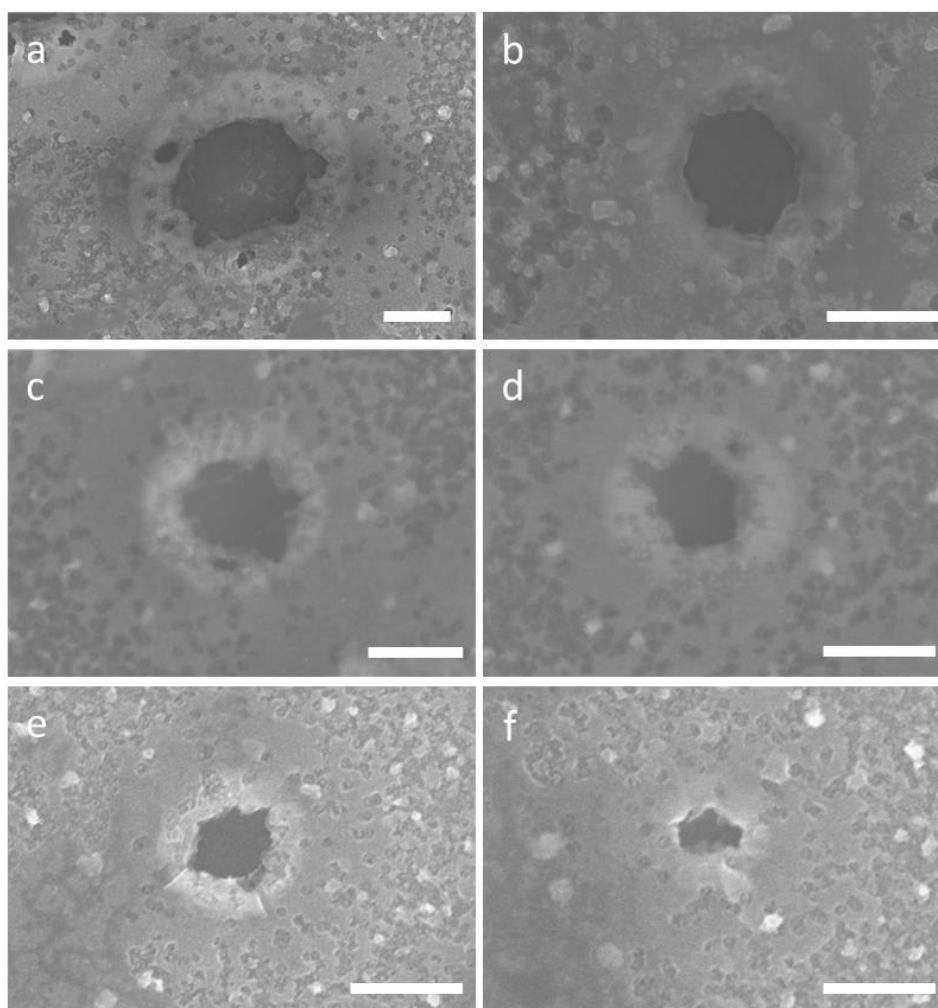


Figure 7.7 SEM images for (a, c, e) 24.7 μm and (b, d, f) 16.6 μm microsphere with different Z focus position. (a,b) 25mm (c,d) 27mm and (e,f) 29mm away from laser focus position. Scale bar is 1 μm .

	Average Hole Diameter (μm) by 3 size microspheres		
Distance away focus (mm)	24.73 μm	16.60 μm	7.48 μm
23	2.17	1.53	0.45
25	1.69	0.95	Cannot resolve
27	1.20	0.70	Cannot resolve
29	0.83	0.42	Cannot resolve
31	Cannot resolve	Cannot resolve	Cannot resolve

Table 7.1 Average patterning future size by three different size microspheres and at different focal plane.

7.5.2 Scanning patterning

In our scanning patterning system, laser beam continuously scanned over an area which covers microsphere superlens. The microsphere superlens in CMS form was in contact with target sample and dragged by high-resolution nano-stage. Therefore, machined patterns were following the scanning path of microsphere superlens. In this section, arbitrary patterning shape was evaluated. In the experiment, 'P' scanning path with 30 μm in height and 15 μm in width was programmed by stage control software, hence it provided an automatic movement during laser operation. Sample was placed 23 mm away from focus. Figure 7.8 displays that letter 'P' is produced by scanning operation. Figure 7.8 (b) is generated by 17.66 μm microsphere and (c) is a group of 'P' patterns produces by (d) corresponding a group of microspheres. As illustrating, smaller particle can produce thinner lines which verifies particle size effect discussed in previous section. Meanwhile, it is noted that the laser processed layout follows the shape in program but has slight distortion. The vertical line is marginally slanted, and the width is less than the design. This could be caused by the friction between the CMS and sample surface during relative movement. Similar issue happened in more complicated patterns such as a string of number and a full word (Figure 7.9).

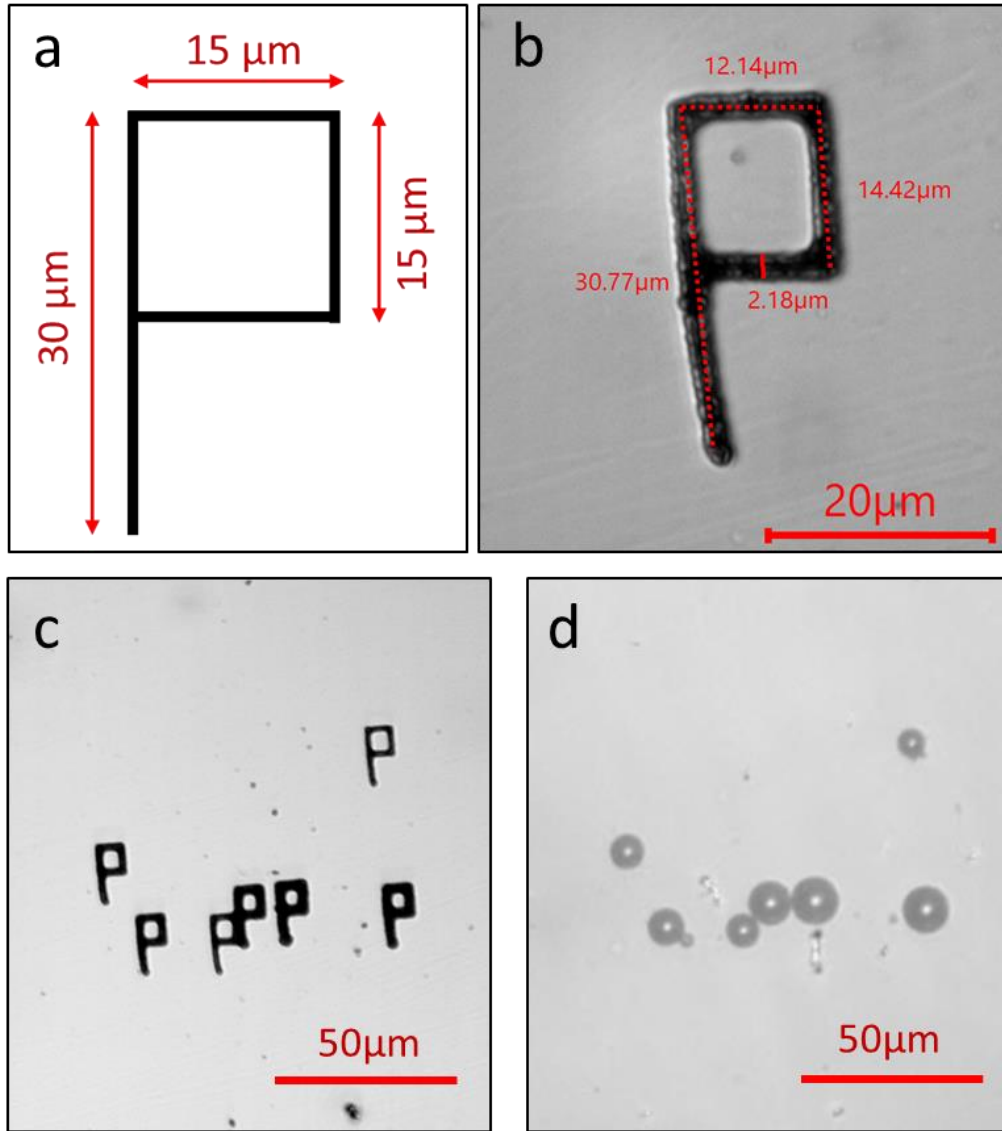


Figure 7.8 'P' Letter pattern by microsphere superlens scanning patterning. (a) Designed pattern (b) 'P' letter with measurement by 17.66 μm microsphere. (b) A group of 'P' letter patterns (c) generated by corresponding microsphere.

Furthermore, with the assist of microsphere arrangement by photolithography micro-structure template (please refer to **Chapter 3.3.4**), microspheres with size around 20-30 μm were effectively aligned in a square periodic array with 100 μm spacing, as shown in Figure 7.10 a. Therefore, repeating patterns can be generated in single processing. Figure 7.10 (b-d) demonstrates repetitive patterns with arbitrary shapes can be realised via the control of high-resolution nano-stage. To summarise, this development still provides simple method and possibility of arbitrary patterning for near-field fabrication methods, and this new approach

could be further developed to eliminate the dragging issues by applying tapping mode or different particle host medium.

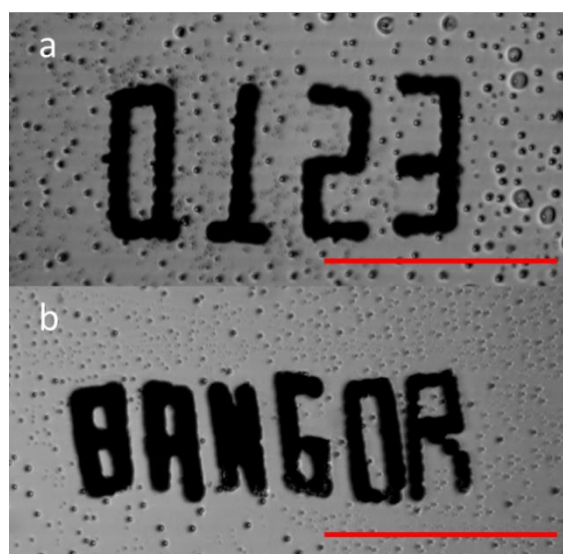


Figure 7.9 Scanning patterning for (a) a string of number '0123' and (b) full word 'BANGOR' patterning. Scale bar in both figure is 50 μm .

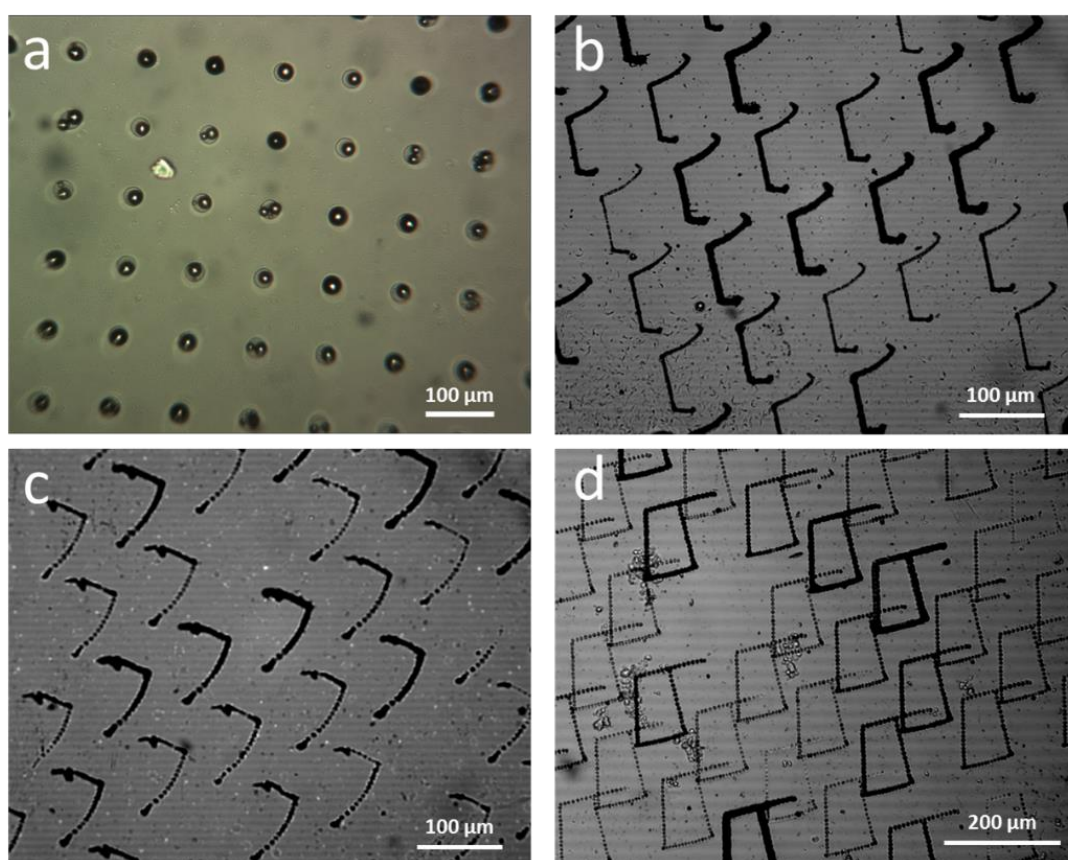


Figure 7.10 Scanning patterning by microsphere array.

7.6 Conclusion

To conclude, we have demonstrated a new type of microscope objective lens, a superlensing objective lens that integrates a conventional objective lens and a coverslip-like microsphere superlens. The new lens has advantage in usability and is able to image the sample with super-resolution in both static and scanning mode. A resolution of 100 nm under white light illumination has been demonstrated. In addition, this technique also works compatibly with laser fabrication. With the assistance of microsphere superlens, sub-diffraction nano patterns $\approx \lambda/2.53$ can be generated. Furthermore, scanning mode offers a new potential near-field approach for arbitrary shape nano-patterning. The developed superlensing objective lens has potential to be further developed into a commercial product which would transform an existing microscope into a nanoscope.

Chapter 8. Bio-superlens and On-chip Microfluidic Nanoscope

In an effort to make superlens technology accessible to a wider range of users, we have studied naturally occurring material (spider silk) as optical superlens. We also extended the superlens application to lab-on-chip devices.

8.1 Introduction

Superlensing microsphere and microfibers can be manufactured via engineering processes including chemical synthesis and photolithography. These processes, however, are complex and inaccessible for non-professionals. Now biomining (searching Nature for suitable materials and models) led us to look for a naturally occurring superlens in spider silks, which are transparent in nature and have micron-scale cylinder structure. In this chapter, we demonstrate that minor ampullate spider silk spun by the *Nephila edulis* spider is an outstanding candidate.

In addition, we further developed our coverslip microsphere superlens (CMS) to incorporate with microfluidic chip. The basic idea is to use our PDMS-CMS as a top microfluidic channel cover, meanwhile acting as super-resolution lens to illustrate biological samples which flow inside channel. Comparing with engineering samples such as IC chip and Blu-ray disc, biological samples are more difficult to be observed by generic microscopy under white light condition due to its transparency, low contrast in liquid, three-dimension structure and strong mobility. Fluorescence or SEM techniques are frequently used. However, these approaches always require particular treatments onto bio-samples which may sacrifice sample's activity.

This chapter is organised as follows; Section 2 reports a nature existed cylindrical superlens – spider silk. The optical imaging performance is characterised by sub-diffraction samples. The optical mechanism is given in the section; Section 3 demonstrates potential applications of microsphere superlens incorporating with microfluidic device. Different biological samples with different features are evaluated; Section 4 is the conclusion.

8.2 Bio-superlens: spider silk

It was recently discovered that transparent micro-spheres and cylinders can function as super-resolution lens to focus light beyond the diffraction limit. A number of high-resolution applications based on these lenses have been successfully demonstrated and span nanoscopy, imaging and spectroscopy[13], [67], [69], [87], [72], [88], [92], [167], [181]. Superlensing microsphere and microfibers can be manufactured via engineering processes including chemical synthesis and photolithography. These processes, however, are complex and inaccessible for non-professionals. Now bio-mining (searching Nature for suitable materials and models) led us to look for a naturally occurring superlens in spider silks, which are transparent in nature and have micron-scale cylinder structure. Our study demonstrates that Minor Ampullate spider silk spun by the *Nephila edulis* spider is an outstanding candidate. That silk can clearly resolve 100 nm features under a conventional white-light microscope, attaining a resolution of $\lambda/6$, which goes well beyond the diffraction limit of $\lambda/(2NA)$. The experimental configuration can be found in **Chapter 3.3.7**.

8.2.1 Optical imaging

The silk lens is essentially a microfiber lens. As long as the lens is in close contact with imaging object, the near-field evanescent waves of objects can be picked up by the silk and transferred to the far-field objective lens. Such near-to-far field conversion leads to optical super-resolution and only occurs for small sized transparent spherical or cylindrical micro-lenses whose optical aberrations are small or negligible[117]. Typical diameter of these lenses are around 3 to 100 μm , with a best resolution of 50 nm demonstrated by Wang et al. in 2011 for 5-10 μm microspheres[67]. Comparing to the spherical lens, which is an isotropic two-dimensional (2D) magnifying device, the cylindrical silk lens used in this study is expected to have different imaging characteristics - because a cylinder lens produces line-shaped focusing rather than the dot-spot focusing of a spherical case. Thus, the cylindrical lens is essentially a 1D magnifying device that only magnifies objects along the direction perpendicular to the optical axis and hence provides an anisotropic magnifying device.

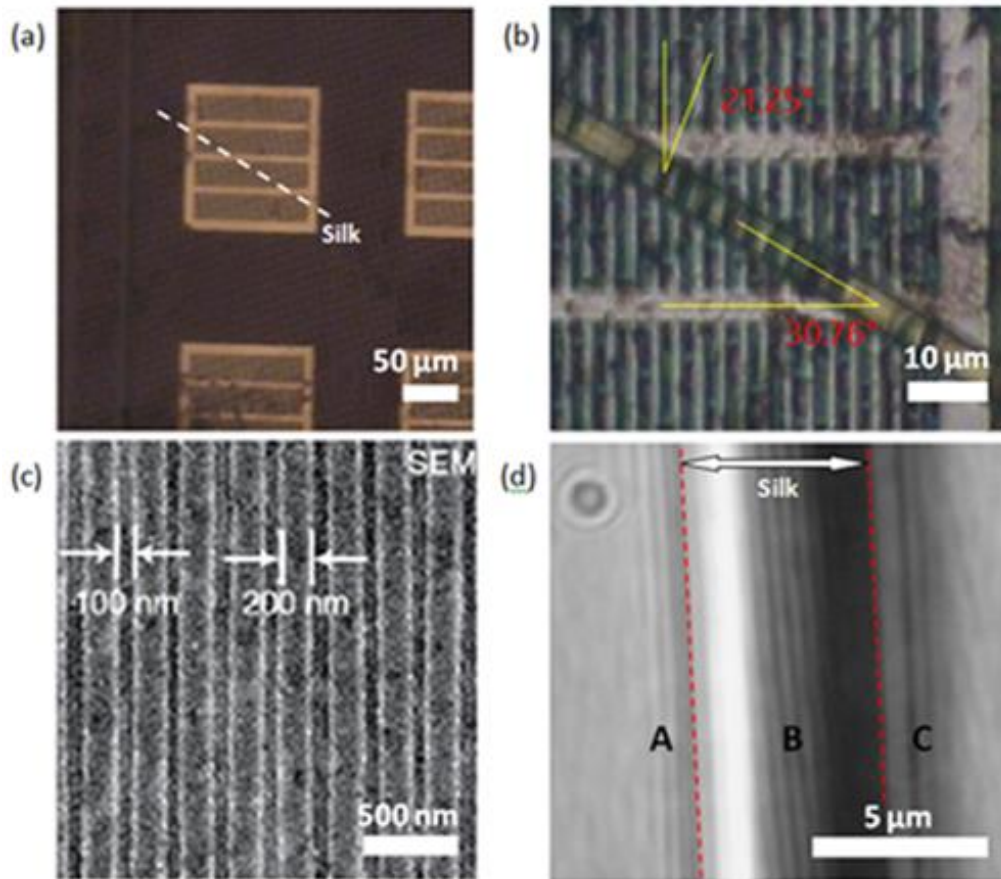


Figure 8.1 A typical imaging example of silk superlens nanoscope in reflection mode imaging a surface of an integrated circuit and commercial Blu-ray disc. The 100- μm thick transparent protection layer of the Blu-ray disc has been removed prior to using the minor ampullate spider silk (diameter of 6.8 μm).

Micro dimensional integrated surface pattern (a; Optical imaging) is magnified by the spider silk (b; Optical Nanoscope image). The sub-diffraction 100 nm channels (c; SEM image) are resolved by the spider silk superlens (d; Optical Nanoscope image) and correspond to a magnification fact of 2.1X.

This 1D effect is demonstrated in Figure 8.1(a-b), in which a semiconductor chip sample with line features 400-500 nm (Figure 8.1a) was imaged with silk lens placed on top (Figure 8.1b). Here, one can clearly see the silk generates a clear image of underlying line objects, but with a twisted angle. This twisted angle is the result of anisotropic magnification effect of cylindrical lens. Exact twist angle, as shown in the labels of Figure 8.1(b) is slightly smaller than the twist angle of spider silk orientation with respect to the line objects, which is resulted by the angular incident beam used in the project. In fact, one may easily observe such angle-twisting effect at home, using a plastic bottle filled with water (as cylindrical lens) and any objects like drawing lines and shapes.

After measuring the basic imaging characteristics of microfiber lens, we proceeded to test the super-resolution imaging performance of the silk. A sub-diffraction Blu-ray disc (Figure 8.1c) containing 200 nm and 100 nm features was used as the imaging objects. As expected, without silk, the microscope cannot resolve these features due to the optical diffraction limit ($600/2NA = 333.3$ nm, where $NA=0.9$). However, clearly magnified ($M \sim 2.1$) super-resolution images could be obtained after carefully adjusting the illumination angle of the lighting; best images were obtained at roughly an angle of 20-40 degree measured from the vertical axis. This angular illumination effect can be observed in Fig. 2(d) image, on silk's left side a bright strip exists (Zone A) while on right side a dark strip appears (Zone C). Note that only images appearing inside the marked viewing windows (Zone B) are 'true' images of underlying Blu-ray features, while the line images that appear in zone A and C are 'false' images. When a non-structured sample was used as the imaging specimen, the same phenomenon of 'false' images in Zone A and C was observed. This supports the hypothesis that 'false' images are not caused by the surface structures, but by the interferences between incident light, light scattered by the silk and reflection of the scattered light by substrates[176], [182]. Experimentally, the issue of 'true' or 'false' image can be verified by rotating the underlying sample, where the 'true' images will follow the rotation of sample while the 'false' images will not. Artificial images are an issue in microsphere/cylinder based super-resolution technology and one must pay attention to it in order to avoid wrong interpretation of experimental observations.

We further compared the super-resolution imaging of the silk superlens with a microsphere superlens as shown in Figure 8.2. Here, we used a Barium Titanate ($BaTiO_3$) microsphere, with a similar diameter to the spider silk and a refractive index of 1.9, which was placed next to the silk strand and then encased both spherical and cylindrical lenses with a Polydimethylsiloxane (PDMS). $BaTiO_3$ microspheres have the proven ability to resolve sub-diffraction patterns when immersed in liquid or PDMS[69], [87], [181], as shown in Figure 8.2 where the 200 nm wide channels and the 100 nm separation lines are clearly distinguished. Due to microsphere is an isotropic 2D magnifying lens of microsphere, the image orientation in the central zone of the viewing window is perfectly aligned with the object orientations and there is no twisting angle effect.

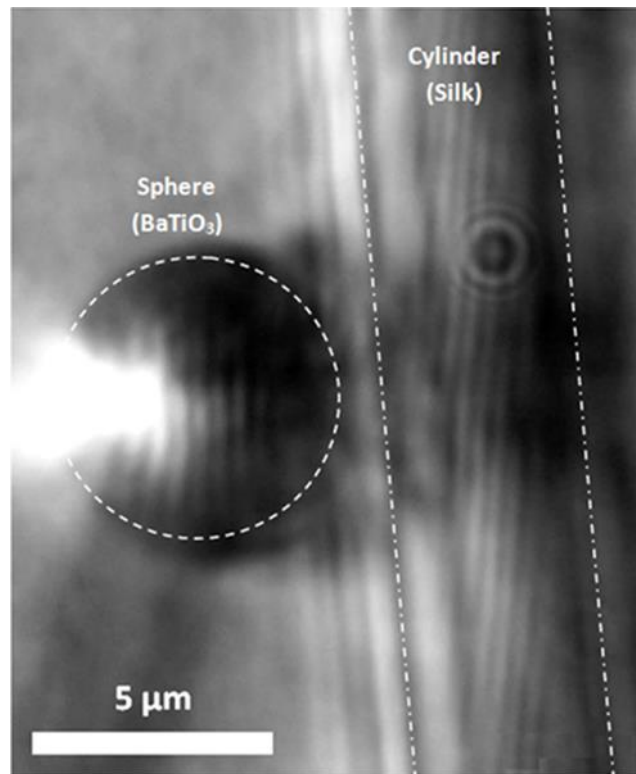


Figure 8.2 Microsphere positioned beside the minor ampullate spider silk in reflection mode, images a commercial Blu-ray disc. The image resolved within the spider silk is rotated by approximately four degrees compared to the real direct of the sub-diffraction 100 nm channels shown by the microsphere

Similar to Figure 8.1d, the spider silk in Figure 8.2 can also clearly resolve the 100/200nm patterns while under the reflection mode. But the spider silk projects the pattern at an angled image, i.e. with the twisting effect as discussed above. The focal lens plane of the spider silk differs slightly from that of the microspheres, which explains why the microsphere images are slightly out of focus. One obvious advantage of spider silk is the fact that its viewing window is extended along the fibre. This can easily reach centimetres, which makes it potentially attractive for large-area super-resolution imaging. In principle, it is possible to rotate the encapsulated silk lens and capture super-resolution images at different angles (with respect to objects) from 0 to 180-deg; and then use a software system to process and analyse the images and thus construct a whole super-resolution image over squared centimetres scale. Technically, we may achieve this by attaching the silk superlens to a nano-resolution scanning head and integrate it with an optical microscope. Such image reconstruction will be the immediate focus of our next technical developments following on the present work. More complex nanostructures will be used in future studies.

8.2.2 Theoretical calculation

The focusing property of spider silk was accurately simulated using CST Studio software, which is a full wave numerical solver of Maxwell equations based on Finite Integral Technique (FIT)[86]. In our technique, super-resolution arises from the near-field interaction between the silk and underlying nano-objects, which leads to the conversion of surface-bounded high spatial frequency evanescent waves into propagating waves[87], [166]. We note that such conversion process is extremely sensitive to the gap distance between silk and object. The technique requires gap distances below 100 nm with a zero-distance gap being ideal[87]. In dry conditions, we failed to achieve super-resolution imaging with spider silk, most probably due to the poor contacting between silk and sample for an elongated object. Filling the gap zone with IPA helps eliminate the problem; a near-perfect contacting is formed due to capillary binding force occurring in the interfacial zone. Under an angular incident beam, the cylindrical spider silk lens produces an angled focus around 10 μm away from the lens (measured from lens centre), as shown in Figure 8.3. By varying the incident angle, the distance between object and lens (i.e., d and d' in Figure 8.3 b) can be changed so that magnification factor $M=f/(f-d)$ can be tuned. Generally, the magnification factor will increase with incident angle (see analysis in Figure 8.3b) as d increases. However, magnifications that are too large will cause the rapid decrease of imaging contrast, thus imposing a practical limit on the maximum usable angle in experiments. Our tests show that 20-40 degree angles provide best results. A smaller sized spider silk may be used if a higher magnification of imaging is required.

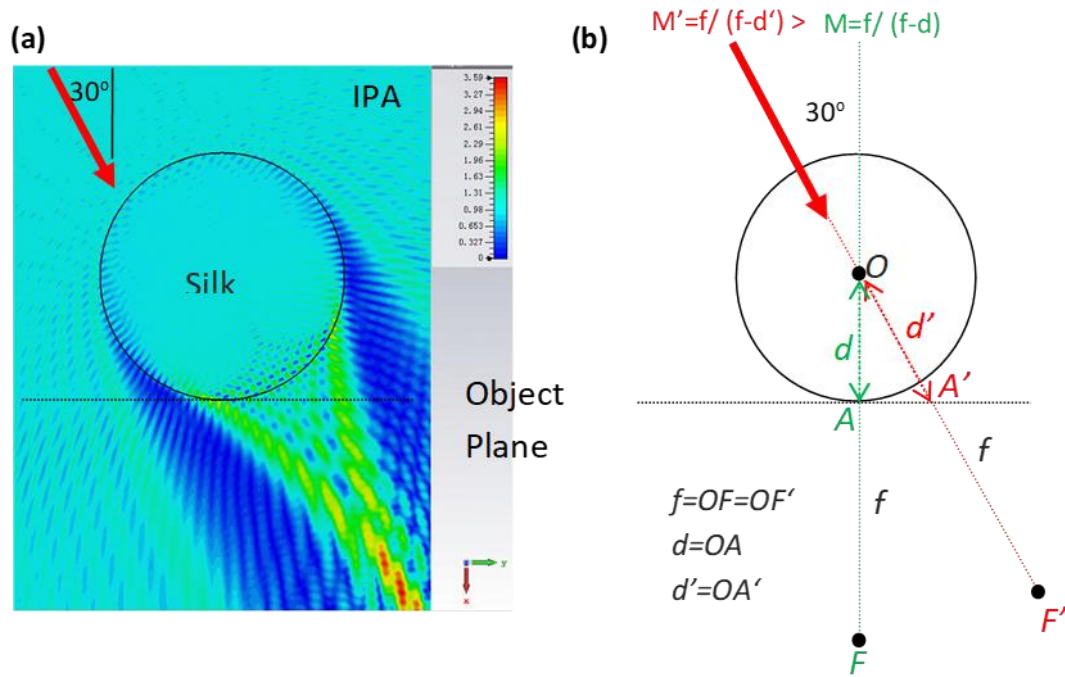


Figure 8.3 (a) Light focusing by the 6.8 μm -diameter minor ampullate spider silk immersed in IPA solution under 600 nm wavelength illumination incident at 30 degree angle. (b) Schematics for magnification factor M calculation, the M generally increases with incident angle.

Theoretically the optical resonances in spherical cavity would cause variation of brightness and resolution in image versus wavelength and particle size. At some wavelengths or particle sizes such resonance could be quite sharp. However, these sharp resonances would be ‘smeared’ out by averaging effect when a broadband lighting source is used, such as the white lighting source used in our study. Such averaging effect was demonstrated previously when we tested wavelength effects using color filters, and confirmed the changes in brightness and resolution are not significant for red, green and blue lights[183]. In most cases such variations are almost negligible. It is the incident angle of light, which provided more significant conditions for determining the super-resolution image quality.

The research reported and outlined here provides a solid foundation for the development of bio-superlens technology and it is the first expose of spider silk in this context. Now we expect further biological superlenses to be discovered. Indeed, interesting and important recent work by other researchers is heading in that direction. For example, Schuergers et al. reported that spherically-shaped cyanobacteria *Synechocystis* cells can focus light like a micro-lens,

which contributes to the cell's ability to sense the direction of lighting source[184]. We suspect that these cells might work also as a superlens suitable for super-resolution imaging.

8.3 Bio-sample imaging through an integration device of microsphere superlens and microfluidic channel

Previous chapters have demonstrated microsphere's abilities of converging light to sub-diffraction focal spot and super-resolution imaging. This nanoscopy technique has a number of distinct features including easy utility, label-free, high-resolution and visualisation in real-time under white-light. Due to a tiny scale of microsphere superlens, it has advantage of being integrated in other microsystems, such as microfluidics and optical fibre system, to form a multifunctional on-chip device. An example of microlens-based trapping and detection device was reported by Yuchao Li et al.[76]–[78]. In their work, microsphere lenses were attached on an optical fibre probe in order to generate photonic nanojet for performing manipulation and detection sub-100-nm objects, for instance nanoparticles and biomolecules. In addition, Hui Yang et al. revealed that when a microsphere-lens-array was integrated with a microfluidic channel, photonic-nanojet-array was formed to expose the content within the channel. Au nanoparticles with size of 50 nm and fluorescent nanoparticle down to 20 nm were able to be detected[79]. The aim of our project is to explore and extend the capability of directly visualisation of moving live biological samples. In this section, microsphere superlens was introduced to a microfluidic channel for real-time high-resolution imaging of biological objects. Preparations and experimental setup was detailed in **Chapter 3.3.8**.

8.3.1 Optical imaging

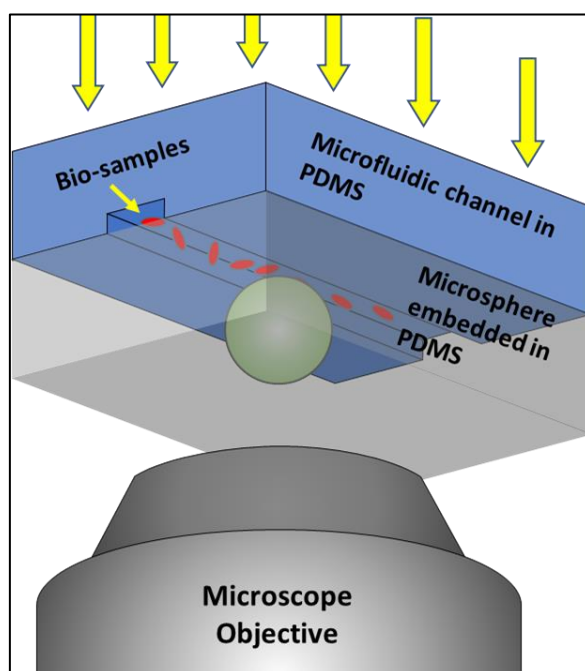


Figure 8.4 Schematic setup of on-chip microfluidic superlens. The microfluidic superlens is placed onto an inverted white light microscope.

As previously mentioned, the overall resolution is determined by Coverslip Microsphere Superlens (CMS) which consists of BaTiO_3 microsphere (60-90 μm) inside PDMS sheet. In our experiment, three different biological samples with different features were selected, with aim of demonstrating the ability of achieving high-resolution. They are human red blood cells (RBCs), trypanosome and adenoviruses (replication deficient human adenovirus serotype 5 vector). All samples are tested in live condition. It is noteworthy that microspheres imaging occurs in near-field zone, which requires objects very close to the microsphere. In order to ensure very short distance between samples inside channel and microsphere, the microfluidic superlens was placed inverted and an inverted microscope (Carl Zeiss Primovert) equipped with a 40x (NA=0.50) and an 80x (NA=0.80) objective lenses in transmission mode was incorporated with the device for biological sample imaging (Figure 8.4).

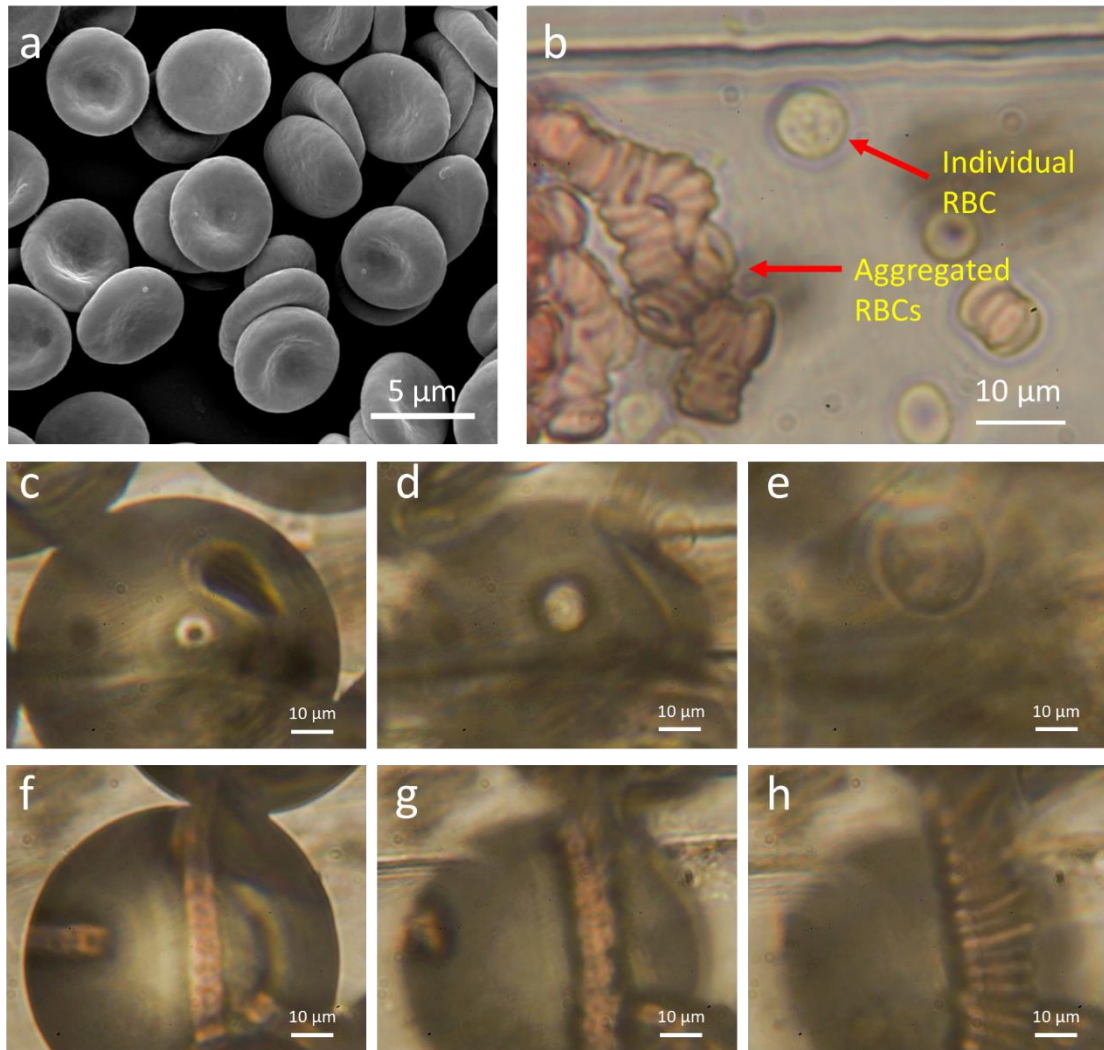


Figure 8.5 Human red blood cells (RBC) imaging. (a) SEM image. (b) RBCs flow in microfluidic channel. (c-e) single RBC imaging at different focuses. (f-h) aggregation of RBCs in chain form is captured by microsphere lens at different focuses.

The RBCs, abundant in human body, appear flexible and oval biconcave disk profile (Figure 8.5 a) with a diameter of 6 – 8 μm . The RBCs were injected into microfluidic channel and exhibited in two forms, individual and aggregated into a cluster (Figure 8.5b). Virtual images of an individual cell (Figure 8.5 c-e) and stack of cells (Figure 8.5 f-h) generated by an 80 μm BaTiO₃ microsphere above the channel were picked up by microscope objective lens (80x NA=0.9) at different imaging plane. . Figure 8.5 (c, f) are images focus at microsphere and Figure 8.5 (d, g) focus at RBCs. With further rolling focus towards objects, resolvable and magnified images were achieved, showing in Figure 8.5 (e, h) respectively. With assist of microsphere, RBCs aggregated in chain-cluster were able to be clear isolated. The magnified cell size is about 24

μm in Figure 8.5 (e), while the real cell size is around $8\ \mu\text{m}$. Therefore, the $80\ \mu\text{m}$ BTG superlens offers a magnification factor around 3 under experimental condition.

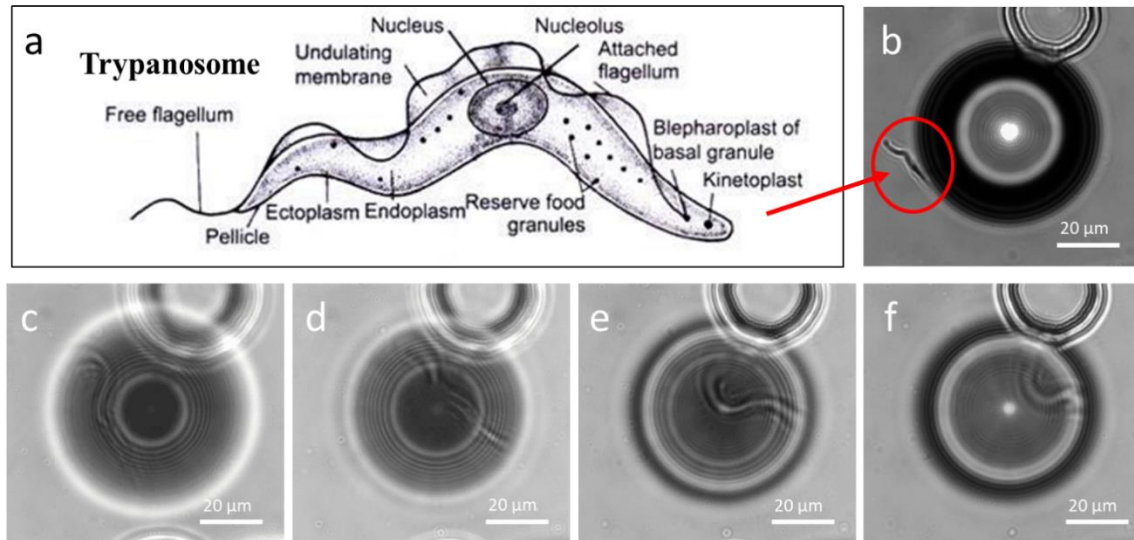


Figure 8.6 Trypanosome sample imaging. (a) diagram of trypanosome. (b) live trypanosome flows in microfluidic channel. (c-f) from left to right. Magnified images are captured by microsphere superlens.

Let's turn our eye on another sample, the trypanosome sample. This is a flagellate pathogenic parasite growing in humans and animals causing sleeping sickness and nagana. The name of trypanosome is derived from "borer body" in Greek language due to their corkscrew-like motion. The trypanosome sample was provided by Dr Miranda Walker from Swansea University. It has colourless, elongated and flattened leaf like body with $8\text{--}50\ \mu\text{m}$ in length and $1\text{--}5\ \mu\text{m}$ in width. Figure 8.6 reveals the magnified image of live trypanosome obtained by developed device formed by microfluidic channel and $60\ \mu\text{m}$ BaTiO_3 microsphere. The trypanosome has strong mobility, moving from left to right. Figure 8.6 (c-f) capture the magnified images taken at different spatial positions. Comparing the image without microsphere lens (Figure 8.6b), the microsphere contributes to clearly magnified images with more details during sample passing under microsphere without sacrificing its activity. The magnified sample width is about $4.3\ \mu\text{m}$ in Figure 8.6 (f), while the real cell size is around $1.7\ \mu\text{m}$. Therefore, the $60\ \mu\text{m}$ BTG superlens offers a magnification factor around 2.5 under experimental condition.

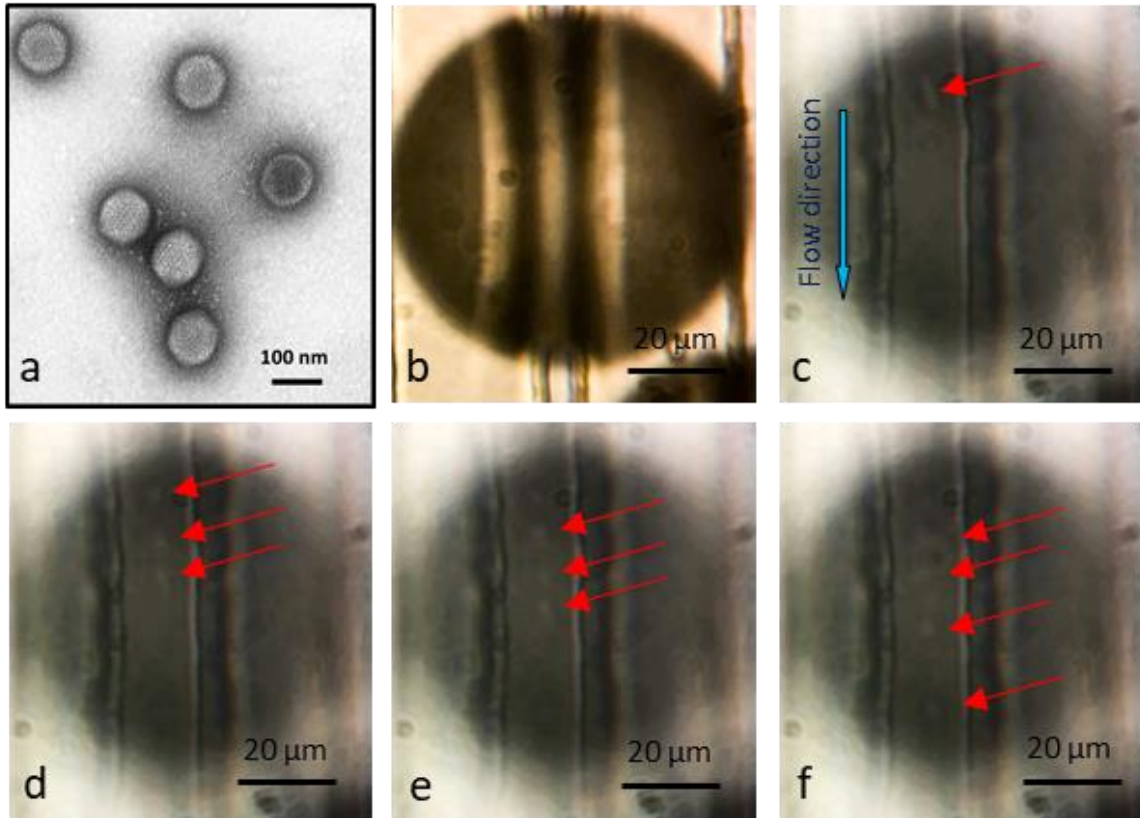


Figure 8.7 Imaging of adenoviruses with size about 90-100 nm. (a) SEM image. (b) 70 μm microsphere-lens located on top of 10 μm width fluidic channel. (c-f) adenoviruses flow inside channel from top to bottom. Adenoviruses labelled by arrows are magnified images captured by microsphere-lens.

To further explore the resolution limit of our device, sample with sub-diffraction feature were applied. Adenoviruses (replication deficient human adenovirus serotype 5 vector) are nearly spherical in shape with size about 90-100 nm (Figure 8.7a). They are sub-diffraction-limited and difficult to be observed using conventional microscopes. Figure 8.7 shows that super-resolution image captured by 70 μm BaTiO₃ during viruses flowing inside 10 μm channel. Viruses were flowing from up to down. Due to its low optical contrast and fast flow speed in liquid, magnified viruses images are not clear but still can be resolved. The red arrows point out the location of spherical particles inside channel. We believe the image quality can be improved by using a high resolution and slow-motion camera.

8.4 Conclusion

In summary, we have demonstrated that the minor ampullate silk of the *Nephila edulis* spider, has the ability to perform as an optical superlens able to resolve sub-diffraction 100-nm

objects and patterns under a white light source illumination. This type of lens is the first biological superlens system that has successfully overcome the diffraction limit. The cylindrical silk lens has advantages in larger field-of-view when compared to microsphere superlens. Importantly for potential commercial applications, a spider silk nanoscope would be robust and economical, which in turn could provide excellent manufacturing platforms for a wide range of applications.

In addition, microsphere superlens has advantage of being integrated in other microsystems, such as microfluidics. A microfluidic chip cooperates with microsphere superlens offering the possibility of high-resolution imaging performance on biological samples without sacrificing their activity. Several samples with different features, including size, transparency, low contrast and strong mobility, have been tested. This integrated device provides a new way to allow researchers to directly visualise biological specimens in real-time by a conventional microscope. This technique can be further improved by coupling multi-functional microfluidic chip which has precise cell manipulation, sensing and stimulation inside channel (example as Figure 8.8).

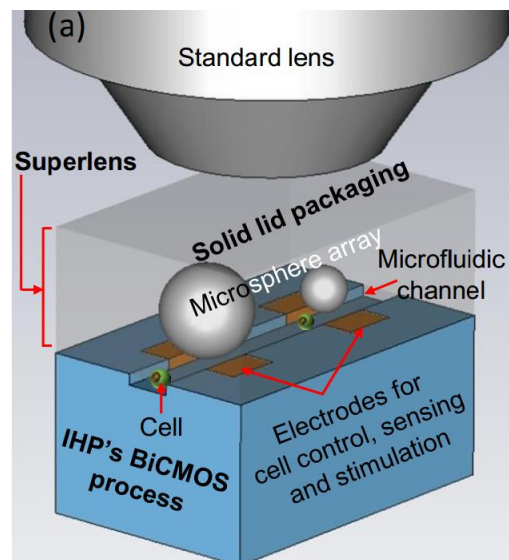


Figure 8.8 Microsphere superlens cooperating with multifunctional microfluidic chip.

Chapter 9. Conclusions and Future Work

9.1 Conclusions

Recently, the advent of a new imaging method of microsphere nanoscopy has attracted numerous attentions, owing to its simplicity in experimental setup and extraordinary imaging performance. Studying optical near-fields of small all-dielectric particles are of particular importance and interests for nanoscale optical engineering such as field localisation, fabrication, characterization, sensing and imaging. The term ‘photonic nanojet’ (PNJ) describes dielectric particle super-resolution focusing at the shadow side. Investigation and adoption of this advantage for sub-diffraction purposes become a hot topic. The overall objective of this project is to significantly advance the super-resolution technology that was built upon these micro/nano scale superlenses. Significant theoretical and experimental efforts have been paid to improve the superlens imaging performance (resolution, clarity) and usability (easy-to-use).

In the first part, a systematic investigation was made on the focusing characteristics (focal length, field enhancement, spot size) for a given refractive-index microsphere ($n=1.6$) with a varying size parameter q_0 across a wide range. Conditions for super-resolution foci were analysed in detail. It was shown that optical resonances inside microspheres would lead to highly oscillating features of the field focus enhancement and focus position as particle size changes. The super-resolution was observed for particular sets of size parameters and often manifests an elliptical focus shape. Extreme sharp super-resolution foci with resolution of $\lambda/5.5$ has been seen for an $n=1.6$ particle in air. Apart from the well-known PNJ focusing pattern, several unique electric field features occurred at internal sphere, such as whispering-gallery-mode like distribution, were also discovered by particular sets of size parameter and could be potentially useful in sensing system. In addition, principles of field-invariant scaling of the Mie parameters were also derived which is important for experimental scaling of the super-resolution designs. Moreover, we also provided a simulation result which considers the

wide-band lamp source as an incident condition to perform a more realistic understanding of super-resolution imaging mechanism.

From the above investigation, we understand that the resolution of microsphere is limited by its intrinsic characters, including particle size, its refractive index with respect to surrounding medium and incident wavelength. However, there is a restricted number of selections of available microsphere materials and imaging working environment in reality. In the second part, we theoretically proposed multiple ways to modify the focusing abilities and enhance the resolution through engineered structures on dielectric micro-lenses. Unlike conventional ways of modifying the PNJ, phase mask and solid immersion techniques which have function of improving imaging quality were integrated on to microsphere.

In first design, a circular pupil mask is created on top of a microsphere ($n=1.46$) to block centre light. As consequence, PNJ is only contributed by light from side and shrinkage of PNJ is realised. The modification of PNJ at various mask coverage was discussed. With increase of mask dimension, focal length tends to be reduced and shifted from external to internal eventually. Meanwhile the optimised external lateral resolution of PNJ was tuned down to $\lambda/3$, $\lambda/3.11$, $\lambda/3.05$, $\lambda/3.24$ and $\lambda/2.87$ with particle size of $1\text{ }\mu\text{m}$, $1.5\text{ }\mu\text{m}$, $2\text{ }\mu\text{m}$, $2.5\text{ }\mu\text{m}$, and $3\text{ }\mu\text{m}$ respectively.

The second design applied the concept of solid immersion mechanism which enhances the spatial resolution by high refractive index of material. Unlike typical solid-immersion lens which has semi-spherical structure, we proposed a microsphere-based composite design which consists of a high-index material in lower part and lower-index material in upper part (fixed at $n_{p1}=1.46$). Simulations were made through varying volume and refractive index of lower part. This design exhibits excellent capability of modifying PNJ. The external resolution can be reached to $\lambda/5.03$ with optimising set of parameters ($n_{p2}=1.76$ and low part height= 133 nm). With increasing the lower part index, the external waist of PNJ is effectively shrunk to $\lambda/6.62$ when $n_{p2}=2.56$. It is noted that not only the resolution has been improved, but also a strong side-lobes effect was observed. This phenomenon has higher electric field enhancement around centre peak that makes it unfavourable for imaging and other applications. Therefore, with the aim of refining focal spot and meanwhile reducing the interferences from sidelobe, another design was suggested. Last design is the combination of

above two. With assist of pupil mask, the composite microsphere can still surpass the diffraction limit $\lambda/2n$, and moreover reduced sidelobe interference.

In addition, we proposed a concept of using high-index nanoparticles-derived dielectric metamaterial to further enhance the resolution. Owing to near-field coupling among neighbouring high RI nanoparticles, this composited metamaterial superlens can contribute to a unique photophysical properties that are not existing in homogeneous material lens. The simulation results showed that near-field evanescent information consist of 45 nm features can be resolved in far-field zone. Owing to the inherent low loss in the all-dielectric metamaterial, these processes can be carried out in a truly 3D structure and over long distances.

Theoretical analysis gives us a comprehensive understanding how light will interact with small particles and also provides possibilities of modifying near-field optical properties of microsphere superlens. In the next part, we adverted our attention to experimental works. In microsphere imaging techniques, lenses are always close or in contact with imaged object, since it effectively collects near-field evanescent waves which consist of sub-diffraction information of object surface. Most experiments were carried out by directly depositing microsphere on to sample. Therefore, the lack of manipulation of microsphere leads limitation in practical use. We proposed a coverslip microsphere superlens (CMS) by encapsulating high-index microspheres (BaTiO_3) inside a transparent host material (such as PMMA and PDMS). In addition, the CMS was integrated onto a conventional microscope objective by a custom-made lens adaptor, thus offering synchronised images during a scanning process. The imaging performance was evaluated by sub-diffraction sample with 100 nm feature size. Besides, due to the near-field sub-diffraction focusing effect by the microspheres and the reversibility principle of light path, attempt was made via integrating this imaging system into a laser marking system, thus offering possibility for nano-scale surface structuring. A minimum pattern with size about $\lambda/2.53$ was achieved. Meanwhile, scanning mode offers a new potential near-field approach for arbitrary shape nano-patterning. This developed design provide ease of usability and is a commercial viable product which may transform an existing microscope into a nanoscope.

Resolution of ordinary microsphere lens techniques is usually limited to about 100 nm under white light illumination. Most of microsphere lens sustain poor contrast, low magnification,

narrow field of view and interference fringes. Inspired from the concept of nanoparticle-derived dielectric metamaterial superlens, we develop a new chemical synthesis method to simply assembly TiO_2 nanoparticles to form transparent and high RI hemispheres with width up to 20 μm . Experimental results reveal that nanoparticles-derived dielectric metamaterial solid immersion lens (mSIL), it can produce a high contrast and wide field of view virtual image with a super-resolution of at least 45 nm under a white-light optical microscope. In the meantime, we developed a ZrO_2/PS nanohybrid colloidal microsphere which has highly controllable in shape, size and refractive index. By increasing the volume of ZrO_2 material in the fabrication process, the RI can be effectively increased, resulting better imaging resolution down to 60 nm under white light illumination and 50 nm under laser confocal microscope.

Furthermore, we also extend our research to natural materials which could be simply acquired. Our study demonstrates that Minor Ampullate spider silk spun by the *Nephila edulis* spider is an outstanding candidate. That silk can clearly resolve 100 nm features under a conventional white-light microscope, attaining a resolution of $\lambda/6$, which goes well beyond the diffraction limit of $\lambda/(2\text{NA})$. This finding provides a simple and accessible way for public to realise super-resolution imaging.

Due to the tiny scale of microsphere superlens, it has advantage of being integrated in other microsystems. In the last part, an integration device consists of microsphere lens and microfluidic channel was demonstrated to establish a convenient platform for biological sample imaging. Various bio-samples with different features, including small size, high transparency, low contrast and strong mobility, have been tested. This integrated device provides a new way to allow researchers to directly visualise biological specimens in real-time by a conventional microscope.

9.2 Future work

In this thesis, we have theoretically and experimentally investigated microsphere nanoscopy technique. The efforts are extensive but not exhaustive. Some works need to be continuously developed. Recommendations are list as follows:

- 1. Proposed engineering microsphere has excellent ability of controlling focusing properties. However, the simulation results only cover small microspheres with**

size under 3 μm . This is because of large mesh condition in finite-element method consuming lots computing resource and personal computer has poor calculation ability. In practical application, it often needs larger particle size, range from 10 to 80 μm . Therefore, high computing performance server is necessary.

2. It has been proved that superlensing objective lens design has advantage for solving the synchronisation problem during scanning imaging. The postprocessing imaging stitching was realised by in-house developed MATLAB coding. This program need to be further developed to be a compact microscope software which can generate stitching image instantly during observing.
3. Arbitrary shape nano-patterning was realised by cooperation of scanning CMS and laser marking system. The friction between the CMS and sample surface during relative movement causes slight distortion in machined patterns. This problem can be solved via reducing the contact area and using tapping mode.
4. The metamaterial solid immersion lens exhibits extraordinary super-resolution imaging performance under white light illumination. It can be attributed to high-index closely-packed TiO_2 ($n=2.5$) nanoparticles converting evanescent wave to propagational wave with losses. The super-resolution of mSILs is readily expected to be further improved by increasing the refractive index of nanoparticles, for example, by using rutile TiO_2 nanoparticles ($n=2.7$) or smaller anatase TiO_2 nanoparticles.
5. The cooperation of microsphere lens and microfluidic channel provides a new way to allow researchers to directly visualise biological specimens in real-time through a conventional microscope. This technique can be further improved by coupling multi-functional microfluidic chip which has precise cell manipulation, sensing and stimulation inside channel.

References

- [1] E. Betzig, J. K. Trautman, T. D. Harris, J. S. Weiner, and R. L. Kostelak, "Breaking the Diffraction Barrier: Optical Microscopy on a Nanometric Scale," *Science* (80-.), vol. 251, pp. 1468–1470, 1991.
- [2] J. B. Pendry, "Negative refraction makes a perfect lens," *Phys. Rev. Lett.*, vol. 85, no. 18, pp. 3966–3969, 2000.
- [3] B. Huang, M. Bates, and X. Zhuang, "Super resolution fluorescence microscopy," *Annu. Rev. Biochem.*, vol. 78, pp. 993–1016, 2010.
- [4] M. G. L. Gustafsson, "Surpassing the lateral resolution limit by a factor of two using structured illumination microscopy," *J. Microsc.*, vol. 198, pp. 82–87, 2000.
- [5] F. M. Huang, T. S. Kao, V. A. Fedotov, Y. Chen, and N. I. Zheludev, "Nanohole array as a lens," *Nano Lett.*, vol. 8, no. 8, pp. 2469–2472, 2008.
- [6] E. T. F. Rogers *et al.*, "A super-oscillatory lens optical microscope for subwavelength imaging," *Nat. Mater.*, vol. 11, no. 5, pp. 432–435, 2012.
- [7] Z. Chen, A. Taflove, and V. Backman, "Photonic nanojet enhancement of backscattering of light by nanoparticles: a potential novel visible-light ultramicroscopy technique," *Opt. Express*, vol. 12, no. 7, p. 1214, 2004.
- [8] Y. F. Lu, L. Zhang, W. D. Song, Y. W. Zheng, and B. S. Luk'yanchuk, "Laser writing of a subwavelength structure on silicon (100) surfaces with particle-enhanced optical irradiation," *J. Exp. Theor. Phys. Lett.*, vol. 72, no. 9, pp. 457–459, 2000.
- [9] R. Ye *et al.*, "Experimental imaging properties of immersion microscale spherical lenses," *Sci. Rep.*, vol. 4, p. 3769, 2014.

- [10] L. Li, W. Guo, Y. Yan, S. Lee, and T. Wang, "Label-free super-resolution imaging of adenoviruses by submerged microsphere optical nanoscopy," *Light Sci. Appl.*, vol. 2, pp. 1–9, 2013.
- [11] S. Lee, L. Li, Y. Ben-Aryeh, Z. Wang, and W. Guo, "Overcoming the diffraction limit induced by microsphere optical nanoscopy," *J. Opt. (United Kingdom)*, vol. 15, p. 125710, 2013.
- [12] X. Hao, C. Kuang, X. Liu, H. Zhang, and Y. Li, "Microsphere based microscope with optical super-resolution capability," *Appl. Phys. Lett.*, vol. 99, p. 203102, 2011.
- [13] A. Darafsheh, N. I. Limberopoulos, J. S. Derov, D. E. Walker, and V. N. Astratov, "Advantages of microsphere-assisted super-resolution imaging technique over solid immersion lens and confocal microscopies," *Appl. Phys. Lett.*, vol. 104, p. 61117, 2014.
- [14] Z. Wang *et al.*, "Optical virtual imaging at 50 nm lateral resolution with a white-light nanoscope," *Nat. Commun.*, vol. 2, no. 1, pp. 216–218, 2011.
- [15] E. Abbe, "Beiträge zur Theorie des Mikroskops und der mikroskopischen Wahrnehmung: I. Die Construction von Mikroskopen auf Grund der Theorie," *Arch. für mikroskopische Anat.*, vol. 9, pp. 413–418, 1873.
- [16] L. I. Schiff, *Quantum Mechanics*, First Edit. New York: McGRAW-HILL BOOK COMPANY, INC, 1949.
- [17] E. H. Synge, "A suggested method for extending the microscopic resolution into the ultramicroscopic region," *Phil. Mag.*, vol. 6, p. 356, 1928.
- [18] T. Roy, "CONTROL AND LOCALISATION OF LIGHT WITH ENGINEERED NANO-STRUCTURES," UNIVERSITY OF SOUTHAMPTON FACULTY, 2014.

- [19] D. W. Pohl, W. Denk, and M. Lanz, "Optical stethoscopy: Image recording with resolution $\lambda/20$," *Appl. Phys. Lett.*, vol. 44, no. 7, pp. 651–653, 1984.
- [20] J. Wessel, "Surface-enhanced optical microscopy," *J. Opt. Soc. Am. B*, vol. 2, no. 9, p. 1538, 1985.
- [21] S. Patane, P. G. Gucciardi, M. Labardi, and M. Allegrini, "Apertureless near-field optical microscopy," *Riv. Del Nuovo Cim.*, vol. 27, pp. 1–46, 2004.
- [22] A. Bek, R. Vogelgesang, and K. Kern, "Apertureless scanning near field optical microscope with sub-10nm resolution," *Rev. Sci. Instrum.*, vol. 77, no. 4, p. 43703, 2006.
- [23] X. Zhang and Z. Liu, "Superlenses to overcome the diffraction limit," *Nat. Mater.*, vol. 7, pp. 435–441, 2008.
- [24] Z. Liu, N. Fang, T. J. Yen, and X. Zhang, "Rapid growth of evanescent wave by a silver superlens," *Appl. Phys. Lett.*, vol. 83, no. 25, pp. 5184–5186, 2003.
- [25] N. Fang, Z. Liu, T.-J. Yen, and X. Zhang, "Regenerating evanescent waves from a silver superlens," *Opt. Express*, vol. 11, pp. 682–687, 2003.
- [26] N. Fang, H. Lee, C. Sun, and X. Zhang, "Sub-Diffraction Limited Optical Imaging with a Silver Superlens," *Science (80-.)*, vol. 308, pp. 534–537, 2005.
- [27] H. Lee *et al.*, "Realization of optical superlens imaging below the diffraction limit," *New J. Phys.*, vol. 7, pp. 0–16, 2005.
- [28] Z. Liu *et al.*, "Far-Field Optical Superlens," *Nano Lett.*, vol. 7, no. 2, pp. 403–408, 2007.
- [29] S. Durant, Z. Liu, J. M. Steele, and X. Zhang, "Theory of the transmission properties of an optical far-field superlens for imaging beyond the diffraction limit," *J. Opt. Soc. Am. B*,

vol. 23, no. 11, p. 2383, 2006.

- [30] Z. Liu *et al.*, “Experimental studies of far-field superlens for sub-diffractive optical imaging,” *Opt. Express*, vol. 15, no. 11, pp. 6947–6954, 2007.
- [31] Z. Liu, H. Lee, Y. Xiong, C. Sun, and X. Zhang, “Far-Field Optical Hyperlens Magnifying Sub-Diffraction-Limited Objects,” *Science (80-.)*, vol. 315, pp. 1686–1686, 2007.
- [32] E. Shamonina, V. A. Kalinin, K. H. Ringhofer, and L. Solymar, “Imaging, compression and Poynting vector streamlines for negative permittivity materials,” *Electron. Lett.*, vol. 37, pp. 1243–1244, 2001.
- [33] P. A. Belov and Y. Hao, “Subwavelength imaging at optical frequencies using a transmission device formed by a periodic layered metal-dielectric structure operating in the canalization regime,” *Phys. Rev. B*, vol. 73, pp. 1–4, 2006.
- [34] B. Wood, J. B. Pendry, and D. P. Tsai, “Directed subwavelength imaging using a layered metal-dielectric system,” *Phys. Rev. B - Condens. Matter Mater. Phys.*, vol. 74, no. 11, pp. 1–8, 2006.
- [35] J. Rho *et al.*, “Spherical hyperlens for two-dimensional sub-diffractive imaging at visible frequencies,” *Nat. Commun.*, vol. 1, no. 9, pp. 143–145, 2010.
- [36] S. A. Schelkunoff, “A Mathematical Theory of Linear Arrays,” *Bell Syst. Tech. J.*, vol. 22, no. 1, pp. 80–107, 1943.
- [37] G. T. Di Francia, “Super-gain antennas and optical resolving power,” *Nuovo Cim.*, vol. 9, pp. 426–438, 1952.
- [38] J. A. Bucklew and B. E. A. Saleh, “Theorem for high-resolution high-contrast image synthesis,” *J. Opt. Soc. Am. A*, vol. 2, no. 8, pp. 1233–1236, 1985.

- [39] Y. Aharonov, D. Z. Albert, and L. Vaidman, "How the result of a measurement of a component of the spin of a spin-(1/2 particle can turn out to be 100," *Phys. Rev. Lett.*, vol. 60, pp. 1351–1354, 1989.
- [40] M. V. Berry, "Evanescent and real waves in quantum billiards and Gaussian beams," *J. Phys. A. Math. Gen.*, vol. 27, no. 11, 1994.
- [41] E. T. F. Rogers, S. Savo, J. Lindberg, T. Roy, M. R. Dennis, and N. I. Zheludev, "Super-oscillatory optical needle," *Appl. Phys. Lett.*, vol. 102, no. 3, 2013.
- [42] W. Lukosz, "Optical Systems with Resolving Powers Exceeding the Classical Limit," *J. Opt. Soc. Am.*, vol. 51, pp. 1463–1472, 1966.
- [43] B. Bailey, D. L. Farkas, D. L. Taylor, and F. Lanni, "Enhancement of axial resolution in fluorescence microscopy by standing-wave excitation.," *Nature*, vol. 366, pp. 44–8, 1993.
- [44] R. Fiolka, L. Shao, E. H. Rego, M. W. Davidson, and M. G. L. Gustafsson, "Time-lapse two-color 3D imaging of live cells with doubled resolution using structured illumination," *Proc. Natl. Acad. Sci.*, vol. 109, no. 14, pp. 5311–5315, 2012.
- [45] T. A. Klar and S. W. Hell, "Subdiffraction resolution in far-field fluorescence microscopy," *Opt. Lett.*, vol. 24, no. 14, p. 954, 1999.
- [46] E. Betzig *et al.*, "Imaging Intracellular Fluorescent Proteins at Nanometer Resolution," *Science (80-.)*, vol. 313, pp. 1642–1646, 2006.
- [47] S. W. Hell *et al.*, "The 2015 super-resolution microscopy roadmap," *J. Phys. D. Appl. Phys.*, vol. 48, p. 443001, 2015.
- [48] E. G. Van Putten, D. Akbulut, J. Bertolotti, W. L. Vos, A. Lagendijk, and A. P. Mosk, "Scattering lens resolves sub-100 nm structures with visible light," *Phys. Rev. Lett.*, vol.

- 106, no. 19, pp. 1–4, 2011.
- [49] J. H. Park *et al.*, “Subwavelength light focusing using random nanoparticles,” *Nat. Photonics*, vol. 7, no. 6, pp. 454–458, 2013.
 - [50] C. Park *et al.*, “Full-field subwavelength imaging using a scattering superlens,” *Phys. Rev. Lett.*, vol. 113, p. 113901, 2014.
 - [51] S. Hell and E. H. K. Stelzer, “Fundamental improvement of resolution with a 4Pi-confocal fluorescence microscope using two-photon excitation,” *Opt. Commun.*, vol. 93, pp. 277–282, 1992.
 - [52] J. Bewersdorf, A. Egner, and S. W. Hell, “4Pi-Confocal Microscopy Is coming of Age,” *Imaging Microsc.*, pp. 24–25, 2004.
 - [53] M. C. Lang, T. Staudt, J. Engelhardt, and S. W. Hell, “4Pi microscopy with negligible sidelobes,” *New J. Phys.*, vol. 10, 2008.
 - [54] Z. B. Wang, “OPTICAL RESONANCE AND NEAR FIELD EFFECTS: SMALL PARTICLES UNDER LASER IRRADIATION,” National University of Singapore, 2005.
 - [55] A. Heifetz, S. C. Kong, A. V. Sahakian, A. Taflove, and V. Backman, “Photonic nanojets,” *J. Comput. Theor. Nanosci.*, vol. 6, no. 9, pp. 1979–1992, 2009.
 - [56] W. Guo, Z. B. Wang, L. Li, Z. Liu, B. Luk’yanchuk, and D. J. Whitehead, “Chemical-assisted laser parallel nanostructuring of silicon in optical near fields,” *Nanotechnology*, vol. 19, no. 45. 2008.
 - [57] W. Guo, “Laser Parallel Nanopatterning of Lines and Curves by Micro-particle Lens Arrays,” *J. Laser Micro/Nanoengineering*, vol. 2, no. 3, pp. 212–215, 2007.

- [58] W. Guo, Z. B. Wang, L. Li, D. J. Whitehead, B. S. Luk'Yanchuk, and Z. Liu, "Near-field laser parallel nanofabrication of arbitrary-shaped patterns," *Appl. Phys. Lett.*, vol. 90, no. 24, pp. 2005–2008, 2007.
- [59] G. X. Chen *et al.*, "Large-area parallel near-field optical nanopatterning of functional materials using microsphere mask," *J. Alloys Compd.*, vol. 449, no. 1–2, pp. 265–268, 2008.
- [60] Y. Zhou, M. H. Hong, J. Y. H. Fuh, L. Lu, B. S. Lukyanchuk, and Z. B. Wang, "Near-field enhanced femtosecond laser nano-drilling of glass substrate," *J. Alloys Compd.*, vol. 449, pp. 246–249, 2008.
- [61] A. Khan, Z. Wang, M. A. Sheikh, D. J. Whitehead, and L. Li, "Parallel near-field optical micro/nanopatterning on curved surfaces by transported micro-particle lens arrays," *J. Phys. D: Appl. Phys.*, vol. 43, no. 30, 2010.
- [62] A. Khan, Z. Wang, M. A. Sheikh, D. J. Whitehead, and L. Li, "Laser micro/nano patterning of hydrophobic surface by contact particle lens array," *Appl. Surf. Sci.*, vol. 258, no. 2, pp. 774–779, 2011.
- [63] X. Li, Z. Chen, A. Taflove, and V. Backman, "Optical analysis of nanoparticles via enhanced backscattering facilitated by 3-D photonic nanojets," *Opt. Express*, vol. 13, no. 2, pp. 526–533, 2005.
- [64] S. Kong, A. Sahakian, A. Taflove, and V. Backman, "Photonic nanojet-enabled optical data storage," *Opt. Express*, vol. 16, pp. 13713–13719, 2008.
- [65] K. J. Yi, H. Wang, Y. F. Lu, and Z. Y. Yang, "Enhanced Raman scattering by self-assembled silica spherical microparticles," *J. Appl. Phys.*, vol. 101, no. 6, 2007.
- [66] R. J. Potton, "Reciprocity in optics," *Reports Prog. Phys.*, vol. 67, no. 5, pp. 717–754, 2004.

- [67] Z. Wang *et al.*, "The optical microscopy with virtual image breaks a record: 50-nm resolution imaging is demonstrated," *Nat. Commun.*, vol. 2, p. 218, Jun. 2010.
- [68] Y. L. Sun *et al.*, "Dynamically tunable protein microlenses," *Angew. Chemie - Int. Ed.*, vol. 51, no. 7, pp. 1558–1562, 2012.
- [69] A. Darafsheh *et al.*, "Optical super-resolution by high-index liquid-immersed microspheres," *Appl. Phys. Lett.*, vol. 101, p. 141128, 2012.
- [70] R. h Webb, "Confocal optical microscopy," *Rep. Prog. Phys*, vol. 59, pp. 427–471, 1996.
- [71] Z. Wang, "Microsphere super-resolution imaging," *Nanoscience*, vol. 3, pp. 193–210, 2016.
- [72] Y. Yan, L. Li, C. Feng, W. Guo, S. Lee, and M. Hong, "Microsphere-coupled scanning laser confocal nanoscope for sub-diffraction-limited imaging at 25 nm lateral resolution in the visible spectrum," *ACS Nano*, vol. 8, no. 2. pp. 1809–1816, 2014.
- [73] L. A. Krivitsky, J. J. Wang, Z. Wang, and B. Luk'Yanchuk, "Locomotion of microspheres for super-resolution imaging," *Sci. Rep.*, vol. 3, pp. 3–7, 2013.
- [74] J. Li *et al.*, "Swimming Microrobot Optical Nanoscopy," *Nano Lett.*, vol. 16, no. 10, pp. 6604–6609, 2016.
- [75] F. Wang *et al.*, "Scanning superlens microscopy for non-invasive large field-of-view visible light nanoscale imaging," *Nat. Commun.*, vol. 7, pp. 1–10, 2016.
- [76] Y. Li, H. Xin, X. Liu, Y. Zhang, H. Lei, and B. Li, "Trapping and Detection of Nanoparticles and Cells Using a Parallel Photonic Nanojet Array," *ACS Nano*, vol. 10, no. 6, pp. 5800–5808, 2016.

- [77] Y. C. Li *et al.*, “Manipulation and detection of single nanoparticles and biomolecules by a photonic nanojet,” *Light Sci. Appl.*, vol. 5, no. 12, pp. 1–9, 2016.
- [78] H. Xin, R. Xu, and B. Li, “Optical trapping, driving, and arrangement of particles using a tapered fibre probe,” *Sci. Rep.*, vol. 2, p. 818, 2012.
- [79] H. Yang, M. Cornaglia, and M. A. M. Gijs, “Photonic nanojet array for fast detection of single nanoparticles in a flow,” *Nano Lett.*, vol. 15, pp. 1730–1735, 2015.
- [80] Z. Wang, “PCT/GB2014/052578,” 2014.
- [81] M. Wu *et al.*, “Super-focusing of center-covered engineered microsphere,” *Sci. Rep.*, vol. 6, pp. 1–7, 2016.
- [82] M. X. Wu *et al.*, “Modulation of photonic nanojets generated by microspheres decorated with concentric rings,” *Opt. Express*, vol. 23, no. 15, p. 20096, 2015.
- [83] G. Mie, “Beitrage zur Optik truber Medien, speziell kolloidaler Metallosungen,” *Ann. Phys.*, vol. 330, pp. 377–445, 1908.
- [84] J. M. Jin, *The finite element method in electromagnetics*. New York: John Wiley, 2002.
- [85] A. Taflove and S. C. Hagness, *Computational electrodynamics: the finite-difference time-domain method*, 3rd ed. Norwood: Artech House, 2005.
- [86] T. Weiland, “Time domain electromagnetic field computation with finite difference methods,” *Int. J. Numer. Model. Electron. Networks, Devices Fields*, vol. 9, no. 4, pp. 295–319, 1996.
- [87] Z. Wang, “Microsphere super-resolution imaging,” *Nanoscience*, vol. 3, pp. 193–210, 2016.

- [88] A. Darafsheh, G. Wu, S. Yang, and J. C. Finlay, "Super-resolution optical microscopy by using dielectric microwires," *Proc. SPIE*, vol. 9713, p. 97130U, 2016.
- [89] R. Ye *et al.*, "Experimental far-field imaging properties of a $\sim 5\text{-}\mu\text{m}$ diameter spherical lens," *Opt. Lett.*, vol. 38, no. 11, p. 1829, 2013.
- [90] G. Gu, R. Zhou, H. Xu, G. Cai, and Z. Cai, "Subsurface nano-imaging with self-assembled spherical cap optical nanoscopy," *Opt. Express*, vol. 24, no. 5, p. 4937, 2016.
- [91] L. Yue, B. Yan, and Z. Wang, "Photonic nanojet of cylindrical metalens assembled by hexagonally arranged nanofibers for breaking the diffraction limit," *Opt. Lett.*, vol. 41, no. 7, pp. 1336–1339, 2016.
- [92] B. Yan, L. Yue, and Z. Wang, "Engineering near-field focusing of a microsphere lens with pupil masks," *Opt. Commun.*, vol. 370, pp. 140–144, 2016.
- [93] M. Brust and C. J. Kiely, "Some recent advances in nanostructure preparation from gold and silver particles: A short topical review," *Colloids Surfaces A Physicochem. Eng. Asp.*, vol. 202, pp. 175–186, 2002.
- [94] S. D. Evans, S. R. Johnson, Y. L. Cheng, and T. Shen, "Vapour sensing using hybrid organic–inorganic nanostructured materials," *J. Mater. Chem.*, vol. 10, no. 1, pp. 183–188, 2000.
- [95] H. Wohltjen and A. W. Snow, "Colloidal Metal-Insulator-Metal Ensemble Chemiresistor Sensor," *Anal. Chem.*, vol. 70, no. 14, pp. 2856–2859, 1998.
- [96] L. Li, T. Zhai, H. Zeng, X. Fang, Y. Bando, and D. Golberg, "Polystyrene sphere-assisted one-dimensional nanostructure arrays: synthesis and applications," *J. Mater. Chem.*, vol. 21, no. 1, pp. 40–56, 2011.

- [97] W. Wu, A. Katsnelson, O. G. Memis, and H. Mohseni, "A deep sub-wavelength process for the formation of highly uniform arrays of nanoholes and nanopillars," *Nanotechnology*, vol. 18, no. 48, 2007.
- [98] V. Pacheco-Peña, I. Minin, O. Minin, and M. Beruete, "Increasing Surface Plasmons Propagation via Photonic Nanojets with Periodically Spaced 3D Dielectric Cuboids," *Photonics*, vol. 3, no. 1, p. 10, 2016.
- [99] A. Ashkin, J. M. Dziedzic, J. E. Bjorkholm, and S. Chu, "Observation of a single-beam gradient force optical trap for dielectric particles," *Opt. Lett.*, vol. 11, pp. 288–290, 1986.
- [100] A. Ashkin, "Acceleration and Trapping of Particles by Radiation Pressure," *Phys. Rev. Lett.*, vol. 24, no. 4, pp. 156–159, 1970.
- [101] S. R. Pettersen *et al.*, "Electrical four-point probing of spherical metallic thin films coated onto micron sized polymer particles," *Appl. Phys. Lett.*, vol. 109, no. 4, 2016.
- [102] S. Darwich, K. Mougin, A. Rao, E. Gnecco, S. Jayaraman, and H. Haidara, "Manipulation of gold colloidal nanoparticles with atomic force microscopy in dynamic mode: influence of particle–substrate chemistry and morphology, and of operating conditions," *Beilstein J. Nanotechnol.*, vol. 2, pp. 85–98, 2011.
- [103] H. Wu, T. W. Odom, D. T. Chiu, and G. M. Whitesides, "Fabrication of complex three-dimensional microchannel systems in PDMS," *J. Am. Chem. Soc.*, vol. 125, no. 2, pp. 554–559, 2003.
- [104] D. B. Wolfe, J. Christopher Love, and G. M. Whitesides, "Nanostructures Replicated by Polymer Molding," *Dekker Encycl. Nanosci. Nanotechnol.*, p. 2657, 2004.
- [105] A. J. Liu and S. R. Nagel, "Jamming is not just cool any more," *Nature*, vol. 396, no. 6706, pp. 21–22, 1998.

- [106] G. Biroli, "Jamming: A new kind of phase transition?," *Nat. Phys.*, vol. 3, no. 4, pp. 222–223, 2007.
- [107] G. Garnweitner, L. M. Goldenberg, O. V. Sakhno, M. Antonietti, M. Niederberger, and J. Stumpe, "Large-scale synthesis of organophilic zirconia nanoparticles and their application in organic-inorganic nanocomposites for efficient volume holography," *Small*, vol. 3, no. 9, pp. 1626–1632, 2007.
- [108] D. J. Little and D. M. Kane, "Hybrid immersion-polarization method for measuring birefringence applied to spider silks," *Opt. Lett.*, vol. 36, no. 20, p. 4098, 2011.
- [109] T. M. Squires and S. R. Quake, "Microfluidics: Fluid physics at the nanoliter scale," *Rev. Mod. Phys.*, vol. 77, no. 3, pp. 977–1026, 2005.
- [110] V. Yannopapas, "Photonic nanojets as three-dimensional optical atom traps: A theoretical study," *Opt. Commun.*, vol. 285, no. 12, pp. 2952–2955, 2012.
- [111] A. Ya. Dzyublik, G. Gosselin, V. Mèot, and P. Morel, "Role of screening in Coulomb excitation of nuclei by electrons in hot plasma," *EPL (Europhysics Lett.)*, vol. 102, p. 62001, 2013.
- [112] Y. Liu, C. F. Kuang, and Z. H. Ding, "Strong confinement of two-photon excitation field by photonic nanojet with radial polarization illumination," *Opt. Commun.*, vol. 284, no. 19, pp. 4824–4827, 2011.
- [113] M.-S. Kim, T. Scharf, S. Mühlig, C. Rockstuhl, and H. P. Herzig, "Engineering photonic nanojets," *Opt. Express*, vol. 19, no. 11, p. 10206, 2011.
- [114] A. V. Itagi and W. A. Challener, "Optics of photonic nanojets," *J. Opt. Soc. Am. A*, vol. 22, no. 12, p. 2847, 2005.

- [115] D. Grojo, L. Charmasson, A. Pereira, M. Sentis, and P. Delaporte, "Monitoring Photonic Nanojets from Microsphere Arrays by Femtosecond Laser Ablation of Thin Films," *J. Nanosci. Nanotechnol.*, vol. 11, no. 10, pp. 9129–9135, 2011.
- [116] M. Gerlach, Y. P. Rakovich, and J. F. Donegan, "Nanojets and directional emission in symmetric photonic molecules," *Opt. Express*, vol. 15, no. 25, p. 17343, 2007.
- [117] H. Guo *et al.*, "Near-field focusing of the dielectric microsphere with wavelength scale radius," *Opt. Express*, vol. 21, no. 2, pp. 2434–43, 2013.
- [118] M. T. Hill *et al.*, "Lasing in metallic-coated nanocavities," *Nat. Photonics*, vol. 1, no. 10, pp. 589–594, 2007.
- [119] Z. Hengyu, C. Zaichun, C. T. Chong, and H. Minghui, "Photonic jet with ultralong working distance by hemispheric shell," *Opt. Express*, vol. 23, no. 5, p. 6626, 2015.
- [120] Y. E. Geints, E. K. Panina, and A. A. Zemlyanov, "Control over parameters of photonic nanojets of dielectric microspheres," *Opt. Commun.*, vol. 283, no. 23, pp. 4775–4781, 2010.
- [121] V. Paeder, T. Scharf, P. Ruffieux, H. P. Herzig, R. Voelkel, and K. J. Weible, "Microlenses with annular amplitude and phase masks," *J. Eur. Opt. Soc.*, vol. 2, 2007.
- [122] N. Yao *et al.*, "Improving resolution of superlens lithography by phase-shifting mask," *Opt. Express*, vol. 19, no. 17, p. 15982, 2011.
- [123] M. Martínez-Corral, P. Andrés, C. J. Zapata-Rodríguez, and M. Kowalczyk, "Three-dimensional superresolution by annular binary filters," *Opt. Commun.*, vol. 165, no. 4, pp. 267–278, 1999.
- [124] G. Yang, "An optical pickup using a diffractive optical element for a high-density optical

- disc," *Opt. Commun.*, vol. 159, pp. 19–22, 1999.
- [125] C. Sheng, H. Liu, Y. Wang, S. N. Zhu, and D. A. Genov, "Trapping light by mimicking gravitational lensing," *Nat. Photonics*, vol. 7, no. 11, pp. 902–906, 2013.
- [126] M. Rothschild *et al.*, "Nanopatterning with UV Optical," *MRS Bull.*, vol. 30, pp. 942–946, 2005.
- [127] J. Zhang, Y. Kim, S.-H. Yang, and T. D. Milster, "Illumination artifacts in hyper-NA vector imaging," *J. Opt. Soc. Am. A*, vol. 27, no. 10, pp. 2272–2284, 2010.
- [128] P. Scholz, C. Gallrapp, U. Kerst, T. Lundquist, and C. Boit, "Optimizing focused ion beam created solid immersion lenses in bulk silicon using design of experiments," *Microelectron. Reliab.*, vol. 50, no. 9–11, pp. 1441–1445, 2010.
- [129] F. Hakan Köklü, B. B. Goldberg, and M. Selim Ünlü, "Dielectric interface effects in subsurface microscopy of integrated circuits," *Opt. Commun.*, vol. 285, no. 7, pp. 1675–1679, 2012.
- [130] D. A. Fletcher *et al.*, "Refraction contrast imaging with a scanning microlens," *Appl. Phys. Lett.*, vol. 78, no. 23, pp. 3589–3591, 2001.
- [131] B. D. Terris, H. J. Mamin, D. Rugar, W. R. Studenmund, and G. S. Kino, "Near-field optical data storage using a solid immersion lens," *Appl. Phys. Lett.*, vol. 65, pp. 388–390, 1994.
- [132] B. D. Terris, H. J. Mamin, and D. Rugar, "Near-field optical data storage," *Appl. Phys. Lett.*, vol. 68, p. 141, 1996.
- [133] K. Yamamoto, K. Osato, I. Ichimura, and F. Maeda, "0.8-Numerical-Aperture Two-Element Objective Lens for the Optical Disk," *Jpn. J. Appl. Phys.*, vol. 36, pp. 456–459, 1997.

- [134] I. Ichimura, S. Hayashi, and G. S. Kino, "High-density optical recording using a solid immersion lens.," *Appl. Opt.*, vol. 36, no. 19, pp. 4339–48, 1997.
- [135] M. Lang, T. D. Milster, T. Minamitani, G. Borek, and D. Brown, "Fabrication and characterization of sub-100 nm diameter gallium phosphide solid immersion lens arrays," *Japanese Journal of Applied Physics, Part 1: Regular Papers and Short Notes and Review Papers*, vol. 44, no. 5 B, pp. 3385–3387, 2005.
- [136] L. P. Ghislain *et al.*, "Near-field photolithography with a solid immersion lens," *Appl. Phys. Lett.*, vol. 74, no. 4, pp. 501–503, 1999.
- [137] A. V. Kildishev, A. Boltasseva, and V. M. Shalaev, "Planar Photonics with Metasurfaces," *Nat. Mater.*, vol. 339, p. 1232009, 2013.
- [138] N. I. Zheludev, "Obtaining optical properties on demand," *Science (80-.)*, vol. 348, no. 6238, pp. 973–974, 2015.
- [139] N. Yu and F. Capasso, "Flat optics with designer metasurfaces," *Nat. Mater.*, vol. 13, no. 2, pp. 139–150, 2014.
- [140] Y. Liu and X. Zhang, "Metamaterials: a new frontier of science and technology," *Chem. Soc. Rev.*, vol. 40, no. 5, p. 2494, 2011.
- [141] C. M. Soukoulis and M. Wegener, "Past achievements and future challenges in the development of three-dimensional photonic metamaterials," *Nat. Photonics*, vol. 5, pp. 524–530, 2011.
- [142] C. M. Soukoulis and M. Wegener, "Optical Metamaterials— More Bulky and Less Lossy," *Science (80-.)*, vol. 330, pp. 1633–1634, 2010.
- [143] Q. Zhao, J. Zhou, F. Zhang, and D. Lippens, "Mie resonance-based dielectric

- metamaterials,” *Mater. Today*, vol. 12, no. 12, pp. 60–69, 2009.
- [144] J. B. Khurgin, “How to deal with the loss in plasmonics and metamaterials,” *Nat. Nanotechnol.*, vol. 10, no. 1, pp. 2–6, 2015.
- [145] S. Jahani and Z. Jacob, “All-dielectric metamaterials,” *Nat. Nanotechnol.*, vol. 11, no. 1, pp. 23–36, 2016.
- [146] S. J. Corbitt, M. Francoeur, and B. Raeymaekers, “Implementation of optical dielectric metamaterials: A review,” *J. Quant. Spectrosc. Radiat. Transf.*, vol. 158, pp. 3–16, 2015.
- [147] R. C. Dunn, “Near-Field Scanning Optical Microscopy,” *Chem. Rev.*, vol. 99, no. 10, pp. 2891–2928, 1999.
- [148] D. Lu and Z. Liu, “Hyperlenses and metalenses for far-field super-resolution imaging,” *Nat. Commun.*, vol. 3, pp. 1–9, 2012.
- [149] H. Yang, N. Moullan, J. Auwerx, and M. A. M. Gijs, “Super-resolution biological microscopy using virtual imaging by a microsphere nanoscope,” *Small*, vol. 10, no. 9, pp. 1712–1718, 2014.
- [150] S. M. Mansfield and G. S. Kino, “Solid immersion microscope,” *Appl. Phys. Lett.*, vol. 57, no. 0, p. 2615, 1990.
- [151] K. A. Serrels *et al.*, “Solid immersion lens applications for nanophotonic devices,” *J. Nanophotonics*, vol. 2, p. 21854, 2008.
- [152] A. Vlad, I. Huynen, and S. Melinte, “Wavelength-scale lens microscopy via thermal reshaping of colloidal particles,” *Nanotechnology*, vol. 23, no. 28, 2012.
- [153] J. Y. Lee *et al.*, “Near-field focusing and magnification through self-assembled nanoscale

- spherical lenses,” *Nature*, vol. 460, no. 7254, pp. 498–501, 2009.
- [154] D. Kang *et al.*, “Shape-controllable microlens arrays via direct transfer of photocurable polymer droplets,” *Adv. Mater.*, vol. 24, no. 13, pp. 1709–1715, 2012.
- [155] D. A. Weitz, “Packing in the spheres,” *Science (80-.)*, vol. 303, pp. 968–969, 2004.
- [156] C. Lü and B. Yang, “High refractive index organic–inorganic nanocomposites: design, synthesis and application,” *J. Mater. Chem.*, vol. 19, no. 19, p. 2884, 2009.
- [157] S. Lee, H.-J. Shin, S.-M. Yoon, D. K. Yi, J.-Y. Choi, and U. Paik, “Refractive index engineering of transparent ZrO₂–polydimethylsiloxane nanocomposites,” *J. Mater. Chem.*, vol. 18, pp. 1751–1755, 2008.
- [158] C. Lu, C. Guan, Y. Liu, Y. Cheng, and B. Yang, “PbS/polymer nanocomposite optical materials with high refractive index,” *Chem. Mater.*, vol. 17, no. 9, pp. 2448–2454, 2005.
- [159] M. N. Tchoul *et al.*, “Assemblies of titanium dioxide-polystyrene hybrid nanoparticles for dielectric applications,” *Chem. Mater.*, vol. 22, no. 5, pp. 1749–1759, 2010.
- [160] C. Lü, Y. Cheng, Y. Liu, F. Liu, and B. Yang, “A facile route to ZnS-polymer nanocomposite optical materials with high nanophase content via γ -ray irradiation initiated bulk polymerization,” *Adv. Mater.*, vol. 18, no. 9, pp. 1188–1192, 2006.
- [161] S. Yang, Y. Wang, and H. D. Sun, “Advances and Prospects for Whispering Gallery Mode Microcavities,” *Adv. Opt. Mater.*, vol. 3, no. 9, pp. 1136–1162, 2015.
- [162] D. Wildanger *et al.*, “Solid immersion facilitates fluorescence microscopy with nanometer resolution and sub-Ångström emitter localization,” *Adv. Mater.*, vol. 24, no. 44, pp. 309–313, 2012.

- [163] K. W. Allen *et al.*, “Super-resolution microscopy by movable thin-films with embedded microspheres: Resolution analysis,” *Ann. Phys.*, vol. 527, no. 7–8, pp. 513–522, 2015.
- [164] V. N. Astratov and A. Darafsheh, “Methods and systems for superresolution optical imaging using high-index of refraction microspheres and micro-cylinders,” patent 20140355108 A1, 2014.
- [165] J. N. Monks, B. Yan, N. Hawkins, F. Vollrath, and Z. Wang, “Spider Silk: Mother Nature’s Bio-Superlens,” *Nano Lett.*, vol. 16, no. 9, pp. 5842–5845, 2016.
- [166] X. Hao *et al.*, “From microscopy to nanoscopy via visible light,” *Light Sci. Appl.*, vol. 2, no. OCTOBER, 2013.
- [167] W. Fan, B. Yan, Z. Wang, and L. Wu, “Three-dimensional all-dielectric metamaterial solid immersion lens for subwavelength imaging at visible frequencies,” *Sci. Adv.*, vol. 2, no. 8, p. e1600901, 2016.
- [168] G. Wysocki, J. Heitz, and D. Bäuerle, “Near-field optical nanopatterning of crystalline silicon,” *Appl. Phys. Lett.*, vol. 84, no. 12, pp. 2025–2027, 2004.
- [169] R. Riehn, A. Charas, J. Morgado, and F. Cacialli, “Near-field optical lithography of a conjugated polymer,” *Appl. Phys. Lett.*, vol. 82, no. 4, pp. 526–528, 2003.
- [170] E. Betzig *et al.*, “Near - field magneto - optics and high density data storage Near-field and high density data storage,” *Appl. Phys. Lett.*, vol. 61, pp. 142–144, 1992.
- [171] Y. F. Lu, Z. H. Mai, Y. W. Zheng, and W. D. Song, “Nanostructure fabrication using pulsed lasers in combination with a scanning tunneling microscope: Mechanism investigation,” *Appl. Phys. Lett.*, vol. 76, no. 9, pp. 1200–1202, 2000.
- [172] J. Jersch and K. Dickmann, “Nanostructure fabrication using laser field enhancement in

- the near field of a scanning tunneling microscope tip," *Appl. Phys. Lett.*, vol. 68, pp. 868–870, 1996.
- [173] J. Boneberg, H.-J. Münzer, M. Tresp, M. Ochmann, and P. Leiderer, "The mechanism of nanostructuring upon nanosecond laser irradiation of a STM tip," *Appl. Phys. A Mater. Sci. Process.*, vol. 67, no. 4, pp. 381–384, 1998.
- [174] S. M. Huang, M. H. Hong, B. Lukiyanchuk, and T. C. Chong, "Nanostructures fabricated on metal surfaces assisted by laser with optical near-field effects," *Appl. Phys. A*, vol. 77, no. 2, pp. 293–296, 2003.
- [175] G. Wysocki, R. Denk, K. Piglmayer, N. Arnold, and D. Bäuerle, "Single-step fabrication of silicon-cone arrays," *Appl. Phys. Lett.*, vol. 82, no. 5, pp. 692–693, 2003.
- [176] Z. B. Wang, M. H. Hong, B. S. Luk'yanchuk, Y. Lin, Q. F. Wang, and T. C. Chong, "Angle effect in laser nanopatterning with particle-mask," *J. Appl. Phys.*, vol. 96, no. 11, pp. 6845–6850, 2004.
- [177] R. Piparia, E. W. Rothe, and R. J. Baird, "Nanobumps on silicon created with polystyrene spheres and 248 or 308 nm laser pulses," *Appl. Phys. Lett.*, vol. 89, no. 22, pp. 2004–2007, 2006.
- [178] M. Mosbacher, H.-J. Münzer, J. Zimmermann, J. Solis, J. Boneberg, and P. Leiderer, "Optical field enhancement effects in laser-assisted particle removal," *Applied Physics A Materials Science & Processing*, vol. 72, no. 1, pp. 41–44, 2001.
- [179] W. Srituravanich, S. Durant, H. Lee, C. Sun, and X. Zhang, "Deep subwavelength nanolithography using localized surface plasmon modes on planar silver mask," *J. Vac. Sci. Technol. B Microelectron. Nanom. Struct.*, vol. 23, no. 6, p. 2636, 2005.
- [180] Z. W. Liu, Q. H. Wei, and X. Zhang, "Surface plasmon interference nanolithography,"

Nano Lett., vol. 5, no. 5, pp. 957–961, 2005.

- [181] A. Darafsheh, C. Guardiola, A. Palovcak, J. C. Finlay, and A. Cárabe, “Optical super-resolution imaging by high-index microspheres embedded in elastomers,” *Opt. Lett.*, vol. 40, pp. 5–8, 2015.
- [182] X. D. Wang, B. Chen, and Z. S. Wang, “Youngs interference in light scattering by spheres,” *Opt. Lasers Eng.*, vol. 50, no. 3, pp. 349–353, 2012.
- [183] B. S. Luk’yanchuk, N. Arnold, S. M. Huang, Z. B. Wang, and M. H. Hong, “Three-dimensional effects in dry laser cleaning,” *Appl. Phys. A*, vol. 77, pp. 209–215, 2003.
- [184] N. Schuergers *et al.*, “Cyanobacteria use micro-optics to sense light direction,” *Elife*, vol. 5, pp. 1–16, 2016.